Organic Lateral Heterojunction Devices for Vapor-phase Chemical Detection

by

John C. Ho

Submitted to the Department of Electrical Engineering and Computer Science
in partial fulfillment of the requirements for the degree of

Doctor of Philosophy in Electrical Engineering and Computer Science

at the

MASSACHUSETTS INSTITUTE OF TECHNOLOGY

June 2009

Author .....
Department of Electrical Engineering and Computer Science
May 21, 2009

Certified by .....
Vladimir Bulović
Professor
Thesis Supervisor

Accepted by .....
Terry P. Orlando
Chairman, Department Committee on Graduate Students

Organic Lateral Heterojunction Devices for Vapor-phase Chemical Detection

by

John C. Ho

Submitted to the Department of Electrical Engineering and Computer Science
on May 21, 2009, in partial fulfillment of the
requirements for the degree of
Doctor of Philosophy in Electrical Engineering and Computer Science

Abstract

As the U.S. is engaged in battle overseas, there is an urgent need for the development of sensors for early warning and protection of military forces against potential attacks. On the battlefields, improvised explosive devices (IEDs) have resulted in 54% of all coalition deaths in Iraq and 59% in Afghanistan. The U.S. military has responded with an intensive program of technology development, spending $12.4 billion over the past three years on counter-IED equipment, technology R&D, training, and other measures through the Joint Improvised Explosive Device Defeat Organization (JIEDDO). "Sniffing"technology, based on fluorescent polymers, has emerged as one of the most sensitive tools in the military's explosives-detecting arsenal. Fluorescent polymer sensors have demonstrated effective ultra-trace, vapor-phase detection of trinitrotoluene (TNT) at security checkpoints and during vehicular sweeps, achieving sensitivity levels comparable to the canine nose. In this sensor scheme, a large contribution to the noise signal is the inefficient transduction of the polymer's chemically sensitive, photoluminescent signal into an electrical signal. The poor optical coupling of the polymer's photoluminescence into a photodetector, reduces the signal-to-noise ratio (SNR) and overall sensor performance. In this work we have developed a novel transduction mechanism and device structure that enable more efficient photon-to-electron conversion resulting in direct transduction of the chemical signature into an electrical signal. Device models detailing the physical processes of device operation will be presented along with supporting experimental evidence. In addition, detection of as little as 1 picogram of TNT has been demonstrated. Ultimately, this work results in a solid-state sensor platform that can be readily engineered to accept any chemosensitive fluorescent polymer for a variety of ultra-trace sensing applications with potential uses in the medical diagnostic, industrial processing, environmental, and defense industries.

Thesis Supervisor: Vladimir Bulović
Title: Professor

Acknowledgments

First and foremost, I want to thank my "adventure buddy" Sara for being by my side from day one of my Ph.D. I have and will always maintain that she is my "lucky" charm, and as luck would have it I met her just as I was starting on the sensor project. I am most grateful for her unconditional patience and tireless support over the last several years as I navigated the tricky, winding road towards a degree. Getting my degree is that much more rewarding knowing that I get to share my achievement with her. She was there through all the highs and the lows and still found a way to love me anyway. I look forward to this next chapter in our lives, and I can't wait to get started.

To my family, thank you for providing me with a support network outside of MIT. I was lucky to have all of them so close to Cambridge during my time at MIT. It's a blessing that few other students at MIT can have.

I also have to thank my advisor and friend, Vladimir, for allowing me to be a part of his lab over the last seven years. His genuine enthusiasm for science and creativity are second to none, and I am grateful to have worked with him. It was his trust in my work that allowed me to grow and thrive as a scientist.

To my mentor and officemate, Alexi, I owe a great debt. When I was a clueless student with no research experience, Alexi was an excellent role model, tutor, teacher, and friend. We went through MIT on parallel tracks, and we helped each other to stay on course. I will never forget his limitless patience and excellent scientific intuition, which I relied on throughout our time together. I can honestly say that my experience at MIT has been better for knowing and working with him.

I can't forget to mention Jill and Tim for their curiosity and youthful energy, which enabled me to see my research in new ways. Jill's been a great help to me as soon as she joined our group, and I will always appreciate her warmhearted nature. She will make a great professor someday. Tim's been a very generous and caring office mate, and I will miss his inquisitive mind and probing "what if" scenarios. I look forward to great things from him.

To Aimee, thank you for sharing this important research with me. Without her chemistry skills and tireless heroics on my behalf, none of this would be possible. I sincerely hope we get the chance to work together in the future.

To my "brother from another" lab, Ivan. Thanks for always providing the comic relief that is so hard to find at a graduate school like MIT. I will miss our day-to-day interactions, but I know that we'll find ways to stay connected. After all, how many Martin Lawrence fans can there be?

Finally, to the rest of the members of LOOE (former and present), who have contributed to this work in countless ways, thank you. We have one of the great research groups at MIT, and that's a direct product of all of the wonderful people in our group. It was my honor to work with all of you, and I can't express enough gratitude for that.

Contents

List of Figures

List of Tables

Chapter 1

Introduction

A journey of a thousand miles must begin with a single step.

LAO TZU

Chinese Philosopher

Devices incorporating organic (carbon-containing) semiconducting films have steadily achieved commercialization starting with photoreceptors in xerography [1], then progressing to organic light emitting diode (OLED) displays [2] and thin film photovoltaics [3, 4], and finally to chemical sensors [5]. Chemical sensor research represents a rich field of study, utilizing a diverse array of technologies to accomplish the difficult task of transducing sensory information into a quantifiable chemical, optical, or electrical signals. The need to extract increasing amounts of sensory information from our environment, fuels the development of sensors that are easier to manufacture, capable of miniaturization, and more sensitive to vapors of interest. Vapor-phase sensors have the advantage of employing a non-destructive, non-invasive method of detection with the potential for high degrees of sensitivity. Depending on the vapor pressure of the analyte (the chemical species being detected), some vapor-phase sensors are capable of detecting as little as a femtogram of material (e.g. several thousand molecules) [6]. A promising class of materials for ultra-trace, vapor-phase chemical sensing is the fluorescent conjugated polymer [7]. Pioneering research by the Swager Group in the Department of Chemistry at MIT, has led to the development of a poly-

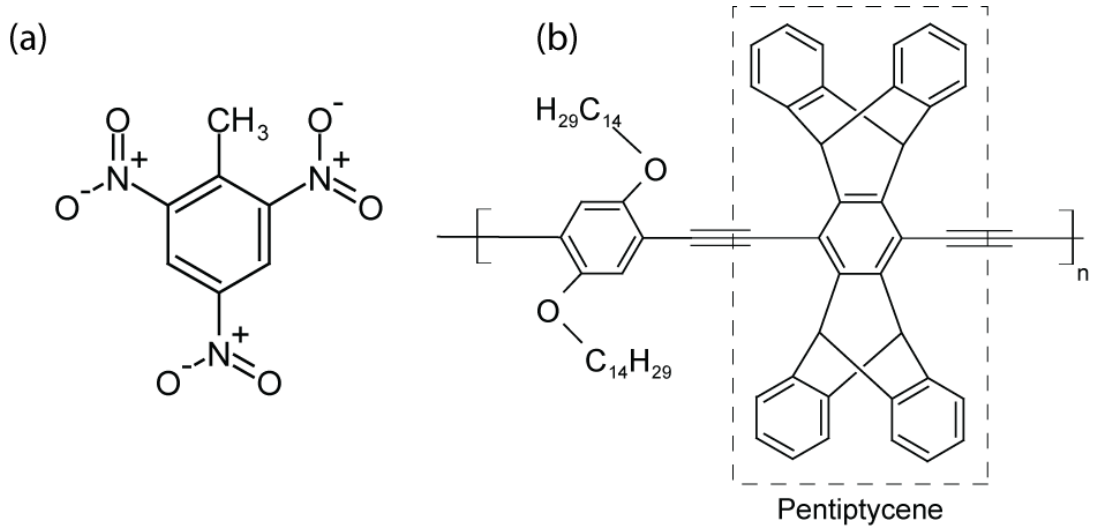

Figure 1-1: (a) Chemical structure of 2,4,6-trinitrotoluene (TNT) and (b) a fluorescent polymer with pentiptycene molecules incorporated in backbone.

mer that retains its photoluminescent efficiency in thin films. Attached pentiptycene molecules create scaffolding to allow the polymer strands to maintain adequate separation, preventing self-quenching processes in the solid state [Fig. 1-1]. In addition to its favorable optical properties, this polymer is capable of exhibiting luminescence quenching upon the introduction of TNT vapor [Fig. 1-2]. Once TNT molecules bind to the polymer, excitons generated by photoluminescent excitation can diffuse along the polymer backbone to transfer charge to the TNT molecules. The large exciton diffusion lengths in conjugated polymers allow the TNT molecules to quench excitons that are generated many monomer units away from the binding site. In this manner, these conjugated fluorescent polymers can exhibit a large differential luminescence signal with very small amounts of TNT.

Organic materials, such as fluorescent conjugated polymers, have the advantages of being both synthetically flexible [8] and amenable to room temperature processing, which allows for the development of an infinite library of chemical sensors at lower costs. While using sensors to detect explosives or as medical diagnostics tools may seem straightforward, each application presents a unique set of challenges and specifications. What may work for the detection of land mines underfoot may not necessarily be useful for detecting disease within a human body. In fact, much of the bottleneck

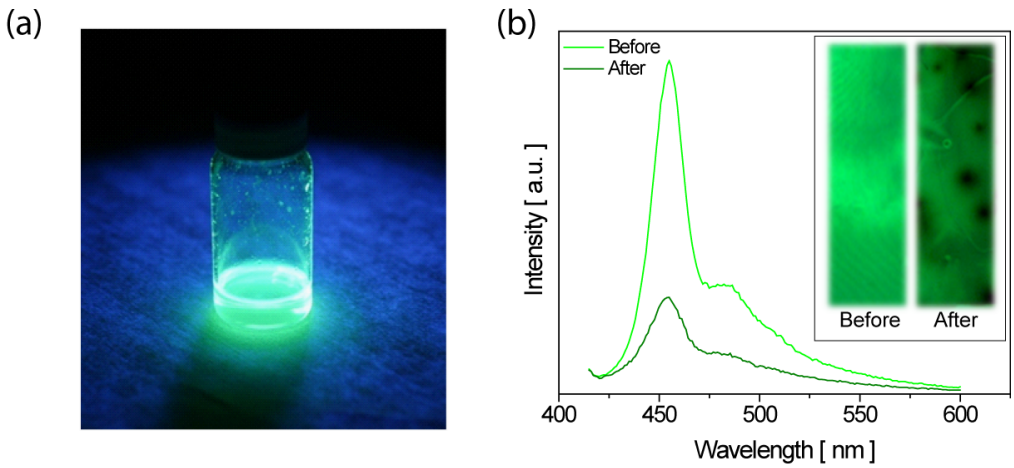

Figure 1-2: (a) Fluorescent conjugated polymer solvated in toluene. (b) Digital image depicting a thin film of fluorescent polymer before and after exposure to TNT vapor.

in commercializing chemical sensor research has been framing the right problem to be solved with the given sensor technology, all while minimizing production costs.

1.1 Problem Statement

State-of-the-art sensors utilizing fluorescent polymers have been commercialized, with success, in the area of ultra-trace vapor-phase explosives detection. Figure 1-3(a), details a typical fluorescent polymer sensing scheme. Land mine and improvised explosive device (IED) detection has played an increasingly important, life-saving role in the war theaters of Iraq and Afghanistan. Developed by ICx Technologies, the Fido XT™ portable explosives detector [Fig. 1-3(b)] can be combined with autonomous robots to safely find and disarm hidden explosives. The combined approach of using the Fido™ sensor in conjunction with the conventional method of canine explosives detection, has proven effective in vehicular sweeps and at security checkpoints.

While the Fido™ detector represents a technological milestone in explosives detection, there is room for improvement and innovation. Despite representing the world's best TNT vapor detector with parts-per-quadrillion sensitivity, Fido™ cannot always adequately sense plastic explosive compounds (i.e. RDX) which have low vapor pressures. In order to improve upon this chemical sensor, an important quantity

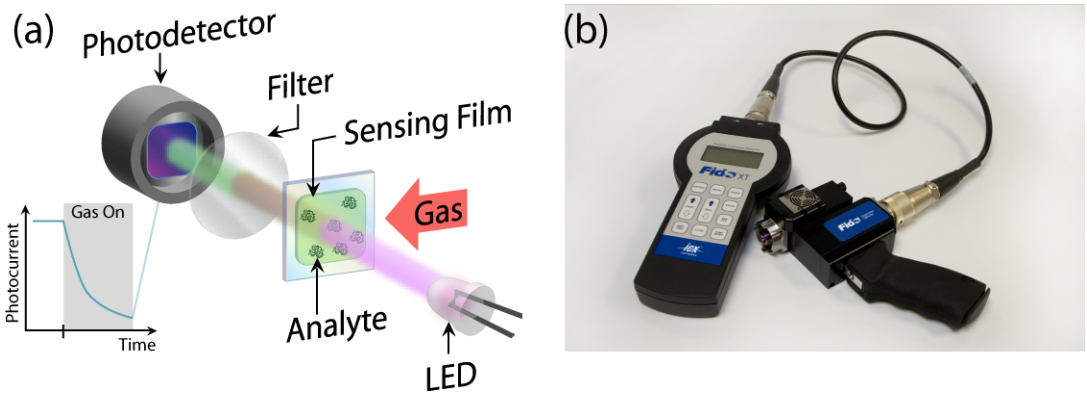

Figure 1-3: (a) An illustration detailing a state-of-the art sensing scheme utilizing a chemosensitive fluorescent polymer. (b) Image of commercially available Fido XT™ explosives detector manufactured by ICx Technologies.

to consider is the signal-to-noise ratio (SNR). There are two routes to improving SNR, increasing the signal intensity or reducing the noise signal. Signal noise can be attributed to both the optical and electrical components of the sensor. Thus, one strategy is to investigate new sensor architectures that can simplify the sensor design and reduce sources of electrical and optical noise.

For inspiration on ways to improve solid state fluorescent polymer chemical sensors, we can investigate two related device structures - photoconductors and chemiresistors. Photoconductors consist of an absorptive material sandwiched between two electrodes. When light is absorbed by the active material, excitons are generated and dissociated within the bulk of the film and the photogenerated charge is measured as an increase in conductivity between the two contacts. One useful feature of photoconductors is the ability to exhibit gain. Gain is the unitless ratio between the carrier lifetime and the carrier transit time, reaching values above unity when the photogenerated carriers take longer to recombine than to traverse the distance between the two contacts. Typical inorganic photoconductors have gains up to 10^6. For higher levels of gain, the fundamental tradeoff between device sensitivity and response time becomes more pronounced as the photoconductor can take milliseconds to respond to light at high gain levels [9].

Just as a photoconductor changes its conductivity with incident light intensity, the chemiresistor responds with an analogous change in conductivity when exposed to

chemical analytes in the ambient environment. The chemiresistor consists of a chemically sensitive film deposited between two electrical contacts, where analytes (the species being detected) can alter the chemosensing film conductivity in two ways. The analyte can either be absorbed to alter film density or be adsorbed to the surface of the film. During analyte absorption, molecules diffuse through the film, increasing the distance between neighboring conduction centers which reduces the overall conductivity of the film. In this case the chemosensing film can be engineered to operate at a percolation threshold that can result in large changes in conductivity for small amounts of analyte [10]. During adsorption the analyte can either chemically react with the film (chemisorption) by transferring charge, or the analyte can physically adhere to the surface of the film through weak intermolecular forces (physisorption).

Chemiresistors offer a simple, direct transduction mechanism of a chemical signal into an electrical signal. However, the lack of chemical specificity and relatively low sensitivity levels limit the applications for this type of sensor. Chemical specificity can be added to the active material through functionalization chemistry, however this has a direct effect on film conductivity. Because a single chemoresistive film has difficulty distinguishing specific analytes, oftentimes these sensors are incorporated into sensor arrays that yield chemical distinction capabilities, but this comes with the added complexity of calibration routines and algorithms needed to interpret the aggregate signals.

In order to design a chemical sensor that can utilize the simple transduction mechanism of the chemiresistor while exhibiting electrical signal amplification similar to a photoconductor, we can extend the paradigm of the bi-layer photoreceptor drums used in xerography. The photoreceptor drum is comprised of two films, each supporting a different physical function. The first film is referred to as the charge generation layer (CGL) and typically consists of dye molecules suspended in a solid matrix. The dye molecules act as absorption sites and generate excitons (bound electron/hole pairs) in response to light excitation. The other film is the charge transport layer (CTL), an electrically conductive film that transports the photogenerated charge from the CGL to the surface where they can recombine with oppositely charged carriers deposited

by a corona field [1]. In addition to playing a key role in separating the functions of charge generation and charge transport, the bi-layer heterojunction allows each film in the photoreceptor to be optimized independently to change overall device performance.

Observing that a chemosensitive fluorescent conjugated polymer can generate excitons much like the CGL of a photoreceptor, we can imagine pairing the polymer with a CTL to create a heterojunction that can dissociate excitons into charge carriers. Consider what happens if we incorporate a CTL and a fluorescent conjugated polymer into a photoconductor/chemiresistor device structure. By virtue of utilizing lateral electrodes, one surface of the device will be exposed to the environment, providing an opportunity to utilize the fluorescent conjugated polymer as the topmost film. Additionally, the chemically active film will be relieved from having to transport charge by the presence of an underlying CTL that can efficiently move charge through the device.

In a chemosensitive fluorescent polymer the exciton generation rate of the film not only depends on the intensity of incident light excitation, but also the presence of analytes in the local environment [7]. The photoluminescence efficiency, η, of chemosensitive fluorescent polymers can be strongly modulated by a chemical signal, which is a signature of a change in the population of excitons that can radiatively decay. The change in exciton population corresponds to a change in charge carrier density at the heterojunction interface, which is measured as a change in photocurrent. Because the fluorescent polymer introduces excited charge carriers from its photogenerated excitons, there remains the possibility that the carrier lifetimes can exceed the transit times, amplifying the transduced chemical signal. The photoconductive gain is related to the incident light intensity, implying that the sensor's sensitivity can be tuned by changing the incident light signal, giving the sensor a large dynamic range. In addition, the chemosensitive lateral heterojunction photoconductor can be driven with a modulated light signal, allowing for locked-in measurements of the photogenerated, transduced chemical signal. These AC measurements remove the contributions from the background DC current flowing through the CTL, remov-

ing the constraint of high signal-to-noise ratios that are a requirement for extracting useful measurements from chemiresistors. The development of this novel solid-state, vapor-phase chemical sensor platform will reflect the interdisciplinary nature of the maturing Organic Optoelectronic field by utilizing thin film characterization and fabrication techniques (Materials Science), device characterization and microfabrication (Electrical Engineering), and device modeling (Physics). As such, there are both scientific and engineering motivations that underlie this work.

1.1.1 Engineering Motivations

Ideally, a chemical sensor technology would reliably detect a specific chemical analyte, in real-time, with sensitivities ranging from a single molecule up to a few grams enabling sensor usage in a wide range of applications. However, reality dictates that chemical sensors must be engineered to satisfy the requirements of the specific sensing application. Thus, it is useful to evaluate sensor technologies with the following metrics: 1) Sensitivity 2) Specificity 3) Dynamic range 4) Response time and 5) Durability. While a number of these attributes are determined by the chemosensitive film alone, the key to overall sensor performance lies in the transduction mechanism of the chemical signal into a measured quantity.

In a rugged, portable chemical sensor an electrical signal is favored over an optical signal because precise alignment of optical components is not a requirement. Fluorescent polymer sensing schemes utilize a photodetector to accomplish the transduction from an optical signal into an electrical one. However, approximately 1% of the luminescence signature is coupled into the photodetector, due to the lambertian emission profile of the polymer and the physical distance between the film and the photodetector. By increasing this coupling efficiency there stands to be a concomitant increase in the SNR. Additionally, integrating the transduction mechanism into the heterojunction structure itself, removes the need for filters and photodetectors, which ultimately helps to reduce components and sensor complexity.

By separating the sensor functionality into a chemosensitive exciton generation layer (EGL) and a CTL, we have essentially created a modular sensor platform with

interchangeable layers that can be engineered for optimum sensor performance. Using a library of developed organic synthesis techniques, fluorescent conjugated polymers can be tailored to detect particular analytes with high sensitivity, while maintaining photoluminescent efficiency in the solid state. In addition, once the energy bands of the polymer are determined, the polymer can be paired with an underlying CTL to create a Type-II heterojunction that can effectively dissociate excitons. Film thicknesses and electrode configurations can also be varied to alter sensor sensitivity and response times. Once the specifications for a sensing application are known, these parameters become the engineering tools for solid-state sensor design.

1.1.2 Scientific Motivations

While organic heterojunctions play a key role in most organic optoelectronics (i.e. photovoltaics, photoreceptors, and light emitting devices), the physical processes at the interface between two dissimilar materials are not completely understood. Controversy stems from the difficulty of directly measuring carrier concentrations and the recombination rates in active device structures. Nearly all two terminal, organic bilayer heterojunction devices are fabricated in a vertical stack, with the heterojunction sandwiched on the top and bottom by the two electrodes. In this configuration, carrier recombination becomes difficult to distinguish from other field-dependent processes such as carrier transport and exciton dissociation. With the electrodes in a lateral, planar arrangement, the carrier transport now flows orthogonally to the carrier generation and recombination processes. This suggests that it may be possible to experimentally observe the recombination lifetime at an organic heterointerface with relatively simple measurements. Such measurements would fill a gap in our understanding of organic semiconducting materials and would enable better designs and simulations of organic devices, with the ultimate goal being the development of simulation/design tools similar to those used in the inorganic semiconductor industry.

Another method to explore the recombination lifetime at a heterointerface is through the fabrication of a multi-layer heterojunction device. The simplest version of this structure consists of an EGL, a CTL, and a charge spacer layer (CSL) that

is placed between the CTL and the EGL to form a cascading energy band structure. The thin CSL spatially separates the dissociated carriers to reduce the likelihood of bimolecular recombination across the EGL/CTL interface. A thickness study of the spacer layer can experimentally demonstrate the dependence of the carrier lifetime and photoresponse efficiency on the spatial separation of dissociated charge. While there are exotic experimental methods (i.e. Photo-CELIV [11], etc.) that have been used to determine bimolecular recombination rates, the potential benefits to organic device design that arise from having simple measurements and models to extract difficult-to-measure properties (i.e. carrier lifetimes) form the scientific underpinnings of this work.

1.2 Structure of Thesis

This work is organized into seven chapters. In Chapter 2, we begin by introducing the field of organic optoelectronics and discussing some of the material properties that make organic films unique. Chapter 3 follows with a review of state-of-the-art solid-state vapor phase chemical sensors in order to build some context for the applications of this research. After this, the operational theory of bilayer heterojunction photoconductors will be discussed, in Chapter 4, along with experimental demonstrations. The bilayer heterojunction photoconductor is an important proof-of-concept device that represents the first step towards the development of vapor-phase chemical sensors. Chapter 5 focuses on the extension of the heterojunction photoconductor architecture to include multiple layers and the consequent changes in device operation. Chapter 6 details a proof-of-concept bilayer chemosensor platform that specifically detects TNT vapor. The final chapter will conclude the thesis with a look at some of the possible extensions of this research.

Chapter 1 References

[1] P. M Borsenberger and D. S. Weiss. *Organic photoreceptors for xerography*. Optical Engineering. Marcel Dekker, New York, 1998.

[2] L. Zhou, A. Wanga, S. Wu, J Sun, S. Park, and T. N Jackson. All-organic active matrix flexible display. *Applied Physics Letters*, 88(8):083502, 2006.

[3] P. Peumans, A. Yakimov, and S. R. Forrest. Small molecular weight organic thin-film photodetectors and solar cells. *Journal of Applied Physics*, 93(7):3693–3723, 2003.

[4] B. P Rand, J. Genoe, P. Heremans, and J. Poortmans. Solar cells utilizing small molecular weight organic semiconductors. *Progress in Photovoltaics: Research and Applications*, 15(8):659–676, 2007.

[5] H. Chen, M. Josowicz, and J. Janatax. Chemical effects in organic electronics. *Chemistry of Materials*, 16(23):4728–4735, 2004.

[6] C. J Cumming, C. Aker, M. Fisher, M. Fox, M. J la Grone, D. Reust, M. G Rockley, T. M Swager, E. Towers, and V. Williams. Using novel fluorescent polymers as sensory materials for above-ground sensing of chemical signature compounds emanating from buried landmines. *IEEE Transactions on Geoscience and Remote Sensing*, 39(6):1119–1128, 2001.

[7] S. W Thomas, G. D Joly, and T. M Swager. Chemical sensors based on amplifying fluorescent conjugated polymers. *Chemical Reviews*, 107:1339–1386, 2007.

[8] H. M Huang, K. Wang, W. H Tan, D. An, X. H Yang, S. S Huang, Q. Zhai, L. Zhou, and Y. Jin. Design of a modular-based fluorescent conjugated polymer for selective sensing. *Angewandte Chemie-International Edition*, 43(42):5635–5638, 2004.

[9] S. M. Sze and K. K. Ng. *Physics of Semiconductor Devices*. John Wiley & Sons, Hoboken, third edition, 2007.

[10] B. C Sisk and N. S Lewis. Vapor sensing using polymer/carbon black composites in the percolative conduction regime. *Langmuir*, 22(18):7928–7935, 2006.

[11] A. J. Mozer, N. S. Sariciftci, L. Lutsen, D. Vanderzande, R. Osterbacka, M. Westerling, and G. Juska. Charge transport and recombination in bulk heterojunction solar cells studied by the photoinduced charge extraction in linearly increasing voltage technique. *Applied Physics Letters*, 86(11):112104–3, March 2005.

Chapter 2

Introduction to Organic Semiconductor Properties and Applications

Education is a progressive discovery of our own ignorance.

WILLIAM J. DURANT
Professor/Writer

Organic nanostructured optoelectronics encompasses the application of carbon-based or molecular-sized material sets for the development of optical and electrical devices, supplanting traditional semiconductor materials such as silicon. The key properties of organic nanostructured materials that sets them apart from bulk inorganic semiconductors are 1) Strong optical absorption/emission across the visible wavelengths (λ = 300 - 800 nm), 2) Low melting points, which allows for low-temperature processing and deposition of thin films over large areas on a wide variety of substrates, 3) Chemical flexibility, enabling synthesis of a vast library of novel materials from which to experiment, and 4) Weak intermolecular interactions, which yield hopping charge transport.

In this chapter, the focus will be on the building block of virtually all organic

electronic devices - the organic semiconductor. Organic semiconductors encompass a wide range of chemical compounds, each with unique material properties. Rather than attempting to profile and categorize all of the available materials, we will attempt to identify and present the common physical principles underlying organic semiconductor materials. In addition, we provide the reader with a brief look at the organic electronics (OE) industry's present and future.

2.1 Concepts from Quantum Mechanics and Solid-state Physics

In order to build a common knowledge and language base with the reader, this section will act as an introduction to the fundamentals of quantum mechanics and solid-state physics. Many of the concepts presented here will provide the necessary framework and tools to progress through the later chapters of this work. It is not the goal of this section to be comprehensive of all topics covered or mathematically rigorous, but merely to introduce the reader to some of the key concepts that play a role in organic and nanostructured materials.

2.1.1 Atomic Orbitals: Particle in a Box

Atoms are the basic building blocks of matter, consisting of three types of sub-atomic particles: the proton, the neutron, and the electron. A basic atomic model consists of negatively charged electrons orbiting a positively charged nucleus (made of protons and neutrons). Classical mechanics and electromagnetism cannot explain the stability of atoms, predicting the eventual collision of the orbiting electron and the oppositely charged nucleus. Thus, the push for more accurate models of the atom helped to motivate the initial development of quantum mechanics.

Quantum mechanics is a tool that is used to explain experimental results, and its ability to accurately predict and explain data regarding atomic properties (i.e. bond energy, spectrum of emitted light, etc.) drives its widespread acceptance. Using

the mathematical formalism developed in quantum mechanics, the state of any atom at a given time can be described by a complex wave function. This mathematical abstraction in conjunction with the Heisenberg uncertainty principle enables the conceptualization of an electron "cloud" around each atom's nucleus, which represents the probability of finding the electrons somewhere within that region of space but with the exact positions unknown.

Despite the uncertainty, useful results regarding atomic energy levels can be derived. Consider the situation where a single particle is located within an infinitely deep potential well. This situation is known as the "particle in a box", and in physical terms, the particle is defined as a single point enclosed in a box where it experiences no forces (i.e. zero potential energy). The impenetrable walls of the box are formed by potentials that rise to infinity. This simple model can serve as a useful analogy to an electron orbiting a nucleus: inside the atomic orbital (or the box) the electron is allowed, outside it is forbidden [Fig. 2-1].

In classical mechanics, the equations of motion governing the particle within the energy well are trivial: the particle moves in a straight line at a constant velocity until it is reflected off of the boundaries of the well. In quantum mechanics, when solving for the electron wavefunction in Schrodinger's equation and applying infinite potential boundary conditions, the results are not as intuitive. The particle's confinement leads to three quantum results that agree with experimental observation but contrast with classical mechanics: 1) discrete energy levels 2) a nonzero lowest energy level (zero-point energy) and 3) spatial nodes at each energy level that imply positions where the particle can never be found. While, the "particle-in-a-box" approximation accurately describes these results and the trend of increasing difference in energy levels with decreasing box dimensions, it does not accurately describe the simplest atom with a single electron (hydrogen).

A more rigorous analytical model which uses an isotropic coulomb potential is used in the Hamiltonian that describes the electron wavefunction of a one electron atom [1]. The atomic orbitals can be identified by a unique set of four quantum numbers: the principal (n), the azimuthal (l), the magnetic (m), and the spin projection (s) [Fig.

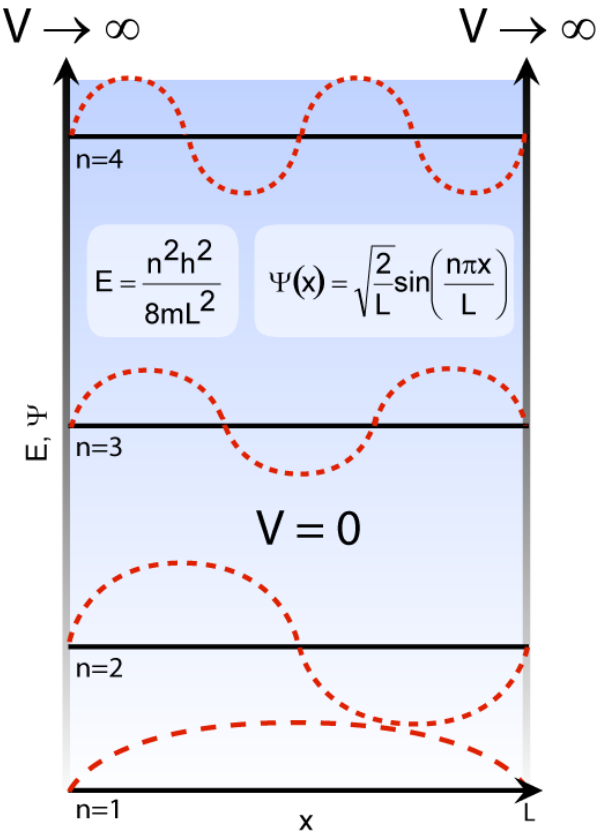

Figure 2-1: Schematic of 1-D particle in a box. Spatial confinement leads to discrete energy levels and wavefunctions (Ψ) following the inset equations, where E is energy, V is potential energy, m is mass, L is the length of the box, and h is Plancks constant.

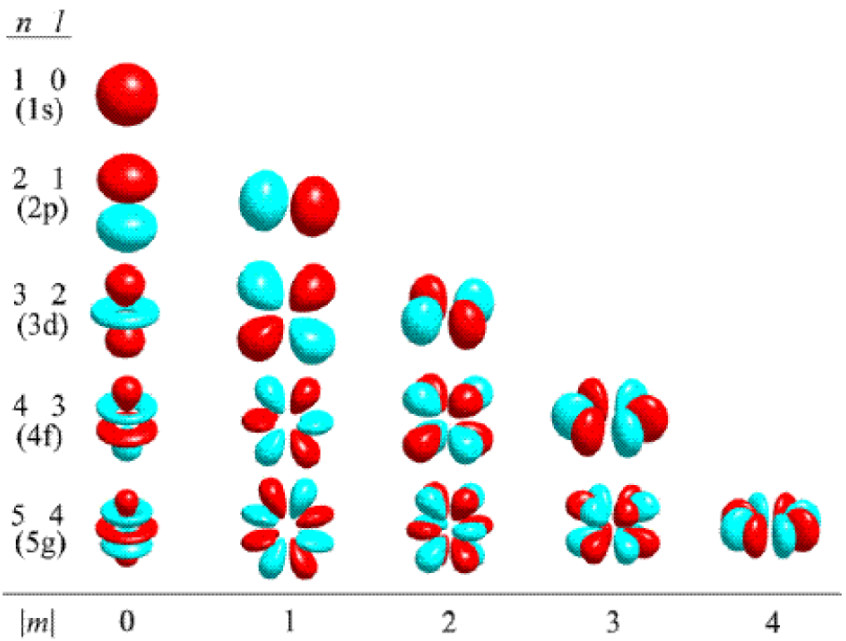

Figure 2-2: Table of 3-D visualizations of hydrogen atomic orbitals with varying quantum numbers [2].

2-2]. The principal quantum number describes the energy level of a given atomic orbital, which is also referred to as an "electron shell". The azimuthal quantum number describes angular momentum of the orbital, which specifies the shape of the orbital (s, p, d, f, etc.) and influences chemical bonds and bond angles. The magnetic quantum number describes the projection of the angular momentum of the orbital along a specified axis. The spin angular momentum describes the spin of the electron.

Spectroscopic experiments indicate that each orbital can contain no more than two electrons. In addition, two electrons can never have the exact same quantum state (i.e. set of quantum numbers) according to Pauli's exclusion principle. The set of rules restricting the values of the quantum numbers can be used to explain not only the experimental spectroscopic results (i.e. Stark and Zeeman effects), but also the electron configuration of atoms and the periodic table.

The hydrogen atom can be solved analytically, because the wavefunction describes the probability for one electron and one nucleus. For atoms with two or more electrons, analytical solutions become much more difficult to achieve due to electron-electron and electron-nucleus interactions, and the governing equations require nu-

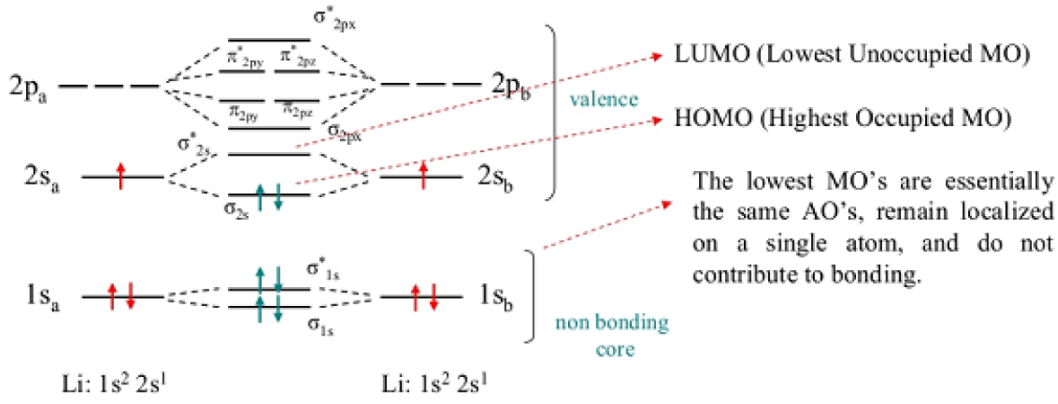

Figure 2-3: Schematic of energy level splitting that occurs in molecular orbitals of diatomic Li. σ (in-line) and π (out of plane) bonding orbitals are differentiated by the way the atomic orbitals overlap, * indicates anti-bonding orbitals [4].

merical simulations to reach approximate solutions.

2.1.2 Molecular Orbital Theory

The optical and electrical properties of covalently bonded organic small molecules result from the overlap of the atomic orbitals of the constituent atoms. According to molecular orbital theory [3], linear combinations of atomic orbitals (LCAO) can be used to construct molecular orbitals (MOs). These MOs can be categorized as bonding, anti-bonding, or non-bonding orbitals. A bonding orbital is a type of orbital where the electrons in that state have a higher probability of being between nuclei than elsewhere, and it will tend to hold nuclei together (hence the name). If the electrons tend to spend more time elsewhere than between the nuclei, the orbital will function as an anti-bonding orbital and weaken the bond. Electrons in non-bonding orbitals are usually in low energy (nearly atomic) orbitals that associate almost entirely with one nucleus or the other, and thus spend equal time between nuclei or not with no effect on bond strength [Fig. 2-3].

In diatomic molecules, a lower-energy bonding orbital is created by the in-phase addition (constructive interference) of two atomic orbitals while a higher-energy anti-bonding orbital is formed by the out-of-phase addition (destructive interference) of the two atomic orbitals. The amount of splitting of the energy levels associated with

the molecular orbitals is determined by the interaction between the atoms. A definite energy is associated with each orbital (whether atomic or molecular), and it can be interpreted as the energy required to remove the electron from the orbital into free space. In the ground state (unexcited) of an atom or molecule, electrons will settle into the lowest-energy orbitals available. The available shared electrons then populate each molecular orbital according to the Pauli exclusion principle (no more than two electrons in each orbital, and if there are two the spins must be opposite) to yield a highest occupied molecular orbital (HOMO) and a lowest unoccupied molecular orbital (LUMO). The energy gap between these two molecular orbitals determines the transition energies and consequently the absorption and emission spectrum of a single molecule.

In general, the calculations of energy levels and wavefunctions for a polyatomic molecule can be a difficult task that is made simpler by the approximation that electronic transitions occur instantaneously in the time frame of the nuclear system. This approximation is known as the Born-Oppenheimer (BO) approximation and can be thought of as heavy nuclei moving more slowly than light electrons. The success of the BO approximation is due to the high ratio between nuclear and electron masses. The mathematical consequence of the BO approximation is that it allows the wavefunction of a molecule to be separated into its electronic and nuclear components:

$$H_e \left|\psi_e\left(r;R\right)\right\rangle = E_e\left(R\right)\left|\psi_e\left(r;R\right)\right\rangle \tag{2.1.1}$$

$$H_e = -\frac{\hbar^2}{2m_e}\sum_{i=1}^{N}\nabla_{\mathrm{i}}^2 + V_{ee} + V_{en} \tag{2.1.2}$$

$$H_n \left|\psi_n\right\rangle = E\left|\psi_n\right\rangle \tag{2.1.3}$$

$$H_n = -\frac{\hbar^2}{2}\sum_{j=1}^{M}\frac{\nabla_{\mathrm{j}}^2}{m_j} + E_e\left(R\right) \tag{2.1.4}$$

Here r and R are the positions, m_e and m_j are the masses, ψ_e and ψ_n are the wavefunctions of the electrons and nuclei respectively. The first term in the electron Hamiltonian represents the kinetic energy of the electrons, the second term (V_{ee}) is the electron coulomb potential, and the third term (V_{en}) is the electron-nucleus

coulomb potential. The first term in the nuclear Hamiltonian represents the kinetic energy of the nuclei, while the second term represents the electron energy potential. Thus, Schrodinger's equation can be solved using the electronic wavefunction independent of the nuclear motion, as if the nuclei are fixed in a certain configuration. Then, Schrodinger's equation can be solved again for the nuclear wavefunction where the effective potential is defined by the electronic energy solved previously. Computational techniques such as the Hartree-Fock self consistent field method and density functional theory enable the calculation of near exact energies (within 0.05 eV) [5].

2.1.3 Spectroscopic Transitions

Molecular spectra are more complex than atomic spectra, which arises from the complicated structure of the molecule. The spectra of atoms is due only to the electronic transitions, whereas the spectra of molecules in the gas phase reflect the complex interaction between electronic, vibrational, and rotational transitions. Thus, molecular spectroscopic data can yield a great deal of information regarding the shape and size of molecules or the strength and stiffness of bonds.

The energy associated with electronic transitions (~1 eV) is usually greater than the energy of vibrational transitions (~100 meV), which is usually greater than the energy of rotational transitions (~10 meV). Thus, while it is possible to observe pure rotational transitions, a vibrational transition is normally accompanied by rotational transitions. Likewise, electronic transitions are accompanied by both vibrational and rotational transitions making them more complicated to interpret. In the solid-state, molecules do not have the rotational degree of freedom, thus only electronic and vibrational transitions can be observed in thin films.

Absorption and Emission

The spectrum of atoms arises from permitted transitions between its energy levels, and the difference in energy between those states is transferred to a photon of energy $h\nu$. Not all transitions between states are allowed, and the rules that specify the

permitted transitions are based on the transition dipole moment between the two states. The transition dipole moment between states $|i\rangle$ and $|f\rangle$ can be defined as

$$\mu_{if} = \langle i|\,\hat{\mu}\,|f\rangle \tag{2.1.5}$$

where $\hat{\mu} = -e\hat{r}$ is the electric dipole operator. The transition dipole moment can be thought of as a measure of the degree to which the electron perturbs the electromagnetic field when it makes a transition between the states. The wavelength of light is related to its energy through de Broglie's relation, which codifies the wave-particle duality of matter:

$$E = \frac{h\lambda}{c} \tag{2.1.6}$$

where h is Planck's constant, λ is wavelength, and c is the speed of light. A simple rule of thumb for converting wavelength to energy is to use the relation $E = 1254$ nm·eV/λ.

Macroscopically, when light illuminates a piece of semiconductor (organic/inorganic) a number of different events can occur. A photon having little mass can reflect (specular and diffuse) off the surface of the material, transmit through the material, or get absorbed by the material. Different wavelengths of light will experience differing amounts of absorption, since the energy of the incoming photon must be similar to an allowed electronic transition. This results in the characteristic absorption spectrum of the material.

The absorption coefficient (α) is one way to describe the amount of light (at a given wavelength) absorbed by a material, and the coefficient is employed in the empirical relation known as Beer's Law: $I = I_o e^{-\alpha L}$. This relationship can be used to quantify the absorption of light by a material as long as the following conditions apply: 1) the material has homogeneously distributed and independent absorption centers that do not scatter light, 2) the light is at normal incidence, and 3) the light is of low enough intensity that it does not optically saturate or pump the material to cause stimulated emission. The absorption of a photon results in an excited state of matter, where the energy of the photon transfers to the material as an electric potential energy.

There are several mechanisms for the energy to relax back to its ground state which can be categorized as radiative or non-radiative pathways: 1) emission of a photon (fluorescence), 2) dissipation into vibrational modes in the material (i.e. heat), and 3) transition to a state with a different spin angular momentum (intersystem crossing) before relaxing from that triplet state.

The fluorescence spectrum of emitted photons is always shifted towards lower energies (red-shifted) relative to the absorption spectrum; the difference in energy is known as the Franck-Condon shift. The origin of the shift can be explained by considering the time evolution of a molecule following the absorption of a photon. Invoking the BO approximation, the electronic transition to an excited state will occur within a fixed nuclear framework. At this point the nuclear wavefunction evolves into its final state to accommodate the excited phonon mode. This occurs on the time scale of a nuclear oscillation ($\sim 10^{-13}$ s) and results in a new nuclear configuration. Internal conversion happens on the same time scale to allow the excited state to couple to lower vibrational modes, lowering the energy. Finally, the electron relaxes back to its ground state, which emits a photon and triggers another nuclear reconfiguration to accommodate the electronic ground state in addition to internal conversion to the lowest vibrational mode [Fig. 2-4].

2.1.4 Excitons

In general terms, an exciton can be defined as an excited state consisting of a bound electron-hole (hole = absence of electron) pair. Exciton formation occurs when a photon interacts with a semiconductor to excite an electron into a higher energy state. The promotion of the electron leaves a positively charged environment behind, which can be treated as a quasi-particle known as a hole. As a result of the coulombic attraction between the electron and its hole, there is a slight reduction in energy (with respect to free carriers) resulting in a bound excited state. It is useful to treat the bound excited state as a neutral quasiparticle, which can either diffuse through the molecular crystal, transfer its energy to another exciton, recombine to produce luminescence, or dissociate to form free carriers.

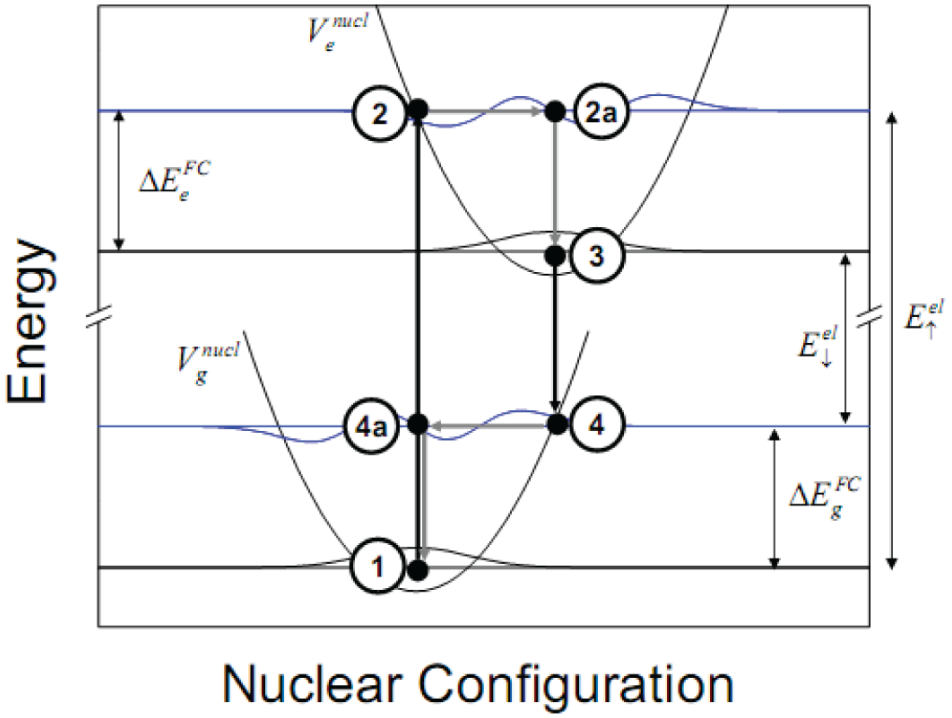

Figure 2-4: Illustration of the Franck-Condon shift observed in electronic transitions. V_g^{nucl} and V_e^{nucl} are the nuclear potential energy functions of the ground and excited electronic states respectively. ΔE_g^{FC} and ΔE_e^{FC} are the Franck-Condon relaxation energies of the ground state and excited state respectively. $E_{\uparrow}^{el}$ and $E_{\downarrow}^{el}$ are the dominant electronic excitation and relaxation transitions respectively [6].

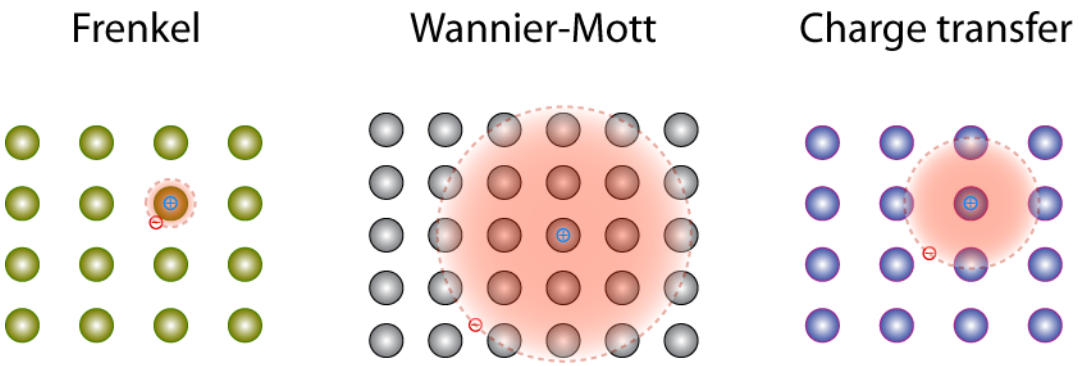

Figure 2-5: Illustration of the different types of excitons. After [7].

There are three types of excitons: 1) Frenkel excitons, 2) Wannier-Mott excitons, and 3) charge transfer excitons. In organic materials the dielectric constant tends to be small, which allows a strong coulomb interaction to occur between an electron and its hole. This type of exciton is known as a Frenkel exciton, where the binding energy is on the order of 1 eV and large enough to restrict the electron and hole to the same molecule. A Wannier-Mott exciton has a radius that is much larger than the lattice spacing. This type of exciton is more commonly found in covalently bonded crystals that have large dielectric constants that tend to screen the Coulombic interaction between electrons and holes. Typically, the binding energy of a Wannier-Mott exciton is on the order of 0.1 eV. An intermediate case occurs when the electron and hole occupy adjacent molecules. This situation is known as a charge-transfer exciton and is the precursor to the generation of free carriers [Fig. 2-5].

Aside from the spatial differences in the types of excitons, the total spin angular momentum of exciton states can be used to classify them as either singlet or triplet excitons. As previously noted, any given molecular orbital can only contain at most two electrons. According to Pauli's exclusion principle the spins of the electrons in the same orbital cannot be the same. Therefore, one electron must be "spin up" (s = $+1/2$) while the other is "spin down" (s = -1/2). Excitons do not share this restriction, consisting of an electron in one orbital and a hole in a lower orbital. This leads to the slightly more complex situation where there are four possible spin combinations of the electron-hole pair. Constructing the set of spin wavefunctions yields one exciton state with a total spin of 0 (singlet) and three degenerate exciton states with a total

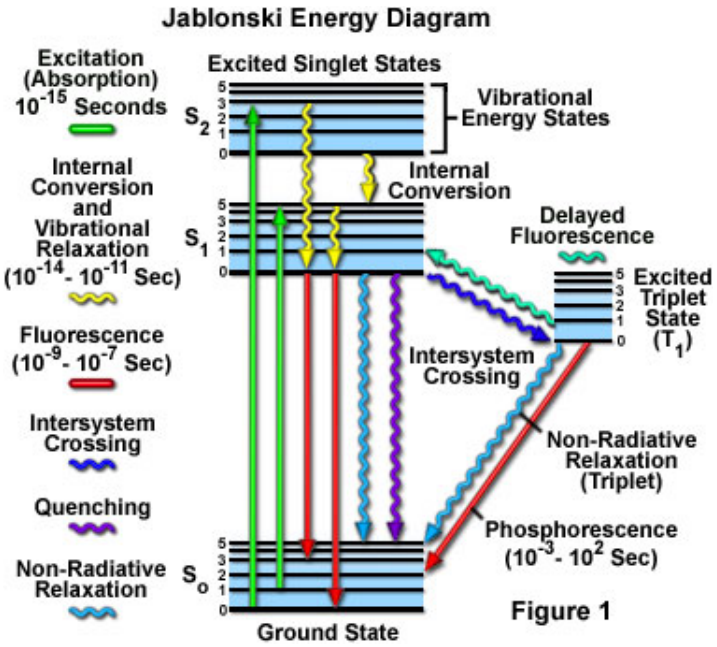

Figure 2-6: A typical Jablonski diagram that illustrates many of the possible electronic transitions associated with a molecule [8].

spin of 1 (triplet). The distinction between singlets and triplets will prove important in electronic transitions, because angular momentum must be conserved. Therefore, a triplet excited state is forbidden from relaxing to a singlet ground state unless there is a process available that can change the total spin of the system from 1 to 0 (spin orbit coupling) [Fig. 2-6].

2.2 Organic Thin Film Properties

Organic semiconductor films are generally assemblies of molecule or polymer chains. Regardless of the orientation of the molecules in a thin film, organic materials (crystalline or amorphous) are held together by weak intermolecular forces called Van der Waals forces [9]. These Van der Waals forces preclude covalent and ionic bonding and consists of repulsive and attractive components. The repulsive component prevents the collapse of molecules as entities are placed closer together. The attractive component itself has three distinct contributions: 1) the electrostatic interaction between charges and permanent multipoles 2) the polarization effect, which is the interaction

	Molecular crystals	Covalent crystals
Lattice interaction	Van der Waals (~ 10^{-3} - 10^{-1} eV)	Covalent (~ 2 - 4 eV)
Carrier mobility	Low (<1 $cm^2V^{-1}s^{-1}$)	High
Mean free path	Short (order of lattice constant)	Long (10^2 - 10^3 times lattice constant)
Carrier effective mass	Large (10^2 - 10^3 times electron mass)	Small (less than electron mass)
Charge transport type	Hopping	Band
Exciton type	Frenkel excitons (0.3 - 1.0 eV binding)	Wannier excitons (0.01 - 0.1 eV binding)
Melting point	Low	High
Mechanical strength	Low	High
Compressibility	High	Low

Table 2.1: Comparison of properties of molecular and covalent crystals. After [10].

between a permanent mulitpole on one molecule and an induced multipole on another, and 3) the transient (fluctuating) multipole effect which is temporarily induced by the probabilistic movement of the electron density cloud.

The weak intermolecular forces result in narrow electronic bandwidths and localized excitations, restricting conduction to hopping transport. Organic semiconductors are often highly disordered (both spatially and energetically), hence charge carrier mobility is smaller relative to their covalently-bonded counterparts. Due to poor electrical conductivity, organic materials are employed in applications that exploit their strong optical properties or their potential for large-area fabrication. A comparison of some of the major differences between molecular crystals and covalent crystals is provided in the table above.

2.3 Overview of Organic Electronics Industry

Organic electronics (OE) covers a wide array of consumer electronics and photonics products enabled by the use of organic materials. These materials may be insulating or conducting and light emitting or absorbing. A number of reports state that the organic electronics industry, which reported less than $400M in revenue in 2007, would likely grow to $15B in 2015 [11, 12]. The key drivers of this explosive growth rate (CAGR >50%) will be the adoption of more cost effective processing techniques (primarily printing) and the shift in focus on applications that utilize simple, large-area electronics rather than the more impressive display technologies.

2.3.1 Manufacturing Processes: Printing is the Future

Although OE products are created using a variety of techniques including evaporation and thermal transfer, there is considerable interest in using solution processing because of its potential as a cost effective manufacturing approach. Printing is fundamental to OE technology's primary attraction - the ability to produce low-cost electronics on large-area, flexible substrates [13]. Roll-to-roll capital equipment costs are relatively small, with virtually no masking requirements, and throughputs are suitable for many applications [14]. The promise of cost savings in printed OE is so great that several manufacturers are attempting to turn their existing organic materials into "inks"for compatibility with future printing equipment.

Almost every known printing technique has been used to print electronics, but the three most important are direct contact printing (including screen printing [15], flexography [16], and gravure [17]), ink-jet printing [18, 19], and organic vapor jet printing [20].

Screen printing has been used for decades to make EMI shielding, capacitors, membrane switches and several other applications, and it has been used with a variety of conductive polymers, such as PPV:PCBM (poly [p-phenylene vinylene] and P3HT (poly-3-hexylthiophene). In the traditional screen printing process a fine mesh screen (made of steel, nylon, or polyester) is suspended above a patterned stencil resting on the substrate, with the resolution of the print determined by the mesh size. A flood bar is used to fill the mesh with ink, after which a squeegee is used to push the mesh in contact with the substrate, transferring the ink where the stencil is not blocking [Fig. 2-7(a)]. The thickness of the print is a controllable parameter, and the use of viscous inks enables thicker films than can be achieved with other printing techniques.

Rotary screen presses are designed for continuous, high-speed screen printing. Seamless metal mesh cylinders act as the screens. The open-ended cylinders are filled with ink from one end of the cylinder so that a fresh supply is constantly maintained. The squeegee is a free floating steel bar inside the cylinder and the squeegee pressure is maintained and adjusted by magnets mounted under the substrate [Fig. 2-7(b)].

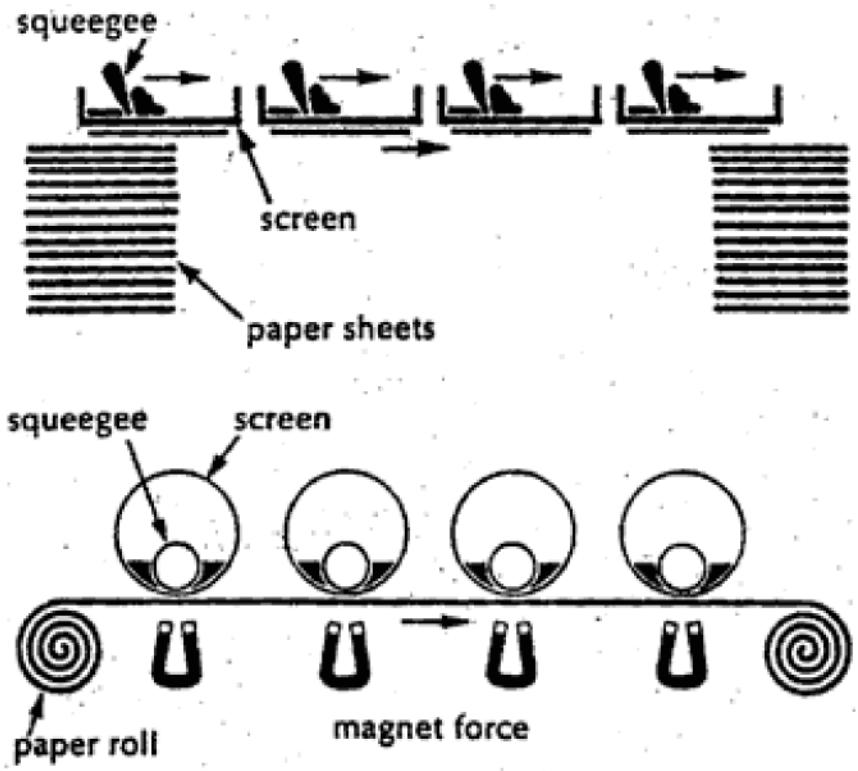

Figure 2-7: Schematic illustrations of a) flatbed screen printing and b) rotary screen printing [21].

Rotary screen presses are most often used for printing textiles, wallpaper, and other products requiring unbroken continuous patterns [21].

Flexography is the approach most often cited as the way to ramp up to high volume printed electronics and is a printing technique where the printing plate is flexible [Fig. 2-8]. The patterned stamp is inked with the material to be deposited and then brought into contact with the substrate to transfer the ink. In general, the lower print quality and resolution relegates flexography to applications with large tolerances, currently being used to print RFID antennas on labels using silver inks, batteries, organic circuits, photovoltaics, and low-cost lighting. Soft lithography is a related laboratory technique where patterned PDMS is used as the flexible stamp. While it has been suggested that soft lithography is compatible with roll-to-roll printing processes [22], both flexography and soft lithography suffer from stamp distortions preventing accurate pattern registration over large areas.

Gravure printing is a high-throughput process limited to print runs in excess of a million copies due to the large fixed costs involved. This technique is based on engraving a metal cylinder with a pattern of cells of variable size and depth. A metal blade is used to wipe excess ink off of non-printing areas while leaving ink within the cells (a.k.a. doctor blading). When a flexible substrate is brought into contact with the engraved cylinder the ink transfers and is able to achieve low film thicknesses due to the use of lower viscosity inks [Fig. 2-9]. There are many factors influencing gravure print quality including substrate properties (smoothness, compressibility, porosity, ink receptivity, wettability, etc.) and ink properties (ink chemistry, viscosity, drying, etc.). Furthermore, process parameters, such as doctor blade angle and doctor blade pressure, impression pressure, and printing speed have a tremendous effect on the quality of the printed ink film. Despite the large parameter space, the robustness of the metal cylinder carrying the image recommends the process for large-scale manufacturing lines. The engraved cylinder will have good printing stability over time, whereas the chlorinated solvents used in flexography tends to degrade the photopolymer print plates.

Inkjet printing has already been widely used with organic materials and can print

Figure 2-8: Using a laboratory printing machine, printed electronics, such as RFID tags, are being developed by PolyIC. By using a roll-to-roll flexography printing process it is possible to produce large volumes at very low cost. Source: PolyIC press picture

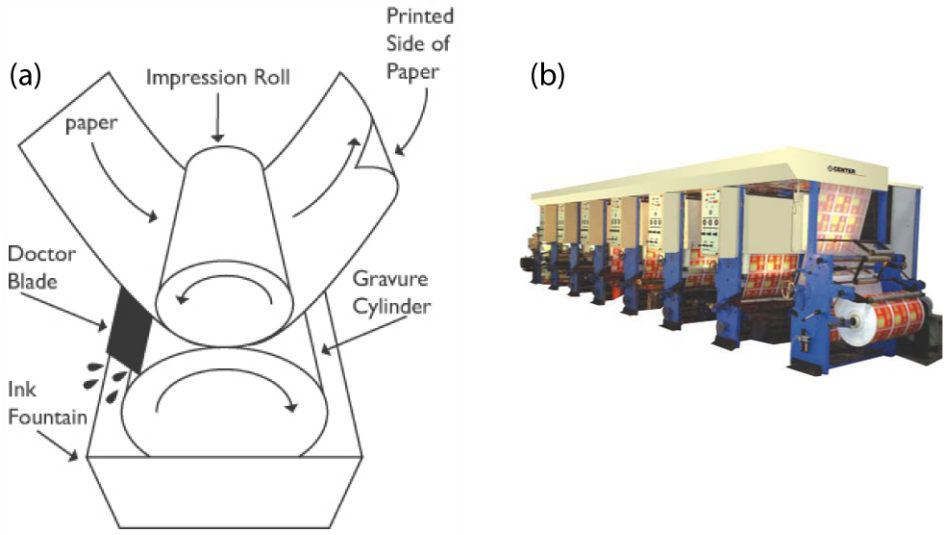

Figure 2-9: (a) Diagram of rotogravure printing process (b) Multi-color rotogravure printing machine. Source: R.H. Technocrates Center

layers with thin ink film, which not only saves on material costs, but is often critical for large-area applications such as displays, lighting panels and sensor arrays. A traditional drawback of inkjet printing is its lower throughput capability relative to gravure or flexography. The two main types of inkjet printing technologies are thermal and piezoelectric. In thermal inkjet printing droplets are generated by heating the wall of the ink chamber causing formation of vapor bubbles and ejection of droplets through the nozzle [Fig. 2-10]. In piezoelectric printing a pressure wave (driven by an applied voltage waveform) in the ink chamber results in formation of droplets at the nozzle [Fig. 2-11]. Both types of inkjet printing are inexpensive to implement, reliable, and compatible with "drop on demand" (DoD) applications. One major difference in the technologies is that drop size in thermal inkjet printing is determined by the chamber size, while the drop size in piezoelectric inkjet printing can be changed by applying different voltage waveforms. The other key difference is that piezoelectric inkjet printing enables the use of heat-sensitive inks as it does not rely on heating to generate droplets.

A simple extension of inkjet printing enables an entirely new printing process, with the potential for high throughput. Kateva, a start-up company based in CA, is commercializing molecular jet printing [24, 25] technology by developing print heads

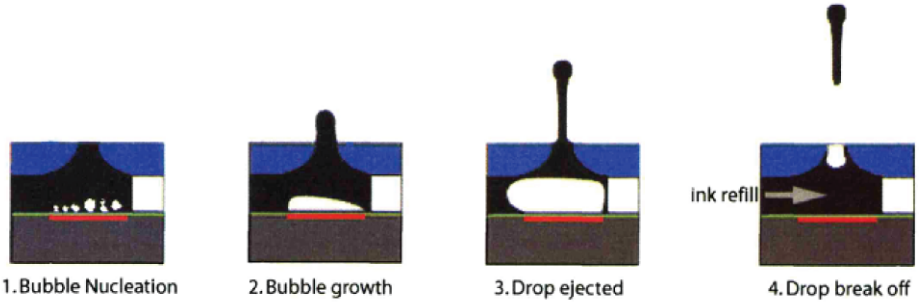

Figure 2-10: Schematic of thermal inkjet printing process [23].

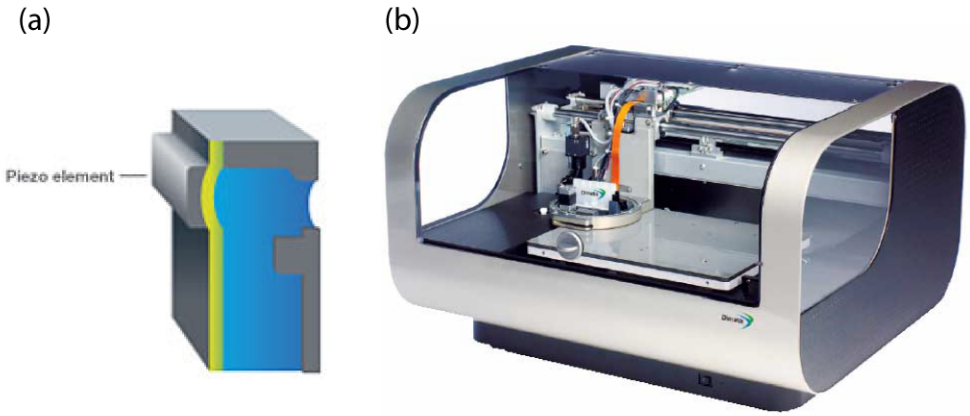

Figure 2-11: (a) Cross-sectional view of piezoelectric ink chamber (b) Dimatix's benchtop DMP 2800 piezoelectric inkjet printer. Source: Dimatix

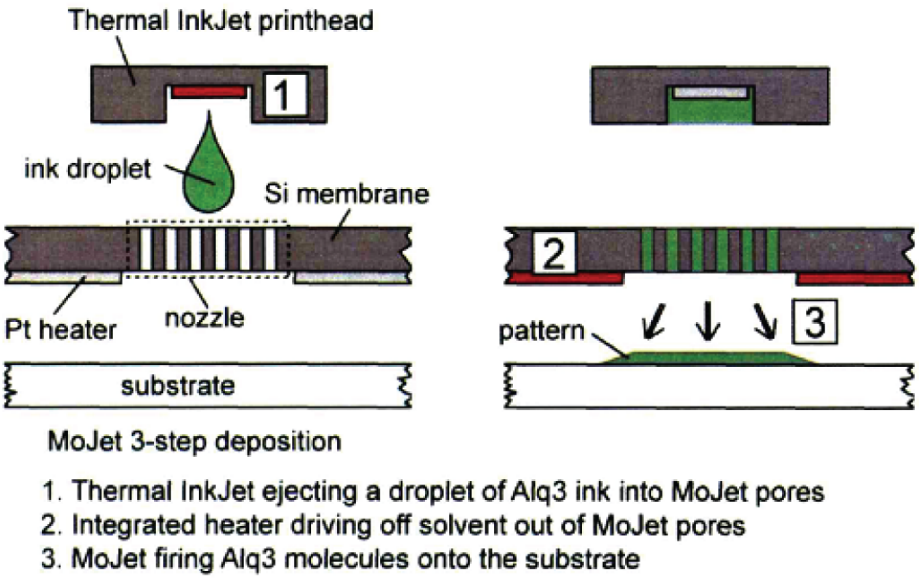

Figure 2-12: Cross sectional schematic view of the molecular jet print head and the steps involved in deposition [23].

that can be retrofitted onto existing inkjet printing capital equipment lines used for display technologies. The thermal inkjet nozzles load porous membranes with solvated organic material, after which heating is applied to eject the evaporated material onto a nearby substrate [Fig. 2-12]. High throughput is achieved by arraying the nozzles for simultaneous printing. This deposition technique should prove useful for small-molecule organic materials, whose electronic and optical properties and film uniformity are significantly degraded when undergoing solvent processing.

2.3.2 Organic Electronic Products: OLEDs Light the Way for Adoption

New applications for OE are constantly being invented. While these new applications are almost always intellectually interesting, few are likely to become revenue generating products within the next few years. One example is organic memory for which various formulations and architectures have been available for several years. While many important firms have patents on various organic memory products, it seems unlikely that this kind of memory will find its way into a commercial product

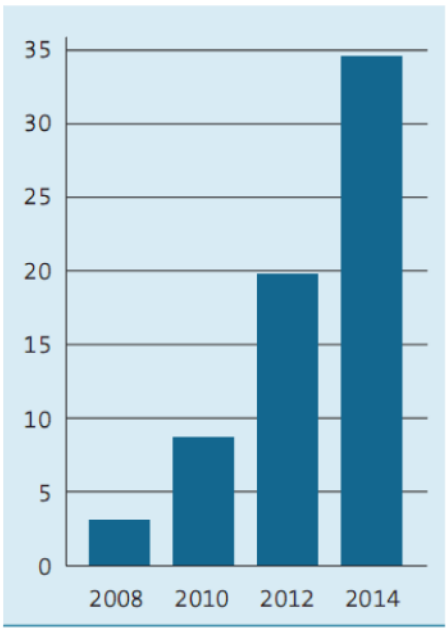

(a)

Displays	13,815.0
Signage	493.2
Lighting	1,200.0
Backplanes	2,764.2
Sensors	1,600.0
RFIDs	11,073.3
PV	127.2
Memory	1,500.0
Toys and novelties	1,400.0
Other	468.3
Total	**34,441.3**

(b)

Figure 2-13: (a) Revenue projections for OE markets ($ Billions) (b) Revenue projections for OE by application, 2014 ($ Millions). Source: Nanomarkets LC (2007) [26]

until organic radio frequency identification (RFID) tags and other disposable products start to take on a much higher degree of sophistication. OLED technology is the biggest consumer of organic semiconductor materials and the largest source of revenue in the OE industry, accounting for $308.5M in 2008 and potential to reach $6B by 2015 [11].

Organic Light Emitting Diode (OLED) Displays

The most commercially significant market opportunity today is OLED (Organic Light-Emitting Diode) technology [Fig. 2-14]. OLED displays have the following advantages over the current industry leader liquid crystal display (LCD) technology: 1) emissive technology with no backlight requirement 2) better color saturation 3) better contrast ratio 4) smaller power requirements. Only in the last several years have OLED displays started to generate significant revenue, with the market projected to grow to $4.5B in 2010 [27]. Today 25 to 30 firms produce OLED displays,

Figure 2-14: Prototype 40" OLED display (worlds largest). Source: Samsung

primarily using small-molecule fluorescent and phosphorescent materials. The key players in this space are Samsung, LG Electronics, Univision, Sony, Epson-Seiko, Pioneer, and TDK. A few firms are actively producing polymer OLED displays, with OSRAM and Delta Optoelectronics actively shipping products.

OLED Lighting

While displays dominate the present OE market, OLED lighting technology [Fig. 2-15] is expected to account for an increasing share and is getting attention from a select group of OLED makers. Lighting places special demands on materials with regard to lifetimes, color, and power consumption. For example, the brightness of the OLED lamp is inversely proportional to its lifetime, while the most power-efficient lamp may not provide the most aesthetically pleasing light. Color stability is a major issue for OLED lighting that is exacerbated by differential aging of the red, green, and blue materials used to create white light. Despite these challenges, OLED lighting's high power efficiency and thin, flexible form factor is driving adoption among architects and designers as viable substitutes for more traditional lighting such as incandescent, fluorescent, and high intensity discharge (HID) lamps. In the future, the OLED

Figure 2-15: White, small molecule OLED measuring 4 x 12 cm^2. Source: Philips Lighting

lighting industry is projected to reach $6B in 2018 [28] with Philips, GE, Konica Minolta, Lumiotec and OSRAM entering mass production in 2011.

Over the next several years, the markets for radio-frequency identification (RFID) tags and display backplanes will drive the production of OTFTs. OTFTs have steadily achieved market traction as device performance matches or exceeds that of some silicon TFTs and as significant capital investments have been made in production facilities. The market for organic RFID tags is presently quite small reaching sales of $13.7M in 2007 and forecasted revenues of $11.6B by 2015 [11]. PolyIC is one of the key players in this market.

OTFT backplanes are finding their way into electronic ink (e-ink) displays, which helped them to garner $2.1M in 2008 with projections of $3.3B of revenue in 2015 [29]. Plastic Logic is one such startup firm that manufactures flexible e-ink displays by using an OTFT backplane. Polyera is another startup that has developed an n-type polymer material with high mobility (~0.5 $cm^2V^{-1}s^{-1}$) and good solubility. The company aims to ship flexible displays based on complementary OTFT backplanes within 3 years.

It is now being widely suggested that these types of simple electronics could help

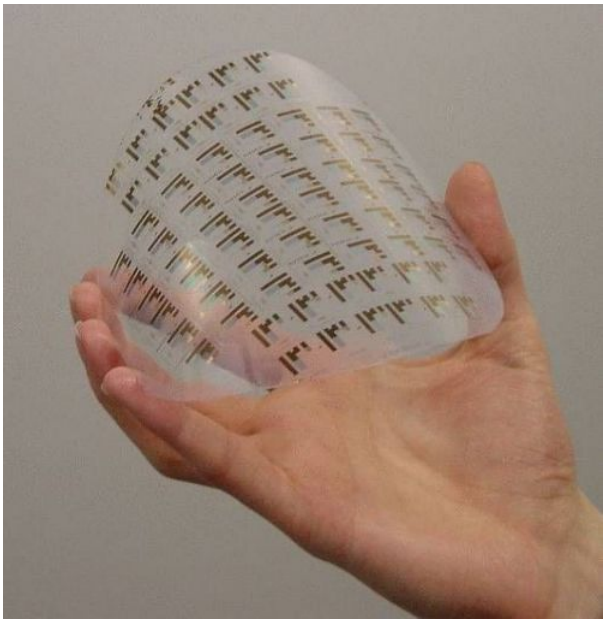

Figure 2-16: Organic rectifier printed on 6" PEN-foil. Source: IMEC

jump start the entire OE industry. Thus, some of the firms that ultimately aim at offering multifunctional organic RFIDs will first produce low function tags that can be used for simple point-of-sale or marketing applications. The focus now is on pushing products out into the marketplace, even if they do not dazzle the customer in the way that a printed, flexible OLED display complete with printed organic backplane might.

Organic Photovoltaics (OPVs)

With the recent push for renewable energy, there has been a widespread proliferation of photovoltaic companies and technologies. The lower power efficiencies of organic photovoltaics (OPV) has kept the market lagging behind its inorganic counterpart. However, OPV's potential will lie in its high throughput production capabilities, which will meet increasing demand for solar over the next few decades as inorganic materials suppliers reach production or material resource limitations. Polymers, small-molecule organics, hybrid organic/inorganic, and nanoparticle-based inks have all been used as active materials to create commercially viable photovoltaic devices with power efficiencies ranging from 5%-11% [30]. The dollars/watt metric

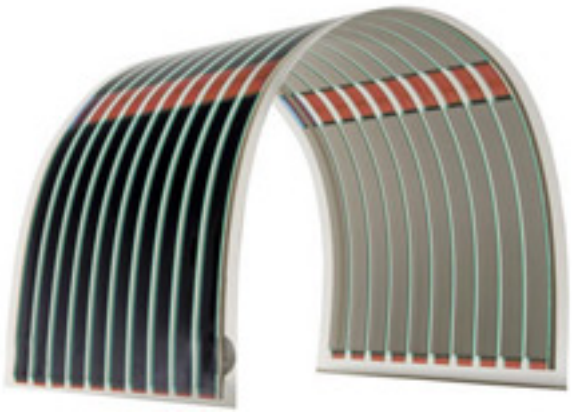

Figure 2-17: Demonstration of flexible organic photovoltaic technology. Source: Konarka

must reach $0.50/watt to be competitive with conventional energy generation methods. This threshold may eventually be surpassed with better materials, new cell designs, and solution-processed manufacturing. Currently, the market is a miniscule $500K (2008) but will reach $223M in 2015 [31]. Some interesting developments in the consumer electronics market are already beginning to emerge. G24i and Konarka will release OPVs targeting the cell phone market, while SWATCH plans to have dye-sensitized solar cell watches in 2009.

2.4 Summary

As nanotechnology enters our communal lexicon and gets tossed around as a marketing buzzword, it's clear that research on the atomic scale has arrived. The formation of an international industry association specific to the organic electronics industry (OE-A) is just another sign that the market for consumer electronics utilizing organic materials is maturing rapidly. Just as the OE industry is maturing and organic device performance is beginning to rival that of its inorganic counterparts, the vision of low-cost, large-area electronics is steadily becoming a reality. With organic materials enabling a wide array of novel technologies, the future of the industry will rely largely on our ability to imagine new, game-changing applications.

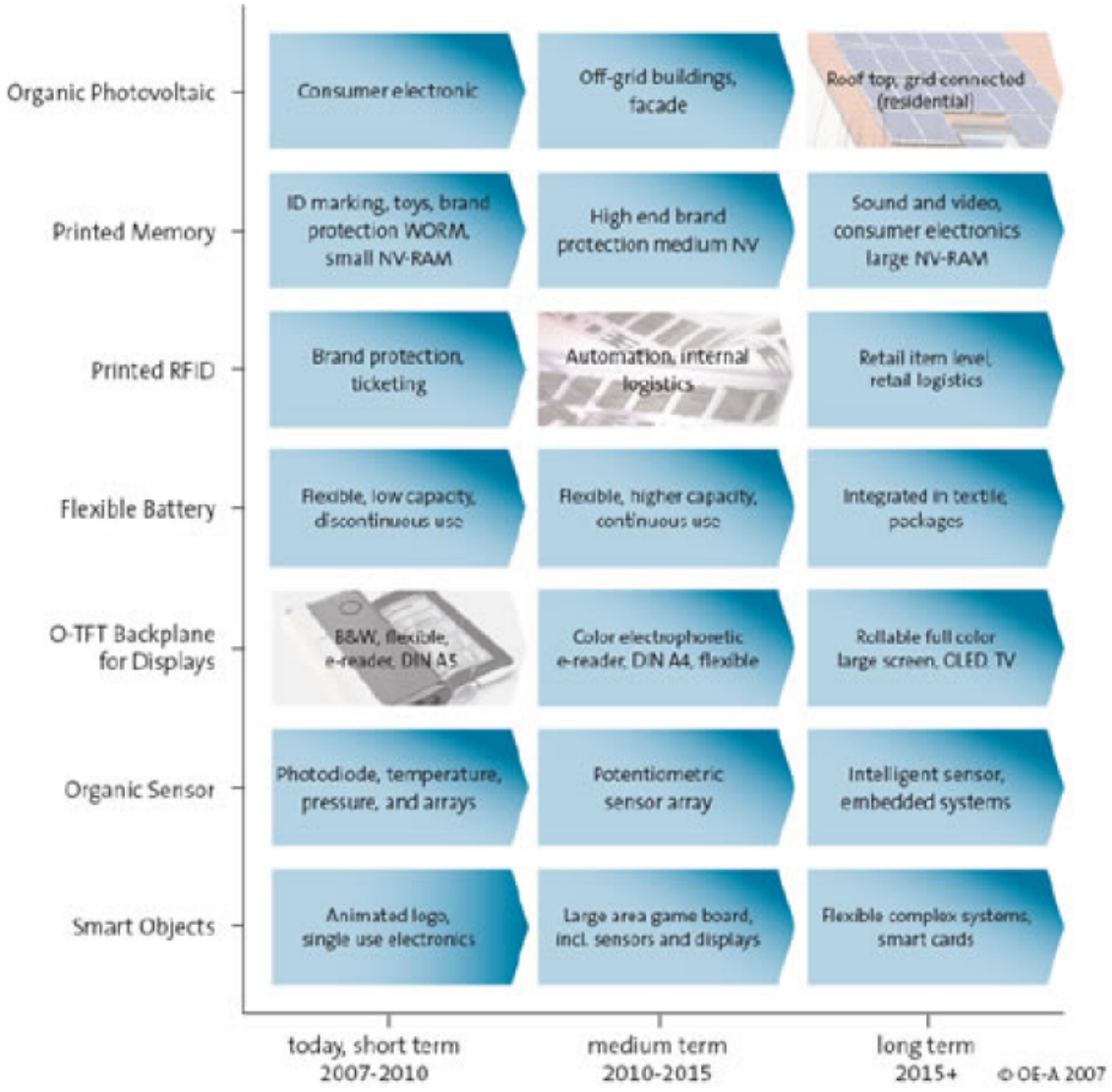

Figure 2-18: Roadmap for organic electronics applications. Source: OE-A [32].

Chapter 2 References

[1] D. J. Griffiths. *Introduction to Quantum Mechanics*. Prentice Hall, Upper Saddle River, NJ, 1995.

[2] S. Tokita, T. Sugiyama, F. Noguchi, H. Fujii, and Hidehiko Kobayashi. An attempt to construct an isosurface having symmetry elements. *The Journal of Computer Chemistry Japan*, 5(3), 2006.

[3] R. S. Mulliken. Spectroscopy, molecular orbitals, and chemical bonding. Nobel Lecture, December 1966.

[4] F. Buth. Organic electronics. Walther Schottky Institut, TU Munchen, 2008. `http://www14.in.tum.de/konferenzen/Jass08/courses/4/buth/slides_buth.pdf`.

[5] P. W Atkins and R. S Friedman. *Molecular Quantum Mechanics*. Oxford University Press, New York, 4th ed edition, 2005.

[6] C. F. Madigan. *Theory and simulation of amorphous organic electronic devices*. Ph.D. thesis, MIT, 2006.

[7] J. D. Wright. *Molecular Crystals*. Cambridge University Press, Cambridge; New York, 1995.

[8] Olympus microscopy resource center. `http://www.olympusmicro.com`.

[9] V. A. Parsegian. *Van der Waals forces*. Cambridge University Press, Cambridge, 2006.

[10] E. A. Silinsh and C. Vladislav. *Organic Molecular Crystals: Interaction, Localization and Transport Phenomena*. American Institute of Physics, New York, 1994.

[11] Opportunities in organic electronic markets. White paper, Nanomarkets, March 2008. `http://www.printedelectronicsnow.com/whitepapers/download/7/NMOEMaterials_032408.pdf`.

[12] P. Harrop. Organic electronics forecasts, players and opportunities. White paper, IDTechEx Ltd., 2005. `http://www.idtechex.com/research/reports/organic_electronics_forecasts_players_and_opportunities_000117.asp`.

[13] R. Parashkov, E. Becker, T. Riedl, H.-H. Johannes, and W. Kowalsky. Large area electronics using printing methods. *Proceedings of the IEEE*, 93(7):1321–1329, 2005.

[14] H. Klauk. *Organic Electronics*. Wiley-VCH, Weinheim, 2006.

[15] Z. Bao, Y. Feng, A. Dodabalapur, V. R. Raju, and A. J. Lovinger. High-Performance plastic transistors fabricated by printing techniques. *Chemistry of Materials*, 9(6):1299–1301, June 1997.

[16] J. Kenny. Printing electronics: Flexo and screen. *Printed Electronics*, February 2009.

[17] E. Hrehorova and R. Kattumenu. Evaluation of gravure print forms for printed electronics. *Gravurezine*, March 2007.

[18] T. R. Hebner, C. C. Wu, D. Marcy, M. H. Lu, and J. C. Sturm. Ink-jet printing of doped polymers for organic light emitting devices. *Applied Physics Letters*, 72(5):519–521, February 1998.

[19] S. Chang, J. L., J. Bharathan, Y. Yang, J. Onohara, and J. Kido. Multicolor organic Light-Emitting diodes processed by hybrid inkjet printing. *Advanced Materials*, 11(9):734–737, 1999.

[20] M. S. Arnold, G. J. McGraw, S. R. Forrest, and R. R. Lunt. Direct vapor jet printing of three color segment organic light emitting devices for white light illumination. *Applied Physics Letters*, 92(5):053301–3, February 2008.

[21] Print process descriptions: Printing industry overview: Screen printing. Technical report, Printers' National Environmental Assistance Center. `http://www.pneac.org/printprocesses/screen/`.

[22] P. Cosseddu, E. Orgiu, and A. Bonfiglio. Soft lithography fabrication of fully flexible and transparent all organic FETs for large area applications. In *Organic Electronics – Materials, Devices and Applications*, volume 965, Boston, 2007.

[23] J. Chen. *Novel Patterning Techniques for Manufacturing Organic and Nanostructured Electronics*. Ph.D thesis, MIT, June 2007.

[24] M. Shtein, P. Peumans, J. B. Benziger, and S. R. Forrest. Direct mask-free patterning of molecular organic semiconductors using organic vapor jet printing. *Journal of Applied Physics*, 96(8):4500–4507, October 2004.

[25] J. Chen, V. Leblanc, S. H. Kang, P. J. Benning, D. Schut, M. A. Baldo, M. A. Schmidt, and V. Bulović. High definition digital fabrication of active organic devices by molecular jet printing. *Advanced Functional Materials*, 17(15):2722–2727, 2007.

[26] Organic electronics: A market & technology assessment. White paper, Nanomarkets, 2007.

[27] Organic light emitting diode (OLED) displays: A global strategic business report. Technical report, Global Industry Analysts, 2008. `http://www.laserfocusworld.com/display_article/322472/12/none/none/INDUS/OLED-display-market-to-top-$4.5-billion-by-2010`.

[28] OLED lighting in 2009 and beyond: The bright future. Technical report, DisplaySearch, 2009. `http://www.displaysearch.com/`.

[29] Next chips: Organic transistors and memories and the applications they will enable. White paper, Nanomarkets, 2008.

[30] Organic photovoltaic markets. White paper, Nanomarkets, 2008.

[31] Materials market for thin-film and organic photovoltaics. White paper, Nanomarkets, 2008.

[32] Organic electronics. White paper, Organic Electronics Association, 2007. http://www.vdma.org/wps/wcm/resources/file/eb697e48f1969d3/OE-A_Brochure%202007_5MB_72dpi.pdf.

Chapter 3

Vapor-phase Chemical Detection

Smell is a potent wizard that transports you across thousands of miles and all the years you have lived.

HELEN KELLER
Author/Educator

Before we survey the wide range of technologies available for chemical sensing, a distinction must be made between chemical sensors and electronic noses (e-noses). Most chemosensing applications favor one of two functionalities when sensing analytes: detection or distinction. For detection, the information regarding a specific chemical's presence in the environment is of utmost importance. For distinction, the relevant information is the identification of the chemical constituents that make up the odor. Typically, individual chemical sensors are implemented for chemical detection, while an array of such devices coupled with signal processing algorithms comprise an e-nose capable of distinction. Clearly, both types of devices will share some of the same technological challenges: reliability, portability, and sensitivity.

Chemical sensors used for detection are designed to be specific, with the ability to exclusively respond to one particular analyte. However, e-noses use arrays of sensors that are (ideally) orthogonal in odor space while also covering a wide range in odor space. In odor space, one can imagine molecules being spatially located based on

their similarity to other odors, as measured by human noses. In other words, two odors judged to have similar odor quality are positioned closer together in the multidimensional odor space, than two different smelling odors. The dimensions of odor space are related to the physical and chemical attributes of the molecules themselves: molecular weight, number of double bonds, number of carbon atoms, etc. Thus, the big challenge for e-noses is to make an array that incorporates enough sensors to cover the application-specific odor space while maintaining orthogonality among the various sensors to minimize the complexity of the data processing algorithms used. Another issue for sensor arrays is the variation in the rate of degradation between different sensors, necessitating complex calibration routines [1]. Algorithms and signal processing techniques are again the main approaches to solving this issue and can be difficult to implement depending on the sensor technology. Another challenge for electronic noses is the creation of an accurate odor space itself. While there are numerous statistical odor classification schemes that weight each physicochemical attribute differently, to date there is no general relationship that can accurately predict the odor quality of molecules from their structure alone [2].

Because electronic noses are composed of an array of chemical sensors, the performance of the sensor array is limited by the properties (sensitivity, selectivity, reproducibility, reversibility, etc.) of the individual sensors. Therefore, this chapter will focus on the individual chemical sensing approaches and their transduction mechanisms, rather than the aggregate performance of the array coupled with signal processing techniques.

3.1 Survey of State-of-the-art Vapor-phase Solid-state Chemosensing Organic Devices

The basic function of chemical sensors is to transduce a chemical signal into a measured entity. Within this broad class of devices are vapor-phase chemosensors, which convert the presence of specific volatile organic molecules in the gas phase into a

measurable signal. Solid-state organic devices have the additional requirement of using carbon-based materials that are deposited as thin films. Despite these constraints, solid-state vapor-phase organic chemosensors encompass a diverse array of materials and device architectures. One simple sensor classification scheme uses the method of transduction to differentiate the technologies: electrical, optical, calorimetric (thermal) or gravimetric (mass). The electrical group can be further subdivided by device structure into chemiresistors, chemicapacitors, and organic thin-film transistors (OTFT). The optical group consists of chemoresponsive dyes, optical fiber sensors, surface plasmon resonance (SPR) sensors, and luminescent sensing schemes. The gravimetric group consists of surface acoustic wave (SAW) sensors, quartz crystal microbalances (QCM), and microcantilever sensors [Fig. 3-1]. This survey will be limited in scope to cover the most recent advances in solid-state vapor-phase organic chemosensors, and as such, will not be a comprehensive survey of all existing vapor-phase chemosensors. The scope of this chapter restricts the discussion to research performed within the last seven years and will reference older research, when necessary, to illustrate fundamental concepts. The focus of this survey also requires the organic (small-molecule, polymer, or carbon nanotube) materials to play a key role in the transduction mechanism by utilizing their electrical, optical, piezoelectric, or thermoelectric properties, rather than functionalizing an underlying inorganic sensor. Thus, the reader is encouraged to consult other sources to learn more about SAW [3], QCM [4, 5], and microcantilever [6, 7] sensing schemes that incorporate organic materials as functional groups to enhance selectivity.

3.1.1 Electrical Odor Sensors

These chemosensors represent the simplest of gas sensors in that their chemical reactivity is directly transduced into an electrical signal. Changes in resistance, capacitance, voltage, or current indicate the presence of a particular analyte. These types of sensors are widely used for gas and odor measurements in commercial electronic nose sensor arrays.

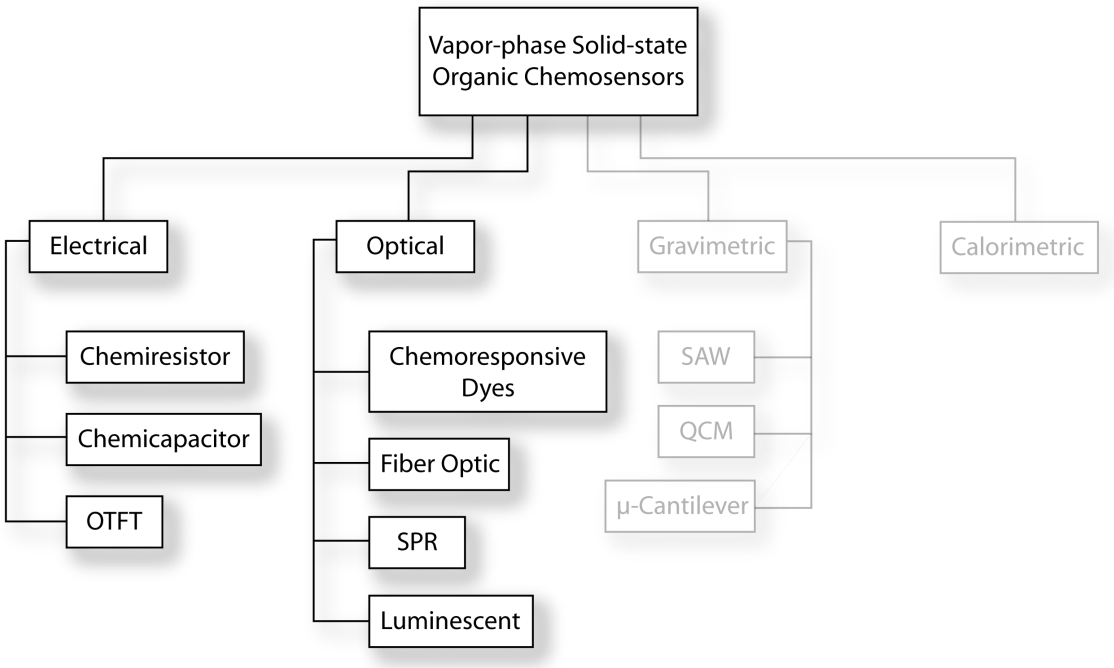

Figure 3-1: Classification tree of different chemical sensor technologies. Lighter boxes will not be covered in this chapter.

Chemiresistor

Chemiresistors represent the most common and simple type of sensor that incorporate organic materials. Generally speaking, the chemiresistor consists of a pair of electrodes that form contacts to the chemosensing material, which is deposited onto an insulating mechanical support [Fig. 3-2].

Normal operation involves applying a constant current through the sensing material while measuring the resulting potential difference at the electrodes. Thus, a change in resistivity would result in a change in the potential difference measured at the contacts. Inherently, this class of sensors requires less overhead electronics than more complex transduction schemes, which makes them suitable for miniaturization and portable applications. Some weaknesses include low signal to noise ratios and the variability in response repeatability to the same analyte, making them less useful when analyte concentrations need to be quantified. In addition, scalability is a major factor limiting the practical application of these sensors because bulk resistance changes are smaller with decreasing device size. Within this class of sensors, there are several

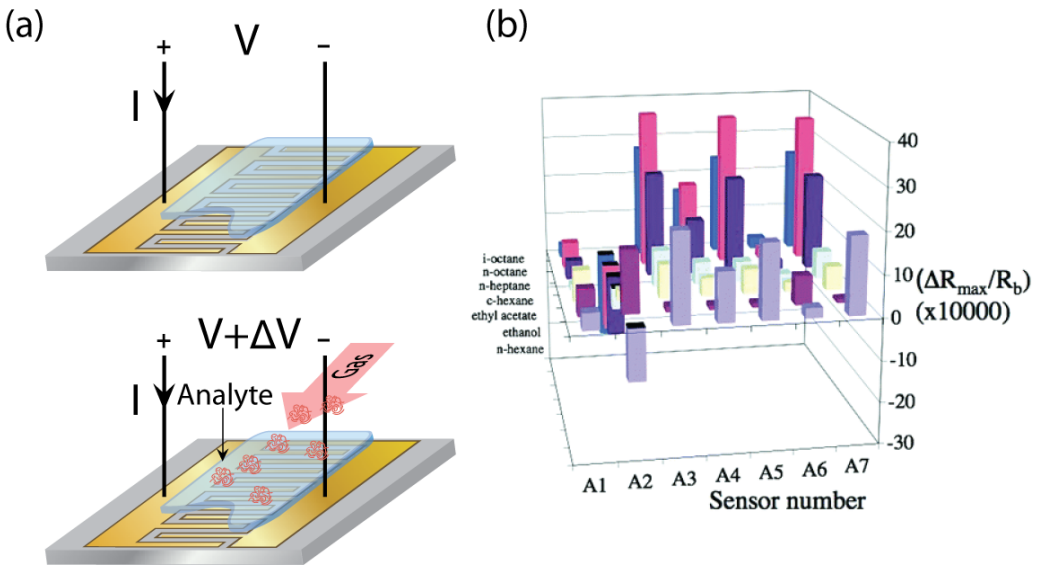

Figure 3-2: (a) Schematic of a typical chemiresistor device using interdigitated electrodes. There are two steady state conditions during operation: 1) no analyte present in the sampling environment, and 2) analyte present in the sampling environment resulting in a change in resistivity of the film. (b) Three-dimensional pattern depicting representative carbon black chemiresistor responses to seven test analytes [8].

classes of materials that are used for the sensing layer: organic conjugated polymers and polymer composites, carbon-black/organic composites, phthalocyanines, and carbon nanotubes. All of these materials exhibit an inherent change in conductivity due to the interaction with gases and can be used in different odor sensor schemes. For clarity, they are introduced here in the simplest sensor architecture.

Organic Conjugated Polymers and Polymer Composites

The alternating single and double bonds in organic conjugated polymers (CPs) allow for the delocalization of carriers along the polymer backbone, which gives the polymer the ability to conduct electricity. When this ability is coupled with the introduction of excess charges through doping, the polymer can then exhibit conductance from that of an insulator to that approaching a metallic conductor [9].

Recently organic conducting polymers have become the focus of much of the materials research in chemosensing devices. Synthetic flexibility allows the chemical and physical properties of polymers to be tailored over a broad range of values for any

given application. In addition, polymers exhibit tunable specificity to volatile organic compounds, which makes them ideal candidates for replacing canonical sensor materials such as metal oxide semiconductors. In a conducting polymer film, when a gaseous analyte is introduced it acts as either an electron donor or an electron acceptor. Most organic conducting polymers are p-type materials with holes as the majority charge carrier, determining the thin film conductance. If the conducting polymer donates an electron to the gas phase analyte, then its hole population and, consequently, its conductivity will increase. Alternatively, if the same conducting polymer receives an electron from the gas, then the hole population will decrease, reducing conductivity. Secondary effects include the slow diffusion of the gas into the conducting polymer itself, which can cause conformational changes in the polymer backbone [10]. Analyte gas diffusion generally results in a slow sensor response with more signal hysteresis.

Current trends in organic conducting polymer chemiresistor research involve the fabrication of nanostructures such as nanowires, nanotubes, or nanofibers made out of conducting polymers. The nanostructured conducting polymers have demonstrated improved sensor performance by increasing the exposed surface area as well as reducing the diffusion depth required for the penetration of gas molecules (due to high surface area to volume ratios) [11–14]. In addition, research into the incorporation of metal oxide nanostructures into the polymer films or incorporation of other polymers has yielded improvements in sensitivity, aging, and the ability to detect non-polar analytes [15–17]. The main advantages to using organic conducting polymer chemiresistors are their ease of fabrication, where polymers can be deposited under room temperature conditions. In addition, their compatibility with microfabricated structures makes them particularly suitable for low-cost high throughput manufacturing. Another advantage organic conducting polymer chemiresistors have is their ability to operate at room temperature. Metal oxide semiconductor chemiresistors are typically heated to between 200 °C and 500 °C for normal operation, which dissipates much more power. These polymers also typically have a sensor response time that is proportional to analyte concentration and the rapid adsorption/desorption kinetics as determined by van-der Waals bonding at the surface, allowing the sensor to

regenerate quickly. At the lowest analyte concentrations, the 10-100 second diffusion-limited response times [18] remain comparable to existing metal-oxide sensors that have response times in the range of a few seconds [19], depending on factors such as operating temperature and analyte concentration. Other weaknesses of organic conducting polymer chemiresistors are their variability from sensor to sensor and sensitivity to moisture.

Carbon-black Polymer Composite

Sensors using carbon-black polymer composites utilize a polymeric insulating matrix to separate and fix conductive carbon-black nanoparticles. The relative concentrations of the carbon-black particles to the polymer and the form factor of the active sensor determine the conductivity of the composite and its signal to noise ratio [1]. With a high enough concentration of carbon black, the composite exhibits a simple, linear response to analyte concentration. Alternately, low concentrations of carbon black enable the composite to operate near the percolation threshold, yielding improvements in sensitivity with higher signal to noise ratios, at the cost of having less reproducibility, less stability, and a more complex, non-linear response to analyte concentration [20].

The carbon black composite is usually spray-deposited onto interdigitated electrodes, where vapors that are introduced to the composite interact with the polymer and cause it to swell, thereby inducing a conformational change in the distance between neighboring carbon-black particles. Swelling results in a decrease in film conductivity. The sensitivity of sorption-based sensors is based on the interactions between the gaseous analyte and the polymer. By incorporating different functional groups into the polymer to target specific functional groups on the analyte, the selectivity of the sensor can be tuned to specific volatile organic compounds [21]. The composite's sensitivity is determined by the amount of vapor that the sensor can absorb. This interaction between gaseous analytes and the polymer matrix depends strongly on the density of functional groups within the matrix available to interact with the analyte.

Recent work being done in this class of sensors has incorporated non-polymeric materials to bind the carbon black particles, such as monomeric, low vapor pressure organic molecules with functional groups attached [8]. The benefit of using smaller organic molecules in the matrix is an increased density of functional groups present in the composite, producing an increase in sensitivity. Also, the random orientation of the organic molecule matrix should create a more permeable structure for enhanced vapor diffusion. Finally, the use of non-polymeric materials allows for new synthetic techniques to add chemical functionality and physical properties to the sensors that are not readily accessible in polymeric materials. Interestingly, these non-polymeric carbon-black composite sensors also exhibit some degree of selectivity to various analytes, making them practical for array-based sensing.

In general, carbon-black composites demonstrate fast response times, good reversibility, reproducibility, and stability. However, they lack the ability to react exclusively to many different gaseous analytes, making them better suited for a sensor array application where pattern recognition algorithms can aid in the identification of analytes.

Phthalocyanines

Phthalocyanines (PCs) are a robust class of semi-conducting organic small molecules that are used in a wide range of applications: photovoltaics, non-linear optics, xerography, and chemical sensing [22]. Chemical sensors based on metallophthalocyanine (MPc) thin films for the detection of donor and acceptor compounds (NH_3 [23, 24], NO_x [25], Halogens) have been developed in the form of chemiresistors for over a decade. The bases for using these molecules as gas sensing materials are their ease of deposition as high quality, thin films (increasing the exposed surface area); their ability to achieve a desired molecular functionality by changing the central metal atom or adding substituents to the phthalocyanine ring; and their thermal and chemical stability.

The conductivity of MPc chemiresistors is sensitive to the presence of oxidizing and reducing gases because a change in carrier concentration in the film occurs when

charge transfer states arise from the adsorption of electron-withdrawing or donating gases. Previous studies have shown that there are many factors that can affect the MPc's ability to sense gases: film morphology, film thickness, operating temperature, and post-deposition annealing [26]. The Pc films can be deposited on electrodes through a number of different methods such as Langmuir-Blodgett, spin-coating, thermal evaporation, or self-assembly.

Carbon Nanotubes

Discovered in 1991 by Sumio Iijima as a byproduct of an electrical discharge between graphite electrodes in an argon atmosphere [27], carbon nanotubes are chemical compounds that consist of concentric cylinders of covalently bonded hexagonal carbon rings. Carbon nanotubes range in size from a few nanometers in diameter and up to hundreds of micrometers in length. Single-walled carbon nanotubes (SWNT) consist of one concentric cylinder, while multiple-walled carbon nanotubes (MWNT) consist of several concentric cylinders. Carbon nanotubes have several unique mechanical and electrical properties that make them interesting from a sensing perspective: 1) carbon nanotubes have a large surface area to volume ratio [28], 2) they can be easily functionalized without disturbing their electronic structure, and 3) their electrical properties are extremely sensitive to the effects of charge transfer and chemical doping by various molecules.

Because of the difficulty in manipulating single nanotubes, carbon nanotube chemiresistors are based on films of spin-casted nanotubes on top of interdigitated electrodes. The interpenetrating network of carbon nanotubes has two sensing mechanisms. The first transduction mechanism is charge transfer from physically adsorbed analyte molecules, which modulate the Fermi level of the nanotube to cause a conductivity change. This intratube modulation is only significant if the nanotube is semiconducting in nature. The second transduction mechanism occurs when analyte molecules adsorb in the spaces between nanotubes, creating hopping conduction pathways between nanotubes that change the film's conductivity. This intertube modulation occurs for all types of molecules and for both metallic and semiconducting nanotubes,

similar to the interaction between conjugated polymers and adsorbed molecules. The intratube modulation dominates the sensor response at lower concentrations with a superlinear dependence on concentration and a high sensitivity, while the intertube modulation shows a linear dependence and lower sensitivity over a broad range of concentrations [29].

In principle, carbon nanotubes are not sensitive to many organic vapors, especially nonpolar molecules that will not transfer charge. Thus, polymer coatings and sputtered Pd films have been used to functionalize the nanotubes to specifically detect Cl_2 and H_2, respectively [30]. Advantages of using carbon nanotube films include detection levels on the order of ppm at room temperature, good reversibility, as well as low variation between sensor response (less than 6%) making them suitable for use in arrays. However, nanosensors based on this mechanism face sizeable challenges for commercialization, such as the inability to selectively grow semiconducting nanotubes and the complex techniques required to handle single nanotubes.

Chemicapacitor

Chemicapacitors are structurally the same as chemiresistors in that they consist of a pair of electrodes and a sensing material. The sensing layer can be either sandwiched between the two contacts [31] or deposited on top of a pair of planar interdigitated electrodes on an inert mechanical support [32, 33]. However, instead of relying on the changes in conductivity to detect the presence of analytes, this class of sensors measures the change in capacitance that develops across the chemosensitive film as the film absorbs the gaseous analyte. Absorption of analyte molecules changes the dielectric constant and other physical properties (e.g. volume) to produce deviations from the baseline capacitance [Fig. 3-3]. The chemicapacitors are usually excited with an AC voltage excitation (ranging from a few kHz up to 500 kHz) while the capacitances are measured using various readout circuits (frequency counters, output voltage, Sigma-Delta-modulators, etc.). Further details on the sensing mechanisms in chemicapacitor sensors can be found in [34].

The simple device design and low power consumption makes this platform attrac-

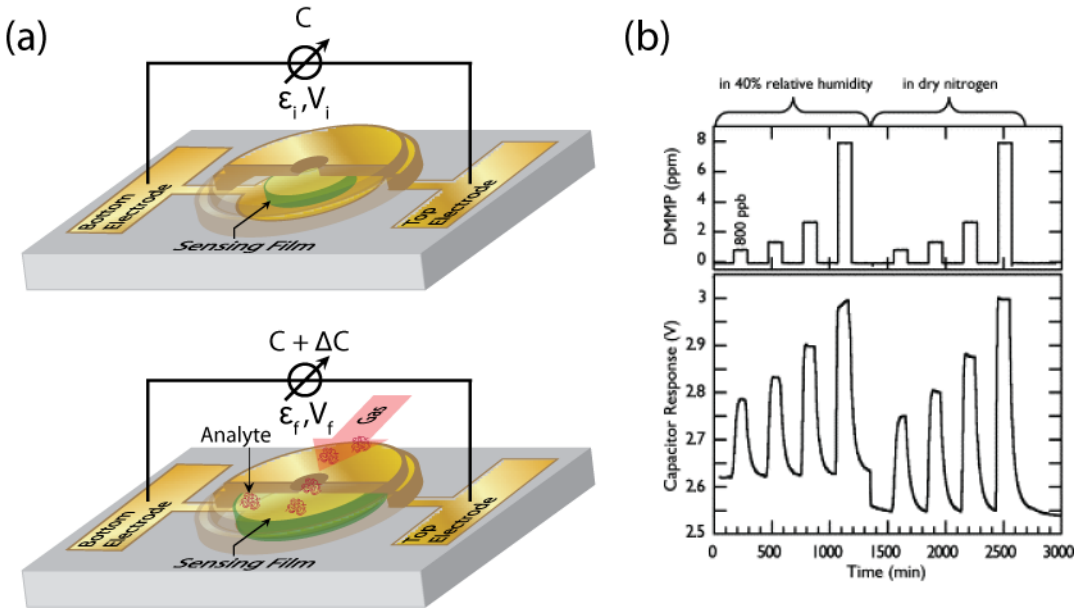

Figure 3-3: (a) Schematic of a typical chemicapacitor device using micro-machined, parallel plate electrodes. In this scheme, swelling of the film causes changes in both the dielectric constant (ϵ) and the voltage (V) which contribute to changes in capacitance. (b) Sample chemicapacitor response of the polymer, siloxanefluoro alcohol (SXFA), to dimethyl methylphosphonate (DMMP) in a background of dry nitrogen and nitrogen with 40% relative humidity [33].

tive for a wide range of gas sensing applications. In addition, the compatibility of the device structure with traditional semiconductor fabrication techniques allows for easy integration with complementary metal oxide semiconductor (CMOS) circuits and reduces the manufacturing costs needed to miniaturize the technology for portable gas sensing applications. While the sensor itself is rugged (no moving parts) and allows for a wide array of polymeric materials to be used as the sensor layer, the reliance on changes in the dielectric constant of the polymer makes these sensors susceptible to the high dielectric constant of moisture in the sampling environment. Humidity leads to large capacitive changes, which initially led to polyimide chemicapacitors being used as humidity sensors [35, 36].

More recent work in the chemicapacitor sensor field includes volatile organic compound detection using a variety of polymers [37] and liquid crystals [38]. However, most of the organic polymers that are used as sensitive coatings are only partially selective to most volatile organic compounds. To achieve finer selectivity of analytes, these sensors are usually placed in an array and combined with pattern recognition algorithms. Another method for enhancing the selectivity in chemicapacitive sensors is the use of configurable electrode configurations to provide two capacitive measurements with the same sensor. For simple, planar interdigitated structures, the electric field is mostly contained in the space above the electrodes to within a distance of half the electrode periodicity [39]. The interdigitated electrode periodicity can be changed by means of CMOS switches on the sensor chip, therefore the effective ratio between sensing layer thickness and electrode periodicity changes. For thinner films, the capacitance change will depend more on the total polarizable material absorbed and less on the dielectric constant. The opposite is true for thicker films, making the differential measurement more robust to ambient humidity [40].

Typically, chemicapacitors have sufficient sensitivity to detect common solvents to below 100 ppm, and below 1 ppm for explosives and chemical warfare agents. However, sensitivity will be temperature dependent as heat increases solvent volatility, decreasing the amount of absorbed analyte. The signal-to-noise ratio generally increases with increasing polymer and analyte polarity. With dedicated signal con-

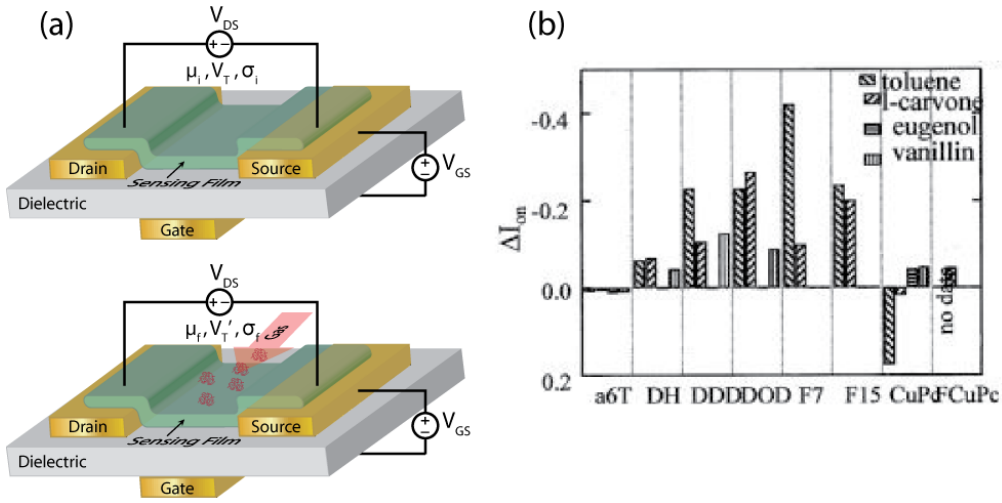

Figure 3-4: (a) Schematic of a typical OTFT gas sensor with a patterned gate electrode. The simultaneous measurement of multiple device properties, yields more information and makes OTFT's a more attractive sensor platform. (b) Fractional changes in drain current (I_{on}) for eight semiconductors upon exposure to four odorants: toluene, eugenol, vanillin, and l-carvone [45].

ditioning circuits the chemicapacitor is capable of resolving changes in capacitance as small as .07 fF [41]. The response times (time to reach 90% of full signal), which range from tens of seconds to minutes, are generally limited by the rates of diffusion of analyte molecules through the polymer [33].

Organic Thin-Film Transistor (OTFT)

Organic thin-film transistor (OTFT) technology is still considered a relatively new research area, with the first working OTFT fabricated out of polythiophene over two decades ago [42]. One argument in favor of using OTFTs as gas sensors is that they can provide more information about a particular analyte than an equivalent chemiresistor by monitoring changes in bulk conductivity, threshold voltage, field-induced conductivity, and field effect mobility [43]. The other advantage OTFT sensors have over chemiresistors is the signal amplification inherent in transistor device structures, which produces gains in sensitivity and signal-to-noise ratio [44].

The basic structure of an OTFT gas sensor is shown in [Fig. 3-4]. Typically, a

conductive mechanical support is used as the gate electrode, upon which an insulating dielectric coating is deposited. Next, a thermally evaporated or spun-coated thin film of active organic semiconductor is added. Finally, the source and drain electrodes are deposited over the semiconductor and are patterned to allow exposure of the active region to the environment. The organic field effect transistor is biased so that a channel of field-induced charge is created at the interface between the organic layer and the dielectric. When a bias is applied across the source and drain contacts, current flows through the device. The transduction of the chemical signal into an electrical signal occurs when the introduction of an analyte changes the current flowing through the sensor. The major difference from a chemiresistor is that the gate voltage allows for a modulation of the carrier density in the active sensing layer, which can enhance sensitivity. Because morphology and attached end/side groups on the organic semiconductor molecules provide sites for analyte interaction, both can be adjusted to provide additional improvements in sensitivity and selectivity [46]. There are several materials that are used for the sensing layer in this class of gas sensors: conducting polymers (CP) [47], phthalocyanines [48], and carbon nanotubes (CNT) [49]. The transduction mechanism for each of these materials remains unchanged from the case when the same materials are used for chemiresistors as discussed above.

Generally, there are three different areas where an analyte can modify the properties of the OTFT sensor: the bulk of the organic semiconductor, the interface between the organic layer and the dielectric material, and the interface between the organic layer and the electrical contacts [50]. Just as with chemiresistors, the conductivity in the bulk organic semiconductor can change with the transfer of charge between the gaseous analyte and the sensing film. The other bulk effect is a change in mobility, which occurs when the interaction between the sensing layer and the analyte causes swelling of the organic semiconductor. Because the active channel of current flow in the OTFT is mainly confined to the first few molecular layers at the interface between the organic layer and the insulating dielectric material, amphiprotic molecules (molecules that act as either an acid or base) such as alcohols, organic acids, water, etc., can react on the surface of the dielectric to increase the device conductivity.

This additional current is typically considered a parasitic conductive pathway and competes with the measured current signal from the organic semiconductor. Lastly, chemical modulation of the interface between the electrical contacts and the organic semiconductor can modulate the contact resistance and be responsible for the observed sensing effect.

Recent work has focused on enhancing the sensitivity of OTFT sensors. Crone et al. have reported that OTFT sensors are easily integrated into sensing circuits that can enhance the performance of the sensor. Ring oscillators and adaptive amplifiers, incorporating OTFT sensors, exhibit improved recovery time, sensitivity, and selectivity [45]. In an effort to increase the incremental change in conductivity from each analyte molecule by reducing the active area, Wang et al. have fabricated organic transistors with channel lengths on the nanometer scale. While the results did not yield the expected gains in sensitivity, the studies have elucidated the dependence of the sensor response on the relative size of the channel length to the grain size [51, 52]. Because of their inherent simplicity and ease of integration with traditional silicon devices, OTFTs will continue to be an active area of vapor-phase chemical sensor research.

3.1.2 Optical Odor Sensors

For this class of chemosensors, changes in the optical properties of the organic sensing layer are used to detect gaseous analytes. Many organic materials have high absorption coefficients, high photoluminescent efficiencies, and absorption and emission profiles that span the visible spectrum (300 nm to 800 nm). For these reasons, organic materials inherently provide a straightforward transduction mechanism to convert chemical signals into visual outputs, which can then be detected by our eyes, photodetectors, or CCD arrays for further processing. Optical odor sensors are versatile in that they can use a range of measurements (absorbance, reflectance, fluorescence, refractive index, polarization, colorimetry, interference, or scattering) to simultaneously collect information regarding intensity and wavelength.

Generally, optical sensors consist of four basic components: a mechanism or a

material that transduces a chemical signal into a change in optical properties, an excitation source to probe the sensor, optics for channeling light to and from the sensor, and a detector for converting optical signals into electrical signals. This class of sensors can be broadly organized into fluorescent and non-fluorescent technologies. Fluorescent technology is represented by amplified fluorescent polymers, non-fluorescent technology by chemoresponsive dyes and surface plasmon resonance (SPR), while optical fiber sensors encompass both types of sensor schemes.

Chemoresponsive Dyes

Colorimetric sensors using chemoresponsive dyes are the simplest of the optical odor sensors and are analogous to simple pH indicator strips that change color in the presence of an acid or base. Colorimetric gas sensors work in much the same way by utilizing dyes that can change color in the presence of vapor-phase analytes. Not only do we acquire qualitative information about the presence of certain gaseous analytes through color changes that can be perceived by the human eye and brain, but if scanned with a CCD, that information can then be processed in a quantitative fashion to determine concentrations. While this type of sensor can use many different instruments to convert the optical signal into an electrical response (the human eye [53], flatbed scanner [54–56], photodetectors [57]), the sensors rely upon the same fundamental shifts in the absorption spectra of the chemoresponsive chromophore to indicate the presence of analyte.

When designing a chemoresponsive dye two principles must be followed: 1) each dye must contain an interaction center that reacts strongly with analytes and 2) each interaction center must be strongly coupled to an efficient chromophore. The first principle requires that the analytes chemically interact with the dyes rather than merely physically adsorbing to the dye molecules. The importance of the strong dye-analyte interaction is highlighted by recent data that suggests that mammalian olfactory receptors are metalloproteins, and that chemical interactions with the metal center are intrinsic to the mechanism of smelling [58].

The metalloporphyrin family of organic molecules has found widespread use in

colorimetric sensors due to their intense coloration, their large spectral shifts upon binding with foreign molecules, and the suite of organic chemistry techniques developed for these compounds. Many different chemoresponsive dyes can be synthesized by combining different metals with the porphyrin structure to form stable metalloporphyrin complexes. In these complexes, the central metal atom plays a primary role in the sensitivity and selectivity properties of the dye. Many volatile organic compounds are excellent ligands for metal ions and readily bind to the central metal atom to provide large color changes in the dye. In addition, the ability to add a wide range of side groups to peripheral positions on the porphyrin ring can enable enhanced selectivity.

Sensor arrays made from these chemoresponsive dyes are sensitive (110 ppb to 2 ppm) to volatile organic compounds and with proper choice of dye and mechanical support are not affected by ambient humidity. Also, the response time of colorimetric sensors is relatively slow (2 min. at 1 ppm analyte concentration) limited by the flow rate of the gas delivery to the sensor or equilibration of low vapor concentrations over large surface areas [59]. The simple, low-cost fabrication techniques for depositing chemoresponsive dye sensor arrays makes them ideal for general-purpose vapor dosimeters or disposable analyte-specific detectors. However, implementation of a gas monitoring system using this technology becomes prohibitively expensive to install and maintain.

Surface Plasmon Resonance

Surface plasmon resonance (SPR) is an optical phenomenon where the conditions for total internal reflection at the interface between materials with different indices of refraction are satisfied, allowing an exponentially decaying evanescent wave to propagate in the medium with the lower index of refraction. When that interface is coated with a thin film of conductive metal (i.e. gold or silver), the evanescent wave can excite surface plasmon waves at the interface that propagate parallel to the interface. The coupling between the incident light with the surface plasmon waves (SPW) in the thin film causes the reflected light to assume a particular wavelength,

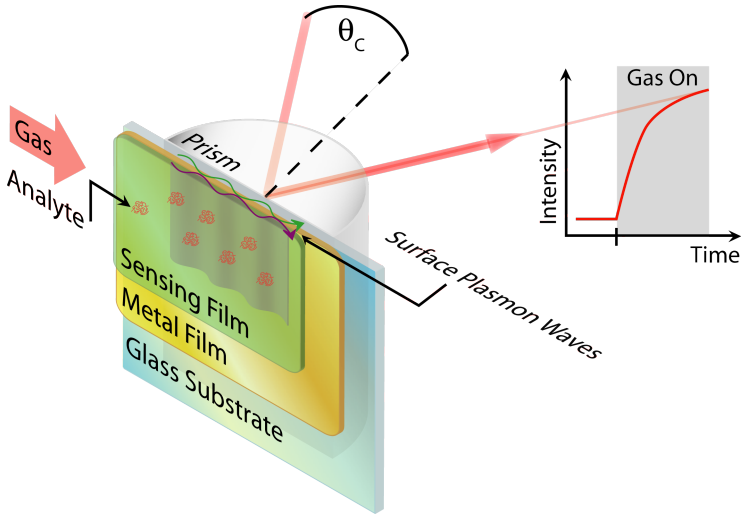

Figure 3-5: Kretschmann configuration of SPR gas sensing method. The graph indicates a real-time measurement of intensity at a given wavelength and angle of reflected light.

angle, intensity, or phase. Thus, any changes in the local refractive index at the interface will change the optical properties of the reflected light from the interface and produce a signal [Fig. 3-5].

SPR chemical sensors consist of an optical system, a transducing medium, and an electronic system for data processing. The transducing medium converts changes in the quantity of detected analyte into changes in refractive index, enabling the use of SPR to probe the variation. Typically, thin films of polymers [60] and small-molecule organics [61] are used as the transducing medium. As with most organic materials, the films can be deposited using spin coating, dip coating, or Langmuir-Blodgett techniques. SPR techniques can even be combined with optical fiber sensors to miniaturize the device design. While comparable sensitivities can be achieved, careful control over the measurement environment (mechanical, temperature, polarization) must be maintained [62, 63].

Sensor sensitivity, stability, and resolution depend upon the combined properties of the optical system and the sensing film. However, the selectivity, reversibility, stability, and response time are primarily determined by the properties of the sensing film. Because the SPR signals are strongly influenced by the optical properties of the

sensing film, SPR sensors are extremely sensitive to small changes in the refractive index (down to 5 x 10^{-7} RIU) corresponding to better than 1 ppm levels of detection. Despite these high sensitivities, SPR will only detect adsorbates that have a molecular weight $>$ 500 Da, which can efficiently change refractive indices [64]. Some recent work has demonstrated the use of nematic liquid crystals [65] and cavitands (a class of supramolecule) [66] for SPR gas sensors. These materials exhibit relatively fast response times ($<$ 1 s) enabling this class of SPR sensors to be used for real-time monitoring of some volatile organic compounds.

Optical Fiber Sensors

Fiber optic technology first developed for the communications industry has been finding its way into chemical sensors. There are many technological reasons that make fiber optics sensors an attractive proposition. Optical fiber sensors are passive, requiring no electricity for operation. This can be important when trying to detect analytes in highly combustible environments or if the analyte itself is flammable at low vapor concentrations. For the same reason, fiber optic sensors are resistant to electromagnetic interference (EMI), making them useful for detecting analytes in environments with high and variable electric fields such as the power industry. In addition, fiber optics are capable of transmitting optical signals for long distances with low losses, enabling a receiver to be placed some distance away from the point of detection for remote sensing capabilities. By using existing optical instrumentation, optical sensing can be readily multiplexed to carry different measurement signals simultaneously. For most applications, however, fiber optic sensors are far more costly to implement than other gas sensing approaches [67].

Recent work has investigated conductive polymers [68, 69], sol-gels [70] and chemoresponsive dyes [71] for use as the gas-sensitive transduction medium in fiber optic sensors. In general, fiber optic sensors can be divided into two different sensing architectures: extrinsic and intrinsic. If the transduction of the chemical signal into an optical signal occurs within the fiber itself, it is known as an intrinsic sensor. Extrinsic sensors perform the transduction outside of the fiber [Fig. 3-6]. In extrinsic

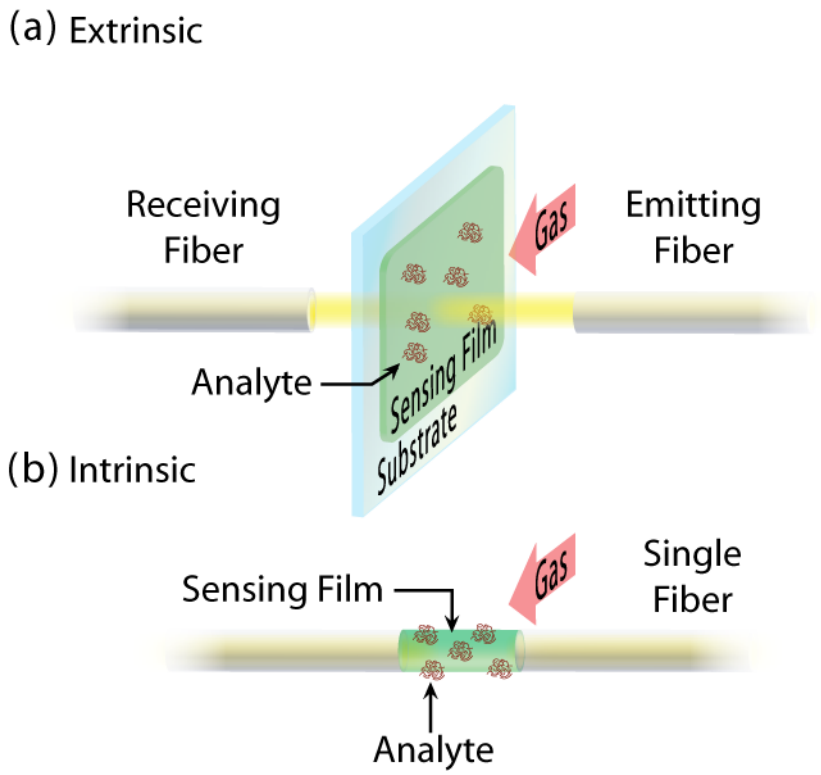

Figure 3-6: (a) Extrinsic optical fiber sensor, where fibers are used to guide input and output signals (b) Intrinsic optical fiber sensor, where the sensing film is incorporated into fiber structure as a cladding material.

sensors the fiber acts as a transmission line to bring light to a detection cell and to guide the light output to a photodetector or a spectrometer [72]. The detection cell contains the organic materials that provide selective gas detection. However, most fiber optic sensor research focuses on intrinsic sensors, with the most common being evanescent wave sensors.

In evanescent wave sensors, a small section of the passive cladding of the fiber is replaced with a chemically active sensing material. Thus, any interaction between a gaseous analyte and the sensitive material will manifest in a change in the effective index of refraction in the fiber, changing its transmission properties [68]. The chemically active material can be deposited onto the fiber in a number of ways once the silica cladding is removed through polishing or etching: dip coating, sol-gel deposition, or Langmuir-Blodgett [73]. For more information regarding the operation and theory of evanescent wave fiber optic sensors the reader is directed to literature [74].

A major limitation of the sensitivity of the intrinsic fiber sensor is the ability to transfer optical power into the evanescent field. Recent work has incorporated new types of fibers to increase the sensitivity of measurements. Newly developed hollow core fibers, which guide light mainly in the cladding, can be used to couple more power into the chemosensitive materials [75]. If the hollow core fiber is used as the active sensing area between two silica core fibers, then the transitions between the fibers will force the light to travel from the core into the cladding then back into the core. Another type of fiber is the microstructure fiber or photonic crystal fiber, which incorporates air holes into the silica cladding to enhance the interaction between the evanescent field and the gaseous analyte. By adjusting the size and placement of the air holes, light propagation in the fiber can be controlled [76].

Other advances in intrinsic fiber optic sensors include Bragg grating fiber sensors [77, 78], active fiber core [70], optodes [73, 79], fluorescent fibers [80, 81], and some hybrid combination of the previous sensor schemes [63]. In general, the selectivity of the fiber optic sensor is governed by the light source wavelength and the chemical and physical properties of the sensing material. Special input signal modulation techniques can be used to enhance the selectivity of the sensors by reducing the cross-reactivity of other gases. Sensitivities are competitive with other sensor technologies (low ppm) and response times are relatively fast (~10 s), allowing for real-time monitoring of gaseous analytes such as ammonia [82]. However, prohibitive manufacturing costs, careful calibration requirements, and large amounts of overhead electronics and optics make fiber optic sensor systems less robust and more difficult to integrate into existing silicon circuit architectures. In addition, low dynamic range (as compared to other sensing schemes) and unsustainable reversibility limit the number of suitable applications.

Photoluminescent Sensors

Photoluminescence (PL) techniques are at the heart of many optical sensing schemes for a wide range of applications and can be extremely sensitive, enabling the detection of single molecules [83]. In general, PL is generated by fluorophores that absorb light

at wavelengths within their absorption spectrum and emit light at longer wavelengths, corresponding to the emission spectrum. The energy difference in emission and absorption spectra is referred to as a Stoke shift and represents vibrational relaxation and other energy loss mechanisms following absorption of a photon by a molecule. The PL sensor scheme is surprisingly simple and can yield high sensitivities [Fig. 3-7]. A thin film of the chemoresponsive material is excited by an excitation source (LED, laser, etc.) and a photodetector is used to collect the emission of the transducing material. The introduction of an analyte vapor will result in a change in optical properties yielding a differential measured signal. An increase in emission results in a "turn-on" signal, while emission quenching results in a "turn-off" signal. "Turn-on" schemes require that the photoluminescent material be highly quenched. As a result, the distance between quenching sites will be less than the exciton diffusion length. In this situation, the sensitivity of the "turn-on" response will be decreased relative to the "turn-off" response, which relies on long exciton diffusion lengths to yield the high sensitivities necessary for ultra-trace detection. Additionally, the measured quantity in both cases is a differential intensity signal, making the lower limit of the signal-to-noise ratio (SNR) the determining factor of sensitivity. Thus, the only case where the "turn-on" response is easier to observe is if the new signal is produced against a completely dark background, so that the detection is no longer based on a ratio of signals. This is usually not the case, as background fluorescence often negates the sensitivity advantage of the "turn-on" response with regard to SNR. However, for trace detection in complex environments, "turn-on" detection schemes do have an advantage in selectivity as there are many more "false-positives" caused by adventitious quenching as opposed to fluorescence enhancement [84].

With the ability to measure a number of different parameters (decay time, energy transfer, polarization, quenching efficiency, intensity) and simple instrumentation, luminescent sensor techniques have become standard practice [85]. The ubiquity of luminescent sensing schemes and low-cost, high quality electronics, has even made possible the use of a computer screen as a programmable light source and a web camera as a photodetector in a chemical sensing technique known as the computer

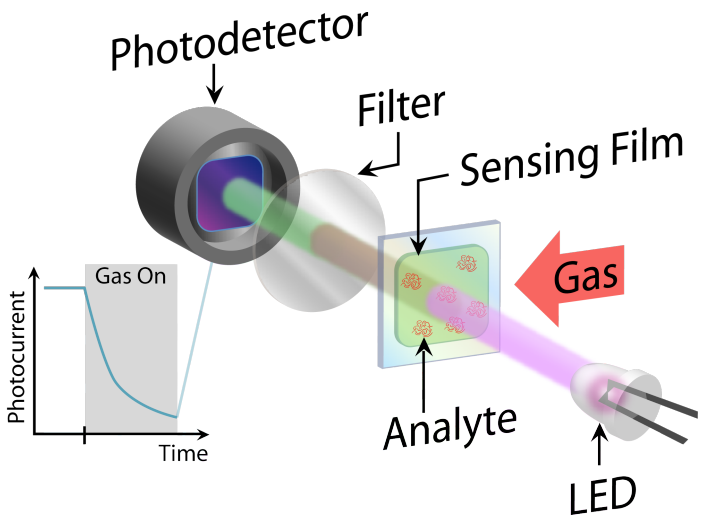

Figure 3-7: Schematic of a typical configuration of a PL gas sensor. The LED is used to excite the sensing film, while the filter acts to prevent the excitation from reaching the photodetector. Upon introduction of a gaseous analyte, the sensing film's luminescence is quenched, producing a reduction in the PL intensity measured by the photodetector.

screen photo assisted technique (CSPT) [86]. As luminescent sensing methods have matured, much of the ongoing research in this field focuses on the synthesis of new luminescent chemoresponsive materials to enhance analyte sensitivity and selectivity. Organic PL chemoresponsive materials span a wide range of compounds including metalloporphyrin dye molecules [87], supramolecules, conjugated organic polymers [88], conjugated inorganic polymers [89], and phosphorescent molecules [90]. These luminescent compounds are either deposited as thin films [91], used as coatings for particles [92], or incorporated into inert, permeable matrices [93].

3.1.3 Summary

While much of the surveyed research exhibits promising vapor-phase sensing performance, many of the technologies remain experimental and bound to a laboratory setting [Table 3.1]. Most of the commercial gas sensors available today utilize older, more mature technologies such as electrochemical cells, catalytic beads, photoionization detectors (PID), SAW, metal oxide semiconductors (MOS), and QCM. The dearth of viable organic solid-state vapor-phase chemosensors indicates that there is

much work still to be done (in terms of material stability, selectivity, etc.) before commercialization becomes commonplace for organic sensors.

Chemosensor Type	Material classes	Analytes	Applications	Companies
Chemiresistor	OCP	VOCs	Medical diagnosis, Food/Beverage, Process control, Security	Scensive Technologies
	OCP	VOCs	Pharmaceutical, Quality control	Alpha M.O.S.
	OCP	VOCs	Breath analysis	Abtech Scientific Inc.
	Pc/MPc	NO_x, NH_3, O_2, Halogens	Environmental monitoring	(Research only)
	Carbon black composite	VOCs	Petrochemical, Food/Beverage, Packaging, Plastics, Pet food	Smiths Detection (Cyranose)
	CNT	H_2, CO_2	Industrial gas detection, Breath analysis	Nanomix
Chemicapacitor	OCP	VOCs, CWAs, TICs	Environmental monitoring, Security, Process control	Seacoast Science Inc.
	OCP	H_2O	Indoor air quality (Relative Humidity)	Jackson Systems
OTFT	OCP	VOCs	Environmental monitoring	(Research only)
	CNT	H_2S, NO_x, CO_x, NH_3, N_2	Environmental monitoring	(Research only)
Chemoresponsive Dyes	Metalloporphyrins	Toxic Gas	Toxic gas dosimeter	Honeywell Analytics
	Metalloporphyrins	VOCs	Bacteria identification, Breath analysis	ChemSensing Inc.
	Metalloporphyrins	Hydrocarbon	Meat spoilage	FQSI
	Metalloporphyrins	H_2S, Cl_2, CO, N_2H_4, O_3	Toxic gas dosimeter	American Gas and Chemical Co.
SPR	Metalloporphyrins	O_2	Oxygen sensing	Sentronic
Optical Fiber	Dye/Polymer matrix	Hydrocarbons	Environmental monitoring	PetroSense
	Dye/Polymer matrix	O_2	Oxygen sensing	Sentronic
	Dye/Polymer matrix	VOCs, O_2	Environmental monitoring, Process control	Interlab (Optosen)
	Dye/Polymer matrix	O_2	Oxygen sensing	Ocean Optics
PL Sensors	OCP	Explosives, CWAs	Security, Life Sciences	ICx Technologies
	OCP	VOCs	Air quality, Security, Process control	CogniScent
	OCP	VOCs	(In development)	Nanoident
	Metalloporphyrins	O_2	Oxygen sensing	Sentronic

Table 3.1: Commercially available and research-grade solid-state organic vapor-phase chemical sensors and e-nose instruments as of May 2007. Abbreviations: Organic Conjugated Polymer (OCP), Phthalocyanine (Pc), Metallophthalocyanine (MPc), Carbon Nanotube (CNT), Volatile Organic Compound (VOC), Chemical Warfare Agents (CWA), Toxic Industrial Compound (TIC), Organic Thin Film Transistor (OTFT), Surface Plasmon Resonance (SPR), and Photoluminescent (PL).

Chapter 3 References

[1] B. C Sisk and N. S Lewis. Comparison of analytical methods and calibration methods for correction of detector response drift in arrays of carbon black-polymer composite vapor detectors. *Sensors and Actuators B-Chemical*, 104(2):249–268, 2005.

[2] L. Turin. *Structure-odor relations: A modern perspective*. Handbook fo Olfaction and Gustation. Marcel Dekker, New York, 2002.

[3] M. Thompson and D. C Stone. *Surface-Launched Acoustic Wave Sensors*, volume 144 of *Chemical Analysis*. John Wiley & Sons, Inc., New York, 1997.

[4] R. Lucklum and P. Hauptmann. Acoustic microsensors-the challenge behind microgravimetry. *Analytical and Bioanalytical Chemistry*, 384(3):667–682, 2006.

[5] C. K O'Sullivan and G. G Guilbault. Commercial quartz crystal microbalances - theory and applications. *Biosensors & Bioelectronics*, 14(8-9):663–670, 1999.

[6] Y. Jin, K. M Wang, and R. Jin. Development of novel and sensitive sensors based on microcantilever of atomic force microscope. *Progress in Natural Science*, 16(5):445–451, 2006.

[7] A. Hierlemann, O. Brand, C. Hagleitner, and H. Baltes. Microfabrication techniques for chemical/biosensors. *Proceedings of the IEEE*, 91(6):839–863, 2003.

[8] T. Gao, M.D. Woodka, B.S. Brunschwig, and N.S. Lewis. Chemiresistors for Array-Based vapor sensing using composites of carbon black with low volatility organic molecules. *Chemistry of Materials*, 18(22):5193–5202, October 2006.

[9] A. J Heeger. Semiconducting and metallic polymers: The fourth generation of polymeric materials (Nobel lecture). *Angewandte Chemie-International Edition*, 40(14):2591–2611, 2001.

[10] W. Zheng, Y. Min, A. G MacDiarmid, M. Angelopoulos, Y. H Liao, and A. J Epstein. Effect of organic vapors on the molecular conformation of non-doped polyaniline. *Synthetic Metals*, 84(1-3):63–64, 1997.

[11] J. X Huang, S. Virji, B. H Weiller, and R. B Kaner. Polyaniline nanofibers: Facile synthesis and chemical sensors. *Journal of the American Chemical Society*, 125(2):314–315, 2003.

[12] J. Huang, S. Virji, B. H Weiller, and R. B Kaner. Nanostructured polyaniline sensors. *Chemistry-a European Journal*, 10(6):1315–1319, 2004.

[13] B. Liu and G. C Bazan. Optimization of the molecular orbital energies of conjugated polymers for optical amplification of fluorescent sensors. *Journal of the American Chemical Society*, 128(4):1188–1196, 2006.

[14] R. Kessick and G. Tepper. Electrospun polymer composite fiber arrays for the detection and identification of volatile organic compounds. *Sensors and Actuators B-Chemical*, 117(1):205–210, 2006.

[15] B. Li, G. Sauve, M. C Iovu, M. Jeffries-El, R. Zhang, J. Cooper, S. Santhanam, L. Schultz, J. C Revelli, A. G Kusne, T. Kowalewski, J. L Snyder, L. E Weiss, G. K Fedder, R. D McCullough, and D. N Lambeth. Volatile organic compound detection using nanostructured copolymers. *Nano Letters*, 6(8):1598–1602, 2006.

[16] L. M Dai, P. Soundarrajan, and T. Kim. Sensors and sensor arrays based on conjugated polymers and carbon nanotubes. *Pure and Applied Chemistry*, 74(9):1753–1772, 2002.

[17] M. K Ram, O. Yavuz, V. Lahsangah, and M. Aldissi. CO gas sensing from ultrathin nano-composite conducting polymer film. *Sensors and Actuators B-Chemical*, 106(2):750–757, 2005.

[18] S. L. Tan. Velocity-optimized diffusion for ultra-fast polymer based resistive gas sensors. *IEEE Proc.-Sci. Meas. Technol.*, 153(3):94–100, 2006.

[19] T. C Pearce, S. S Schiffman, H. T Nagle, and J. W Gardner, editors. *Handbook of Machine Olfaction*. Wiley-VCH, Weinheim, 2003.

[20] B. C Sisk and N. S Lewis. Vapor sensing using polymer/carbon black composites in the percolative conduction regime. *Langmuir*, 22(18):7928–7935, 2006.

[21] E. S Tillman, M. E Koscho, R. H Grubbs, and N. S Lewis. Enhanced sensitivity to and classification of volatile carboxylic acids using arrays of linear poly(ethylenimine)-carbon black composite vapor detectors. *Analytical Chemistry*, 75(7):1748–1753, 2003.

[22] N. Kobayashi. Phthalocyanines. *Current Opinion in Solid State & Materials Science*, 4(4):345–353, 1999.

[23] B. Schollhorn, J. P Germain, A. Pauly, C. Maleysson, and J. P Blanc. Influence of peripheral electron-withdrawing substituents on the conductivity of zinc phthalocyanine in the presence of gases. part 1: reducing gases. *Thin Solid Films*, 326(1-2):245–250, 1998.

[24] J. P Germain, A. Pauly, C. Maleysson, J. P Blanc, and B. Schollhorn. Influence of peripheral electron-withdrawing substituents on the conductivity of zinc phthalocyanine in the presence of gases. part 2: oxidizing gases. *Thin Solid Films*, 333(1-2):235–239, 1998.

[25] W. F Qiu, W. P Hu, Y. Q Liu, S. Q Zhou, Y. Xu, and D. B Zhu. The gas sensitivity of a substituted metallophthalocyanine, tetra-iso-propoxyphthalocyaninato copper (II). *Sensors and Actuators B-Chemical*, 75(1-2):62–66, 2001.

[26] Y. L. Lee. NO2 sensing characteristics of copper phthalocyanine films: Effects of low temperature annealing and doping time. *Sensors and Actuators B-Chemical*, 119:174–179, 2006.

[27] S. Iijima. Helical Microtubules of Graphitic Carbon. *Nature*, 354(6348):56–58, 1991.

[28] J. Li, Y. Lu, and M. Meyyappan. Nano chemical sensors with Polymer-Coated carbon nanotubes. *IEEE Sensors Journal*, 6(5):1047–1051, 2006.

[29] J. Li, Y. Lu, Q. Ye, M. Cinke, J. Han, and M. Meyyappan. Carbon nanotube sensors for gas and organic vapor detection. *Nano Letters*, 3(7):923–933, 2003.

[30] I. Sayago, E. Terrado, M. Aleixandre, M. C Horrillo, M. J Fernandez, J. Lozano, E. Lafuente, W. K Maser, A. M Benito, M. T Martinez, J. Gutierrez, and E. Munoz. Novel selective sensors based on carbon nanotube films for hydrogen detection. *sensors and Actuators B-Chemical*, 122:75–80, 2007.

[31] H. Shibata, M. Ito, M. Asakursa, and K. Watanabe. A digital hygrometer using a polyimide film relative humidity sensor. *IEEE Transactions on Instrumentation and Measurement*, 45(2):564–569, 1996.

[32] R. Igreja and C. J Dias. *Capacitance response of polysiloxane films with interdigital electrodes to volatile organic compounds*, volume 455-456 of *Materials Science Forum*, pages 420–424. Trans Tech Publications Ltd, Zurich-Uetikon, 2004.

[33] S. V Patel, T. E Mlsna, B. Fruhberger, E. Klaassen, S. Cemalovic, and D. R Baselt. Chemicapacitive microsensors for volatile organic compound detection. *Sensors and Actuators B-Chemical*, 96(3):541–553, 2003.

[34] A. M Kummer, A. Hierlemann, and H. Baltes. Tuning sensitivity and selectivity of complementary metal oxide semiconductor-based capacitive chemical microsensors. *Analytical Chemistry*, 76(9):2470–2477, 2004.

[35] T. Boltshauser and H. Baltes. Capacitive Humidity Sensors in SACMOS Technology with Moisture Absorbing Photosensitive Polyimide. *Sensors and Actuators A-Physical*, 26(1-3):509–512, 1991.

[36] T. Boltshauser, L. Chandran, H. Baltes, F. Bose, and D. Steiner. Humidity Sensing Properties and Electrical Permittivity of New Photosensitive Polyimides. *Sensors and Actuators B-Chemical*, 5(1-4):161–164, 1991.

[37] F. Josse, R. Lukas, R. N Zhou, S. Schneider, and D. Everhart. AC-impedance-based chemical sensors for organic solvent vapors. *Sensors and Actuators B-Chemical*, 36(1-3):363–369, 1996.

[38] F. L Dickert, G. K Zwissler, and E. Obermeier. LIQUID-CRYSTALS ON INTERDIGITAL STRUCTURES - APPLICATIONS AS CAPACITIVE CHEMICAL SENSORS. *Berichte Der Bunsen-Gesellschaft-Physical Chemistry Chemical Physics*, 97(2):184–188, 1993.

[39] Van Gerwen P.[1], Laureyn W., Laureys W., Huyberechts G., Op De Beeck M., Baert K., Suls J., Sansen W., Jacobs P., Hermans L., and Mertens R. Nanoscaled interdigitated electrode arrays for biochemical sensors. *Sensors and Actuators B: Chemical*, 49:73–80, June 1998.

[40] A. M Kummer and A. Hierlemann. Configurable electrodes for capacitive-type sensors and chemical sensors. *IEEE Sensors Journal*, 6(1):3–10, 2006.

[41] R. Igreja and C. J Dias. *Organic vapour discrimination using sorption sensitive chemocapacitor arrays*, volume 514-516 of *Materials Science Forum*, pages 1064–1067. Trans Tech Publications Ltd, Zurich-Uetikon, 2006.

[42] A. Tsumura, H. Koezuka, and T. Ando. Macromolecular Electronic Device - Field-Effect Transistor with a Polythiophene Thin-film. *Applied Physics Letters*, 49(18):1210–1212, 1986.

[43] L. Torsi, A. Dodabalapur, L. Sabbatini, and P. G Zambonin. Multi-parameter gas sensors based on organic thin-film-transistors. *Sensors and Actuators B-Chemical*, 67(3):312–316, 2000.

[44] J. T Mabeck and G. G Malliaras. Chemical and biological sensors based on

organic thin-film transistors. *Analytical and Bioanalytical Chemistry*, 384(2):343–353, 2006.

[45] B. K Crone, A. Dodabalapur, R. Sarpeshkar, A. Gelperin, H. E Katz, and Z. Bao. Organic oscillator and adaptive amplifier circuits for chemical vapor sensing. *Journal of Applied Physics*, 91(12):10140–10146, 2002.

[46] J. Locklin and Z. N Bao. Effect of morphology on organic thin film transistor sensors. *Analytical and Bioanalytical Chemistry*, 384(2):336–342, 2006.

[47] J. B Chang, V. Liu, V. Subramanian, K. Sivula, C. Luscombe, A. Murphy, J. S Liu, and J. M. J Frechet. Printable polythiophene gas sensor array for low-cost electronic noses. *Journal of Applied Physics*, 100(1):7, 2006.

[48] M. Bouvet. Phthalocyanine-based field-effect transistors as gas sensors. *Analytical and Bioanalytical Chemistry*, 384(2):366–373, 2006.

[49] C. S Huang, B. R Huang, Y. H Jang, M. S Tsai, and C. Y Yeh. Three-terminal CNTs gas sensor for n-2 detection. *Diamond and Related Materials*, 14(11-12):1872–1875, 2005.

[50] H. Chen, M. Josowicz, and J. Janatax. Chemical effects in organic electronics. *Chemistry of Materials*, 16(23):4728–4735, 2004.

[51] L. Wang, D. Fine, and A. Dodabalapur. Nanoscale chemical sensor based on organic thin-film transistors. *Applied Physics Letters*, 85(26):6386–6388, 2004.

[52] L. Wang, D. Fine, S. I Khondaker, T. Jung, and A. Dodabalapur. Sub 10 nm conjugated polymer transistors for chemical sensing. *Sensors and Actuators B-Chemical*, 113(1):539–544, 2006.

[53] N. A Rakow and K. S Suslick. A colorimetric sensor array for odour visualization. *Nature*, 406(6797):710–713, 2000.

[54] K. S Suslick. An optoelectronic nose: "Seeing" smells by means of colorimetric sensor arrays. *MRS Bulletin*, 29(10):720–725, 2004.

[55] N. A Rakow, A. Sen, M. C Janzen, J. B Ponder, and K. S Suslick. Molecular recognition and discrimination of amines with a colorimetric array. *Angewandte Chemie-International Edition*, 44(29):4528–4532, 2005.

[56] K. S Suslick, N. A Rakow, and A. Sen. Colorimetric sensor arrays for molecular recognition. *Tetrahedron*, 60(49):11133–11138, 2004.

[57] T. Nakamoto, M. Yosihioka, Y. Tanaka, K. Kobayashi, T. Moriizumi, S. Ueyama, and W. S Yerazunis. Colorimetric method for odor discrimination using dye-coated plate and multiLED sensor. *Sensors and Actuators B-Chemical*, 116(1-2):202–206, 2006.

[58] J. Y Wang, Z. A Luthey-Schulten, and K. S Suslick. Is the olfactory receptor a metalloprotein? *Proceedings of the National Academy of Sciences of the United States of America*, 100(6):3035–3039, 2003.

[59] M. C Janzen, J. B Ponder, D. P Bailey, C. K Ingison, and K. S Suslick. Colorimetric sensor arrays for volatile organic compounds. *Analytical Chemistry*, 78(11):3591–3600, 2006.

[60] A. V Samoylov, V. M Mirsky, Q. Hao, C. Swart, Y. M Shirshov, and O. S Wolfbeis. Nanometer-thick SPR sensor for gaseous HCl. *Sensors and Actuators B-Chemical*, 106(1):369–372, 2005.

[61] T. Basova, E. Kol'stov, A. K Ray, A. K Hassan, A. G Gurek, and V. Ahsen. Liquid crystalline phthalocyanine spun films for organic vapour sensing. *Sensors and Actuators B-Chemical*, 113(1):127–134, 2006.

[62] X. Bevenot, A. Trouillet, C. Veillas, H. Gagnaire, and M. Clement. Surface plasmon resonance hydrogen sensor using an optical fibre. *Measurement Science & Technology*, 13(1):118–124, 2002.

[63] Y. C Kim, W. Peng, S. Banerji, and K. S Booksh. Tapered fiber optic surface plasmon resonance sensor for analyses of vapor and liquid phases. *Optics Letters*, 30(17):2218–2220, 2005.

[64] J. Mavri, P. Raspor, and M. Franko. Application of chromogenic reagents in surface plasmon resonance (SPR). *Biosensors & Bioelectronics*, 22(6):1163–1167, 2007.

[65] E. B Feresenbet, F. Taylor, T. M Chinowsky, S. S Yee, and D. K Shenoy. Optical chemical sensing using nematic liquid crystal. *Sensor Letters*, 2(2):145–152, 2004.

[66] E. B Feresenbet, E. Dalcanale, C. Dulcey, and D. K Shenoy. Optical sensing of the selective interaction of aromatic vapors with cavitands. *Sensors and Actuators B-Chemical*, 97(2-3):211–220, 2004.

[67] B. Culshaw. Optical fiber sensor technologies: Opportunities and-perhaps-pitfalls. *Journal of Lightwave Technology*, 22(1):39–50, 2004.

[68] S. Khalil, L. Bansal, and M. El-Sherif. Intrinsic fiber optic chemical sensor for the detection of dimethyl methylphosphonate. *Optical Engineering*, 43(11):2683–2688, 2004.

[69] E. Scorsone, S. Christie, K. C Persaud, and F. Kvasnik. Evanescent sensing of alkaline and acidic vapours using a plastic clad silica fibre doped with poly(o-methoxyaniline). *Sensors and Actuators B-Chemical*, 97(2-3):174–181, 2004.

[70] T. Shinquan, C. B Winstead, R. Jindal, and J. P Singh. Optical-Fiber sensor using tailored porous Sol-Gel fiber core. *IEEE Sensors Journal*, 4:322–328, 2004.

[71] P. A. S Jorge, M. Mayeh, R. Benrashid, P. Caldas, J. L Santos, and F. Farahi. Applications of quantum dots in optical fiber luminescent oxygen sensors. *Applied Optics*, 45(16):3760–3767, 2006.

[72] S. Christie, E. Scorsone, K. Persaud, and F. Kvasnik. Remote detection of gaseous ammonia using the near infrared transmission properties of polyaniline. *Sensors and Actuators B-Chemical*, 90(1-3):163–169, 2003.

[73] C. Elosua, I. R Matias, C. Bariain, and F. J Arregui. Volatile organic compound optical fiber sensors: A review. *Sensors*, 6(11):1440–1465, 2006.

[74] A. Messica, A. Greenstein, and A. Katzir. Theory of fiber-optic, evanescent-wave spectroscopy and sensors. *Applied Optics*, 35(13):2274–2284, 1996.

[75] I. R Matias, J. Bravo, F. J Arregui, and J. M Corres. Nanofilms onto a hollow core fiber. *Optical Engineering Letters*, 45:1–3, 2006.

[76] Y. L Hoo, W. Jin, H. L Ho, D. N Wang, and R. S Windeler. Evanescent-wave gas sensing using microstructure fiber. *Optical Engineering*, 41(1):8–9, 2002.

[77] S. Luo, Y. Liu, A. Sucheta, M. Evans, and R. V Tassell. Applications of LPG fiber optical sensors for relative humidity and chemical warfare agents monitoring. *Proceedings of SPIE*, 4920:193–204, 2002.

[78] R. Falate, R. C Kamikawachi, M. Muller, H. J Kalinowski, and J. L Fabris. Fiber optic sensors for hydrocarbon detection. *Sensors and Actuators B-Chemical*, 105(2):430–436, 2005.

[79] M. Giordano, M. Russo, A. Cusano, and G. Mensitieri. An high sensitivity optical sensor for chloroform vapours detection based on nanometric film of d-form syndiotactic polystyrene. *Sensors and Actuators B-Chemical*, 107:140–147, 2005.

[80] P. D O'Neal, A. Meledeo, J. R Davis, B. L Ibey, V. A Gant, M. V Pishko, and G. L Cote. Oxygen sensing based on the flourescence quenching of a ruthenium complex immobilized in a biocompatible Poly(Ethylene glycol) hydrogel. *IEEE Sensors Journal*, 4:728–734, 2004.

[81] P. A. S Jorge, P. Caldas, C. C Rosa, A. G Oliva, and J. L Santos. Optical fiber probes for flourescent based oxygen sensing. *Sensors and Actuators B-Chemical*, 130:290–299, 2004.

[82] W. Q Cao and Y. X Duan. Optical fiber-based evanescent ammonia sensor. *Sensors and Actuators B-Chemical*, 110(2):252–259, 2005.

[83] K. D Weston, P. J Carson, J. A DeAro, and S. K Buratto. Single-molecule detection fluorescence of surface-bound species in vacuum. *Chemical Physics Letters*, 308(1-2):58–64, 1999.

[84] S. W Thomas, G. D Joly, and T. M Swager. Chemical sensors based on amplifying fluorescent conjugated polymers. *Chemical Reviews*, 107:1339–1386, 2007.

[85] J. F Callan, A. Prasanna de Silva, and D. C Magri. Luminescent sensors and switches in the early 21st century. *Tetrahedron*, 61:8551–8588, 2005.

[86] D. Filippini, A. Alimelli, C. Di Natale, R. Paolesse, A. D'Amico, and I. Lundstrom. Chemical sensing with familiar devices. *Angewandte Chemie-International Edition*, 45:3800–3803, 2006.

[87] C. Di Natale, R. Paolesse, and A. D'Amico. Metalloporphyrins based artificial olfactory receptors. *Sensors and Actuators B-Chemical*, 121(1):238–246, 2007.

[88] D. T McQuade, A. E Pullen, and T. M Swager. Conjugated polymer-based chemical sensors. *Chemical Reviews*, 100(7):2537–2574, 2000.

[89] S. J Toal, J. C Sanchez, R. E Dugan, and W. C Trogler. Visual detection of trace nitroaromatic explosive residue using photoluminescent metallole-containing polymers. *Journal of Forensic Sciences*, 52(1):79–83, 2007.

[90] I. Sanchez-Barragan, J. M Costa-Fernandez, M. Valledor, J. C Campo, and A. Sanz-Medel. Room-terperature phosphorescence (RTP) for optical sensing. *Trends in Analytical Chemistry*, 25(10):958–967, 2006.

[91] S. J Zhang, F. T Lu, L. N Gao, L. P Ding, and Y. Fang. Fluorescent sensors for nitroaromatic compounds based on monolayer assembly of polycyclic aromatics. *Langmuir*, 23(3):1584–1590, 2007.

[92] S. Bencic-Nagale, T. Sternfeld, and D. R Walt. Microbead chemical switches: An approach to detection of reactive organophosphate chemical warfare agent vapors. *Journal of the American Chemical Society*, 128(15):5041–5048, 2006.

[93] S. Y Tao, Z. Y Shi, G. T Li, and P. Li. Hierarchically structured nanocomposite films as highly sensitive chemosensory materials for TNT detection. *Chemphyschem*, 7(9):1902–1905, 2006.

Chapter 4

Bilayer Heterojunction Photoconductors

Fundamental progress has to do with the reinterpretation of basic ideas.

ALFRED NORTH WHITEHEAD

Philosopher

The bilayer heterojunction photoconductor combines the concept of a heterojunction with the device architecture of a photoconductor. Unlike traditional organic light emitting diodes (OLEDs) or photovoltaics, the heterojunction is aligned along the normal of the applied field. To better understand and model this novel device architecture, we can build upon previously conducted research in organic heterojunctions and photoconductivity of organic solids.

4.1 Organic Heterojunction Theory

Organic heterojunctions play a central role in practically all organic optoelectronic devices. Ever since Ching Tang's [1] seminal work in 1987 that incorporated a heterojunction into an efficient OLED, the organic electronics field has been utilizing the heterostructure in a number of other device structures in order to manipulate carrier concentrations and to boost efficiencies. The fundamental idea behind the

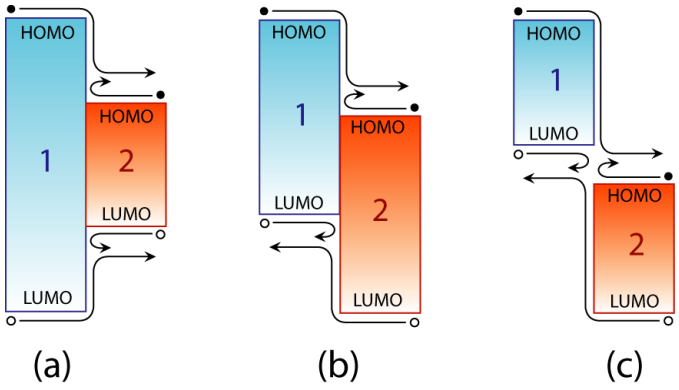

Figure 4-1: (a) Type-I (Straddling) heterojunction (b) Type-II (Staggered) heterojunction (c) Type-III (Broken-gap) heterojunction.

heterojunction is a union of two dissimilar materials, where the heterojunction is categorized by the energy band alignment of the two materials. A Type-I (straddling) [Fig. 4-1(a)] heterojunction consists of a smaller bandgap material that lies entirely within the energy bands of the wider bandgap material. The discontinuities of the bands are such that both types of carriers (electrons and holes) need energy to hop into the larger bandgap material from the smaller bandgap material, while carriers gain energy in the opposite situation. This heterojunction is quite common, and can be found in a number of inorganic optoelectronic devices such as quantum cascade lasers [2] due to the confinement of charge carriers to small regions which enhance electro-optical interactions. Another type of heterojunction is the Type-II (staggered) heterojunction [Fig. 4-1(b)]. In this case, the bandgaps of the two materials overlap and disrupt the symmetrical carrier transport across the interface. For instance, electrons moving from material 1 will find it energetically favorable to hop into material 2, whereas holes will find a large potential barrier to entering material 2. Type-II heterojunctions form the basis for the most efficient OLEDs and organic photovoltaics and are what helped to fuel the developments in the nascent field of organic optoelectronics back in the 1980's. The third and final type of heterojunction is the Type-III (broken-gap) heterojunction, where the bandgaps do not overlap at all. The situation for carrier transfer from material 1 to material 2 is similar to the Type-II case, but more pronounced.

4.1.1 Excitons at Heterojunction Interfaces

Aside from playing a direct role in carrier blocking and injection, heterojunctions also affect the exciton dynamics in devices. As discussed in a previous chapter, the weak intermolecular forces in organic thin films are responsible for the formation of excited states consisting of bound electron-hole pairs, which can be treated as quasi-particles known as excitons. The formation and dissociation of excitons is largely a function of the potential energy landscape in the materials and is accentuated by the abrupt changes in energy present at a heterointerface.

An example of the utility of a heterointerface in an organic optoelectronic device is the role it plays in OLED technology. High efficiency OLEDs require the balanced injection of electrons and holes within the active organic layer [Fig. 4-2] and confinement of the charge to the proper luminescent molecule, thus restricting non-radiative decay pathways and controlling the spectrum of luminescence. Both requirements can be met through the use of a Type-II heterojunction between an electron transporting layer (ETL) and a hole transporting layer (HTL). Ideally, the ETL has a LUMO level near the work function of the cathode to facilitate injection and transport of electrons while the HTL has a HOMO level near the work function of the anode to facilitate injection and transport of holes. Under a forward bias, V_F, electrons are injected into the ETL from the cathode (metal) and get blocked at the interface by the HTL, while holes are injected into the HTL from the anode (ITO) and get blocked at the interface by the ETL. Thus, the energy barriers at the interface act to spatially confine the injected carriers near the interface, which enhances the probability of radiative recombination. In addition, the barriers also prevent recombination from occurring too close to the device contacts, which act as exciton quenching centers.

The energy level alignment at a heterojunction also plays a critical role in the operation of organic photodetectors and solar cells. Power conversion efficiency in photovoltaics is a figure of merit that measures a device's ability to convert incident light into electrical energy collected at the contacts [Fig. 4-3]. Incident light is absorbed by the organic materials to create excitons, which can diffuse with some

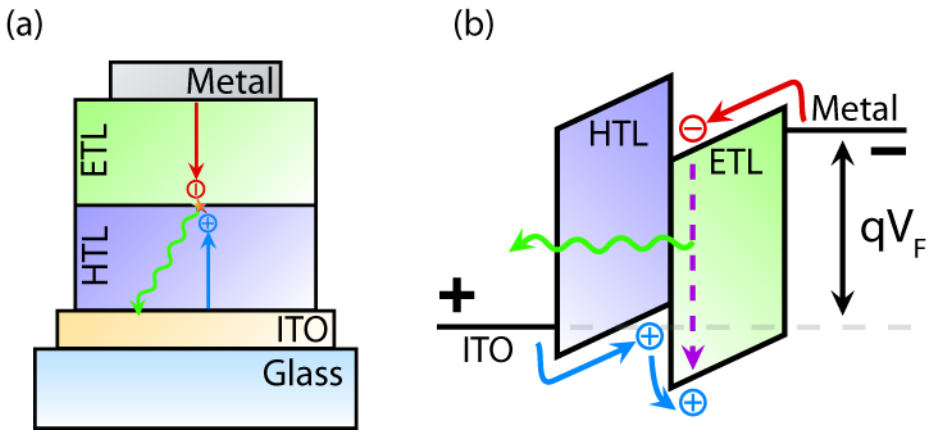

Figure 4-2: (a) Cross section and (b) energy band diagram of a typical OLED device consisting of a transparent indium tin oxide (ITO) anode, a hole transport layer (HTL), an electron transport layer (ETL), and a metal cathode. q is the charge of an electron and V_F is the forward voltage bias.

probability to the interface. Once there, the band offsets make it energetically favorable for the excitons to dissociate, transferring a hole (in the case of a donor exciton) from the donor material to the acceptor material. Excitons created in the acceptor material will transfer an electron to the donor material. Exciton dissociation approaches 100% efficiency in most Type-II heterojunctions if the exciton binding energy is less than the LUMO (in the case of an acceptor exciton) or the HOMO (in the case of a donor exciton) offsets [3]. The band offsets present at the interface enhances the electric-field dependent Onsager dissociation in these devices [4], boosting device efficiency.

4.1.2 Energy Band Alignment

One area of active research is the energy band alignment of dissimilar materials at an organic-organic heterointerface, where the factors determining a common vacuum level and the amount of band bending in organic materials are not well understood. Ultraviolet photoemission spectroscopy (UPS) is one experimental technique used to probe the energy levels of organic materials. The UPS measurement takes advantage of the photoelectric effect and is performed by irradiating a sample film, in vacuum, with high energy monochromatic light while measuring the energy distribution of elec-

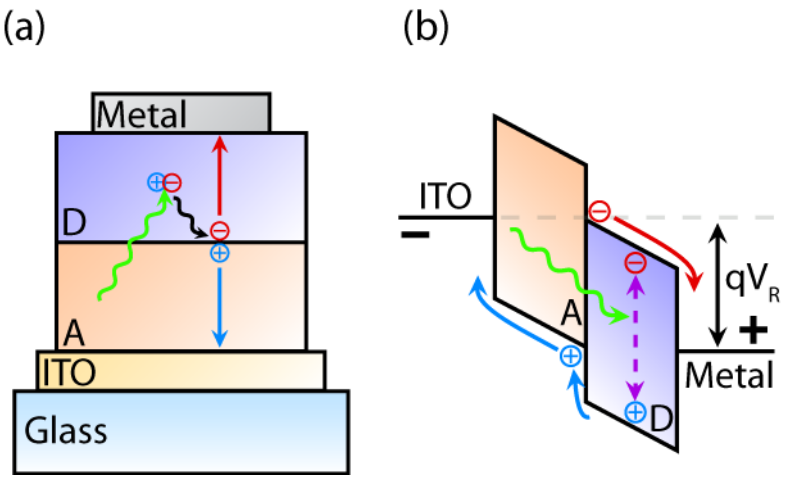

Figure 4-3: (a) Cross section and (b) energy band diagram of a typical photovoltaic device consisting of a transparent indium tin oxide (ITO) anode, an acceptor material (A), a donor material (D), and a metal cathode. q is the charge of an electron and V_R is the reverse voltage bias.

trons emitted from the sample. With this technique the ionization energy or HOMO level can be determined. Ionization energy, I, and electron affinity, A, are defined as the difference in energy between the vacuum level and the HOMO and LUMO, respectively. The work function, Φ_F, is defined as the energy separation between the Fermi level and the vacuum level [Fig. 4-4]. Because the electrons of a molecular solid fill its energy levels according to Fermi statistics, the concept of a Fermi level is still valid [5]. In principle, the value of the LUMO level can be determined through inverse photoemission spectroscopy (IPES), but this measurement often causes radiation damage to the sample [6]. Thus, the LUMO level is typically estimated from the value of the HOMO level minus the optical bandgap[1] (E_g) of the material, which can be determined through absorption measurements. Because all of the relevant energy levels are referenced to the vacuum level, it is important to consider how to define this quantity.

[1]The optical bandgap is in general different from the actual energy required to form an exciton, due to the Coulombic stabilization energy between the electron-hole pair [5] and the polarization energies of the electron and the hole. Only when the Coulombic stabilization energy is equal to the sum of the polarization energies does the optical bandgap become equal to the true bandgap.

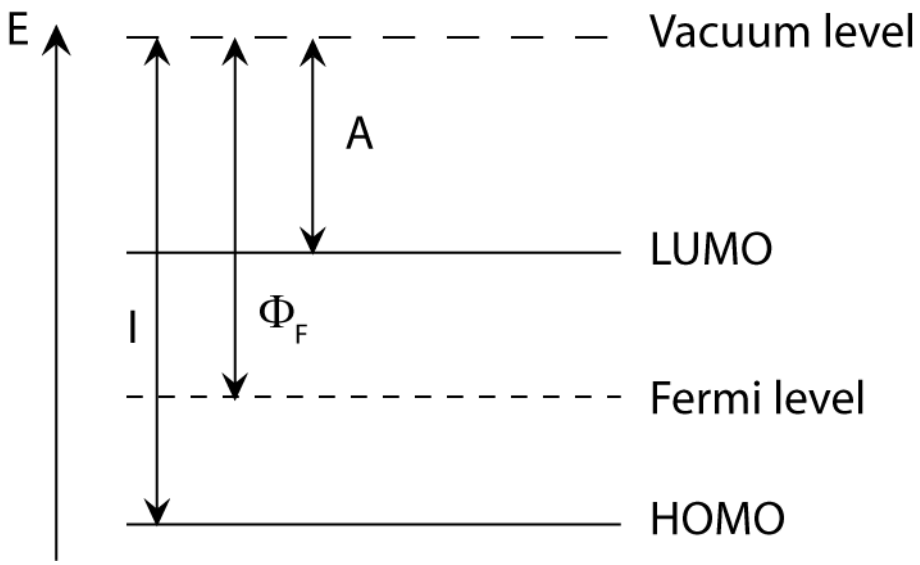

Figure 4-4: Schematic of relevant energy band parameters: ionization energy (I), electron affinity (A), and work function (Φ_F). After [7].

Defining the Vacuum Level

Theoretically, the vacuum level for an electron usually refers to the reference energy where an isolated electron is at rest an infinite distance from the system of interest. For convenience, we can denote this energy as VL(∞). Experimentally, the vacuum level of a solid corresponds to the energy of an electron at rest just outside of the solid, VL(s). Therefore, the experimentally determined VL(s) cannot be used as the invariant reference level VL(∞). More concretely, it has been demonstrated that the work function on the surface of a single crystal of tungsten is dependent upon the crystal orientation of the surface itself [8]. Because the Fermi level is a common level inside the solid material, it stands to reason that the difference in measured work function is due to the differences in the vacuum levels of the surfaces.

For a metal, the difference between the energies of the VL(∞) and VL(s) is mostly due to the surface dipole layer formed by the tail of the electron density distribution at the surfaces [Fig. 4-5(a)]. The extension of the electron cloud into vacuum makes the vacuum side negative, while just inside the surface becomes positive. From the perspective of an electron a small distance x from a dipole layer of finite length L ($x \ll L$), the dipole layer acts like a plane of charge approaching infinite length. In

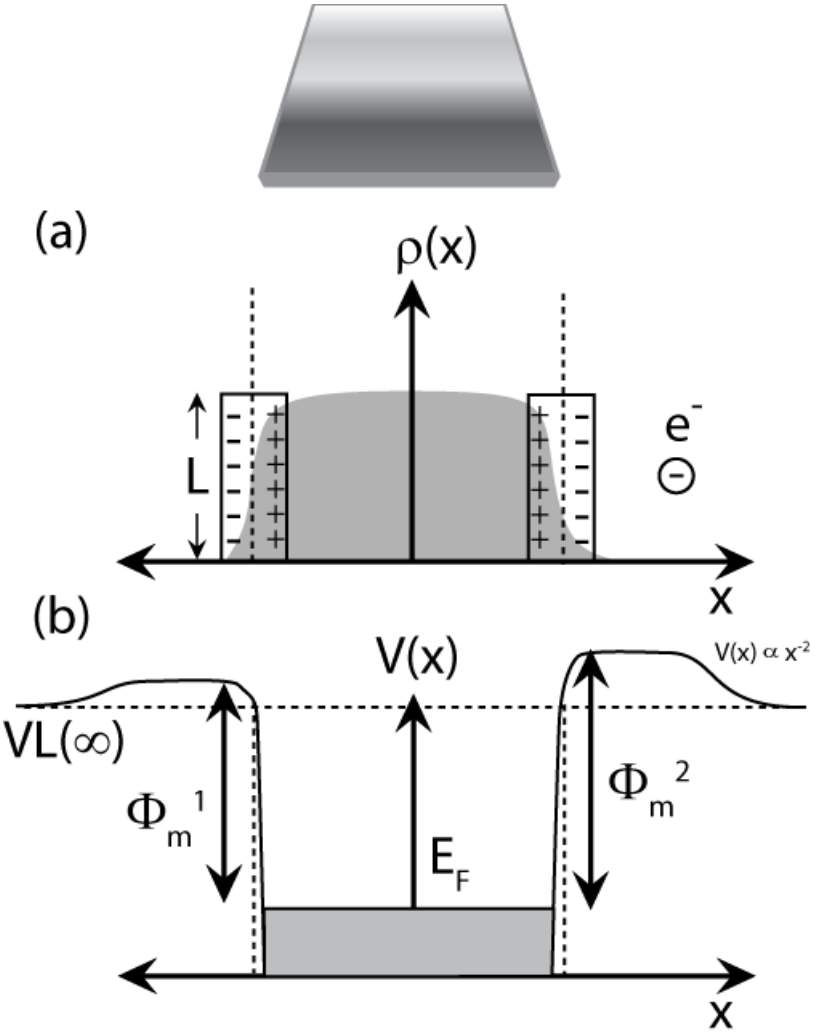

Figure 4-5: (a) Electron density in metal with tailing at the surface to form a dipole layer. (b) Potential energy [V(x)] plot vs. distance of an electron a distance x from a dipole layer. Fermi level (E_F) is uniform throughout solid. $\Phi_m{}^1$ and $\Phi_m{}^2$ are work functions of surfaces with different crystal orientation. After [7]

this case, the potential energy forms a step function across the dipole layer and V(x) on each side becomes a constant value independent of x. When $x \gg L$, the dipole layer can be regarded as a point dipole where the potential V(x) decreases as x^{-2} [Fig. 4-5(b)]. The contribution of the surface dipole layer makes the potential energy for an electron in and out of a metal take the shape shown in Figure 4-5(a). As the distance from the surface becomes large ($x \gg L$), the effect of the surface dipole layer diminishes, and the energy of the free electron converges to a common value, $VL(\infty)$. Note that the dependence of the work function on the surface crystal orientation can be attributed to the differences in the electron cloud distributions at different surfaces [7].

Extending this idea of vacuum level to the interface between a metal and an organic film can lead to insights for organic-organic interfaces. When a metal and an organic solid are far away, their energy levels are aligned so that they share a common $VL(\infty)$ [Fig. 4-6(a)]. When the solids come into contact, neglecting rearrangement of charge, the energy levels merge to form a common vacuum level at the interface, (VL), in an extremely narrow interfacial gap [Fig. 4-6(b)/(c)]. The vacuum level at the interface is a hypothetical concept useful for discussion of interface dipoles and may actually be lower than the VL(s) immediately outside of the interface, due to the merging of potential wells. In the actual system, a dipole layer may be formed at the interface due to a number of processes (i.e. charge transfer across the interface, redistribution of the electron cloud, chemical reaction at the interface, etc.) and recognize that this is an additional dipole to the dipole layer of the free metal surface. The interfacial dipole formation causes an abrupt shift of the potential across the interface [Fig. 4-6(d)], leading to a shift (Δ) of the virtual vacuum level at the interface. The value of Δ is determined by the magnitude of the dipole. A positive charge in the organic material causes a downward shift of VL in the organic layer relative to the VL in the metal layer, making delta negative. This follows the convention in the field of surface science, where delta is positive when VL is raised by deposition [9].

The origin of the interface dipole layer is not well understood, and has been theorized to form as a result of a number of different mechanisms. Charge transfer

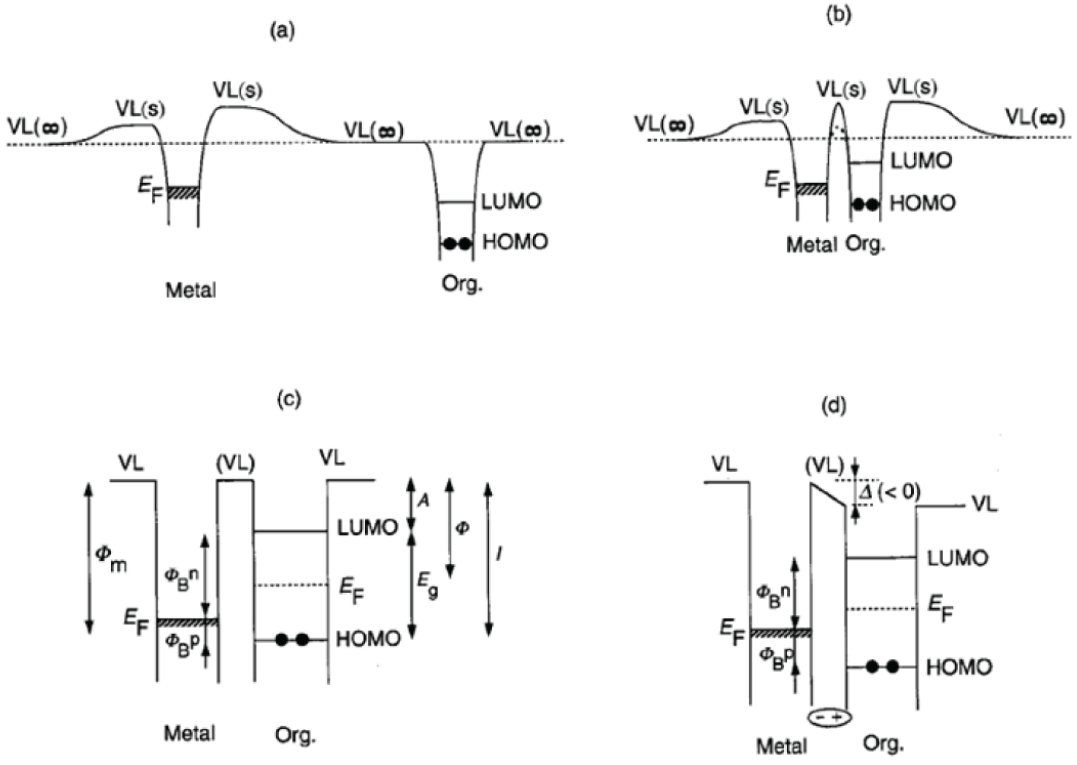

Figure 4-6: (a) Potential surface of a metal and organic which are not in contact. (b) Contact of the metal and a thin film of organic causes the common potential barrier to drop. (c) Schematic representing common VL at interface. $\Phi_B{}^n/\Phi_B{}^p$ denote the injection barriers for electrons/holes. (d) Energy diagram showing shift of VL (Δ) due to dipole formation at the interface [7].

is widely invoked to explain VL shift. However, there have been reported cases of VL shifts even when charge transfer is not possible (for example, using ultra-wide bandgap organic materials) [10, 11].

While there can be large shifts in the VL between a metal and organic ($\Delta \approx$ -1 eV for Alq_3 on Au), the largest reported shift between two organic materials reaches $\Delta \approx$ -0.5eV for PCTDA on Alq_3 [12]. One explanation for this trend is that charge transfer is the only available mechanism for formation of an interface dipole due largely to the lack of free carriers, the nonpolar nature of organic molecules, and the lack of chemical interactions between organics. Thus, the only combinations of organic materials expected to have large deltas are strong electron donor and acceptor pairs such as PTCDA/Alq_3.

Band Bending and Fermi Level Alignment in Organics

In general, the work functions for the two different organic layers are different, which raises two important questions: 1) Does the Fermi level align in organic semiconductors? 2) Is there band bending in organic semiconductors? Fermi level alignment will only occur if the total number of available mobile carriers in the organic layer is sufficiently large so that charge redistribution around the interface can occur within the experimental time window. This is the case when either the organic layer is thick or the organic layer has good semiconductor properties. The number of intrinsic carriers is not expected to be large in purified organic materials under ultrahigh vacuum (UHV), since the bandgaps are typically much larger than the thermal energy at room temperature. Thus, for the very thin layers of materials for UPS measurements, it is a good approximation to use a flat-band description of the organic films at the interface, and unaligned Fermi levels. However, recent experimental work (UPS studies) on a number of organic/organic heterojunction interfaces yields a different insight [13]. Tang et. al. theorize and demonstrate that Fermi level alignment can occur in thermal equilibrium conditions, and that the determining factor is the alignment of the Fermi level in the underlying film with either the HOMO or LUMO of the top film.

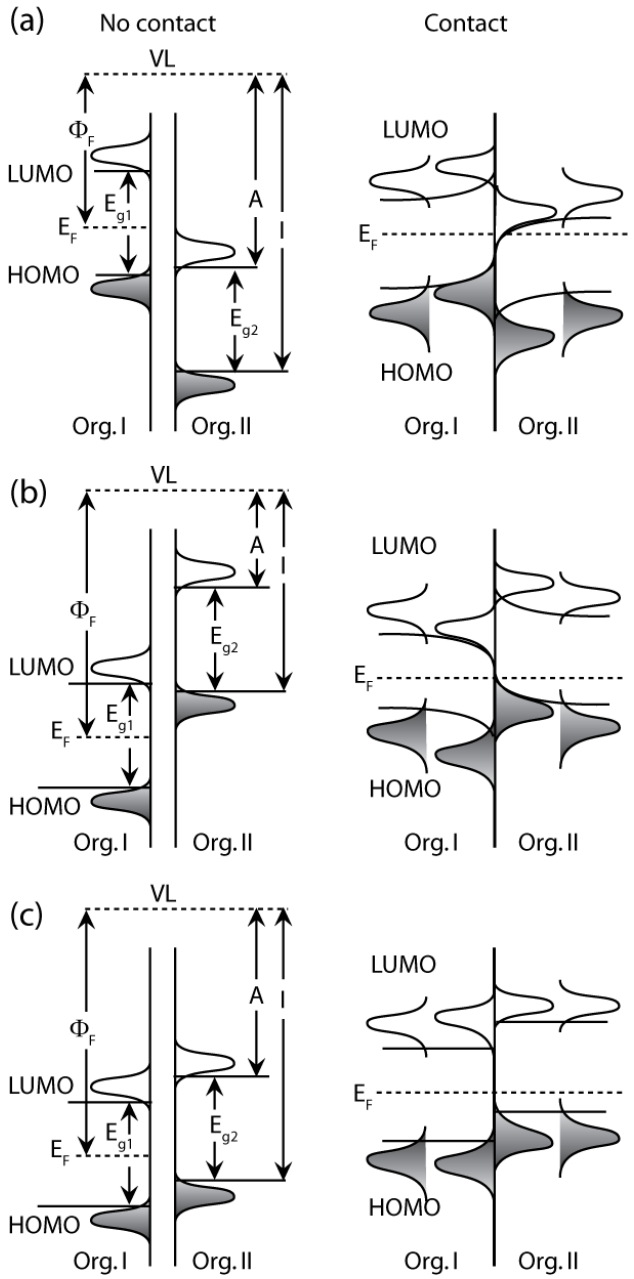

Figure 4-7: Schematic diagrams of organic-organic heterojunctions, where Φ_F is work function, E_F is Fermi level, A is electron affinity, I is ionization potential, and E_g is the bandgap. Subscripts denotes which material the properties belong to. (a) depicts a situation where $\Phi_{FI} < A_{II}$ before and after contact. (b) depicts $\Phi_{FI} > I_{II}$ before and after contact. (c) depicts $\Phi_{FI} > A_{II}$ before and after contact. After [13].

Kelvin probe microscopy work done by Ishii et. al. [14] demonstrated Fermi level pinning in the bulk of organics deposited on different metal substrates. In other words, the Fermi levels measured in the organics were mostly independent of the thickness of the film (for thicknesses >10 nm) and the energy of the Fermi level depended on the underlying metal substrate, suggesting that the Fermi level in the organic film on a metal is not the same as it is in the bulk of an isolated organic film. Tang noted that aside from the abrupt vacuum level shift at the metal-organic interface, the Fermi level in the first organic film (Org I) is determined solely by the substrate it is deposited on. Thus, if a second organic film (Org II) is deposited on top of the first film and the pinned Fermi level of Org I is either above the LUMO or below the HOMO level of Org II, charge redistribution will take place, causing significant band bending to occur as well as an abrupt vacuum level shift at the interface. Charge redistribution is expected to occur in this case because there are a sufficient number of states (due to the tail ends of the density of states in the HOMO and LUMO) that extend into the gap near the Fermi level. On the other hand, if the pinned Fermi level of Org I is near the middle of the energy gap of Org II, then little to no charge redistribution takes place because of the negligible density of states in the middle of the Org II's bandgap. In this case, the traditional picture of vacuum level alignment correctly predicts the band offsets [Fig. 4-7].

4.2 Photoconductor Device Theory

A photoconductor is a two-terminal device that changes its conductivity upon illumination. Typically, interdigitated electrodes are used to maximize both the semiconductor area exposed to the light source and the device bandwidth [15]. As photons are absorbed by the semiconductor, excitons are generated in proportion to the intensity of the incident photon flux. Those excitons can then diffuse with some probability to the surfaces or bulk defects where they can dissociate into free charge carriers in the film. When a bias is applied across the electrodes, an electric field develops across the photoconductive film which sweeps the charges out as photocurrent. In crystalline

inorganic semiconductors, the Wannier-Mott exciton binding energy is small enough (~ 0.1 eV) that excitons readily separate into electrons and holes. However, in organic semiconductors, the photons will generate strongly bound (1 eV) Frenkel-type singlet excitons that are difficult to dissociate without the presence of carriers, dopants, or charged species at interfaces [16]. Much of the photoconductive phenomena in a device can be described by a set of basic processes. In organic photoconductors these processes include 1) optical absorption by which excitons are generated, 2) exciton dissociation to generate free carriers, 3) electrical transport by which the free carriers contribute to electrical current, and 4) the capture of free carriers leading either to recombination or trapping.

4.2.1 Carrier Generation

For simplicity, we can model the photoconductor as a thin film with thickness L [Fig. 4-8]. Illumination occurs from one side with intensity I_o (photons/second). Throughout the film the density of photogenerated excitons is $\varepsilon(x)$, and the excitons can diffuse in either direction (positive or negative x-direction) based on the gradient of the exciton concentration. We can assume that the excitons will recombine in the bulk of the film due to fluorescence or non-radiative decay at a rate represented by the exciton lifetime, τ_{ex}. Additionally, excitons are continuously being generated in the film at a rate that is proportional to the intensity of illumination at that point. The general rate equation describing the change in exciton density, $\frac{d\varepsilon(x)}{dt}$, in an interval dx will be equal to the number of photogenerated excitons (G) minus those lost by diffusion (δ) and spontaneous decay (R)

$$\frac{d\varepsilon(x)}{dt} = G - \delta - R. \tag{4.2.1}$$

Optical absorption can be quantitatively described by an absorption coefficient, α, which is wavelength dependent. Neglecting reflection and scattering effects, if light of intensity I_{o} is incident on a material of thickness L with absorption coefficient α, then the intensity of the transmitted light I is given by the empirical relation known

as Beer's Law,

$$I(x) = I_o e^{-\alpha L}. \tag{4.2.2}$$

In a region dx, that is a distance of x away from the illuminated surface, the rate of exciton generation is of the form $G = Ae^{-\alpha x}$. To find the coefficient A we can imagine creating the same number of excitons as incident photons for an infinitely thick film. This leads to the relation $I_o = \int_0^\infty Ae^{-\alpha x}dx = \frac{A}{\alpha}$ so that $A = I_o\alpha$ [17].

The carrier pairs that leave the region by diffusion can be represented by the relation $\delta = d\xi/dx$, where ξ is the exciton flux. Exciton flux can be described by the following equation

$$\xi = -D\frac{d\varepsilon}{dx}. \tag{4.2.3}$$

where D is the exciton diffusion coefficient. The negative sign here implies that excitons will flow from areas of higher to lower concentration. Finally, the rate of recombination (encompassing all exciton loss mechanisms) can be represented by $R = \varepsilon/\tau_{ex}$, where τ_{ex} is the exciton lifetime in the bulk of the film. This relation holds assuming that we can neglect multiple-particle effects (i.e. exciton annihilation, exciton-polaron quenching) which occur at very high light intensities. Thus,

$$\frac{d\varepsilon(x)}{dt} = \alpha\eta_{PL}I_o e^{-\alpha x} + D\frac{d^2\varepsilon(x)}{dx^2} - \frac{\varepsilon(x)}{\tau_{ex}}, \tag{4.2.4}$$

where η_{PL} is the photoluminescent efficiency (the efficiency of generating excitons from each incident photon). Under steady-state conditions $d\varepsilon(x)/dt = 0$, which gives the general solution

$$\varepsilon(x) = C_1 e^{x/L_D} + C_2 e^{-x/L_D} + \frac{\alpha\eta_{PL}I_o\tau_{ex}}{1-\alpha^2 {L_D}^2}e^{-\alpha x}, \tag{4.2.5}$$

where $L_D = \sqrt{D\tau_{ex}}$ is the exciton diffusion length. Surface-enhanced exciton dissociation models are based on the assumption that the absorption of a photon creates an exciton that diffuses to a surface where it dissociates into a free electron-hole pair, or a free and deeply trapped carrier of opposite sign, through a donor-acceptor interaction associated with the surface [18]. Assuming a dopant and trap-free film, exciton

dissociation should only occur at the surfaces. The exciton flux, ξ, at the surfaces where dissociation occurs is important for determining the boundary conditions. Assuming that the dissociation rate at each surface can be represented by an exciton flux into the surface proportional to the exciton density at the surface

$$x = 0, \quad -\varepsilon(0) S_0 = -D\frac{d\varepsilon(0)}{dx}$$
$$x = L, \quad \varepsilon(L) S_L = -D\frac{d\varepsilon(L)}{dx}$$

where S_0 and S_L are the surface dissociation velocities for both surfaces and act as proportionality constants with units of velocity. Substituting these boundary conditions into Equation (4.2.5) above and solving for the constants C_1 and C_2 yields,

$$C_1 = \frac{\gamma}{\beta^2 - \alpha^2}\left[\frac{(S_L - \alpha D)(S_0 + D\beta) e^{-\alpha L} + (S_0 + \alpha D)(D\beta - S_L) e^{-\beta L}}{(S_L - D\beta)(S_0 - D\beta) e^{-\beta L} - (S_L + D\beta)(S_0 + D\beta) e^{\beta L}}\right]$$
$$C_2 = \frac{\gamma}{\beta^2 - \alpha^2}\left[\frac{(S_L - \alpha D)(D\beta - S_0) e^{-\alpha L} + (S_0 + \alpha D)(S_L + D\beta) e^{\beta L}}{(S_L - D\beta)(S_0 - D\beta) e^{-\beta L} - (S_L + D\beta)(S_0 + D\beta) e^{\beta L}}\right]$$

where $\beta = \frac{1}{L_D}$ and $\gamma = \frac{\alpha\eta_{PL} I_o}{D}$. Examples of exciton concentration profiles for a single film using common organic material parameters and fixed illumination intensity are plotted in [Fig. 4-8]. Note that at any given point x, the exciton concentration has a linear dependence on the light intensity, I_o.

We can use a similar rate equation to calculate the free carrier profiles in the film assuming that carrier generation does not occur in the bulk of the film, but rather at the surfaces where one type of carrier gets trapped (for example, holes) and the other goes free (for example, electrons) [20]

$$\frac{dn(x)}{dt} = D_n\frac{d^2 n(x)}{dx^2} - \frac{n(x)}{\tau_n}. \tag{4.2.6}$$

Here n is the electron concentration, D_n is the electron diffusion coefficient, and τ_n is the lifetime of an electron. Under steady-state conditions $dn(x)/dt = 0$, which gives the general solution

$$n(x) = C_1 e^{x/L_n} + C_2 e^{-x/L_n}, \tag{4.2.7}$$

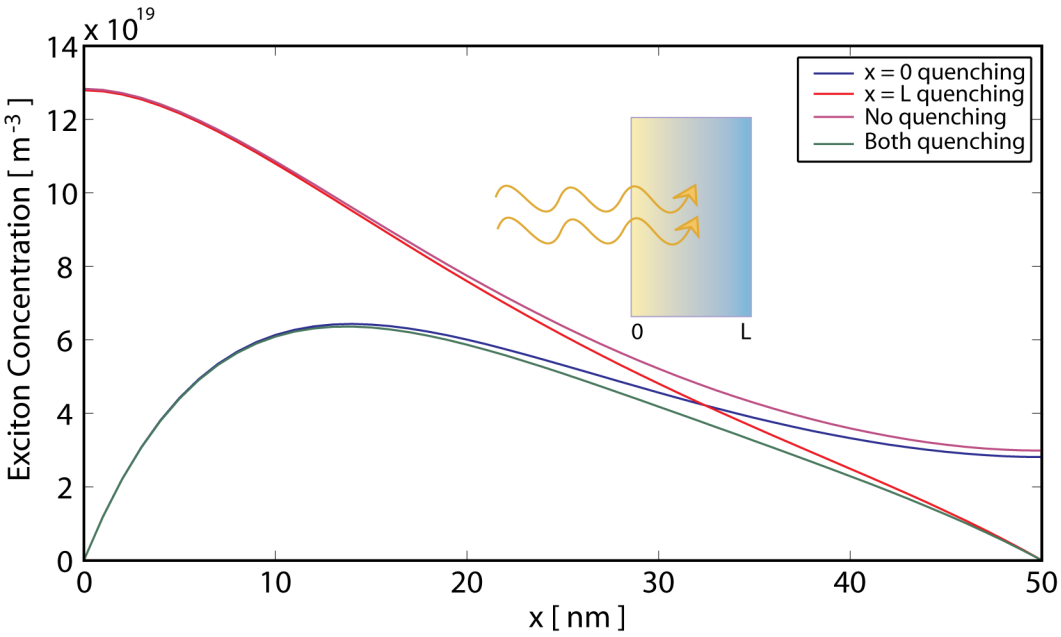

Figure 4-8: Simulated exciton carrier concentration profile across a thin film of organic semiconductor with L = 50 nm, $\alpha = 5\text{x}10^5$ cm^{-1}, D = 1x10^{-3} cm^{2}s^{-1}[19], 100 mW/cm^2 of 2.25 eV photons, and various boundary conditions. S_L=S_0=0 (violet), S_L=S_0=10^{20} (green), S_L=0 and S_0=10^{20} (blue), S_L=10^{20} and S_0=0 (red).

where L_n is the electron diffusion length. If we can assume that one of the surfaces (at $x = 0$) is responsible for carrier generation (due to unsatisfied bonds) and the other surface (at $x = L$) is passivated and has a surface recombination velocity of 0, then we get the following boundary conditions

$$n(0) = n_0$$
$$n(L) S_L = 0 = -D_n \frac{dn(L)}{dx}$$

Solving Equation (4.2.7) with these boundary conditions yields

$$C_1 = \frac{n_0 e^{-L/L_n}}{e^{L/L_n} + e^{-L/L_n}}$$
$$C_2 = \frac{n_0 e^{L/L_n}}{e^{L/L_n} + e^{-L/L_n}}$$

To find the value of n_0 we can use the following electron continuity equation

$$\frac{dn(0)}{dt} = D\frac{d\varepsilon(0)}{dx} - D_n\frac{d^2n(0)}{dx^2}, \tag{4.2.8}$$

where the first term represents the generation rate of electrons at the surface (flux of excitons into surface) assuming every exciton generates an electron and the second term represents the electron diffusion current away from the surface.

4.2.2 Carrier Transport

Under steady-state illumination the rate of charge recombination (n/τ_n) must equal the rate of free carrier generation, G_c, giving the basic relationship that $n = G_c\tau_n$. If more than one charge recombination process is present, the individual rates add. As carriers are generated in the photoconductive film, they drift towards the appropriate electrode given the polarity of the applied field. Those carriers are transported through the film by hopping from one molecule to the next and only stopping at imperfections in the film. A captured carrier at an imperfection can do one of two things; 1) recombine with a carrier of the opposite type or 2) be thermally re-excited to the nearest energy band before recombination occurs (in which case the imperfection is a trap). The rate of capture of a free carrier concentration n by imperfections with density N is given by $R_c = \beta nN$, where β is the capture coefficient. The thermal detrapping rate is given by $R_d = n_t\nu e^{-\Delta E/kt}$, where n_t is the density of trapped carriers, ν is a characteristic attempt to escape frequency, and ΔE is the activation energy for detrapping. If $R_c > R_d$ then the imperfection acts like a recombination center or like a trap if $R_c < R_d$. The process of electrical current flow under illumination involves two processes: the effect of contacts and the nature of the transport of free carriers. The ability of the contacts to replenish carriers to maintain charge neutrality in the material, if carriers are drawn out of the opposite contact by an electric field, plays a key role in determining the photocurrent characteristics. Electrical contacts can be organized into three classes of behavior: 1) blocking contacts, 2) ohmic contacts, and 3) injecting contacts. The characteristic current-voltage curve of each type of contact

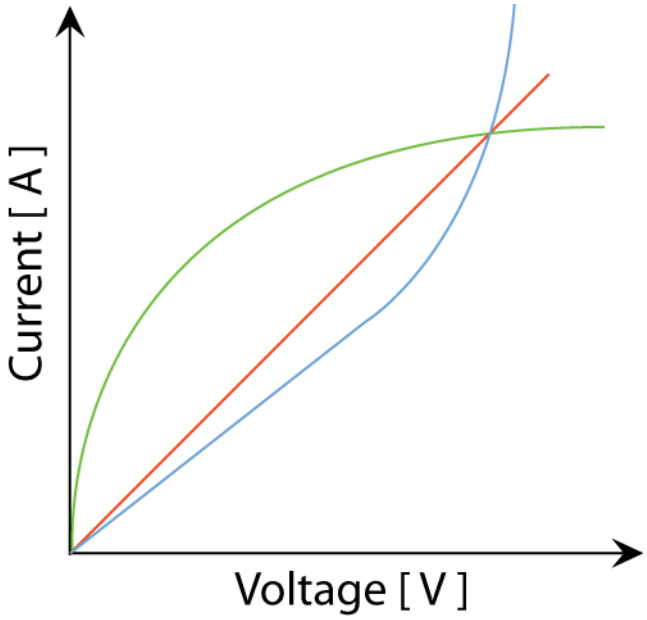

Figure 4-9: Representative current-voltage characteristics for a blocking contact (green), an ohmic contact (red), and an injecting contact (blue).

is shown in [Fig. 4-9]. If a contact is unable to replenish photogenerated carriers when they are leaving the device, then the current varies sublinearly with applied voltage, and may become saturated. An ohmic contact is able to replenish photogenerated carriers that exit the device, such that current varies linearly with applied voltage (with a slope equal to the conductivity of the bulk material). An injecting contact is an ohmic contact at low applied fields, but under sufficiently high fields allows carriers to traverse the distance between electrodes before the material is able to achieve charge neutrality by dielectric relaxation. The result is a regime in which the material is not electrically neutral, and the current flow becomes limited by the build-up of space charge at the injecting contact, hence the name "space-charge-limited" (SCL) current.

The charge transport process is described in terms of drift-diffusion theory. The total current density J_{tot} can be expressed as the sum of a drift current J_{dr} and a diffusion current J_{diff}. The drift current is given by $J_{dr} = \sigma E$, where σ is the electrical conductivity, and the diffusion current (for electrons) is expressed as $J_{diff} = qD_n dn/dx$. Neglecting space charge effects in the lateral photoconductor geometry

implies that the carrier profiles are uniform throughout the channel length, indicating that $J_{diff} = 0$. One distinction to be made here is that $J_{light} = J_{photo} + J_{dark}$. In other words, the current under illumination is the sum of the photogenerated current plus the current that flows under dark conditions.

Consider the effects on the light current to dark current ratio when blocking contacts are used. J_{dark} will decrease with the increased injection barriers from the contacts to the semiconducting film. However, there may be negative effects on J_{photo} as well that may reduce the benefits of decreased carrier injection. For instance, if the photoexcited carriers raise the effective conductivity of the film during their lifetime, then there is the opportunity for injected charge to travel multiple times through the film before the excited carriers relax. A prerequisite for this amplifying behavior is the ability for charge to be injected to replace carriers that are exiting the device. Thus, blocking contacts would prevent amplification by preventing the injection of charge that effectively allows for multiple transits through the film. If J_{photo} is strongly dependent on the photoconductive gain in the device, then blocking contacts may reduce the light to dark current ratio by preventing amplification. However, in cases where gain is not a factor, blocking contacts should improve the light to dark current ratio by suppressing the injection of carriers without illumination.

4.2.3 Figures of Merit

There are three main features of a photoconductor: photosensitivity, the spectral response, and the speed of response.

Photosensitivity

In a material with intrinsic free carriers, the electrical conductivity in the dark can be given by

$$\sigma_d = q\left(n_o\mu_{no} + p_o\mu_{po}\right) \tag{4.2.9}$$

where q is the charge of the carrier, n_o and p_o are the intrinsic carrier concentrations, and μ_{no} and μ_{po} are the effective mobilities. Under illumination, this conductivity is

increased by the photoconductivity $\Delta\sigma$,

$$\sigma_L = \sigma_o + \Delta\sigma. \tag{4.2.10}$$

The possibility that photoexcitation may change both the carrier density and carrier mobility yields the following set of changes:

$$n_o \rightarrow n_o + \Delta n$$

$$p_o \rightarrow p_o + \Delta p$$

$$\mu_{no} \rightarrow \mu_{no} + \Delta\mu_n$$

$$\mu_{po} \rightarrow \mu_{po} + \Delta\mu_p$$

$$\sigma_o + \Delta\sigma = q[(n_o + \Delta n)(\mu_{no} + \Delta\mu_n) + (p_o + \Delta p)(\mu_{po} + \Delta\mu_p)].$$

Therefore,

$$\Delta\sigma = q[\Delta n\mu_{no} + (n_o + \Delta n)\Delta\mu_n + \Delta p\mu_{po} + (p_o + \Delta p)\Delta\mu_p]. \tag{4.2.11}$$

Under steady state illumination, we know that the carrier generation rate equals the recombination rate

$$\Delta n = G_c\tau_n = \Delta p, \tag{4.2.12}$$

where G_c is the carrier generation rate [$m^{-3}s^{-1}$] (which includes exciton formation and dissociation) and τ_n is the electron lifetime. Thus,

$$\Delta\sigma = q\left[G_c\tau_n\mu_{no} + n\Delta\mu_n + G_c\tau_p\mu_{po} + p\Delta\mu_p\right]. \tag{4.2.13}$$

To add to the complexity, the lifetime may be a function of the excitation rate. Thus, there are three types of effects that can occur:

1. Increase in the carrier density with constant lifetime and no change in mobility, such that

$$\Delta\sigma = qG_c\left(\tau_n\mu_{no} + \tau_p\mu_{po}\right). \tag{4.2.14}$$

Plotting photoconductivity on a log-log scale versus G would show a slope of 1.

2. Increase in carrier density with lifetime a function of intensity of illumination. If we assume τ_n varies as $G^{\gamma-1}$, then $\Delta\sigma$ varies as G^{γ}. Thus, if $\gamma < 1$, the lifetime decreases with increasing excitation rate, which yields sublinear behavior. If $\gamma > 1$, the lifetime increases with the excitation rate which is called supralinear behavior.

3. Increase in carrier mobility, so that

$$\Delta\sigma = q\left(n\Delta\mu_n + p\Delta\mu_p\right). \tag{4.2.15}$$

One likely mechanism can give rise to this phenomenon: photoexcitation that excites carriers to fill in traps, raising the effective mobility of the material. In addition, mobilities have been shown to be dependent on carrier concentrations [21, 22].

To first order approximation, given sufficiently high photoexcitation rates, constant mobility, and the fact that organic materials are insulators, $\Delta n \gg n_o$ and $\Delta p \gg p_o$,

$$\Delta\sigma \approx G_c q\left(\tau_n\mu_n + \tau_p\mu_p\right). \tag{4.2.16}$$

This equation can be rearranged to give the ratio of change in conductivity to excitation rate, which is a figure of merit (lifetime-mobility product) for a photoconductor's photosensitivity,

$$\frac{\Delta\sigma}{G_c q} = \tau_n\mu_n + \tau_p\mu_p. \tag{4.2.17}$$

Photoconductive Gain

Under steady state conditions, the photoconductive gain represents the ratio of the photogenerated charge carrier lifetime to the transit time across the device of charge carriers injected at the contacts. In the steady state, the total carrier generation rate must be equal to the total carrier recombination rate, which can be written as the

following relation:

$$\frac{n}{\tau_n} L = \eta_{PL} I_o \tag{4.2.18}$$

where n is the charge carrier number density, τ_n is the carrier lifetime, L is the device thickness, η_{PL} is the photoluminescence efficiency of the active material, and I_o is the incident photon flux. Assuming uniform charge density in the lateral direction along current flow, device photocurrent can be modeled by the one dimensional drift current density equation:

$$J_{photo} = qn\left(\mu_n + \mu_p\right) E \tag{4.2.19}$$

where electron and hole densities are equal ($n = p$), μ_n and μ_p are the electron and hole mobilities, respectively, and E the applied electric field. Substituting the steady state condition relation and solving for the total current density yields:

$$J_{photo} = qn\Phi \frac{d}{L} \times \tau_n \left(\frac{1}{t_n} + \frac{1}{t_p}\right) \tag{4.2.20}$$

where d is the device channel length and t_n and t_p are the electron and hole transit times respectively. The photocurrent gain increases when either of the carrier transit times decreases or if the carrier lifetime increases. When photogenerated carriers are created through the dissociation of an exciton, the carriers will hop among molecular states in response to the applied electric field. In amorphous organic thin films it has been shown that energetic and spatial disorder [23] can lead to a significant population of energetic traps, molecular states that limit carriers from hopping to another site [24]. As the energetic traps are filled by the excess photogenerated carriers, the film will have a higher effective mobility while the trapped charge persists in this non-equilibrium state. The time it takes for trapped charge to relax is dependent on the disorder in the film, so much so that the carrier transit time can be shorter than the carrier lifetime in strongly disordered materials. Thus, for every photoexcited carrier, many more carriers can be transported across the film before the photoexcited carriers relax. This process leads to photoconductive gains above unity.

Speed of response

In a trap-free material, the free carrier lifetime determines the time constant associated with the decay curve (decrease of photoconductivity to the dark value after turning off illumination). The governing rate equation assuming $n \approx \Delta n$ is

$$\frac{dn}{dt} = G_c - \frac{n}{\tau_n}. \tag{4.2.21}$$

Integrating this equation with $G_c = 0$ at time $t = 0$ yields,

$$n(t) = G_c \tau_n e^{-t/\tau_n}. \tag{4.2.22}$$

Given these simplified conditions, we observe that the photocurrent decay follows a single exponential. Thus, plotting current versus time on a semi-logarithmic scale would yield a slope equal to the decay time constant. The capture process of a free carrier at an imperfection can be described through a capture coefficient, C [$m^3 s^{-1}$], which can be thought of as the product of a capture cross section U and the average thermal velocity of the free carrier, v,

$$C = Uv \tag{4.2.23}$$

where the magnitude of C depends on the details of the capture process. The rate of capture R_c [$m^{-3} s^{-1}$] of a species with density n by another species with density N is given by

$$R_c = CnN. \tag{4.2.24}$$

When the capture of free carriers leads to recombination with the opposite species, the lifetime of a free carrier, τ_n, (the average time the carrier is free before recombining), is given by the density of carriers divided by their rate of capture

$$\tau_n = 1/CN. \tag{4.2.25}$$

Comparison with Equation (4.2.24) shows that the rate of capture (in this case recombination) is equal to n/τ_n. In a generalized photoconductor model, the carrier generation rate G_c and thermal excitation rate g are balanced by the carrier recombination across the bandgap with a rate R_c, such that with illumination,

$$G_c + g = C\left(n_o + \Delta n\right)\left(p_o + \Delta p\right) = C\left(n_o + \Delta n\right)^2 = R_c \tag{4.2.26}$$

since $\Delta n = \Delta p$. With no illumination

$$g = C n_o p_o = C n_o^2 \tag{4.2.27}$$

since $n_o = p_o$. For insulating organic materials, $g \ll G_c$, $n_o \ll \Delta n$, so that Equation (4.2.26) becomes

$$G_c \approx C\Delta n^2. \tag{4.2.28}$$

Therefore,

$$\Delta n = \left(G_c/C\right)^{1/2} \tag{4.2.29}$$

$$\tau_n = \frac{1}{C\Delta n} = \frac{1}{\sqrt{C G_c}}. \tag{4.2.30}$$

In this case $\Delta n \propto {G_c}^{1/2}$, which indicates a case of sublinear photoconductivity. In other words, higher intensity light, which yields higher exciton generation rates and subsequently higher carrier generation rates, will have less and less of an effect on the photocurrent. Correspondingly, the carrier lifetime decreases with increasing intensity, $\tau_n \propto {G_c}^{-1/2}$. Cases like this are dominated by bimolecular recombination.

4.3 Bilayer Heterojunction Photoconductor

In a typical organic photodetector, organic thin films absorb the incident light to form excitons (bound electron-hole pairs) that can dissociate into charge carriers that are extracted by applying an external electric field. The vertical photodetector device ge-

ometries task the photoactive films with the dual role of exciton photogeneration and charge transport. The coupling of these two dissimilar roles in a single organic film constrains the design of photodetectors, requiring use of highly absorptive films that can simultaneously efficiently transport the photogenerated charge to the electrodes. Typically, amorphous organic thin films, while having desirable optical absorption characteristics, have low charge carrier mobilities due to the weak electrostatic interactions between van-der-Waals bonded molecules [16]. The key to overcoming this fundamental limitation is to recognize that the coupled functionality is due largely to the device architecture. Thus, by introducing a heterojunction into a lateral device geometry we physically separate the exciton generation from the charge transport, enabling independent optimization of the two processes in an amplifying photoconductor structure.

The two-terminal, lateral photoconductor incorporates a heterojunction between an optically absorptive thin film that is primarily responsible for exciton generation, and another film that is (preferably) optically transparent at the operating wavelength and is primarily responsible for charge transport. The dual-layer structure has its roots in xerography, where photoreceptor drums contain a charge generation layer for absorbing the light from the image exposure and forming free carriers, and a charge transport layer responsible for transferring those carriers to the corona-charged surface, where they recombine to form the electrostatic latent image [18]. By adding the lateral, planar electrodes, we extend the dual-layer photoreceptor paradigm and demonstrate photoactive device structures that also enable direct study of the charge generation and recombination rates at the bilayer heterojunction interface.

4.3.1 Device Model

The lateral bilayer heterojunction photoconductors developed in this model consist of two semiconducting thin films deposited onto interdigitated gold electrodes [Fig. 4-10(a)]. The rest of the figure illustrates two different views of the physical processes that govern operation of the photoconductors. Figure 4-10(b) shows the proposed energy band diagram indicating the highest occupied molecular orbital (HOMO) and

the lowest unoccupied molecular orbital (LUMO) for the two semiconducting organic layers, while Figure 4-10(c) depicts the cross section of the proposed device stack. As shown, the exciton generation layer (EGL) is deposited on top of the charge transport layer (CTL), which is in intimate contact with the gold electrodes. Under steady-state bias conditions, conduction can occur through either the CTL or the EGL. With the proper choice of materials, conduction can predominantly occur in the channel formed between the CTL/EGL [20]. Under illumination, light with an appropriate emission spectrum will be absorbed by the EGL, resulting in the formation of EGL excitons. A fraction of the photogenerated excitons will diffuse to the EGL/CTL interface. If the EGL and CTL are aligned such that their offsets in either the LUMOs or HOMOs are greater than the binding energy of EGL excitons [3], as shown in Figure 4-10(b), then it is energetically favorable for excitons to dissociate at the interface. Exciton dissociation in disordered organic materials has been attributed to both surface and bulk effects [16], with appropriately designed Type-II heterojunction interfaces achieving near complete exciton dissociation. Once created, the photogenerated charge will continue to accumulate at the EGL/CTL interface until equilibrium is achieved between carrier generation, charge recombination (both Langevin and Shockley-Read-Hall), and charge diffusion away from the interface. In these structures, the accumulated, interfacial holes in the CTL will balance the electron charge accumulated in the EGL. The conductivity of the CTL is enhanced by the population of photogenerated charge carriers, which we can measure as an increase in photocurrent from an illuminated, biased device.

To model the carrier concentrations in a device, we can build upon the rate equations used for a single photoconductive film derived earlier. Given that the heterojunction is deposited on glass, the primary surface that is expected to dissociate excitons is the EGL/CTL interface itself. Assuming the EGL preferentially absorbs the illumination, the exciton concentration profile for a bilayer heterojunction would have an exciton quenching surface ($S \rightarrow \infty$) at the interface and an exciton reflecting surface ($S = 0$) at the interface with air. This would yield an exciton profile that resembles the blue curve in Figure 4-8 assuming the EGL/CTL interface is located

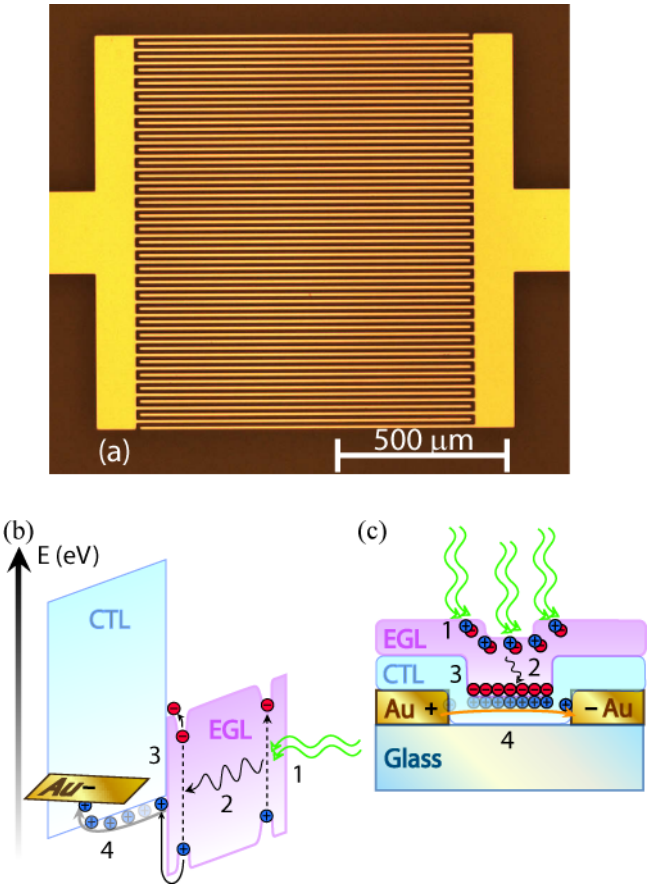

Figure 4-10: The interdigitated gold fingers form 60 photoconductive channels each (1000 ± 1) μm long and (10 ± 1) μm wide yielding an effective device area of (0.6 ± 0.06) mm^2. (a) An optical microscope image of a set of device electrodes. (b) Energy band diagram of a lateral bi-layer heterojunction photoconductor consisting of an exciton generation layer (EGL) and a charge transport layer (CTL). (c) A cross-sectional view of the same bi-layer device is also shown. Both illustrations depict the physical processes involved in steady-state device operation: (1) Light absorption in EGL, (2) Exciton diffusion through EGL, (3) Exciton dissociation at EGL/CTL interface and charge transfer to CTL, and (4) Charge transport in the photoconductive channel.

at x = 0 and the EGL is to the right of the interface.

Again, the carrier profiles can be simulated using the previously derived equations for free carriers, however the boundary conditions need to be developed further. Given the proposed band diagram, when excitons dissociate electrons will remain in the EGL while holes are transferred to the CTL. Thus, only excess holes will be considered for $x < 0$ and excess electrons for $x > 0$. When considering the boundary conditions at the EGL/air and the CTL/glass interfaces, a surface recombination velocity of 0 would imply reflecting surfaces. This assumption is plausible as long as there are negligible deep trap states (i.e. unsatisfied bonds) and therefore few recombination centers:

$$-p\left(-L\right)S_{-L} = -D_p\frac{dp\left(-L\right)}{dx} = 0 = -D_n\frac{dn\left(L\right)}{dx} = n\left(L\right)S_L. \tag{4.3.1}$$

The boundary condition at the EGL/CTL interface can be determined by calculating the carrier concentration at that surface. To do so requires further consideration of the processes that generate free carriers.

Initially, exciton dissociation at the heterointerface produces a pair of charges which are still coulombically bound (a charge-transfer state or polaron pair) [25]. Thus, the generation rate of polaron pairs (G_P) at the EGL/CTL interface is directly proportional to the exciton flux there $-D\frac{d\varepsilon(0)}{dx} = G_P$. These CT states are intermediate states between excitons and free carriers. The coulombic attraction between the electron and hole in the CT state make it quasi-stable and capable of undergoing multiple dissociations and subsequent formations over its lifetime [26]. The CT states can either disappear by recombining monomolecularly (with a rate constant of k_{rec}) [27] or can dissociate into free carriers with a field-dependent rate constant $k_{diss}(E)$ [26]. Additionally, CT states can be formed by Langevin-type (bimolecular capture) recombination of free carriers (Λnp) [28]. In the case of a pristine, trap-free material, the recombination constant is governed by the sum of the electron and hole mobilities $\Lambda = \frac{q}{\epsilon}\left(\mu_n + \mu_p\right)$, where ϵ is the dielectric constant of the material. Therefore, the

general rate equation for the polaron pairs ($P(x)$) may be expressed as

$$\frac{dP(0)}{dt} = G_P - k_{rec}P(0) - k_{diss}P(0) + \Lambda n(0)\,p(0)\,. \tag{4.3.2}$$

To derive a free carrier concentration profile, we can also express the free carrier continuity equation (in this case electrons) as

$$\frac{dn(0)}{dt} = k_{diss}P(0) - \Lambda n(0)\,p(0) - k_{SRH}\frac{n(0)\,p(0)}{n(0)+p(0)}, \tag{4.3.3}$$

where the last term refers to the Shockley-Read-Hall (SRH) form of recombination, which is a trap-assisted recombination effect that is common in polymer interfaces [29]. The SRH rate coefficient k_{SRH} takes into account both the trap densities and capture coefficients of the carriers, while n and p represent the free carrier densities which are assumed to be much larger than the intrinsic carrier densities. However, given that we are concerned primarily with purified organic materials we can neglect this last term. Note that both Equation (4.3.2) and Equation (4.3.3) have units associated with surface densities (particles per area). Combining Equations (4.3.1), (4.3.2), (4.3.3) under steady-state conditions yields,

$$n(0) = \sqrt{\frac{k_{diss}G_P}{k_{rec}\Lambda}}. \tag{4.3.4}$$

Neglecting high intensity effects such as exciton-exciton annihilation and exciton-polaron quenching, we found earlier that the generation rate of polaron pairs is linearly dependent on intensity ($G_P \propto \alpha I_o$). This implies that the carrier concentration at the EGL/CTL interface will follow a sublinear dependence on intensity $n(0) \propto {I_o}^{1/2}$.

4.4 Model System: TPD/PTCBI Bilayer Heterojunction Photoconductors

To test this device model we used two well characterized molecular organic materials: N,N'-bis(3-methylphenyl)-N,N'-diphenyl-1,1'-biphenyl-4,4'-diamine (TPD) as CTL and 3,4,9,10-perylenetetracarboxylic bis-benzimidazole (PTCBI) as EGL, whose absorption spectra and electron energy band levels are depicted in Figure 4-11. TPD (obtained from H.W. Sands) is a common hole transport material ($\mu_p \sim 10^{-3}$ $cm^2V^{-1}s^{-1}$) used in organic LEDs and is optically transparent for wavelengths of $\lambda > 400$ nm, identifying it as suitable for use as the CTL. PTCBI (obtained from Sensient GmBh) is a perylene dye derivative that has found use as an optically absorptive material in organic solar cells [30] with strong absorption across the visible spectrum, making it suitable for use as an EGL. In addition, the high ionization energy of PTCBI makes it a suitable hole donor to TPD and creates large HOMO/LUMO band offsets to aid in dissociation of excitons. From the absorption spectra in Figure 4-11, we note that PTCBI can be optically excited independent of TPD by using a green LED centered at $\lambda = 532$ nm (Lamina Light Engine, BL-3000). The thermally evaporated TPD/PTCBI films are deposited on a series of interdigitated gold electrodes that are photolithographically defined on glass [Fig. 4-10(a)]. These electrodes form a serpentine channel that is (60 ± 1) mm wide and (10 ± 1) μm across, resulting in an effective device area of (0.6 ± 0.06) mm^2.

Thin film absorption measurements are captured using a UV-VIS-NIR spectrophotometer (NKD-8000, Aquila Instruments). The green LED light engine, powered by a sourcemeter (Keithley 2400), provides narrow band excitation (FWHM ~ 50 nm) with intensities up to 40 mW/cm^2 as measured with a calibrated photodetector (Newport, 818-UV). The emission spectrum of the green LED was measured using a spectrometer (Ocean Optics, USB4000). Device current-voltage (I-V) characteristics were measured in a dark box using a picoammeter (Keithley 6487). Photocurrent spectra were measured using a digital lock-in amplifier (Stanford Research Systems, SR830) with monochromatic illumination provided by a 1000 W Xenon arc lamp

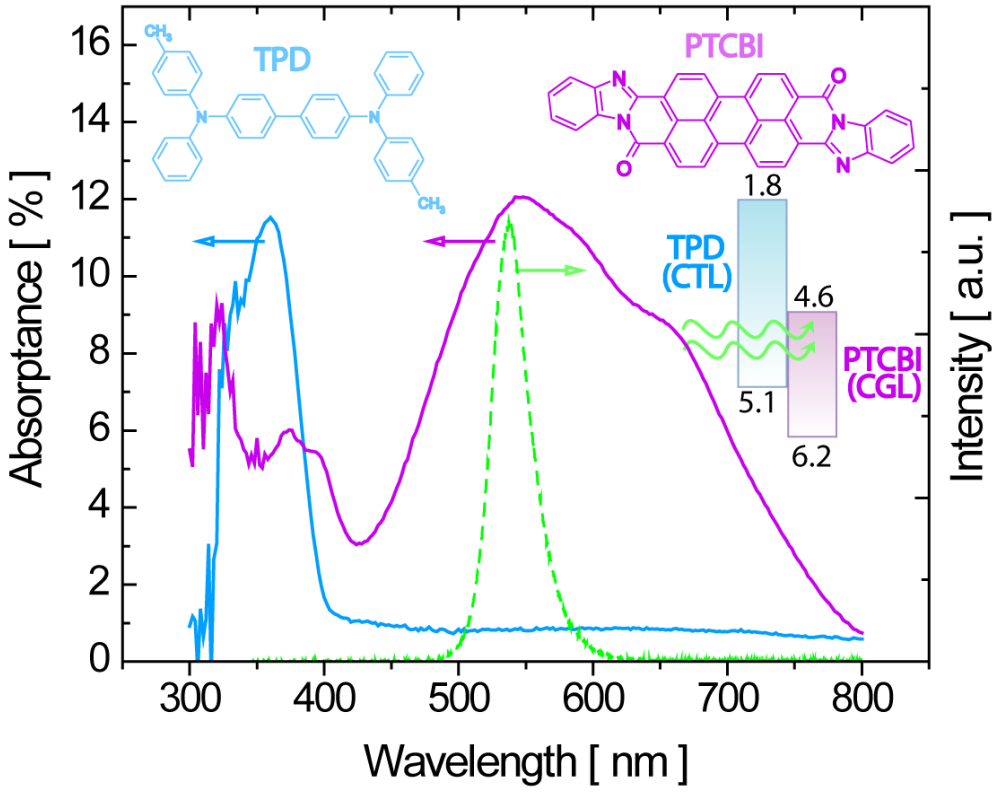

Figure 4-11: Absorption spectra (50 nm thick films), chemical structure, and proposed energy band levels of the materials used in the bi-layer heterojunction photoconductor: N,N'-bis(3-methylphenyl)-N,N'-diphenyl-1,1'-biphenyl-4,4'-diamine (TPD) as CTL and 3,4,9,10-perylenetetracarboxylic bis-benzimidazole (PTCBI) as EGL. Also shown is the emission profile of the green LED (dotted line, λ_{peak} = 532 nm) operated with a forward current of 2 A and an intensity of 40 mW/cm^2. Energy band levels represent experimental values for the HOMO/LUMO based on photoemission spectroscopy data [6, 14]. As shown, the energy bands correspond to transport levels that provide upper and lower limits for the optical bandgap and emphasize the Type-II heterojunction between TPD/PTCBI.

(Oriel) passed through a monochromator (Princeton Instruments/Acton Spectrapro 300i). The optical chopping frequency was set at 40 Hz, giving the device enough time to respond to the illumination. Photocurrent transient measurements were performed with a standard voltage divider circuit, an oscilloscope (Tektronix 3500 Series), and an arbitrary waveform generator (Agilent 3350A). All measurements were taken in a nitrogen glove box (MBraun) environment to prevent device degradation during measurements.

4.4.1 Current-Voltage Characteristics

Figure 4-12 plots the steady state I-V characteristics, both with and without LED illumination, from a series of devices containing either single films or bilayer heterojunctions of PTCBI and TPD. The device that contains a single (50 ± 0.5) nm thick film of TPD generates no measurable photoresponse, which reflects the inability of TPD to absorb green (λ = 532 nm) light. The thin film of PTCBI does generate a moderate photocurrent in response to the green light illumination, which can be seen by comparing the solid blue line to the dashed blue line in Figure 4-12. Despite the absence of a heterojunction, photogenerated excitons are still able to dissociate in the single film (most likely at polycrystalline grain boundaries) of PTCBI contributing to the enhanced film conductance [31]. Comparing the dark currents of PTCBI and TPD, it is evident that PTCBI has a lower overall dark conductivity. Given that there should be little to no electron injection barrier from the gold contacts into PTCBI [6], the decreased conductivity can largely be attributed to the low electron mobility of PTCBI ($\sim 10^{-6}$ $cm^2V^{-1}s^{-1}$). The heterojunction devices show a relative improvement in the photoresponse and a light to dark current ratio of over 100. The lower conductivity exhibited by the PTCBI/TPD device (green curves) is most likely due to the PTCBI film having a lower electron mobility than the hole mobility in TPD [32]. This dataset suggests that the TPD/PTCBI heterojunction interface is efficiently dissociating excitons and generating charge under illumination, which is transported through the CTL. It is also worth mentioning that both heterojunction devices demonstrated an increase (up to a factor of five) in dark currents (red and

green dashed lines) over the dark currents (black and blue dashed lines) of the underlying films alone. This may be evidence of the formation of an interface dipole due to charge transfer at the interface, which forms a conductive channel in dark conditions. The strong electron donor-acceptor nature of TPD/PTCBI makes this a plausible scenario [7]. Fitting the curves on a log-log scale reveals a near-linear dependence of current on electric field, which suggests that over the range of voltages tested, the conduction remained ohmic and that gold does not form a blocking contact with TPD.

By varying the thickness of the underlying CTL it is possible to show, with another series of measurements, the formation of a more conductive channel that is primarily concentrated at the heterointerface. Figure 4-13(a) shows a series of I-V curves that were taken under green LED illumination. Despite illuminating the device through the glass substrate and up through the TPD films, the negligible absorption coefficient of TPD at $\lambda = 532$ nm [33] means that the intensity of light reaching the PTCBI film will essentially remain unchanged from the 50 nm to 500 nm thick TPD/PTCBI device. In addition, the interface exciton dissociation efficiency should not be affected by the underlying CTL thickness, which suggests that the photogeneration rate of carriers should remain the same for all of the devices in the series.

For clarity, the dark currents are not included as the noise floor of the measurement obscures any observable trends. As the thickness of TPD is varied over the range of 50 nm to 500 nm, a clear decrease in the light current occurs for thicker and thicker CTLs. In order for the current levels of the devices to decrease in the linear regime there must be either a decrease in the applied voltage or an increase in the effective resistance of the device. Because the range of applied voltages is fixed the effective resistances of the thicker devices must be increasing. The best way to explain this phenomenon is to model the bilayer device as a simple resistor network [Fig. 4-13(a)], where the bulk resistivities of TPD and PTCBI are much higher than the resistivity of the interface due to charge transfer [20] and the large carrier concentration. Knowing that the interface is the most conductive pathway implies that the conduction in the bilayer devices will be limited by the transport of injected charge

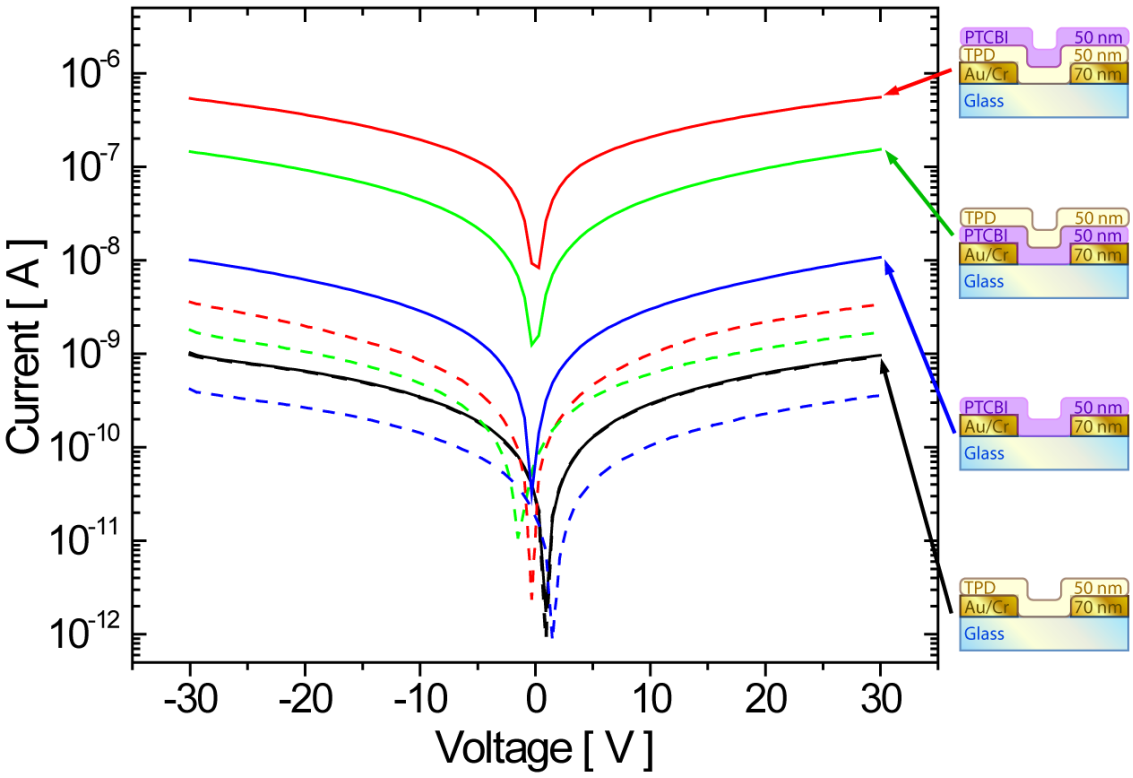

Figure 4-12: Semi-logarithmic plot of the current-voltage characteristics from a series of lateral photoconductor devices using TPD and PTCBI. Current-voltage sweeps are taken in the dark (dashed) and under illumination (solid) through the glass substrate from a 40 mW/cm^2 green LED (λ_{peak} ~ 532 nm). The inset cross-sectional diagrams describe the thicknesses and device structures. Both heterojunction devices (Au/PTCBI/TPD [green] and Au/TPD/PTCBI [red]) exhibit steady-state photoresponse. The Au/TPD device (black) exhibits no photoresponse to the green LED, consistent with its absorption spectrum. The Au/PTCBI device (blue) exhibits a steady-state photoresponse with lower currents than heterojunction devices.

from the bottom contacts through the TPD into the conductive channel at the interface. The bulk resistivity of TPD and injection cross section are independent of thickness, thus we would expect a linear increase in resistance through the TPD film with increasing thickness and a consequent inverse relationship with current. It is not possible, however, to linearly extrapolate the resistance of the interface without assuming linear control over thickness. The height of the gold contacts (70 ± 0.5 nm) can disturb the linearity of resistance with film thickness because TPD films that are below or near the thickness of the contacts may exhibit nonlinear growth characteristics at the sidewalls of the contacts [Fig. 4-13(b)]. This has the potential to yield much more conductive pathways through the sidewalls than would be expected from the thickness of the TPD film. Electron microscopy of the cross section of the devices could be used to ensure that the TPD films are thick enough to ensure conformal growth characteristics.

Another effect to take note of is the transition of the 500 nm thick device (blue curve) from ohmic conduction to space charge limited conduction (SCLC) (the dotted lines in Figure 4-13 are guides for the eye). Space charge builds up in insulators because of the typically slow dielectric relaxation times that cannot quickly screen injected charge. When the transit time of injected carriers is greater than the dielectric relaxation time, SCLC become apparent in the I-V curves and follows a V^2 dependence

$$J = \frac{9}{8}\frac{\epsilon\mu V^2}{L^3}. \tag{4.4.1}$$

The critical voltage onset of SCLC can be derived from the criterion discussed above,

$$t_{tr} = \frac{L^2}{\mu V} \geq \frac{\epsilon}{\sigma}$$
$$V_{crit} = \frac{\sigma L^2}{\mu\epsilon},$$

where L is the distance between electrodes, ϵ is the dielectric constant of the insulator, μ is the mobility of the insulator, and V is the voltage applied across the electrodes. The assumptions here are that 1) there is only one type of charge carrier present

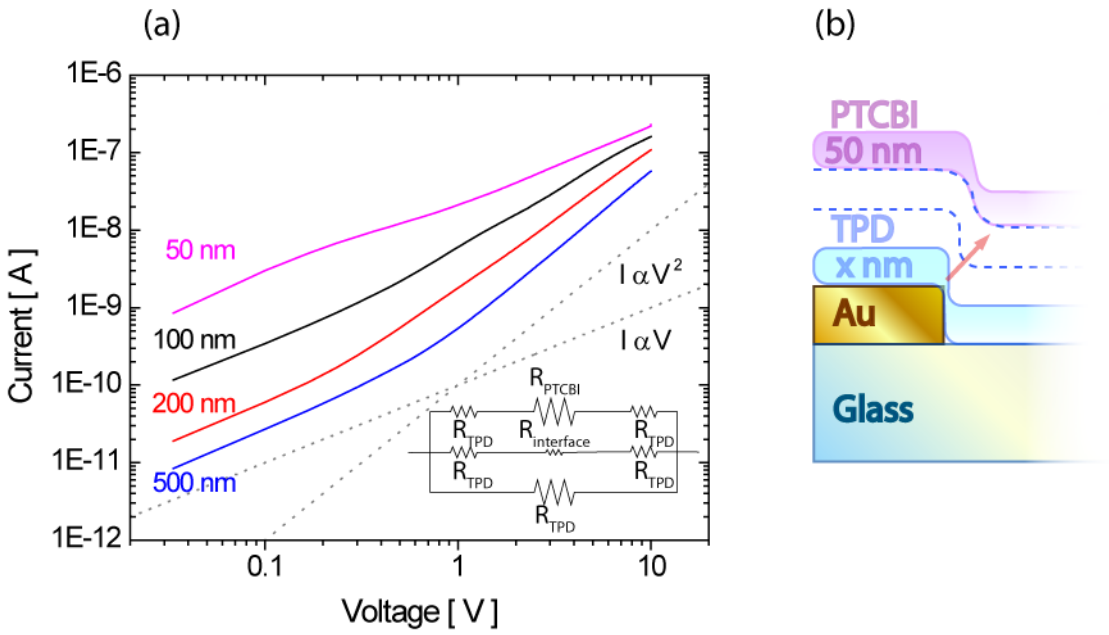

Figure 4-13: (a) Log-log plot of current-voltage characteristics for a series of TPD/PTCBI devices under illumination. The dashed lines are provided to show the transition between ohmic and SCLC in the blue curve (500 nm TPD/50 nm PTCBI). Inset: a circuit model of conduction pathways in the bilayer devices, where the relative size of the resistor is indicated. (b) A schematic drawing depicting the non-linear sidewall growth that can occur with thin films evaporated on bottom contacts.

in the insulator, 2) ϵ and σ are constant throughout the film, and 3) the insulator is trap-free. Thus, the transition from ohmic to SCLC in Figure 4-13(a) indicates trap-free TPD/PTCBI bilayer devices.

4.4.2 Spectral Response

Wavelength-resolved photocurrent spectra from three lateral photoconductors, containing films of PTCBI and TPD, are shown in Figure 4-14. The photoconductor with a single (5 ± 0.5) nm thick film of TPD yields no measurable photocurrent and is omitted from the Figure 4-14 plot. This is most likely due to the amorphous nature of thermally evaporated TPD, which contains few centers or surfaces for exciton dissociation. The spectral response of the photocurrent is measured with the lock-in amplifier locked to the light chopping frequency, effectively filtering out the DC dark current. All of the measured photocurrent curves spectrally match their respective de-

vice's absorption spectra. Comparing the response of the photoconductor with a neat film of PTCBI to the photoconductors containing the TPD/PTCBI heterojunction, we note that the introduction of a heterojunction interface improves the photocurrent over 1000-fold for all wavelengths, reaching an external quantum efficiency of (12 ± 1)% at $\lambda = 552$ nm. This suggests that excitons generated in either TPD or PTCBI are efficiently dissociated by the Type-II heterojunction formed at the interface. Accounting for the number of photons absorbed in our thin films at that wavelength, the internal quantum efficiency for Au/TPD(5 ± 0.5 nm)/PTCBI(10 ± 0.5 nm) is (140 ± 2)%, when illuminated with $\lambda = 552$ nm wavelength light and operated at an applied electric field of 1.25 x 10^5 V/cm. An internal quantum efficiency of greater than 100% indicates an optical-to-electrical conversion gain in the device. Despite the order of deposition of the constituent films, both heterojunction devices yield improvements in photoresponse as compared with the single films. The PTCBI/TPD device's lower quantum efficiency (comparing the green curve to the red curve) can be attributed to the low electron mobility in PTCBI.

4.4.3 Intensity Measurements

Figure 4-15 demonstrates the current as a function of voltage at different incident light intensities for a 50 ± 0.5 nm TPD/50 ± 0.5 nm PTCBI device. At all intensities, the device exhibits ohmic conduction over the range of voltages swept. At 1 V the light current shows a sublinear dependence on intensity as evidenced by the inset of Figure 4-15. The power law fit to the relative photocurrent vs. relative intensity follows a near square-root dependence with an exponent of 0.56. As discussed earlier, bimolecular recombination leads to a square-root dependence of the excited carrier concentration on incident illumination, because of the dependence of carrier lifetime on intensity. Monomolecular recombination leads to a linear dependence on intensity. Models have been developed to describe carrier density versus light intensity curves that fall somewhere between these two regimes with a power law exponent between 0.5 and 1. For monomolecular recombination, the carrier lifetime is independent of the carrier concentration. In the case of bimolecular recombination, the lifetime varies

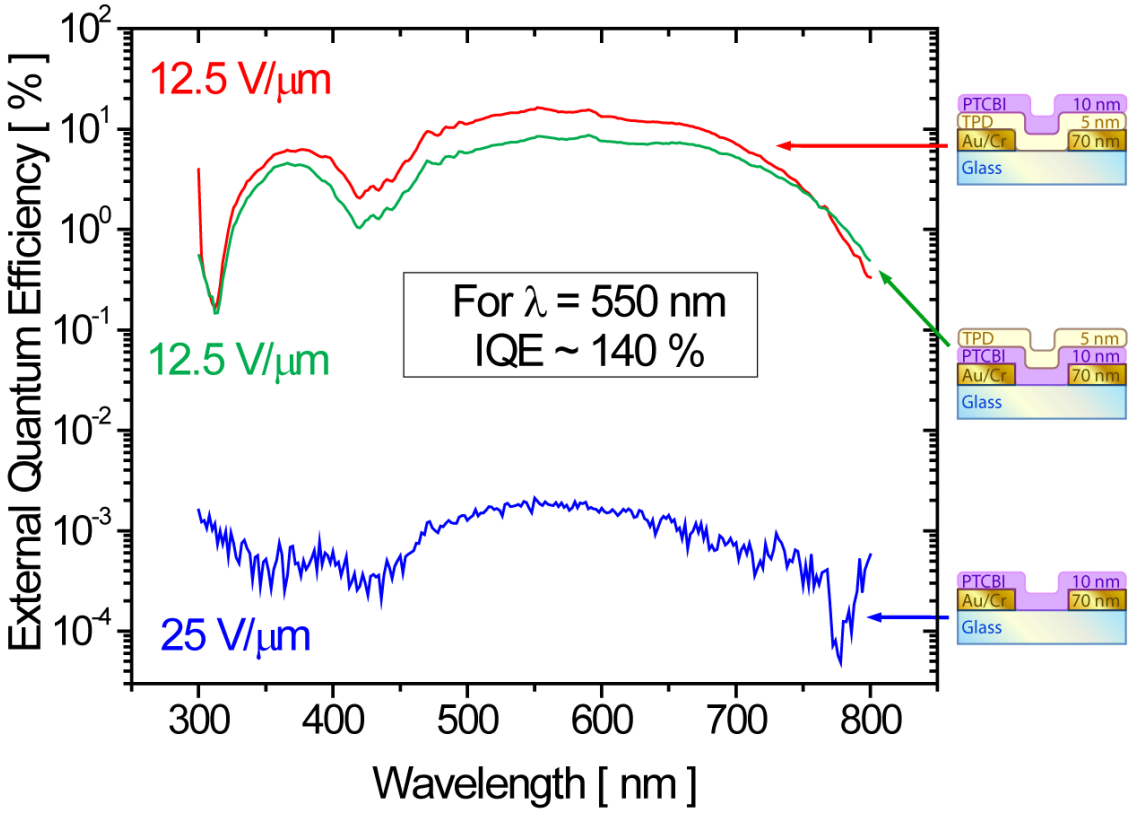

Figure 4-14: Semi-logarithmic plot of external quantum efficiency (EQE) versus wavelength, for a series of device structures illustrated in the inset. Electric fields applied during the measurement are indicated to the left of each curve. The Au/TPD device yields no measurable photoresponse. Both heterojunction devices (solid and dashed lines) exhibit over 1000-fold improvement in the EQE over the Au/PTCBI device (dotted line), at 2-fold lower bias voltages. At $\lambda = 552$ nm, the Au/PTCBI/TPD device and Au/TPD/PTCBI device yield EQEs of $(8 \pm 1)\%$ and $(12 \pm 1)\%$, respectively. Accounting for the absorption of $\lambda = 552$ nm light in the PTCBI/TPD device, we find an internal quantum efficiency (IQE) of $(140 \pm 2)\%$. This result demonstrates that lateral bi-layer heterojunctions are capable of quantum gain.

with the inverse of carrier concentration. It stands to reason that if these two recombination processes are in parallel then there may be an intermediate exponent value as the dependence transitions from linear to square-root. However, this transition will be quite abrupt and should only be observed over a factor of 2 change in light intensity.

Figure 4-15 shows a 0.56 exponent over 3 orders of magnitude suggesting that these bilayer devices follow the model proposed by Tabak and Warter [34]. This model assumes a single film and that there is bimolecular recombination at the illuminated surface and monomolecular recombination in the bulk. This assumption is consistent with the idea that only photogenerated holes are in TPD, while photogenerated electrons are confined to PTCBI. Another consequence of the model is that the bulk of the transporting film is trap-free. This is consistent with the lack of observable trap-charge limited currents in the I-V sweeps. Finally, back surface effects are neglected, which is consistent with our shining light through the glass substrate and having negligible reflection from the films.

Qualitatively, there are three separate regimes of operation for strongly absorbed light. At low intensities, the monomolecular bulk recombination dominates and current is a linear function of light intensity. At intermediate light levels, the bimolecular surface recombination becomes sufficient to cause the current to follow a square-root dependence of the photocurrent on light intensity. At high light levels, the surface recombination becomes a sink for electron-hole pairs which pins the carrier concentration at the surface to a much lower level than the peak concentration levels in the bulk. So, the photocurrent becomes linear with light intensity again, but the sensitivity is much lower than at the low intensity regime. The shape of the photocurrent-intensity curve is controlled by the transition points, which is dependent on one parameter - the product of the carrier diffusion length to the absorption coefficient ($L\alpha$). Considering the TPD layer does not absorb much of the green light, the effective penetration depth of the light approaches 0 ($\alpha \rightarrow \infty$). Thus, the ratio of the carrier diffusion length to the absorption depth in TPD becomes very large. This has the effect of pushing the transition points further apart, ultimately extending the range of intensities for which

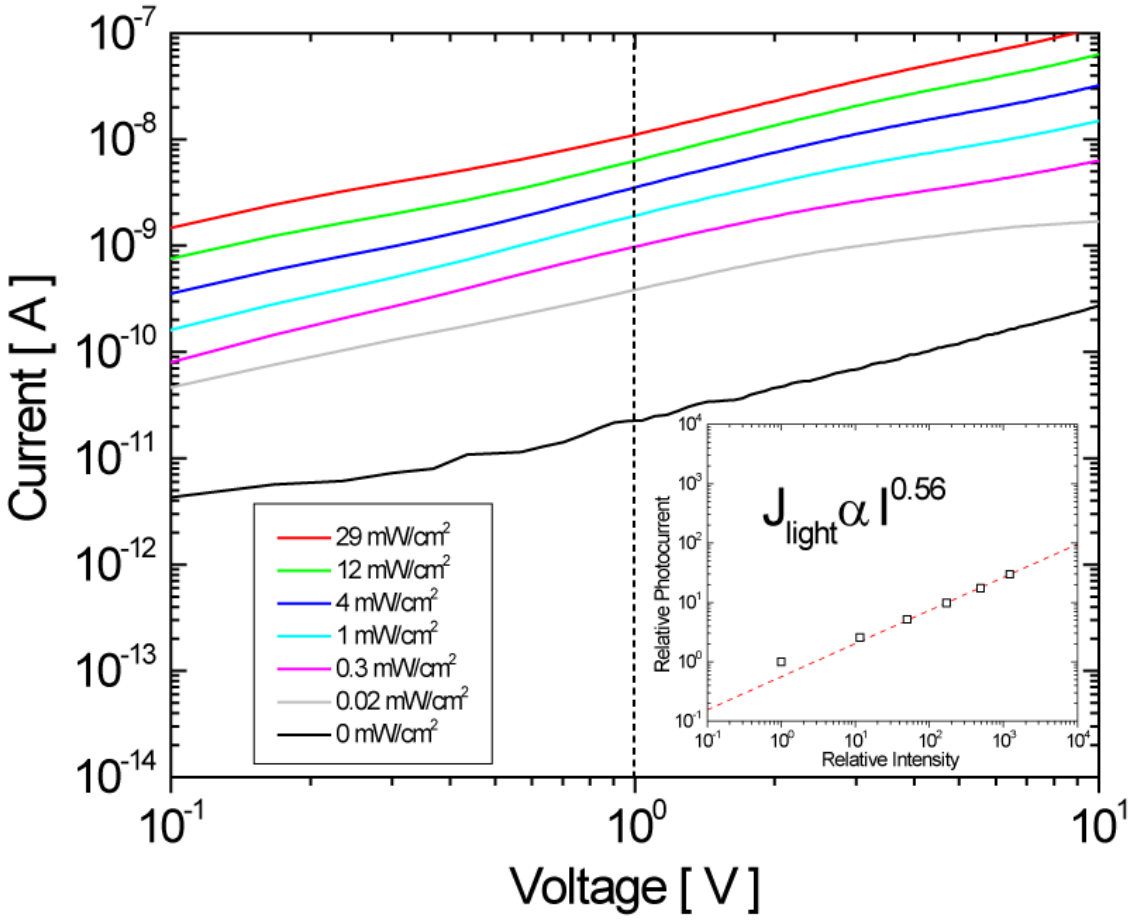

Figure 4-15: Log-log I-V characteristics of 50 nm TPD/50 nm PTCBI device under varying levels of green LED illumination. Inset: Relative photocurrent as a function of relative intensity reveals sublinear dependence.

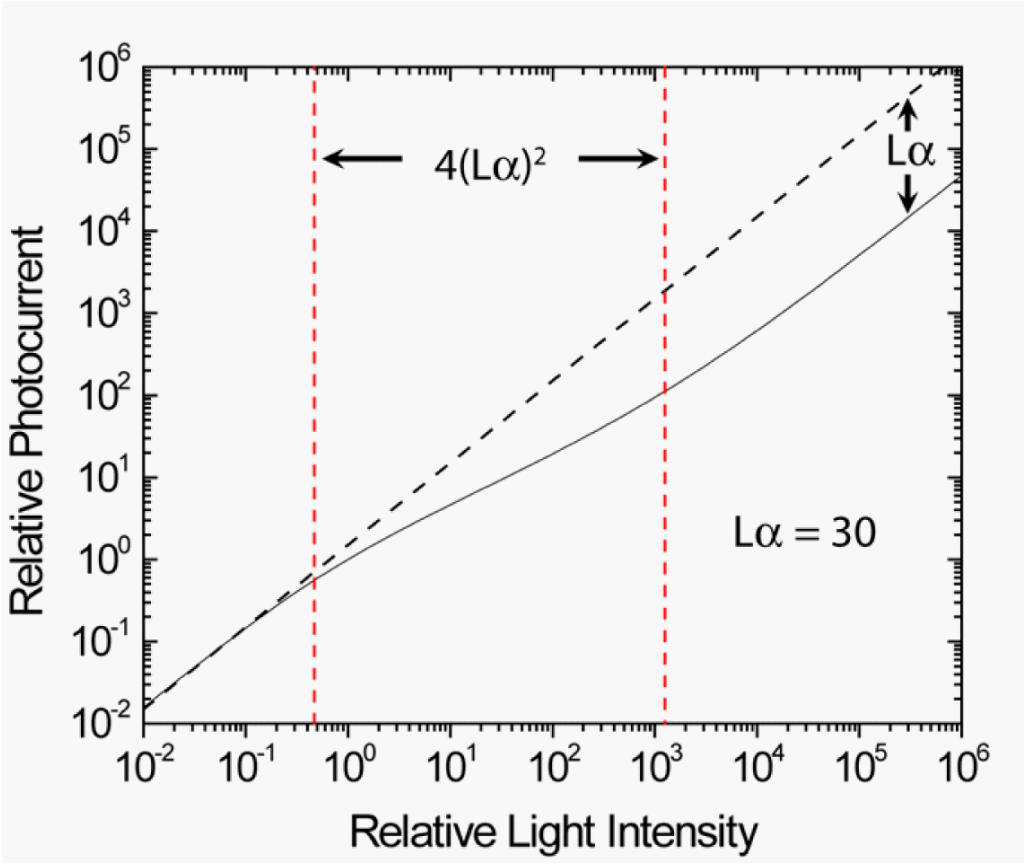

Figure 4-16: Simulated variation of photocurrent with light intensity for the Tabak-Warter model, where L is carrier diffusion length and α is absorption coefficient. Breakpoints between different regimes of dependence are indicated by dashed red lines. After [34].

the current will follow a square-root dependence [Fig. 4-16]. In the measurements of the bilayer photoconductor, the range of intensities samples this large sublinear region between the two linear regions.

4.4.4 Transient Measurements

When measuring the transient aspects of photoconductivity, we can either look at the build-up or relaxation of steady-state photocurrents. While the turn-on transient reflects both the generation and recombination of carriers, the turn-off transient only reflects the recombination effects and is easier to analyze. Turn-off transients that follow a simple exponential decay will only be observed when a unique recombination

path is followed and usually occurs in exceptional cases [35].

When the steady-state illumination is terminated, the generation rate drops to zero while the carrier density and recombination rates are not affected. Thus, the initial photocurrent decay will be governed by whatever recombination mode existed under steady-state conditions. Relaxation of photogenerated carriers in amorphous semiconductors can occur through either monomolecular or bimolecular recombination. Monomolecular recombination occurs if a free carrier encounters a recombination center. As a reminder, recombination centers are traps that have a lower rate of detrapping relative to recombining. Due to the various recombination processes in operating devices and the lack of information regarding the mechanisms involved, the response times have traditionally been used as estimates to carrier lifetimes. An exponential fit to the initial part of the decay is often used to make this approximation [35]. This initial decay does not have to represent the most significant part of the decay process, such as in the case where persistent photoconductivity occurs (one of the relaxation times observed is longer than the observation time). However, in analyzing the transient photocurrent curves for the bilayer devices, we have observed an initial fast decay followed by a much slower response. In this case we take the initial decay to represent the best estimate of carrier lifetime.

Figure 4-17(a) displays the transient photocurrent decay with varying intensities of light ranging from 0.25 to 74 mW/cm^2. The photocurrent is induced by illumination with a green LED (λ = 532 nm) incident through the glass substrate. All curves are normalized to their steady-state photocurrent levels and time-shifted so that the illumination cuts off at time t = 0. A constant voltage of 150 V is applied between the interdigitated electrodes throughout the measurement. It is evident that the decay rate decreases significantly with increasing intensity. Fitting the different intensity curves with a double exponential yields a fast and a slow component time constant. Two-component transient responses are common in experimental work and are an artifact of using photoconductors with a finite length [36]. However, there is ambiguity regarding the proper model to use for extracting time constants from transient data [37]. The decay curve can exhibit two distinct exponential regions if two different

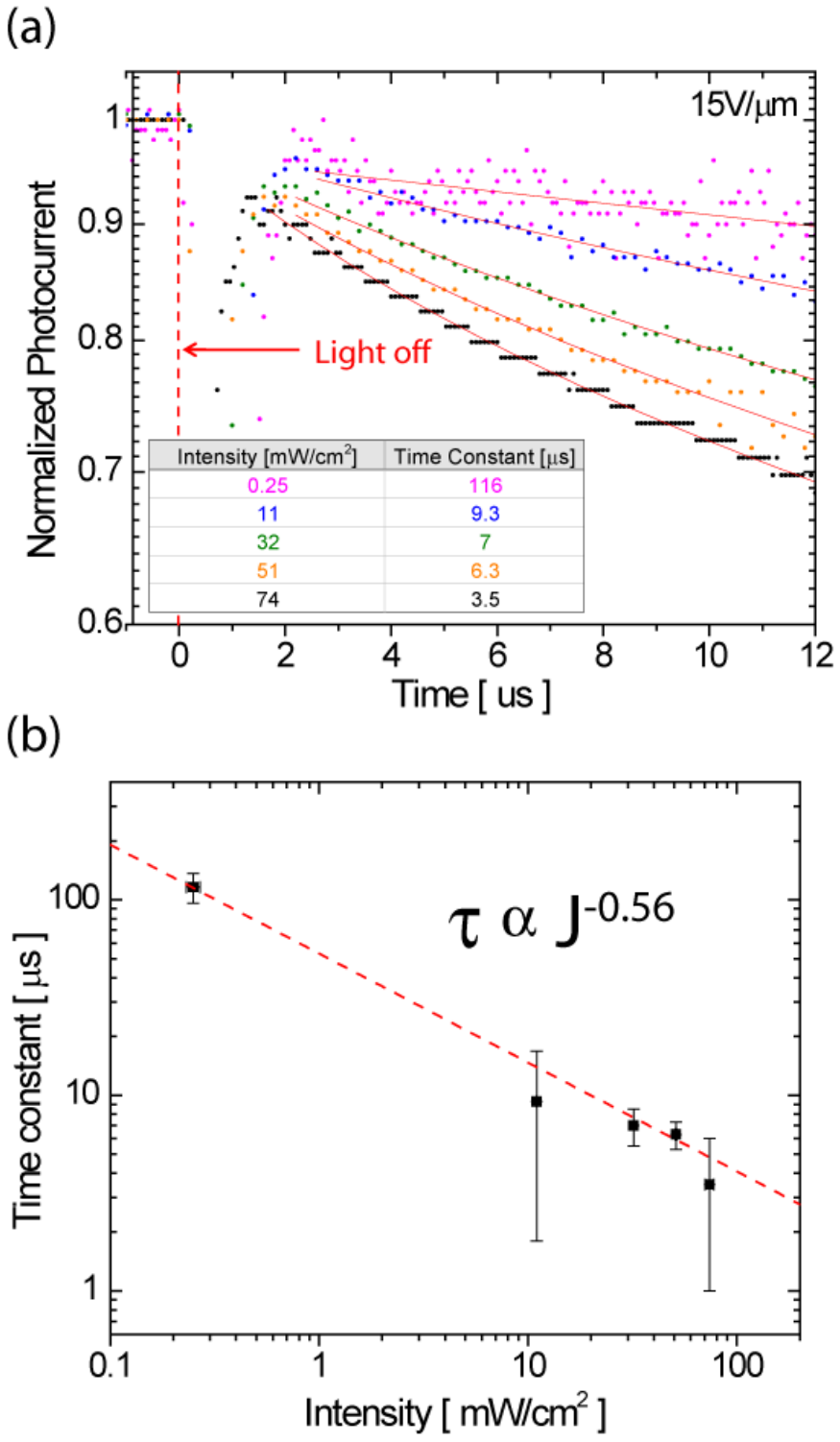

Figure 4-17: (a) Semi-logarithmic plot of normalized photocurrent decay under various intensity illumination and an applied electric field of 15 V/μm. Light is turned off at time t = 0. Dark current is subtracted from all curves before fitting double exponentials over the range 2.8 μs to 12 μs. (b) Fitted time constants plotted versus intensity.

recombination mechanisms dominate at different carrier concentration levels, which is consistent with all recombination mechanisms being carrier concentration dependent. In this work we associate the initial fast time constant to bimolecular recombination across the interface, and those values are provided in the inset table of Figure 4-17(a). The values are all in the microsecond range, which is much slower than the turn off time of the LED light source (~ 100 ns) used for excitation. The slower of the two time constants is associated with bulk recombination in the TPD film. Because TPD is considered an intrinsic semiconductor we would expect the bulk recombination to have a slower rate than at the heterointerface where there are many more of the oppositely charge carrier present one molecular hop away. The dependence of the carrier lifetime on intensity is visualized in Figure 4-17(b) and fits a power law relation with an exponent of γ = -0.56, which is consistent with the bimolecular recombination model exhibited by the photocurrent dependence on intensity. This is a signature of bimolecular recombination, where the carrier lifetime follows an inverse square-root dependence on intensity in a trap-free, insulating film.

The lateral bi-layer photoconductor structure presented here exhibits gain and is shown to generate photocurrent exclusively from absorption in the PTCBI film. In contrast to a single layer photoconductor, the bi-layer device separates the charge generation mechanism from the charge transport mechanism. Doing so allows the engineering of each layer for optimized device performance. In addition, the physical processes that take place in device operation are not specific to the material set. The critical requirement is that the energy band alignment is favorable for exciton dissociation at the interface between the materials.

4.5 Other Material Systems

The heterojunction photoconductor platform is a general device architecture that can exhibit similar optical and electrical characteristics across a wide range of material sets. The only major requirement is the ability to form a Type-II heterojunction between the two materials of interest. Because of the existence of interface dipoles

and the inherent uncertainty in energy level measurements (i.e. UPS/IPES) it will be necessary to try different materials with similar band offsets in order to account for shifts in vacuum level and changes in energy levels due to deposition conditions. Until the origin of the interface dipole is well understood, this process of trial and error may be unavoidable. Two examples of Type-II heterojunction photoconductors that utilize different materials are detailed below: small molecule organic/quantum dots and J-aggregate dye/metal oxide.

4.5.1 CdSe Quantum Dot/Spiro-TPD Heterojunction Photoconductor

Colloidal CdSe (Cadmium Selenide) quantum dots (QD) have been used in conjunction with the hole-transporting small molecule N,N'-Bis(3-methylphenyl)-N,N'-bis(phenyl)-9,9-spirobifluorene (Spiro-TPD) to fabricate bilayer heterojunction photoconductors. QDs are chemically synthesized QD nanocrystals which can be processed from solution and have tunable absorption/emission characteristics based on the material selection and the physical size of the nanocrystals [38, 39].

The heterojunction photoconductor utilizes an evaporated film of the hole-transporting material, Spiro-TPD (Luminescence Technologly Corp.), as the CTL, which is sensitized across visible wavelengths by a thin film of TOPO-capped CdSe nanocrystal QDs, which act as EGL. The device structure is shown in Figure 4-18(a). Electrically, the hole mobility (10^{-5} $cm^2V^{-1}s^{-1}$) of a molecule that is the same in nomenclature as the Spiro-TPD used in this work, but with a slightly different chemical structure is demonstrated to be an order of magnitude higher than the electron mobility in the film of tri-octylphosphine oxide (TOPO) capped CdSe QDs (10^{-6} $cm^2V^{-1}s^{-1}$) [40, 41]. Thus, conduction in the device should predominantly occur in the bulk of the Spiro-TPD film. Optically, the wide bandgap of Spiro-TPD provides an onset in the absorption spectrum at shorter wavelengths ($\lambda < 400$ nm), allowing for the onset of absorption at longer wavelengths to be determined by the QD layer. Under broadband illumination, excitons are generated in the organic and QD layers which

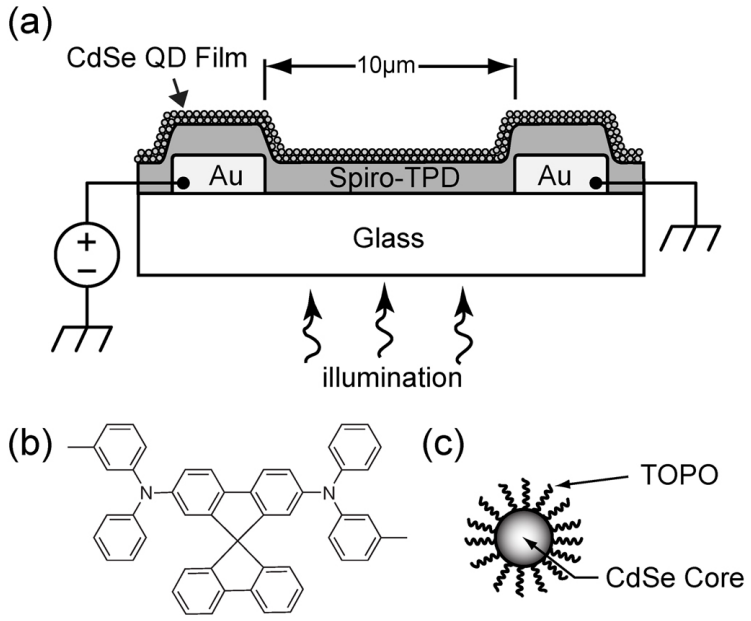

Figure 4-18: (a) Section view of the device structure. The thickness of the Spiro-TPD layer is 200 nm. For each device there are 60 sets of Au electrodes arranged in an interdigitated array forming a serpentine channel (not shown). The channel length is 10 μm and the electrode width is 1000 μm. (b) Chemical structure of the hole-transporting material, Spiro-TPD. (c) Schematic of CdSe nanocrystal (~ 5-7 nm) passivated with TOPO ligands [42].

together form a Type-II heterojunction [Fig. 4-19(a)]. Excitons within a diffusion length of this interface may be dissociated, resulting in the transfer of free electrons to the QDs and holes to the organic charge transport layer. The increase in carrier concentration results in an increase in current when a bias is applied across the electrodes.

The devices consist of interdigitated chrome/gold electrodes (20nm/50nm) on glass that form a serpentine channel with a width of 60 mm and a length of 10 μm. A 200 nm thick Spiro-TPD film is then thermally evaporated over the electrodes. Subsequently, the samples are transferred directly into a nitrogen-filled glove box without exposure to air. CdSe QD cores (~ 5 - 7 nm in diameter) with a lowest energy absorption peak at wavelength $\lambda = 590$ nm are synthesized and passivated with TOPO ligands to provide solubility in chloroform [46]. Micro-contact printing from an untreated polydimethylsiloxane (PDMS) stamp is used to deposit the QDs onto the substrate. Stamps are cleaned with chloroform prior to spin-coating with

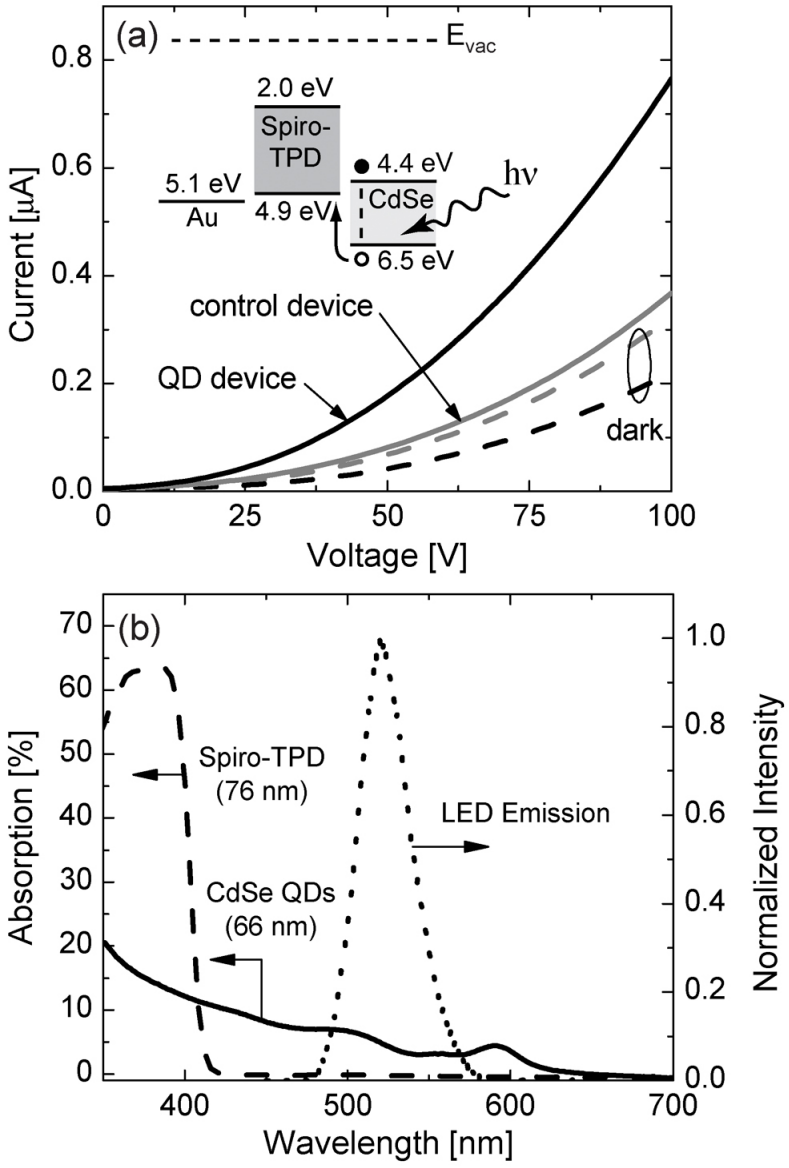

Figure 4-19: (a) Current-voltage characteristics measured for Spiro-TPD (control) and Spiro-TPD/QD (QD) devices. Dashed lines represent dark currents. Solid lines show the device response under illumination from a green LED with an intensity of 74 mW/cm^2 and with emission centered at $\lambda = 521$ nm. The inset shows the energy band diagram for the QD device. The energy levels for the Spiro-TPD were taken from [43]. Energy levels for the CdSe QDs were calculated following the approach reviewed in [44] and using bulk CdSe parameters obtained from [45]. (b) Absorption spectra of Spiro-TPD (dashed line) and CdSe QDs (solid line). Emission from the LED (dotted line) is absorbed primarily by the QD film [42].

QDs at 4000 RPM for 60 seconds. The stamps coated with QDs are then placed in a vacuum environment (~ 10^{-3} Torr) for approximately 1 hour to remove excess solvent. Finally, the PDMS stamp is applied to the device substrate with a small amount of force to transfer the QD film. The thicknesses of transferred QD films were measured to be approximately 50 nm, and completed devices were tested in a nitrogen environment.

I-V measurements are shown in Figure 4-19(a) for a control device, consisting of a 200 nm thick film of Spiro-TPD, and for a bilayer Spiro-TPD/QD heterojunction device. Following the absorption spectra of the materials used, the green LED illumination is primarily absorbed by the QDs [Fig. 4-19(b)]. The Spiro-TPD device shows little photoresponse as evident by comparing the gray solid line to the gray dashed line in Figure 4-19. This behavior is consistent with Spiro-TPD's absorption spectrum, and its inability to absorb the green illumination. The 50% decrease in the dark current from the control device to the bilayer device, while rather large, occurs when the QD film is sufficiently thick. In devices with a single layer of Spiro-TPD, as the Spiro-TPD films grow thicker there is a consistent increase in dark current, suggesting that conduction occurs in the bulk of the Spiro-TPD film. The QD stamping process can negatively affect the overall dark conductivity by removing some of the underlying CTL while transferring the QDs. There exists some evidence to support this theory given that untreated PDMS stamps can be used to lift-off organic and metal thin films [47]. However, this theory relies on the assumption that the organic material that is being stamped is "soft" enough to squeeze through the interstitial spaces or cracks in the QD film to interact with the PDMS stamp. Anecdotally, this seems to be the case given that stamping QD films has been shown to embed the QDs into underlying small-molecule organic materials such as Spiro-TPD. Complete QD films remove little to no underlying organic layer, suggesting that the organic material is being removed through cracks in incomplete films. More careful studies of the microcontact printing process and the effects on the underlying organic material still need to be undertaken to elucidate the physical mechanism for removal of underlying material with QD stamping.

Another insight can be inferred from the decrease in dark conductivity post-stamping. Because we have seen up to this point that dark currents rise after the introduction of the heterojunction due to charge transfer across the interface, a reduced dark current could indicate little to no charge transfer occurring between the QD film and the underlying Spiro-TPD film, which would make the heterointerface less conductive than the bulk Spiro-TPD. Data to support this assumption is shown in Figure 4-20 where for varying thicknesses of Spiro-TPD and varying thicknesses of QDs, the dark current decreases indicating no charge transfer in addition to removal of underlying Spiro-TPD. In order to explain this phenomenon, another piece of information is required concerning the QDs ability to transfer charge. To vary the thickness of the stamped QD films, different concentrations of QD solutions are used, the more dilute solutions yielding on average thinner spun films on the PDMS stamps. When QDs are synthesized, they are naturally capped by TOPO ligands which are in a dynamic equilibrium between being bound to the surface of the dot and being free in solution [48]. This implies that the more dilute the solution of QDs, the lower the density of ligands at the nanocrystal surface. Fewer ligands suggest that there may be a higher probability of charge transfer to occur between the QD and its surrounding medium. Therefore, the ability for charge to transfer between the Spiro-TPD and the QDs may be a function of the concentration of the QD solution used.

Assuming the electric field distribution between the electrodes is uniform, a bias of 100 V is equivalent to an electric field strength of 10^5 V/cm. At this bias, the ratio of the light current to the dark current increases from 1.1, in the control device, to 3.5 for the bilayer QD device. The energy band alignment and high CTL hole mobility in the Spiro-TPD/QD devices would suggest similar device performance to the TPD/PTCBI devices. However, there is a difference of roughly two orders of magnitude in the light to dark current ratios. Comparing data from the I-V curves it is evident that the increased dark current in the Spiro-TPD/QD device is responsible for the reduction in the ratio of light to dark current. Given that Spiro-TPD has a slightly lower field effect mobility than TPD, it cannot account for the higher relative dark conductivity. One possible explanation for this behavior is the energy band

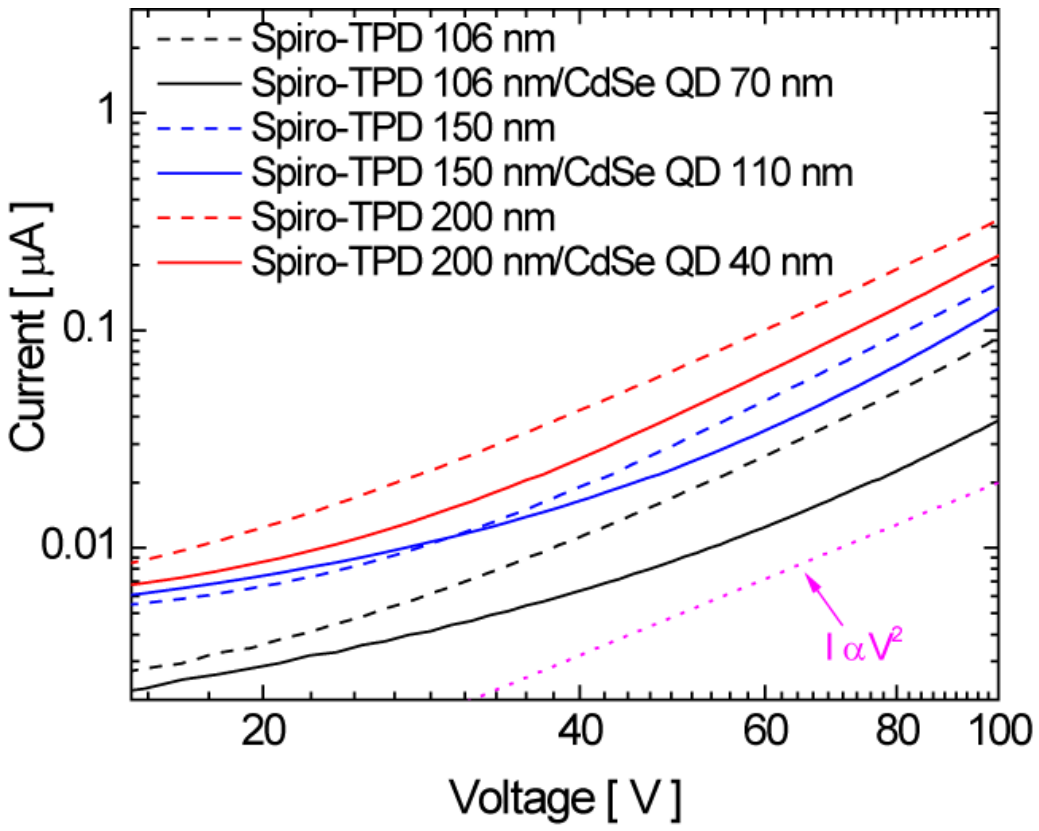

Figure 4-20: Log-log current-voltage characteristics of various Spiro-TPD/QD devices. Dotted lines represent single films of Spiro-TPD, while solid lines represent the QD-stamped bilayer devices. The magenta dotted line is a guide to the eye that represents the functional form of SCLC.

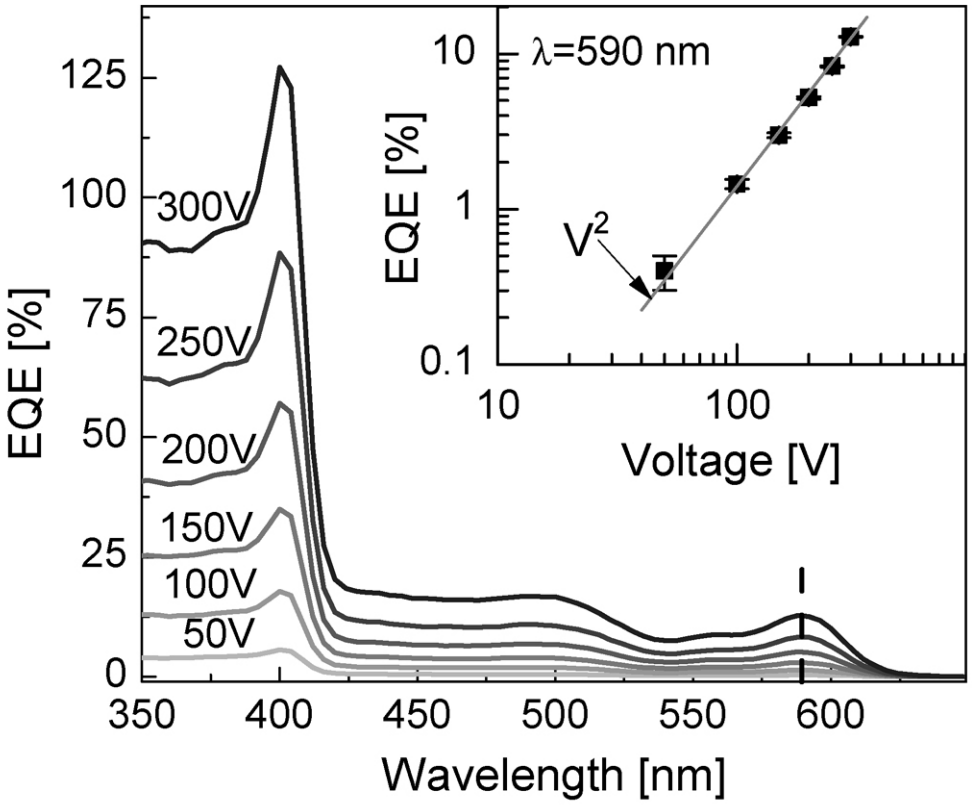

Figure 4-21: EQE spectra for a variety of biases. Inset shows EQE at $\lambda = 590$ nm as a function of bias. Photocurrent follows a nearly V^2 power law indicative of space charge limited conduction in Spiro-TPD.

alignment of Spiro-TPD with respect to the gold contacts. Spiro-TPD has a HOMO at 4.9 eV, effectively presenting a lower barrier to hole injection (as compared to TPD) from gold, which has a work function of c.a. 5.1 eV and a large VL shift of ~ 1 eV [14]. Thus, the lower barrier to charge injection into Spiro-TPD would serve to increase the overall dark conductivity of the device.

Figure 4-21 shows the EQE of the QD device for a variety of biases. A large response peak that occurs between $\lambda = 300$ nm and $\lambda = 400$ nm is attributable to light that is absorbed in the Spiro-TPD layer. There is also a strong photoresponse for $\lambda > 400$ nm that closely follows the absorption spectrum of the QDs. A maximum in the EQE occurs at $\lambda = 590$ nm, the lowest energy absorption peak of the QDs, which reaches 13% at 300V. The corresponding internal quantum efficiency (IQE) at $\lambda = 590$ nm is calculated to be 79%. For a sufficiently high bias applied across

the electrodes an EQE of greater than 100% may be realized, which would suggest that the device is operating in a regime of photoconductive gain. The inset reveals that the EQE measured at λ = 590 nm follows a V^2 power law dependence with bias. This is consistent with space charge limited conduction in the ideal case of a trap-free insulator [49, 50]. We note that there is a strong peak in photoresponse at λ = 400 nm, precisely where Spiro-TPD absorption begins to fall off [Fig. 4-21(b)]. A photoresponse in a layered heterojunction device that is strongest at wavelengths for which absorption is weakest can be described as antibatic (vs. symbatic) and suggests that the heterointerface is effectively dissociating excitons [51]. The presence of the antibatic peak at λ = 400 nm therefore supports the assertion that the interface between Spiro-TPD and the QD film is the site of exciton dissociation in the device.

Comparing the IQE value of the Spiro-TPD/QD device with that of the TPD/PTCBI device, it is evident that at the absorption peak of the EGL, the TPD/PTCBI devices have higher efficiencies at lower applied fields. This is another signature of the lower mobility of Spiro-TPD and of the diminished charge transfer dynamics at the organic/QD interface due to the presence of the organic ligands. It is well known that QD interspacing (which is set by the length of the ligand) affects not only the conductivity of the QD films, but also the dissociation efficiency of excitons where one of the charges has to tunnel through a potential barrier to an adjacent QD [52, 53]. Annealing the QD films is one way to reduce the negative electrical effects of the ligands. However, the CTL would have to be replaced with a material set that can withstand the high temperatures required for annealing (> 100° C) [46].

4.5.2 TDBC J-aggregate dye/Zinc Indium Oxide Heterojunction Photoconductor

Cyanine dyes have traditionally been used to sensitize silver halides in photographic processing. Unlike most organic dye materials, this special class of dyes can form thin films that have very narrow emission and absorption spectra (~ 10 nm FWHM) and exhibit record high optical absorption coefficients (~ 10^6 cm^{-1}) in solid state [54].

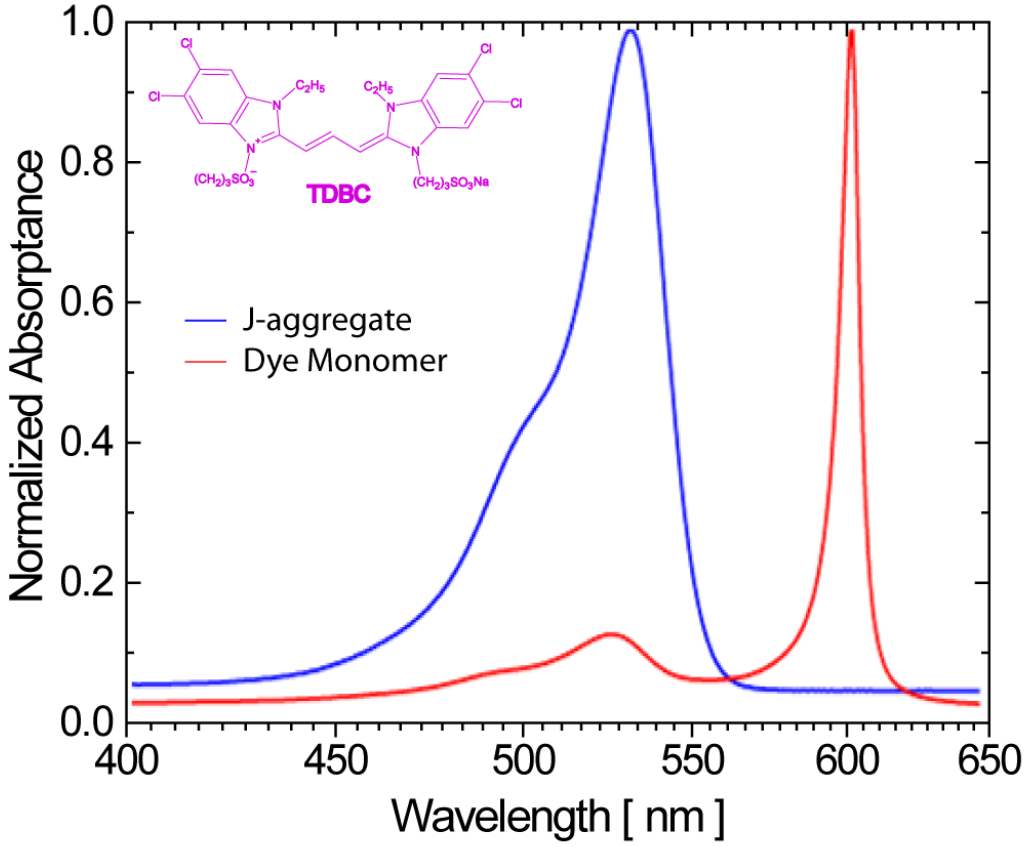

Figure 4-22: Absorption spectra of TDBC dye in monomer phase (blue) and J-aggregate phase (red). Inset: Chemical structure of TDBC dye.

The cyanine dyes aggregate in such a way that their transition dipoles align to form J-aggregates, which are aggregate states that have enhanced resonance in the J-band [Fig. 4-22]. We have used a well-characterized J-aggregating dye [5,6-dichloro-2-[3-[5,6-dichloro-1-ethyl-3-(3-sulfopropyl)-2(3H)-benzimidazolidene]-1-propenyl]-1-ethyl -3-(3-sulfopropyl) benzimidazolium hydroxide (inner salt, sodium salt from Nippon Kankoh Shikiso Kenkyusho Co., Ltd.) (TDBC), in conjunction with Zinc Indium Oxide (ZIO) as the CTL to fabricate bilayer photoconductors.

The TDBC film, acting as the EGL with peak absorption at $\lambda = 595$ nm [Fig. 4-22], was deposited using a layer-by-layer (LBL) process [55–57]. The sequential immersion of the substrate into cationic and anionic solutions allows the J-aggregate

to form highly absorptive films that contain only a few molecular layers. The cationic solution is a 30 mM solution of poly(diallyldimethylammoniumchloride) [(PDAC) obtained from Sigma Aldrich] in deionized water. The anionic solution is a 50 μM solution of the J-aggregating cyanine dye TDBC. Immersing the devices into aqueous solutions during fabrication necessitates the use of a CTL that is impervious to the solvent. A natural material for use as the CTL is a metal oxide, which typically has a wide bandgap (visibly transparent) and is mechanically robust (insoluble and high glass transition temperature).

The heterojunction photoconductor consists of interdigitated chrome/gold electrodes (20nm/50nm) on glass that form a serpentine channel with a width of 60 mm and a length of 10 μm. A 50 ± 0.5 nm RF-sputter-deposited film of the n-type metal oxide, ZIO (target obtained from Plasmaterials, Inc.) is deposited onto the electrodes before dip-coating a 5 ± 1 nm TDBC J-aggregate film. ZIO is a wide bandgap semiconductor whose absorption falls off quickly at wavelengths longer than $\lambda = 550$ nm [Fig. 4-23]. In order to reduce the conductivity of the metal oxide film to the range of the measurement equipment, the ZIO was grown in a 30% O2:70% Ar gas environment (filling the oxygen vacancies resulted in more resistive thin films of ZIO).

I-V measurements are shown in Figure 4-24(a) for a device consisting of a 5 ± 1 nm thick film of TDBC, a device consisting of a 50 ± 0.5 nm thick film of ZIO, and a bilayer ZIO/J-aggregate heterojunction device. While the carrier mobility in TDBC has not been measured, the photoconductor made with a single TDBC film (black) exhibits current levels below the ZIO device (blue). This would suggest that the ZIO (with a resistance of ~ 700 MΩ/□) would be primarily responsible for electrical conduction in the bilayer device. According to the absorption spectra of the materials used, amber LED illumination ($\lambda_{peak} = 590$ nm) is primarily absorbed by the J-aggregate [Fig. 4-23]. However, the low conductivity of the TDBC film yields low currents in both dark and light conditions (black lines). The ZIO device shows a small photoresponse as evident by comparing the blue solid line to the blue dashed line in Figure 4-24. This behavior is consistent with ZIO's absorption spectrum and its long decaying tail that extends across the visible spectrum. The greater than order of magnitude increase

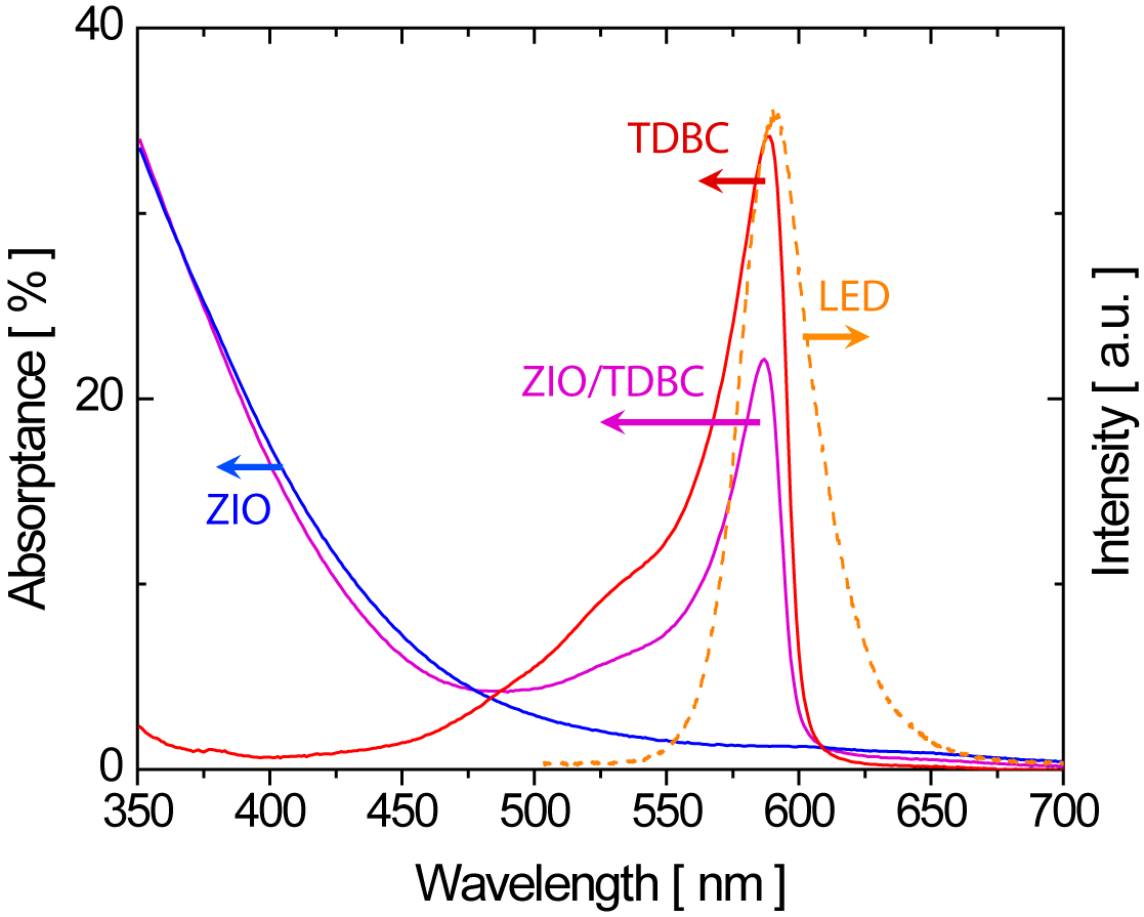

Figure 4-23: Absorption spectra of ZIO and TDBC films. Emission spectrum of amber LED centered at $\lambda = 595$ nm is also shown.

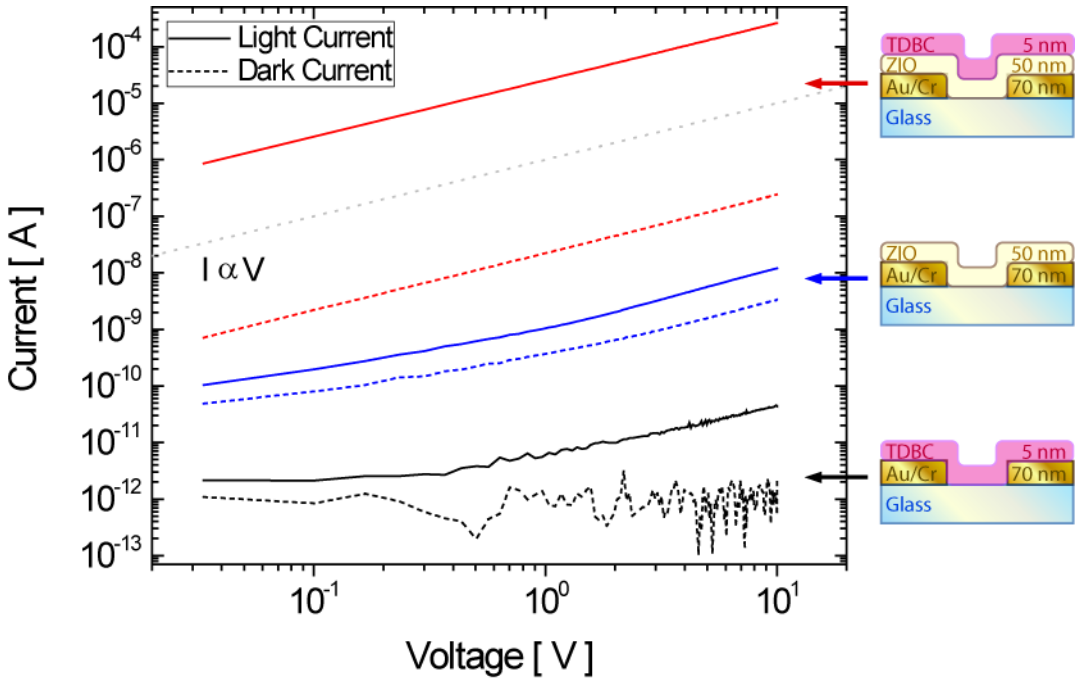

Figure 4-24: Log-log current-voltage characteristics for a series of devices containing ZIO and TDBC. I-V sweeps are collected under both light (solid) and dark (dashed) conditions. Illumination is provided by an amber LED (λ_{peak} = 595 nm). Inset cross-sectional diagrams detail device structures and film thicknesses.

in the dark current from the ZIO device (black dashed line) to the ZIO/J-aggregate bilayer device (blue dashed line) suggests charge transfer across the heterointerface and the creation of a Type-II heterojunction. Examining the red set of lines in Figure 4-24, it is clear that the photoresponse of the ZIO/J-aggregate has benefited from the presence of the interface (where efficient exciton dissociation can occur) as well as the higher conductivity in the underlying ZIO film. OLEDs were demonstrated with TDBC J-aggregate as the emitting layer [58], suggesting that TDBC has a lower electron affinity than the ZIO. Thus, as excitons are dissociated at the interface, electrons travel into the ZIO, while holes remain in the TDBC film.

These bilayer devices demonstrate a light-to-dark current ratio of over 1000, due to a high photocurrent. There are two possible factors that can contribute to this phenomenon, either carriers have a long lifetime or a short transit time. Measurements of the carrier lifetime [Fig. 4-25] yield a 90 μs decay time constant which is on the same order or slightly larger than that of the TPD/PTCBI devices for a given intensity.

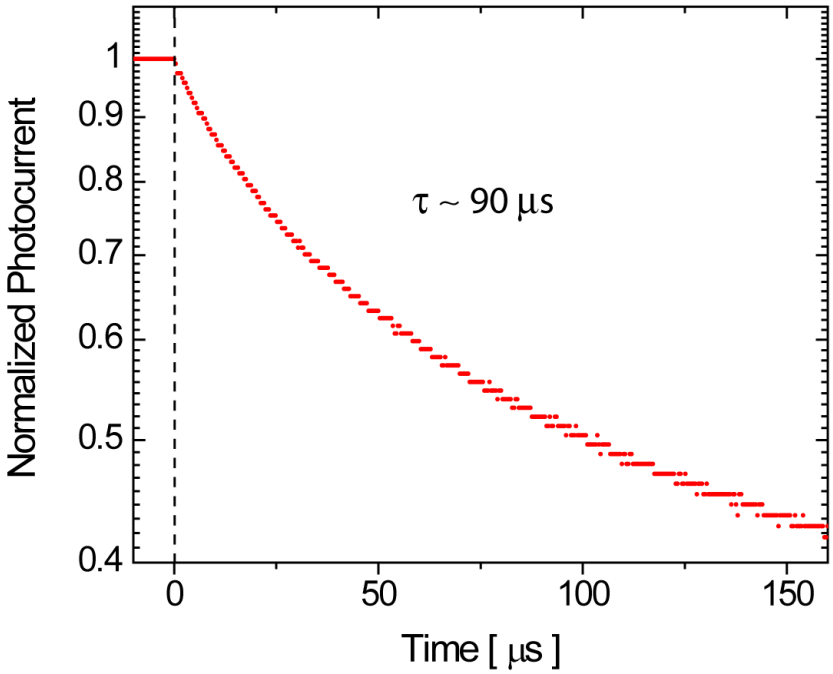

Figure 4-25: Plot of photocurrent decay for a 50.0 ± 0.5 nm ZIO/5.0 ± 0.5 nm TDBC bilayer heterojunction photoconductor. Illumination by an amber LED (λ_{peak} = 595 nm) is turned off at time t = 0 s.

Therefore, it must be that the good conductivity of ZIO and the favorable injection barrier (relative to TPD) keeps carrier transit times short and allows for multiple transits through the channel for every photoexcited carrier.

Figure 4-26 shows the EQE of the ZIO/TDBC device (red curve) at an applied field of 1x10^6 V/μm. The single film of TDBC yielded no measurable quantum efficiency due to the low intensity of the monochromatic illumination as well as the low conductivity of the film. The single film of ZIO (blue curve) exhibits significant photocurrent symbatic with its absorption spectrum. The bilayer device results in an EQE of c.a. 300% at the TDBC peak absorption wavelength. In addition, the ZIO's photoresponse is improved up to a factor of 50 over its absorption spectrum. The improvement in photoresponse of the bilayer device is a signature of efficient exciton dissociation at the Type-II heterojunction. The corresponding internal quantum efficiency (IQE) at λ = 590 nm is calculated to be over 2000%, consistent with a large photon-to-electron conversion gain and a much shorter transit time relative to carrier

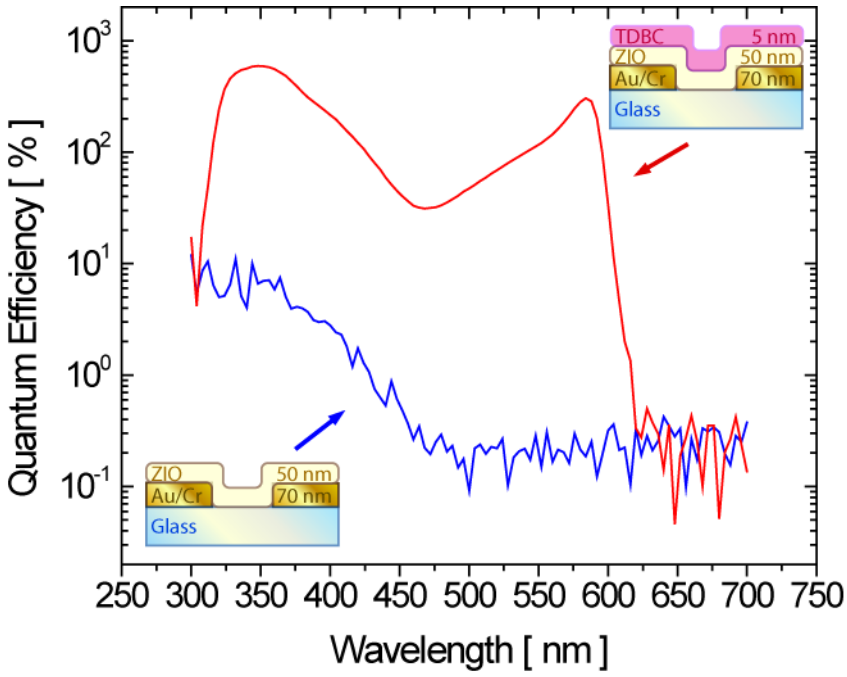

Figure 4-26: Spectral response data for a 50.0 ± 0.5 nm ZIO device and a 50.0 ± 0.5 nm ZIO/5.0 ± 0.5 nm TDBC bilayer device. Inset cross-sectional diagrams detail device structure and film thicknesses. An electric field of 1 x 10^6 V/μm is applied to both devices.

lifetime.

4.6 Summary

In this chapter we have focused on understanding the device physics of a heterojunction and a traditional single layer photoconductor. Understanding the role of both concepts in the bilayer heterojunction photoconductor is crucial to modeling device operation. The device model of the bilayer heterojunction photoconductor is based largely on existing models of photoconductor operation as well as heterojunction dynamics in solar cells. Experimental data collected from heterojunction photoconductors that incorporate a wide variety of material sets, have corroborated our models and yield further insight into pathways for optimization.

Chapter 4 References

[1] C. W Tang and S. A Vanslyke. Organic Electroluminescent Diodes. *Applied Physics Letters*, 51(12):913–915, 1987.

[2] T. Chakraborty and V. M. Apalkov. Quantum cascade transitions in nanostructures. *Advances in Physics*, 52(5):455, 2003.

[3] B. P. Rand, D. P. Burk, and S. R. Forrest. Offset energies at organic semiconductor heterojunctions and their influence on the open-circuit voltage of thin-film solar cells. *Physical Review B (Condensed Matter and Materials Physics)*, 75(11):115327–11, March 2007.

[4] P. Peumans and S. R Forrest. Separation of geminate charge-pairs at donor-acceptor interfaces in disordered solids. *Chemical Physics Letters*, 398:27–31, 2004.

[5] J. D. Wright. *Molecular Crystals*. Cambridge University Press, Cambridge, 2nd edition, 1987.

[6] W. R Salaneck, K. Seki, A. Kahn, and J. Pireaux. *Conjugated Polymer and Molecular Interfaces*. Marcel Dekker, Inc., New York, 2002.

[7] H. Ishii, K. Sugiyama, E. Ito, and K. Seki. Energy level alignment and interfacial electronic structures at Organic/Metal and Organic/Organic interfaces. *Advanced Materials*, 11(8):605–625, 1999.

[8] R. W. Strayer, W. Mackie, and L. W. Swanson. Work Function Measurements

by Field-emission Retarding Potential Method. *Surface Science*, 34(2):225–248, 1973.

[9] J. Hoelzel, F. K. Schulte, and H. Wagner. *Solid State Surface Physics*. Springer Verlag, Berlin, 1979.

[10] H. Ishii, K. Sugiyama, D. Yoshimura, E. Ito, Y. Ouchi, and K. Seki. Energy-level alignment at model interfaces of organic electroluminescent devices studied by UV photoemission: Trend in the deviation from the traditional way of estimating the interfacial electronic structures. *IEEE Journal of Selected Topics in Quantum Electronics*, 4(1):24–33, February 1998.

[11] E. Ito, H. Oji, H. Ishii, K. Oichi, Y. Ouchi, and K. Seki. Interfacial electronic structure of long-chain alkane/metal systems studied by UV-photoelectron and metastable atom electron spectroscopies. *Chemical Physics Letters*, 287(1-2):137–142, April 1998.

[12] A Rajagopal, CI Wu, and A Kahn. Energy level offset at organic semiconductor heterojunctions. *Journal of Applied Physics*, 83(5):2649–2655, March 1998.

[13] J. X. Tang, C. S. Lee, and S. T. Lee. Electronic structures of organic/organic heterojunctions: From vacuum level alignment to fermi level pinning. *Journal of Applied Physics*, 101(6):064504–4, March 2007.

[14] H. Ishii, N. Hayashi, E. Ito, Y. Washizu, K. Sugi, Y. Kimura, M. Niwano, Y. Ouchi, and K. Seki. Kelvin probe study of band bending at organic semiconductor/metal interfaces: examination of fermi level alignment. *Physica Status Solidi (A)*, 201(6):1075–1094, 2004.

[15] S. M. Sze and K. K. Ng. *Physics of Semiconductor Devices*. John Wiley & Sons, Hoboken, third edition, 2007.

[16] M. Pope and C. E Swenberg. *Electronic processes in organic crystals and polymers*. Oxford University Press, New York, 2nd edition, 1999.

[17] H. B. DeVore. Spectral distribution of photoconductivity. *Physical Review*, 102(1):86, April 1956.

[18] P. M Borsenberger and D. S. Weiss. *Organic photoreceptors for xerography*. Optical Engineering. Marcel Dekker, New York, 1998.

[19] A.J. Lewis, A. Ruseckas, O. P.M. Gaudin, G.R. Webster, P.L. Burn, and I.D.W. Samuel. Singlet exciton diffusion in MEH-PPV films studied by exciton-exciton annihilation. *Organic Electronics*, 7(6):452–456, December 2006.

[20] H. Alves, A. S. Molinari, H.. Xie, and A. F. Morpurgo. Metallic conduction at organic charge-transfer interfaces. *Nature Materials*, 7(7):574–580, July 2008.

[21] W. F. Pasveer, J. Cottaar, C. Tanase, R. Coehoorn, P. A. Bobbert, P. W. M. Blom, D. M. deLeeuw, and M. A. J. Michels. Unified description of Charge-Carrier mobilities in disordered semiconducting polymers. *Physical Review Letters*, 94(20):206601, May 2005.

[22] H. J. Snaith and M. Gratzel. Light-Enhanced charge mobility in a molecular hole transporter. *Physical Review Letters*, 98(17):177402–4, April 2007.

[23] C. Madigan and V. Bulovic. Solid state solvation in amorphous organic thin films. *Physical Review Letters*, 91(24):247403, 2003.

[24] C. Madigan and V. Bulovic. Modeling of exciton diffusion in amorphous organic thin films. *Physical Review Letters*, 96:046404, 2006.

[25] D. Cheyns, J. Poortmans, P. Heremans, C. Deibel, S. Verlaak, B. P. Rand, and J. Genoe. Analytical model for the open-circuit voltage and its associated resistance in organic planar heterojunction solar cells. *Physical Review B (Condensed Matter and Materials Physics)*, 77(16):165332–10, April 2008.

[26] C. L. Braun. Electric field assisted dissociation of charge transfer states as a mechanism of photocarrier production. *The Journal of Chemical Physics*, 80(9):4157–4161, May 1984.

[27] J. Nelson, J. Kirkpatrick, and P. Ravirajan. Factors limiting the efficiency of molecular photovoltaic devices. *Physical Review B*, 69(3):035337, 2004.

[28] M. M. Mandoc, F. B. Kooistra, J. C. Hummelen, B. de Boer, and P. W. M. Blom. Effect of traps on the performance of bulk heterojunction organic solar cells. *Applied Physics Letters*, 91(26):263505–3, December 2007.

[29] M. M. Mandoc, W. Veurman, L. J.A. Koster, B. deBoer, and P. W. M. Blom. Origin of the reduced fill factor and photocurrent in MDMO-PPV:PCNEPV All-Polymer solar cells. *Advanced Functional Materials*, 17(13):2167–2173, 2007.

[30] P. Peumans, A. Yakimov, and S. R. Forrest. Small molecular weight organic thin-film photodetectors and solar cells. *Journal of Applied Physics*, 93(7):3693–3723, 2003.

[31] S. B. Rim, R. F. Fink, J. C. Schoneboom, P. Erk, and P. Peumans. Effect of molecular packing on the exciton diffusion length in organic solar cells. *Applied Physics Letters*, 91(17):173504–3, October 2007.

[32] B. P. Rand, J. Xue, S. Uchida, and S. R. Forrest. Mixed donor-acceptor molecular heterojunctions for photovoltaic applications. i. material properties. *Journal of Applied Physics*, 98(12):124902–7, December 2005.

[33] F. Celii, T. Harton, and O. F. Phillips. Characterization of organic thin films for OLEDs using spectroscopic ellipsometry. *Journal of Electronic Materials*, 26(4):366–371, April 1997.

[34] M. D. Tabak and P. J. Warter. Sublinear photocurrents and surface recombination in cadmium sulfide crystals. *Physical Review*, 148(2):982, 1966.

[35] M. Brinza, J. Willekens, M. Benkhedir, E. Emelianova, and G. Adriaenssens. Photoconductivity methods in materials research. *Journal of Materials Science: Materials in Electronics*, 16(11):703–713, November 2005.

[36] N. M. Haegel, D. R. Palmieri, and A. M. White. Current transients in extrinsic photoconductors: comprehensive analytical description of initial response. *Applied Physics A: Materials Science & Processing*, 73(4):433–439, October 2001.

[37] D. A. Redfern, C. A. Musca, E. P. G. Smith, J. M. Dell, and L. Faraone. On the transient photoconductive decay technique for lifetime extraction in HgCdTe. In *Optoelectronic and Microelectronic Materials Devices, 1998. Proceedings. 1998 Conference on*, pages 275–278, 1998.

[38] J. S. Steckel, S. Coe-Sullivan, V. Bulović, and M. G. Bawendi. 1.3 um to 1.55 um tunable electroluminescence from PbSe quantum dots embedded within an organic device. *Advanced Materials*, 15(21):1862–1866, 2003.

[39] E. H. Sargent. Infrared quantum dots. *Advanced Materials*, 17(5):515–522, 2005.

[40] T. P. I. Saragi and J. Salbeck. Organic heterostructure field-effect transistors using C_{60} and amorphous spirolinked compound. *Applied Physics Letters*, 89(25):253516–3, December 2006.

[41] D. Yu, C. Wang, and P. Guyot-Sionnest. n-Type conducting CdSe nanocrystal solids. *Science*, 300(5623):1277–1280, May 2003.

[42] T. P. Osedach, S. M. Geyer, J. C. Ho, A. C. Arango, M. G. Bawendi, and V. Bulovic. Lateral heterojunction photodetector consisting of molecular organic and colloidal quantum dot thin films. *Applied Physics Letters*, 94(4):043307–3, 2009.

[43] T. P. I. Saragi, T. Fuhrmann-Lieker, and J. Salbeck. Comparison of Charge-Carrier transport in thin films of Spiro-Linked compounds and their corresponding parent compounds. *Advanced Functional Materials*, 16(7):966–974, 2006.

[44] A. L. Efros and M. Rosen. The Electronic Structure of Semiconductor Nanocrystals. *Annual Review of Materials Science*, 30, November 2003.

[45] T. C. Chiang and F. J. Himpsel. *Electronic Structure of Solids: Photoemission Spectra and Related Data*, volume 23 of *New Series*. Springer-Verlag Berlin, Berlin, 1989.

[46] M. V. Jarosz, V. J. Porter, B. R. Fisher, M. A. Kastner, and M. G. Bawendi. Photoconductivity studies of treated CdSe quantum dot films exhibiting increased exciton ionization efficiency. *Physical Review B*, 70(19):195327, November 2004.

[47] J. J. Yu. *Improving OLED Technology for Displays*. Ph.D. thesis, MIT, 2008.

[48] J. C Martins, I. Moreels, and Z. Hens. Solution NMR spectroscopy as a useful tool to investigate colloidal nanocrystal dispersions from the capping ligand's point of view. In *2006 MRS Fall Proceedings*, volume 984, 2006.

[49] M. A. Lampert. Simplified theory of Space-Charge-Limited currents in an insulator with traps. *Physical Review*, 103(6):1648, 1956.

[50] A. Rose. Recombination processes in insulators and semiconductors. *Physical Review*, 97(2):322, 1955.

[51] A. K Ghosh and T. Feng. Merocyanine Organic Solar-Cells. *Journal of Applied Physics*, 49(12):5982–5989, 1978.

[52] C. A. Leatherdale, C. R. Kagan, N. Y. Morgan, S. A. Empedocles, M. A. Kastner, and M. G. Bawendi. Photoconductivity in CdSe quantum dot solids. *Physical Review B*, 62(4):2669, July 2000.

[53] A. Franceschetti and A. Zunger. Exciton dissociation and interdot transport in CdSe quantum-dot molecules. *Physical Review B*, 63(15):153304, March 2001.

[54] M. S. Bradley, J. R. Tischler, and V. Bulović. Layer-by-Layer J-Aggregate thin films with a peak absorption constant of 10^6 cm^{-1}. *Advanced Materials*, 17(15):1881–1886, 2005.

[55] H. Fukumoto and Y. Yonezawa. Layer-by-layer self-assembly of polyelectrolyte and water soluble cyanine dye. *Thin Solid Films*, 327-329:748–751, August 1998.

[56] M. Kawasaki, T. Sato, and T. Yoshimoto. Controlled layering of Two-Dimensional J-Aggregate of anionic cyanine dye on Self-Assembled cysteamine monolayer on au(111). *Langmuir*, 16(12):5409–5417, June 2000.

[57] C. Peyratout and L. Daehne. Aggregation of thiacyanine derivatives on polyelectrolytes. *Physical Chemistry Chemical Physics*, 4(13):3032–3039, 2002.

[58] J. R. Tischler, M. S. Bradley, V. Bulovic, J. H. Song, and A. Nurmikko. Strong coupling in a microcavity LED. *Physical Review Letters*, 95(3):036401, July 2005.

Chapter 5

Multilayer Heterojunction Photoconductors

It is through science that we prove, but through intuition that we discover.

JULES HENRI POINCARE
Mathematician/Physicist

Having detailed the carrier dynamics and processes that take place at the herointerface of the bilayer photoconductors, we turn our focus now towards modifying those same processes to engineer better device performance. Because gain is linearly dependent on carrier lifetime, we must look for methods of limiting the possibility of carrier recombination processes at the interface in order to fabricate devices with higher photocurrents. Detailing a number of different device architectures used to manipulate carrier lifetimes will help to motivate the use of multiple layers in the heterojunction devices.

5.1 Quantum Well in an Electric Field

During the 1980's inorganic multiple quantum well (MQW) structures were receiving considerable attention for enabling the ability to engineer their photoluminescent

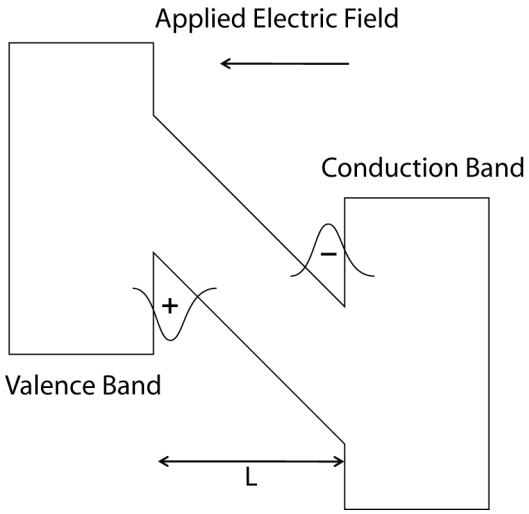

Figure 5-1: Schematic of energy bands and wavefunctions of electrons and holes in a quantum well under an applied electric field.

properties by varying barrier heights and widths, which would allow for the creation of solid-state lasers and LEDs. Around this time it was demonstrated that an applied electric field perpendicular to the layers defining the quantum well could decrease or completely quench the luminescence associated with the MQW structure [1]. This phenomenon was originally associated with field induced separation between the electrons and holes in the quantum well [2]. Thus, increasing the well width significantly decreases luminescence [Fig. 5-1]. However, this initial model neglected the effect of free carrier density and the ability of free charge to screen the applied electric field. A study which detailed the effect of injection current on the recombination rate in a quantum well [3], found that at much higher carrier densities the free-carrier-induced field acted to cancel the applied electric field, which causes the separation of electrons and holes to have a much weaker dependence on the applied field.

5.2 n-i-p-i Structures

In photodetection, the creation of luminescence through recombination represents a loss mechanism to the extracted photocurrent. Thus, one method of improving photocurrent levels in a photodetector is to reduce the bimolecular recombination rate

by physically separating the electrons and holes. One particular class of engineered material that accomplishes this separation is the n-i-p-i crystal. n-i-p-i crystals refer to doped superlattices where periodic n- and p-doping can be used to tune various material properties. The basic idea of doping superlattices is to create a periodic energy band modulation in real space. This is accomplished by growing alternating layers with opposite polarity of dopant. One commonly used scheme to create n-i-p-i crystals is to fabricate a series of alternating homogeneous doped n and p layers. In this case, the intrinsic regions consist of the space-charge regions between the layers due to depletion region formation. Undoped layers can be grown between the two doped layers in order to increase the intrinsic regions. In the most extreme case, intrinsic layers are separated by monolayers of doped semiconductor (also known as δ-doping), which creates a sawtooth potential profile [4, 5].

One benefit of the n-i-p-i architecture is the built-in potential modulation [Fig. 5-2], which leads to a spatial separation of photogenerated electron-hole pairs and thus to a drastic enhancement of the excess carrier lifetime as compared to the bulk semiconductor. This separation can be made nearly perfect by appropriate choice of doping concentrations and layer thicknesses. According to Dohler [6], there are two mechanisms that limit the lifetime in a p-i-n structure: tunneling through the potential barrier due to the quantum mechanical overlap of the electron and hole wave functions, and thermal excitation across the potential barrier so that electrons and holes can meet. Due to the overlap of the electron and hole wavefunctions photon absorption is also possible for photon energies less than the bandgap.

One particular device architecture that has emerged from this class of structures is the p-i-n photodiode. The p-i-n photodiode consists of an insulating film sandwiched between a p-type doped film and an n-type doped film. This architecture physically extends the width of the depletion region (where excitons can be dissociated by the electric field) thereby increasing the area available for capturing light [7]. The p-i-n photodiode has a number of benefits over the p-n photodiode. Increasing the width of the depletion layer reduces junction capacitance and therefore the associated time response. However, the transit time of photogenerated carriers increases with the

width of the depletion region.

Recently, Sista et. al. reported using an interfacial layer between the donor and acceptor layers of an organic solar cell to increase open circuit voltage [8]. In that work, the interfacial layer is used to create a pair of new interfaces where the HOMO-LUMO offsets are much greater between the interfacial layer and the donor (or acceptor) material as compared with the donor-acceptor HOMO-LUMO offset in the original bilayer cell. While it is widely accepted that open circuit voltage is solely due to the difference between the HOMO of the donor and the LUMO of the acceptor [9], this is only the case when recombination is high [10]. Work done by Arango et. al. demonstrated record-high open circuit voltages in nanostructured solar cells incorporating CdSe quantum dots [11]. In this case, the organic ligands that passivate the nanocrystals are believed to prevent bimolecular recombination across the interface between the CdSe QDs and the organic transport material. By reducing the recombination rate at the interface, charge carriers must tunnel through or hop over the barrier posed by the capping groups in order to recombine on the quantum dots, yielding open circuit voltages that are close to the actual band gap of the CdSe (~ 1.5 eV). This work suggests the use of interfacial layers to reduce interfacial recombination rates relative to charge transfer at the interface, providing an experimental mechanism to enhance device efficiency.

5.3 Trilayer Photoconductor Model

Having delineated the benefits of physically separating free carriers to extend their lifetimes, and the use of an interfacial layer to achieve that separation, a new class of trilayer heterojunction photoconductors can be conceived of and fabricated. This multilayer architecture extends the bilayer device by introducing an interfacial layer to form a cascading energy band structure.

Neglecting the effects of interfacial dipoles, it becomes feasible to engineer novel trilayer devices based on the band energies of individual organic materials. These devices would ideally consist of an exciton generation layer (EGL), a charge spacer

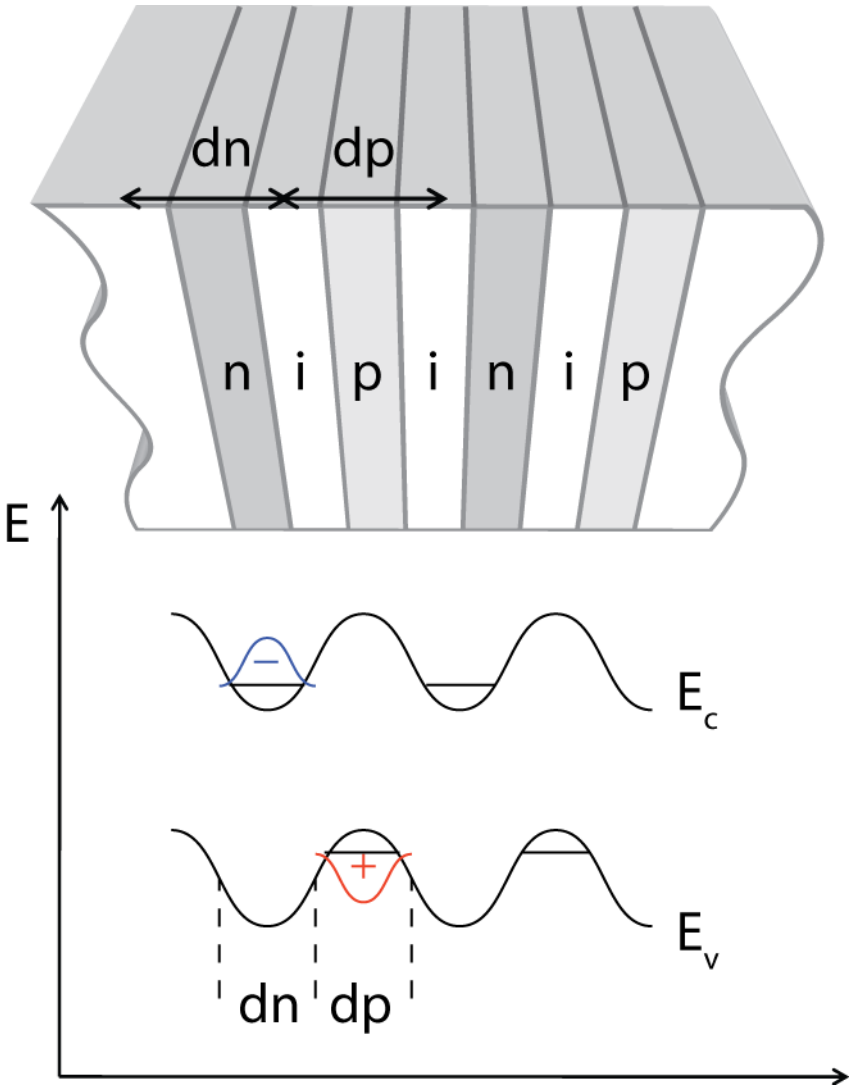

Figure 5-2: Schematic of a n-i-p-i doping superlattice. Space charge regions between the doped slices creates insulating zones. The conduction and valence band edges modulate parabolically with spatially separated electron and hole wavefunctions in their ground states.

layer (CSL), and a charge transport layer (CTL). In devising a working model for device operation, it is useful to start with the energy bands of a bilayer and illustrate all of the possible carrier interactions and decay pathways [Fig. 5-3(a)]. Figure 5-3(b) depicts the same structure with a CSL acting to separate the charge carrier populations over its thickness. In order for the introduced interfacial layer to have the intended effect of increasing carrier lifetimes by reducing the recombination rate across the donor-acceptor interface, the change in that loss mechanism must be greater than the sum of the new loss pathways. In other words, $k_{CTL-CSL} + k_{CSL-EGL} < k_{CTL-EGL}$ so that the dominant recombination pathway is across the thickness of the CSL. This rate should be reduced relative to the bilayer case due to the smaller overlap of the carrier wavefunctions. Because the interfacial recombination rates are dependent on the carrier concentrations that are built up on either side of the interface, k_e and k_h should be greater than zero to ensure the previous assertion. These rates are diffusion-limited and therefore will be highly dependent on the thickness of the CSL. Thus, there will be an optimum thickness above which carriers can no longer diffuse across the thickness of the CSL, resulting in bilayer operation between the CSL/EGL and CTL/CSL interfaces. This crude model captures the larger, qualitative trends we expect to observe. However, it also neglects the availability of other energetically favorable states (i.e. triplet excitons) that may play a significant role in experimental observation of the recombination rates.

5.4 Experiments

While simulations can provide useful guidelines to inform the choice of materials to use in fabricating the trilayer heterojunction photoconductors, simplifying assumptions (such as complete, homogeneous, trap-free films, no interface dipole formation, etc.) must be made to yield reasonable computation times. As the experimental results below will show, these ideal film properties are much more difficult to realize in practice. Chemical structures of all of the materials used in the trilayer experiments can be found in Figure 5-4.

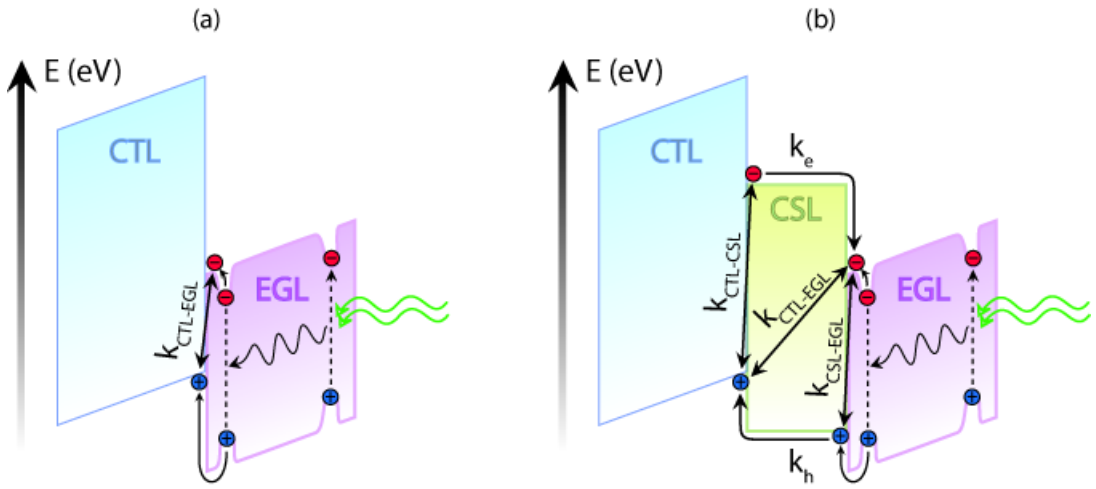

Figure 5-3: Energy band diagrams of (a) a bilayer device consisting of CTL/EGL and (b) a trilayer device consisting of CTL/CSL/EGL. Relevant interfacial recombination rates and carrier diffusion rates are depicted.

5.4.1 Cascading Energy Bands

The first set of experiments involves the use of materials which are likely to form a cascading set of energy bands. For consistency with the previous bilayer data, all of the following trilayer structures make use of TPD as CTL and PTCBI as EGL. Due to the inherent uncertainty in photoemission measurements of energy bands (± 0.1 eV) and the dependence of the energy levels on morphology and deposition conditions [12], the isolated HOMO/LUMO levels in vacuum are used as a starting point for engineering trilayer devices.

TPD/Alq_3/PTCBI Trilayer

Tris(8-hydroxyquinolinato)aluminum(III) (Alq_3) is commonly used as a green emitting layer in OLEDs and was part of the first demonstration of an efficient OLED, along with TPD [13]. The isolated energy bands of the individual materials are depicted in Figure 5-5, which shows a cascade in energy bands and justifies the use of Alq_3 as CSL. Optically, the introduction of Alq_3 plays little role in the absorption characteristics of the device. The CSL is typically much thinner than either the CTL or the EGL making the absorption of the CSL negligible relative to the other films in the device. The absorption spectra of the materials also indicate that the use of

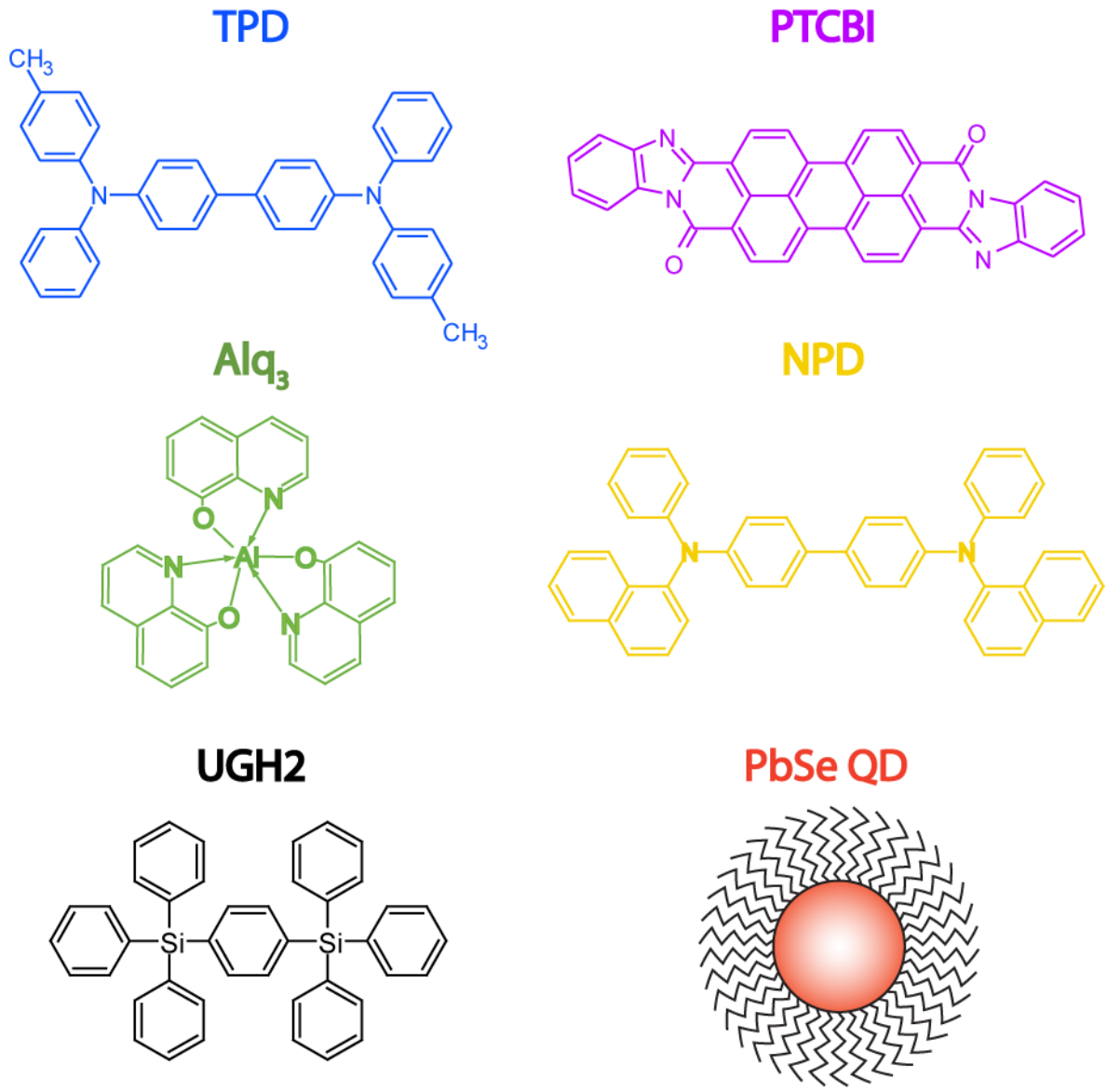

Figure 5-4: Chemical structures of materials used in trilayer devices. Clockwise from top-left corner: N,N'-bis(3-methylphenyl)-N,N'-diphenyl-1,1'-biphenyl-4,4'-diamine (TPD), 3,4,9,10-perylenetetracarboxylic bis-benzimidazole (PTCBI), N,N'-diphenyl-N,N'-bis(1-naphthyl)-1,1'-biphenyl-4,4"-diamine (α-NPD), oleic acid-capped lead selenide quantum dot (4.7 nm PbSe QD), p-bis(triphenylsilyl)benzene (UGH2), tris (8-hydroxyquinolinato) aluminum(III) (Alq_3).

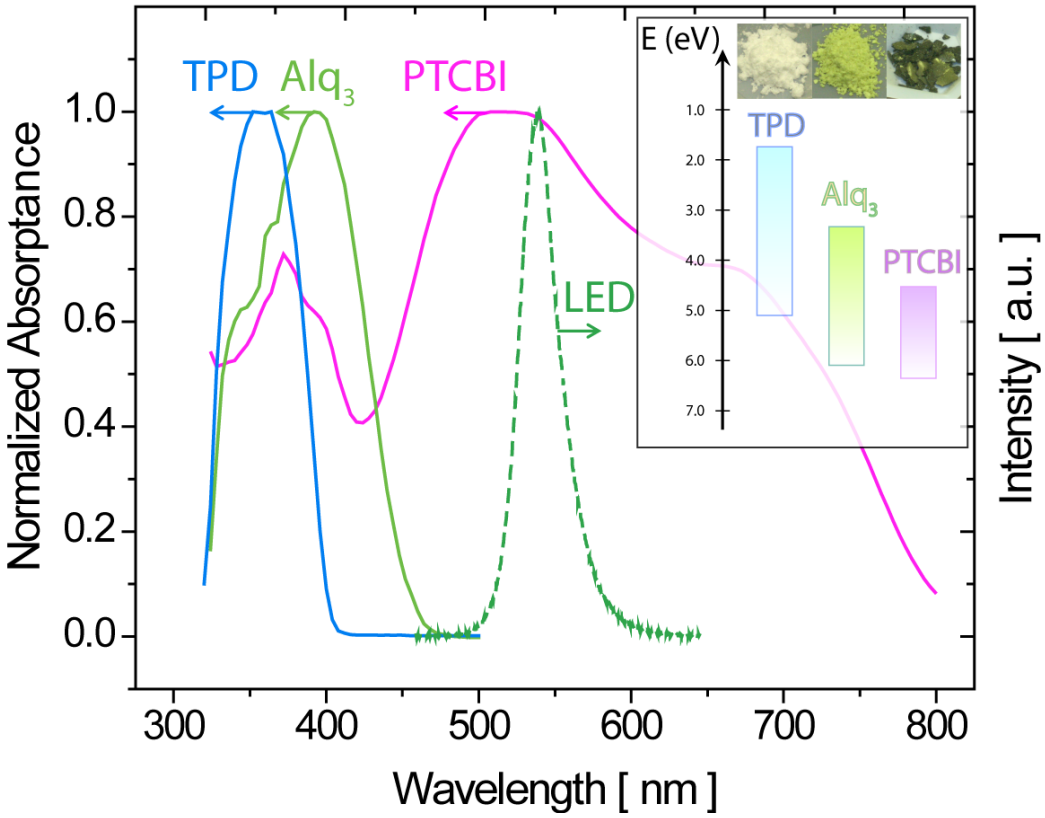

Figure 5-5: Absorption spectra of TPD, Alq_3, and PTCBI films (50 nm thick). The green LED emission spectrum (λ_{peak} = 532 nm), operated at an intensity of 40 mW/cm^2, is included for reference (dashed line). Inset: Suggested energy bands of TPD [14], Alq_3 [15], and PTCBI [16] based on photoemission spectroscopy data and optical bandgaps and digital images of materials in purified, powder form.

a green LED will continue to predominantly excite the PTCBI film [Fig. 5-5]. AFM images [Fig. 5-6] demonstrate good wetting characteristics of the materials following deposition, which ensures complete thin film formation.

The simulations above suggested that there would be an improvement in the photocurrent characteristics of the trilayer devices (relative to the bilayer) with similar energy band alignment as that of the TPD/Alq_3/PTCBI devices used in the experiments. However, after conducting several independent device trials, no clear trend emerged in the photocurrent. Figure 5-7 compiles the results of nine different device runs, where the Alq_3 thickness was varied over a wide range of thicknesses. All of the values were obtained with the same applied electric field (10 V/μm) and have been plotted relative to the quantum efficiency of the bilayer device (control) for that par-

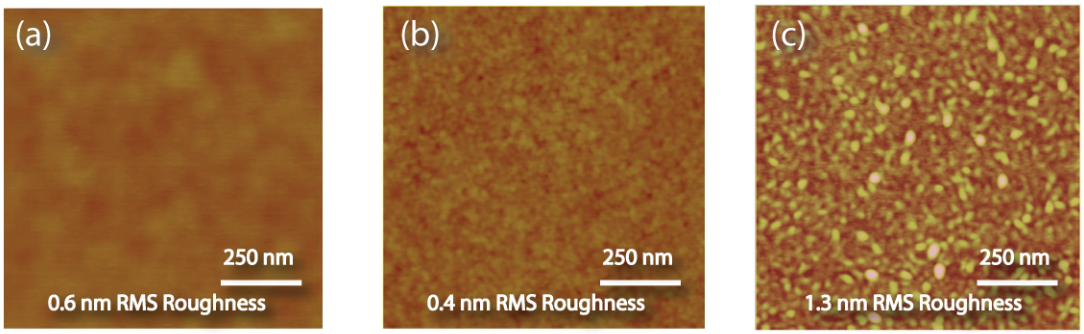

Figure 5-6: Set of AFM images of various films consisting of (a) 50 ± 0.5 nm TPD (b) 50 ± 0.5 nm of TPD/6.0 ± 0.5 nm Alq_3 (c) 50 ± 0.5 nm TPD/6.0 ± 0.5 nm Alq_3/50 ± 0.5 nm PTCBI. All images have same height range of 5 nm. Low RMS roughness in all cases suggests good wetting properties of deposited films.

ticular device trial, near the PTCBI absorption peak ($\lambda = 532$ nm). In addition, all devices were tested in a nitrogen-ambient environment to prevent device degradation during testing.

Individual current-voltage characteristics of the TPD/Alq_3/PTCBI devices varied significantly in magnitude and curvature, making it difficult to assess the conduction mechanisms. However, aggregating the current-voltage characteristics of the various trilayer devices reveals an observable trend of increased dark current [Fig. 5-8]. This evidence indicates charge transfer across either the TPD/Alq_3 or Alq_3/PTCBI interface. Comparison of the dark current levels of the trilayer device with those of a bilayer consisting of TPD/Alq_3 suggests that much of the charge transfer occurs at that interface.

In order to explain the wide variation in the observed device characteristics, we have to take a closer look at Alq_3. The electrical characteristics of organic devices are strongly determined by the inter- and intramolecular charge transport mechanisms, which are influenced strongly by the orientation and packing of the deposited molecules. Thus, the variation in observed current values can mainly be explained by the lack of control over a number of important parameters during deposition of Alq_3.

Although Alq_3 is a well characterized material, it has a number of unique properties that can significantly affect morphological, optical, and electrical film characteristics. Alq_3 is calculated to have a strong, permanent dipole moment of 4.1 D

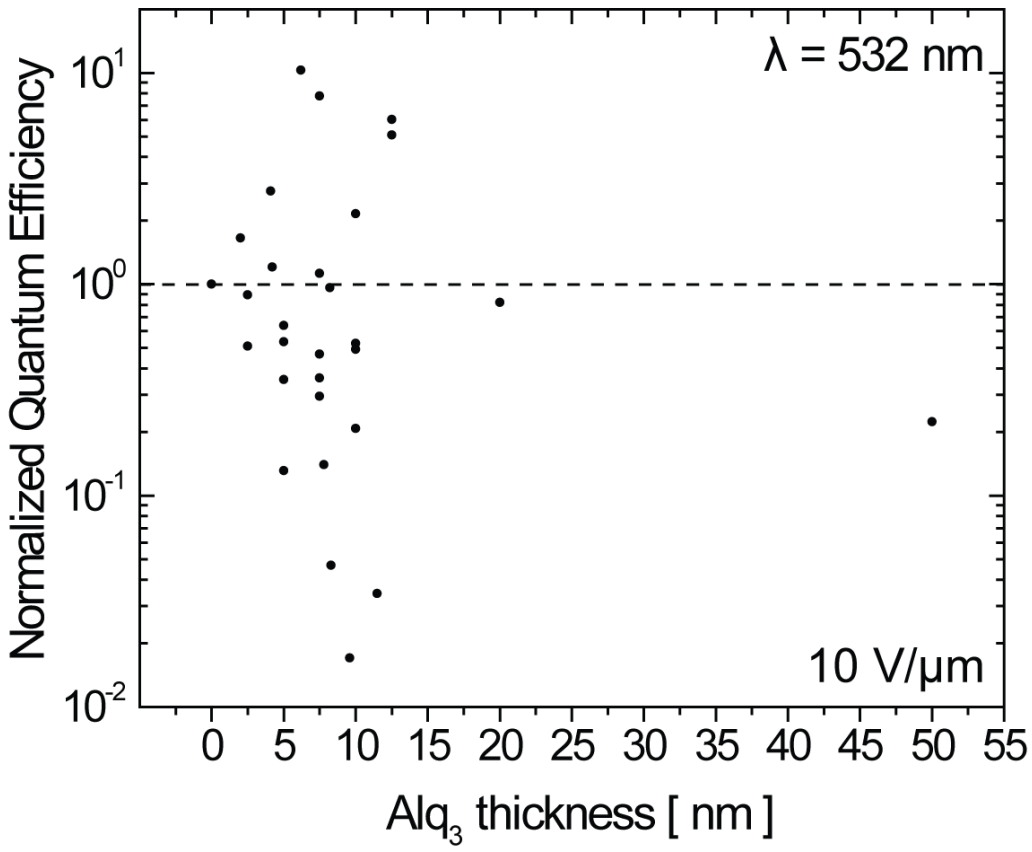

Figure 5-7: Scatter plot of nine separate trilayer device trials consisting of 50 ± 0.5 nm TPD/Alq_3/50 ± 0.5 nm PTCBI, with varying Alq_3 thickness. Quantum efficiency is plotted versus the thickness of Alq_3 and suggests no definite trend. All quantum efficiencies are obtained with the same applied field and wavelength and normalized to the control (bilayer device) of that particular device trial.

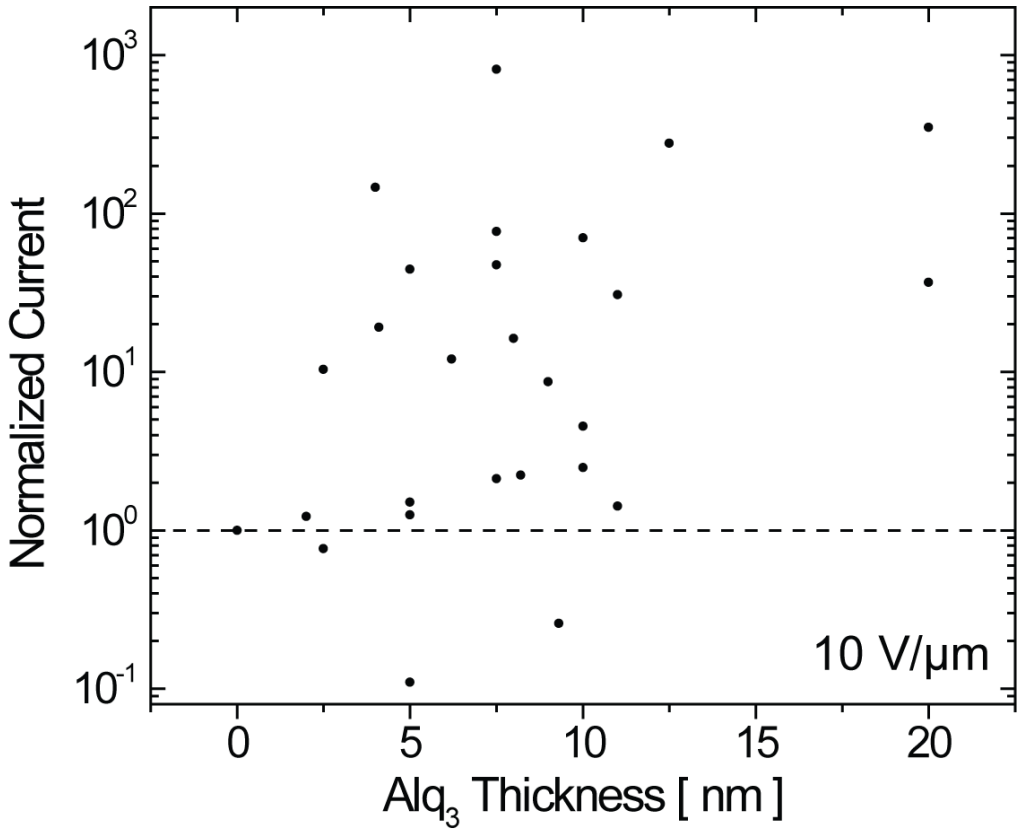

Figure 5-8: Scatter plot of eight separate trilayer device trials consisting of 50 ± 0.5 nm TPD/Alq_3/50 ± 0.5 nm PTCBI, with varying Alq_3 thickness. Dark current is plotted versus Alq_3 thickness and suggests an overall increase due to the presence of Alq_3. All current levels are obtained at the same applied field and are plotted relative to the current levels of the bilayer (control) device for that particular device trial.

and 7.1 D for its two geometric isomeric forms: meridional and facial, respectively [17]. These properties can result in amorphous films with a net polarization and significant concentrations of electron traps. Previous studies have demonstrated the ability of light irradiation to have a significant effect on the orientation of deposited Alq_3 molecules, which can influence the energy level alignment of Alq_3 relative to a metal electrode [14]. It has been theorized that this effect is due to depolarization of the molecules after photon absorption (i.e. rotation of the excited state or formation of paired molecules whose dipoles cancel). In addition, substrate temperature has been shown to have a substantial effect on the RMS roughness and conductivity of amorphous, vacuum-sublimated Alq_3 [18, 19]. There is no substrate temperature or light control for the deposition chambers used in our experiments; the only variable parameters are power delivered to the crucible (i.e. deposition rate) and chamber pressure. Thus, it becomes highly likely that the deposited Alq_3 films will present varying electrical and optical properties and varying interfacial dipole formation between TPD and PTCBI from run to run. The inconsistency of measured current levels in devices incorporating Alq_3 necessitates the use of a less reactive, non-polar material to form the cascading trilayer photoconductor.

TPD/NPD/PTCBI Trilayer

NPD is another well characterized material [20–23] that has a similar chemical structure to TPD, finding use as a hole transport and electron blocking layer in efficient OLED structures [24, 25]. Given NPD's wide bandgap, it is optically transparent to illumination with a green LED [Fig. 5-9]. In addition, the cascading energy band alignment formed from the introduction of NPD makes it a good candidate for the trilayer devices. Although AFM data of NPD deposited on TPD was not obtained, the similarities in chemical structure between the two materials suggests that a thin film of TPD would present a similar free surface energy to deposited NPD molecules as a thin film of NPD [26, 27]. Because evaporated molecules prefer to stick together to form clusters, we can estimate that NPD will exhibit good wetting behavior when deposited on TPD [28, 29].

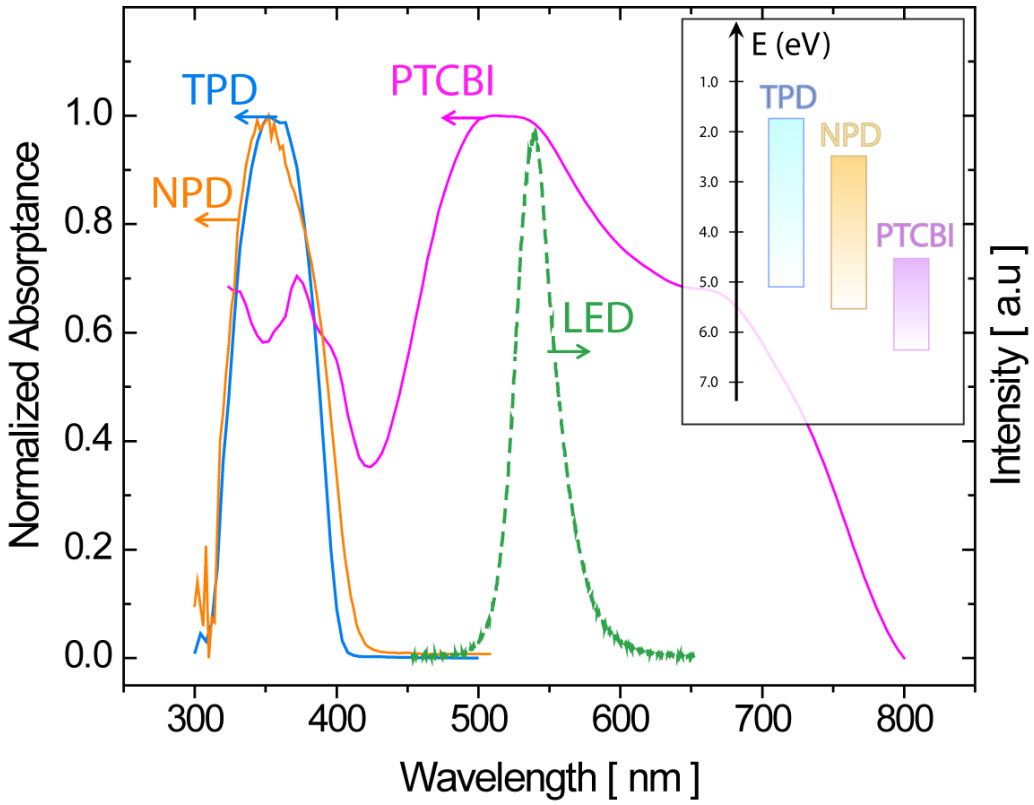

Figure 5-9: Absorption spectra of TPD, NPD, and PTCBI (50 nm thick). The green LED emission spectrum (λ_{peak} = 532 nm), operated at an intensity of 40 mW/cm^2, is included for reference (dashed line). Inset: Suggested energy bands of TPD [14], NPD [15], and PTCBI [16] based on photoemission spectroscopy data and optical bandgaps.

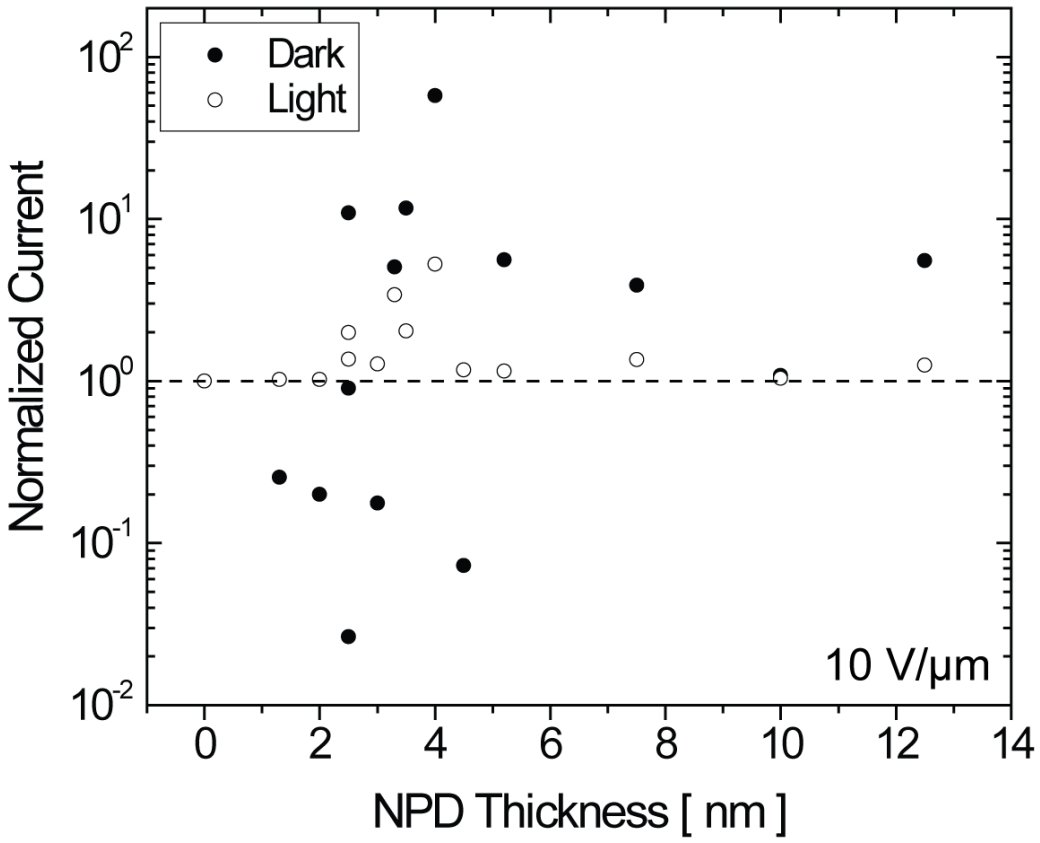

Figure 5-10: Log-log current-voltage characteristics of 50 ± 0.5 nm TPD/NPD/50 ± 0.5 nm PTCBI, with 0, 3.5, and 4 ± 0.5 nm of NPD. Arrows indicate increasing NPD thickness and dashed red lines are guides that depict ohmic and trap-limited conduction.

Figure 5-10 shows the current-voltage characteristics of a series of 50 ± 0.5 nm TPD/NPD/50 ± 0.5 nm PTCBI trilayer devices with varying NPD film thickness. The 50 ± 0.5 nm TPD/50 ± 0.5 nm PTCBI bilayer device exhibits the lowest current levels and demonstrates a dark current transition from ohmic conduction to trap-charge-limited conduction at applied fields greater than 30 V/μm. Introduction of a 3.5 ± 0.5 nm NPD film as CSL, raises the dark current by up to two orders of magnitude relative to the bilayer device, indicating strong charge transfer across the interfaces. However, the light current exhibits a moderate factor of 2 increase. Increasing the thickness of the NPD to 4.0 ± 0.5 nm yields another factor of 2 increase in both light and dark current over the trilayer device with 3.5 ± 0.5 nm of NPD.

Figure 5-11 compiles the dark and light current values for several trilayer device trials of varying NPD thickness at an applied field of 10 V/μm. All of the values are normalized to the bilayer device current values for that particular trial. As projected by the simulations, there is an optimum NPD thickness as evidenced by the peak in light current near 4 nm. The increase in light current due to increasing NPD thickness is attributed to the separation of free carriers at the interface, which will reduce recombination. However, when the NPD is too thick the free holes can no longer diffuse to the TPD/NPD interface and the resulting device characteristics will resemble that of a bilayer between NPD/PTCBI.

The relative dark current levels vary widely and do not show any observable trend. This is again likely due to our inability to adequately control the film deposition process. The distribution of trap states in the devices will largely affect the bilayer dark current as there are not enough injected carriers to populate all of the traps over the range of applied electric fields. Thus, the ratio of the trilayer dark currents to the bilayer currents will be sensitive to changes in trap distribution, which are largely a result of the deposition process.

More evidence supporting the positive influence of a CSL on photocurrent levels can be found by measuring the spectral response of the trilayer devices. Figure 5-12 displays the relative external quantum efficiency values at both the TPD and PTCBI absorption peaks (λ = 368 nm and 532 nm, respectively) for various bias voltages. The increase in photoresponse with increasing NPD thickness is consistent with the data obtained in the steady-state current-voltage characteristics. It is also important to note that increase in photoresponse due to increasing NPD thickness is more pronounced with larger applied electric fields. The optimum NPD thickness represented by the peak in EQE shifts from 4.5 nm at 10 V/μm to 4.0 nm at 20 and 30 V/μm.

5.4.2 Alternate Energy Band Alignments

In the previous section we demonstrated a trilayer heterojunction photoconductor with cascading energy bands. However, there remain other energy band alignments

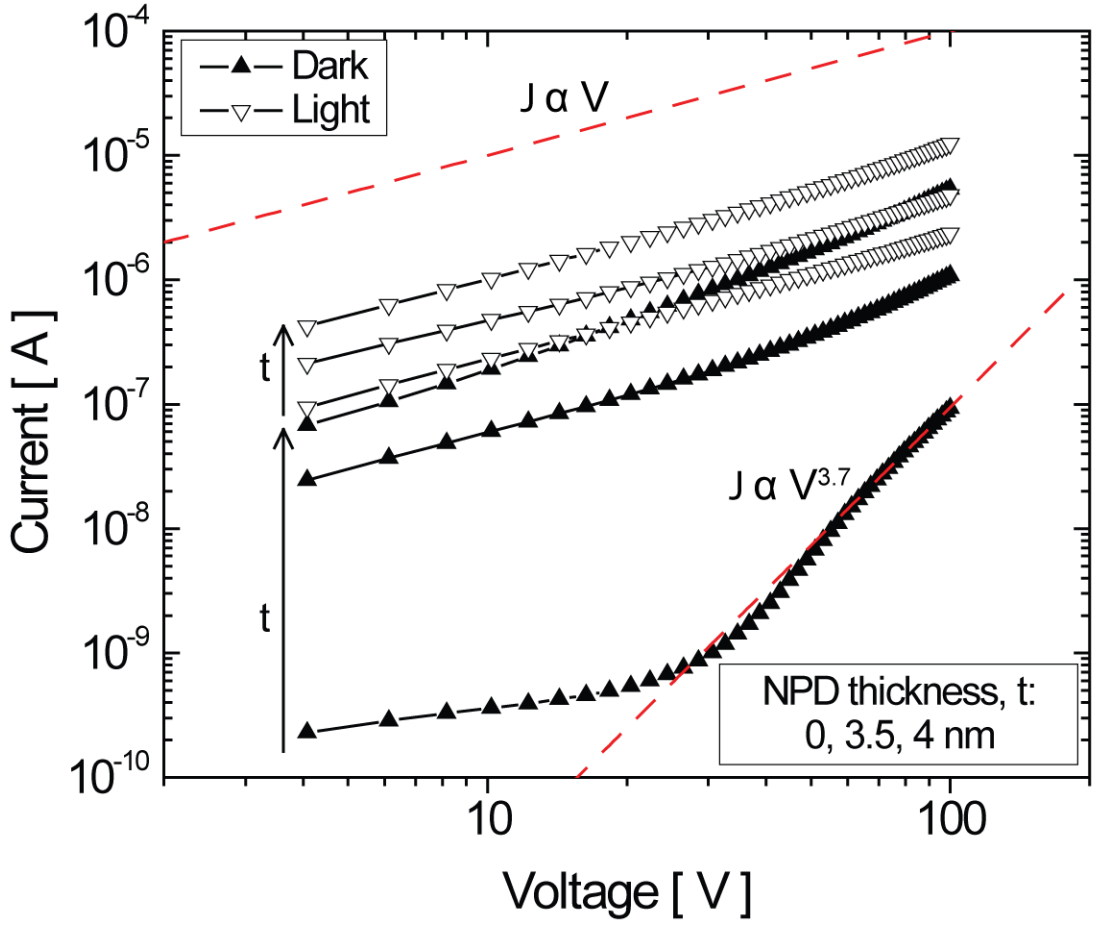

Figure 5-11: Scatter plot of three separate trilayer device trials consisting of 50 ± 0.5 nm TPD/NPD/50 ± 0.5 nm PTCBI, with varying NPD thickness. Light current (▽) is plotted versus NPD thickness and suggests an overall increase due to the presence of NPD up to 4 nm. All current levels are obtained at the same applied field and are normalized to the current levels of the bilayer (control) device for that particular device trial.

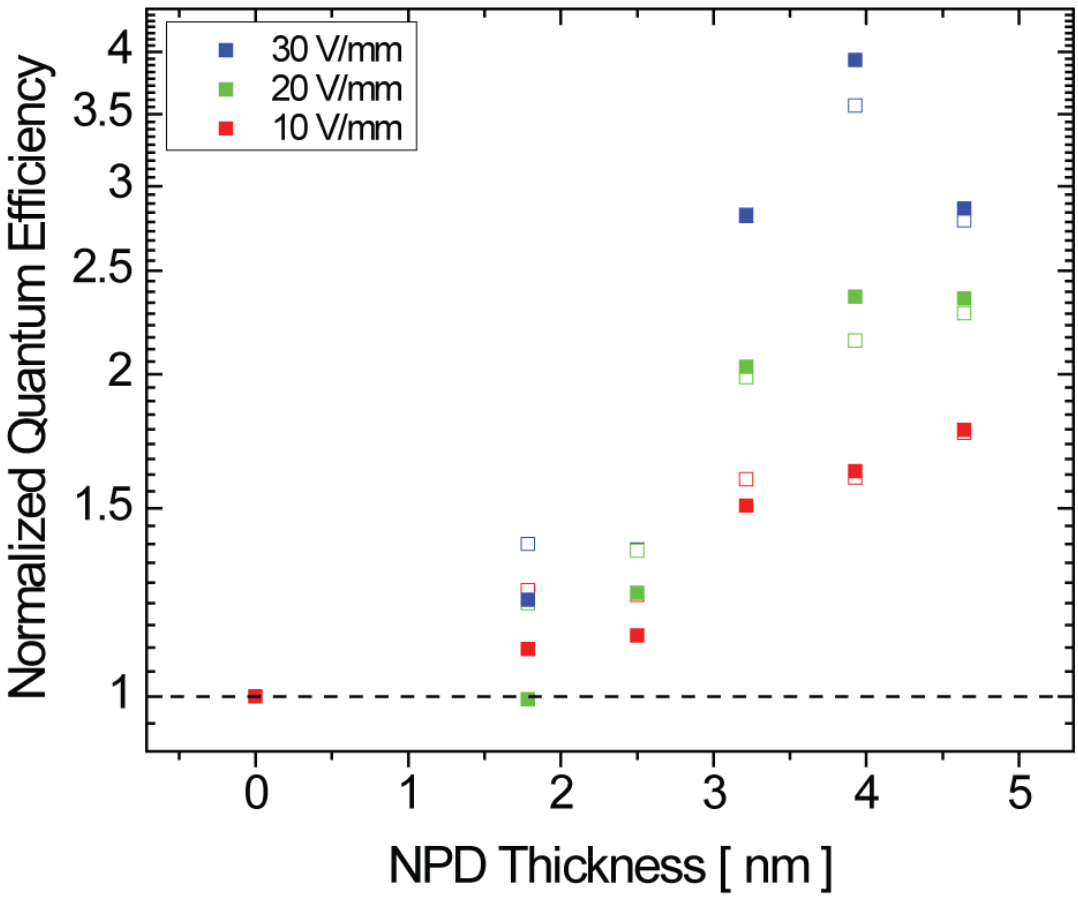

Figure 5-12: Scatter plot of three separate trilayer device trials consisting of 50 ± 0.5 nm TPD/NPD/50 ± 0.5 nm PTCBI, with varying NPD thickness. External quantum efficiency is plotted versus NPD thickness at λ = 368 nm (■) and at λ = 532 nm (□), suggesting an increase in photoresponse due to the presence of NPD. All measurements are obtained at the intensity and are normalized to the photocurrent levels of the bilayer (control) device for that particular device trial. Larger electric fields result in larger improvements.

that can be engineered in trilayer devices. The following trilayer experiments help to expand our understanding of the trilayer device structure.

TPD/UGH2/PTCBI Trilayer

Ultrahigh energy gap hosts such as p-bis(triphenylsilyl)benzene (UGH2) are designed to act as wide bandgap hosts for emissive dopant molecules in efficient OLEDs [30, 31]. In order to prevent charge and energy transfer between the dopant molecules and the host, the optically transparent UGH materials are synthesized to have large singlet and triplet energies (~ 3 - 4 eV). Given the absorption spectrum and the wide bandgap of UGH2 we can expect it to prevent excitons generated in PTCBI from dissociating, resulting in reduced photocurrent levels [Fig. 5-13]. However, excitons generated in the TPD film will continue to experience a Type-II heterojunction and efficiently dissociate.

Figure 5-14 exhibits the current-voltage characteristics of 50 ± 0.5 nm TPD/UGH2/ 50 ± 0.5 nm PTCBI trilayer devices, with varying UGH2 thickness. As is customary with the bilayer device we see ohmic conduction in the light (illumination with green LED) and trap-charge-limited conduction in the dark (black). A 2.0 ± 0.5 nm thick CSL of UGH2 increases the dark current by many orders of magnitude relative to the bilayer, indicating greater charge transfer between the Type-II heterojunction at the UGH2/TPD interface. The light current of this trilayer device also increases by a factor of 10, which is inconsistent with the band alignment at the UGH2/PTCBI interface that should prevent exciton dissociation. One possible explanation for this phenomenon is that 2 nm of UGH2 may be too thin to form a complete film, especially if UGH2 has poor wetting behavior when deposited on TPD. A thicker, presumably more complete film, of 7.0 ± 0.5 nm of UGH2 suppresses the light current by an order of magnitude while marginally affecting the dark current relative to the bilayer device.

AFM images of 10 ± 0.5 nm and 50 ± 0.5 nm thick UGH2 deposited on TPD [Fig. 5-15] confirms the poor wetting characteristics of UGH2. This implies that the trilayer devices with thin (2 nm) UGH2 films are primarily TPD/PTCBI bilayer

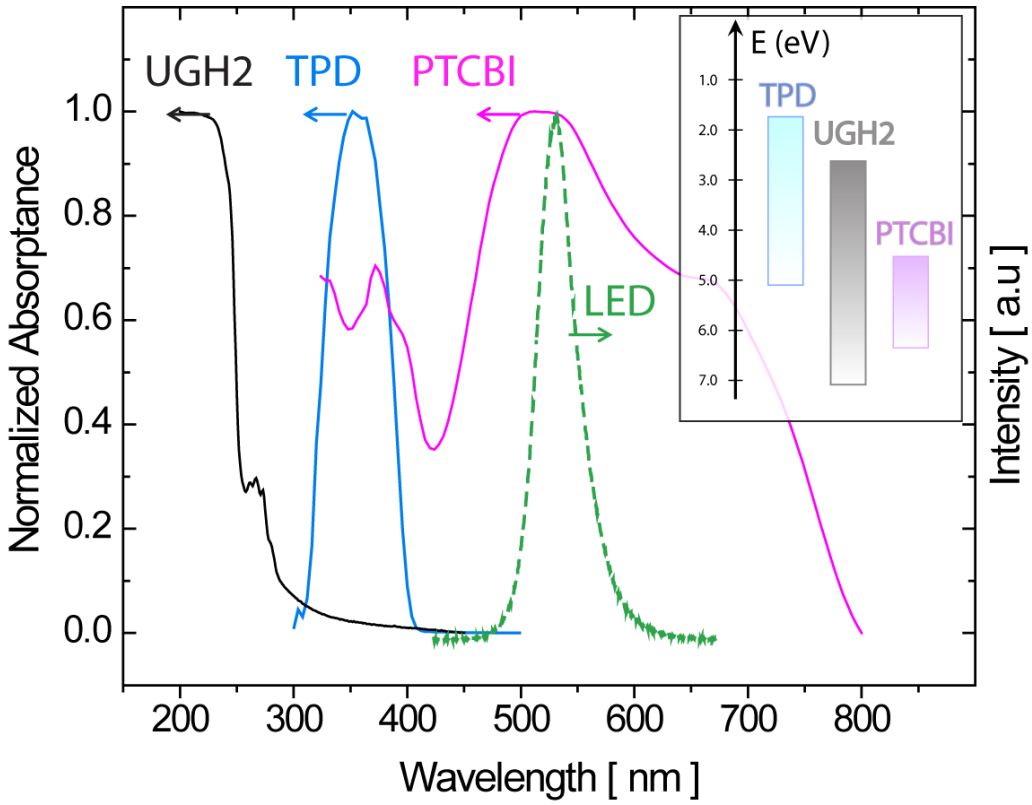

Figure 5-13: Absorption spectra of TPD, UGH2, and PTCBI (50 nm thick). The green LED emission spectrum (λ_{peak} = 532 nm), operated at an intensity of 40 mW/cm^2, is included for reference (dashed line). Inset: Suggested energy bands of TPD [14], UGH2 [30], and PTCBI [16] based on photoemission spectroscopy data and optical bandgaps.

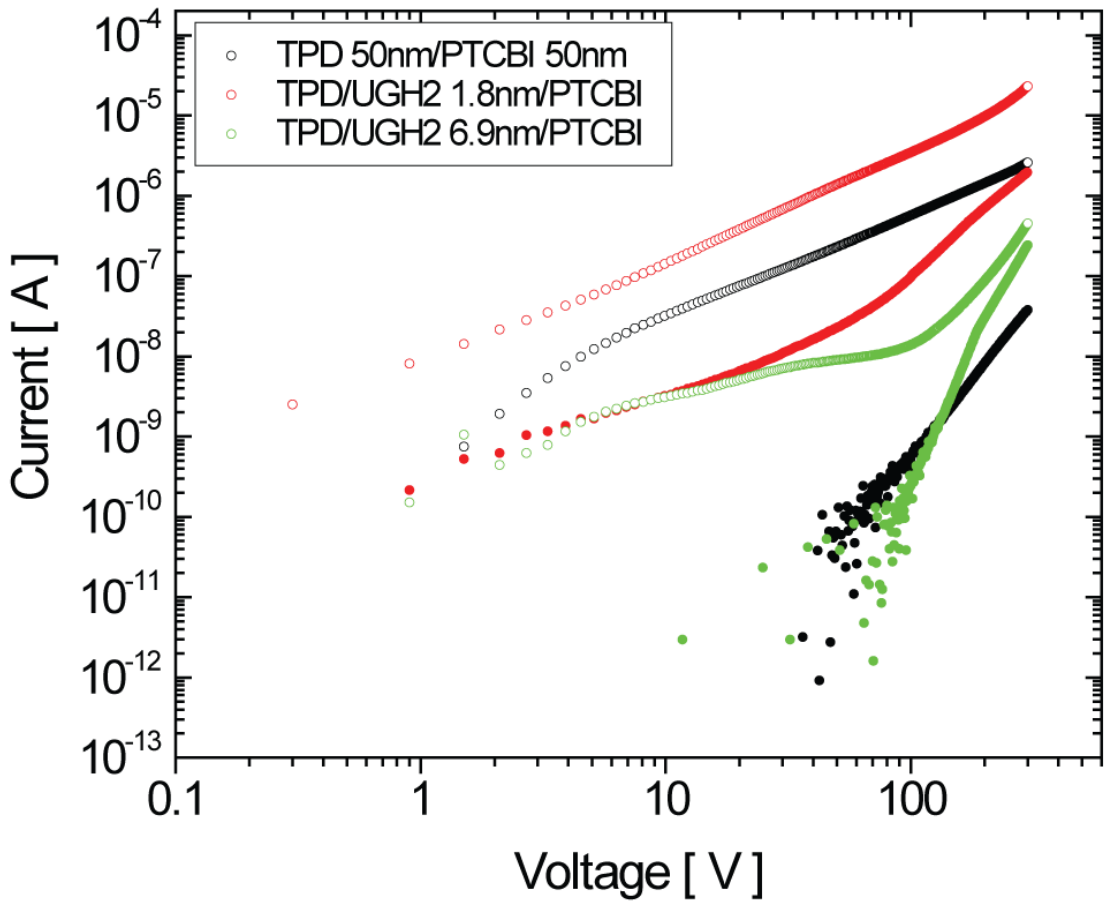

Figure 5-14: Log-log current-voltage characteristics of a TPD/PTCBI bilayer device (black), and two TPD/UGH2 (1.8 nm, 6.9 nm)/PTCBI trilayer devices (red and green respectively).

devices with "islands" of UGH2 embedded at the interface.

The EQE plot vs. UGH2 thickness in Figure 5-16 corroborates the trends in the current-voltage characteristics of the trilayer devices containing UGH2 - increased photocurrent for thin films, reduced photocurrent for thick films. For UGH2 films thinner than 4 nm there is an increase in photoresponse from both TPD and PTCBI. This relative increase over the bilayer device is more prominent for higher applied electric fields. However, beyond 4 nm the trilayer device shows a reduction in photoresponse at all bias levels. Above 6 nm the EQE of the devices cannot be measured with the available equipment as the light current levels are overtaken by the dark current.

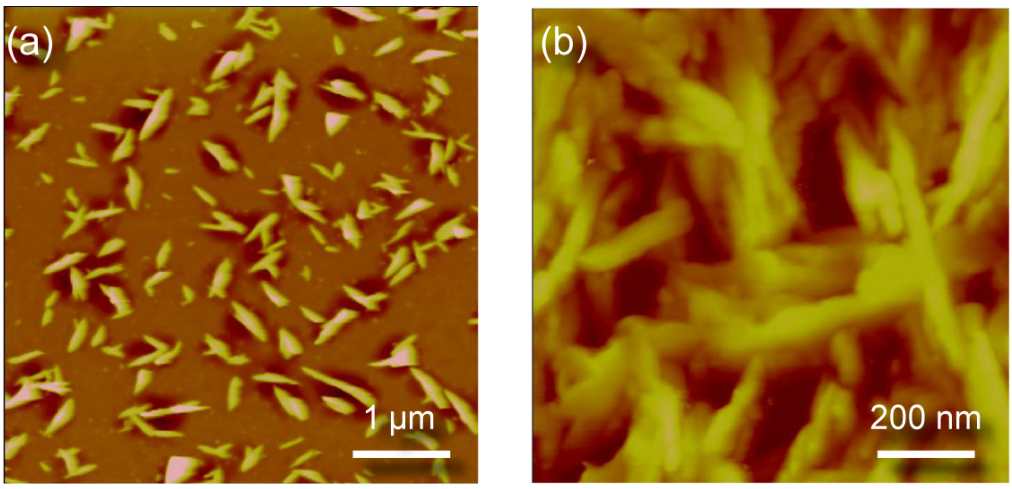

Figure 5-15: Set of AFM images of various films consisting of (a) 50 ± 0.5 nm TPD/4 ± 0.5 nm UGH2 (b) 50 ± 0.5 nm of TPD/50 ± 0.5 nm UGH2. All images have same height range of 100 nm. Island growth suggests poor wetting properties of UGH2 deposited on TPD.

In order to explain the increase in photoresponse due to exciton generation in PTCBI, we can recall the current-voltage data from the previous chapter that demonstrated a single film of PTCBI's capability of dissociating excitons without the presence of an interface. While these free charges are traveling laterally along the interface they will hop from PTCBI molecule to PTCBI molecule and either: 1) recombine monomolecularly with the opposite charge on a PTCBI molecule 2) get blocked from entering TPD by a UGH2 molecule or 3) hop (in the case of holes) onto a TPD molecule. The first scenario is unlikely given the low intensity of illumination (<1 mW/cm^2) and the low carrier mobility in the PTCBI film preventing free carriers from interacting with each other. The more likely scenario is that carriers in PTCBI will recombine across the interface with an oppositely charged carrier in TPD, as evidenced by bilayer intensity data from the previous chapter. On average, the UGH2 molecules will reduce the likelihood of this bimolecular recombination process (by occasionally blocking the hopping of a hole from PTCBI into TPD), effectively increasing carrier lifetime and consequently carrier concentrations. This increased steady-state carrier

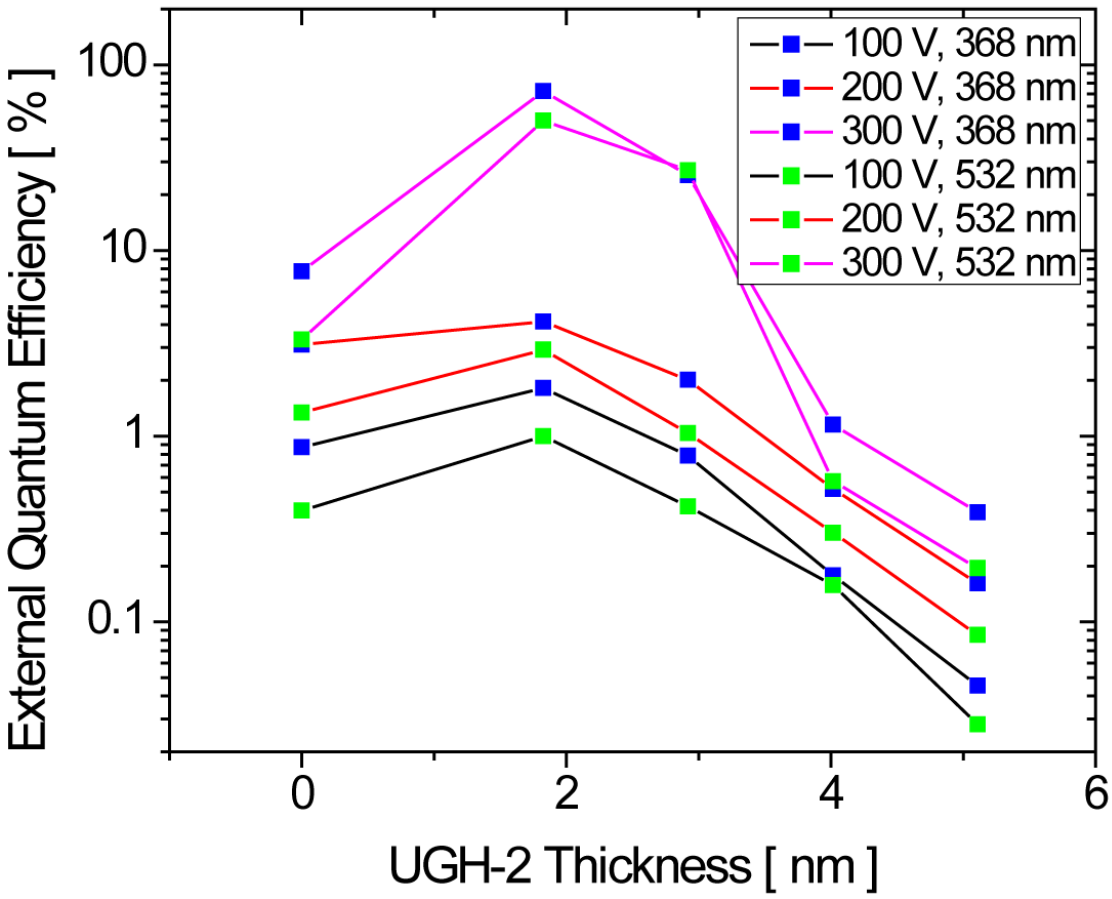

Figure 5-16: External quantum efficiency of TPD/UGH2/PTCBI trilayer device versus UGH2 thickness at λ = 368 nm (■) and at λ = 532 nm (■). Various applied electric fields from 10 V/μm to 30 V/μm are indicated in the legend.

concentration results in an increased photoresponse as demonstrated in Figure 5-16 for thin films of UGH2 (below 4 nm). When UGH2 is made thicker and approaches a complete film, monomolecular recombination in PTCBI will dominate and result in a decreased photoresponse consistent with the observed data. Experimentally, this would result in observing a linear dependence of photocurrent on intensity for thicker UGH2 trilayer devices.

The increase in TPD photoresponse (at $\lambda = 368$ nm) is due to a similar phenomenon. Unlike PTCBI and despite its higher mobilities, TPD's amorphous nature makes the probabilities of field-assisted exciton dissociation in a single TPD film difficult to measure. However, TPD forms a Type-II heterojunction with UGH2 according to the isolated energy band levels. Thus, the excitons generated in the TPD layer will dissociate at the TPD/UGH2 interface to generate a hole in TPD and an electron in UGH2. The electron in UGH2 can diffuse to the PTCBI (provided UGH2 is thin enough) where it will have a longer effective lifetime due to the ability of UGH2 molecules to occasionally block the bimolecular recombination across the TPD/PTCBI interface. For thicker UGH2 films, electrons in UGH2 will not be able to diffuse to the PTCBI and the trilayer device effectively operates like a TPD/UGH2 bilayer (when exciting TPD). Neglecting the effect of interfacial trap states, bimolecular recombination across the interface will be limited by the smaller band offset (either ΔLUMO or ΔHOMO) [32]. Thus, the thick UGH2 trilayer device will have higher recombination rates than the TPD/PTCBI bilayer device due to the ΔLUMO of TPD/UGH2 being smaller than the ΔHOMO of TPD/PTCBI, resulting in a reduced photocurrent.

After accounting for the EQE dependence on thickness we are left to explore the dependence on bias voltage. If we consider the improvement in EQE relative to the bilayer at both wavelengths as the bias voltage increases from 200 to 300 V, then it is clear that this improvement is maximized for thinner UGH2 films below 4 nm in thickness. This improvement is likely due to the onset of a different conduction regime at the higher voltages in the thinner UGH2 trilayer devices. Comparing the light current sweeps in Figure 5-14 of the 1.8 nm trilayer device with the bilayer device

gives experimental verification. At the higher biases the bilayer device maintains ohmic conduction while the trilayer device begins to transition to another regime. Because of the inability to operate these devices at higher applied fields, it is difficult to infer whether SCLC or trap-limited conduction is dominant.

TPD/PTCBI/PbSe QDs Trilayer

Lead selenide (PbSe) nanocrystals (or QDs) have recently been investigated as active materials in optoelectronic devices for their ability to emit and absorb infrared light [33–35]. The PbSe QD cores can be coated with an insulating shell or capped with organic ligands such as oleic acid to passivate surface states. The monodisperse PbSe QDs used in the following experiments were synthesized following the procedure outlined in [36, 37]. Oleic acid is used as the capping group to passivate surface states and increase solubility in chloroform (of unknown concentration). The QD solution is spun-cast onto a PDMS stamp and is deposited onto TPD/PTCBI bilayers following a micro-contact printing process [38].

Given the energy band alignment of PbSe QDs relative to TPD and PTCBI, we can expect excitons generated in PTCBI to dissociate at both of the Type-II heterointerfaces [Fig. 5-17]. However, the PbSe QD's broad absorption across the visible spectrum makes it impossible to preferentially generate excitons in a single layer. Thus, more careful analysis of the I-V curves will be necessary.

Figure 5-18 depicts the current versus voltage sweeps of a 50 ± 0.5 nm TPD/50 ± 0.5 nm PTCBI device (blue) and a similar 50 ± 0.5 nm TPD/50 ± 0.5 nm PTCBI device stamped with a 10 ± 0.5 nm thick PbSe QD film (red). Illumination is provided by a green LED peaked at $\lambda = 532$ nm and is absorbed by both PTCBI and PbSe QDs. The TPD/PTCBI bilayer shows typical photoresponse and ohmic conduction in the light curve. The stamped bilayer exhibits a reduced dark current relative to the bilayer. It is unclear at this point what phenomenon is causing this reduction. Likely, the printing of QDs effectively embeds the dots into the PTCBI film in addition to removing some of the layer. Potentially, the dots would then be close enough to the TPD/PTCBI interface to negatively affect charge transport there, as untreated

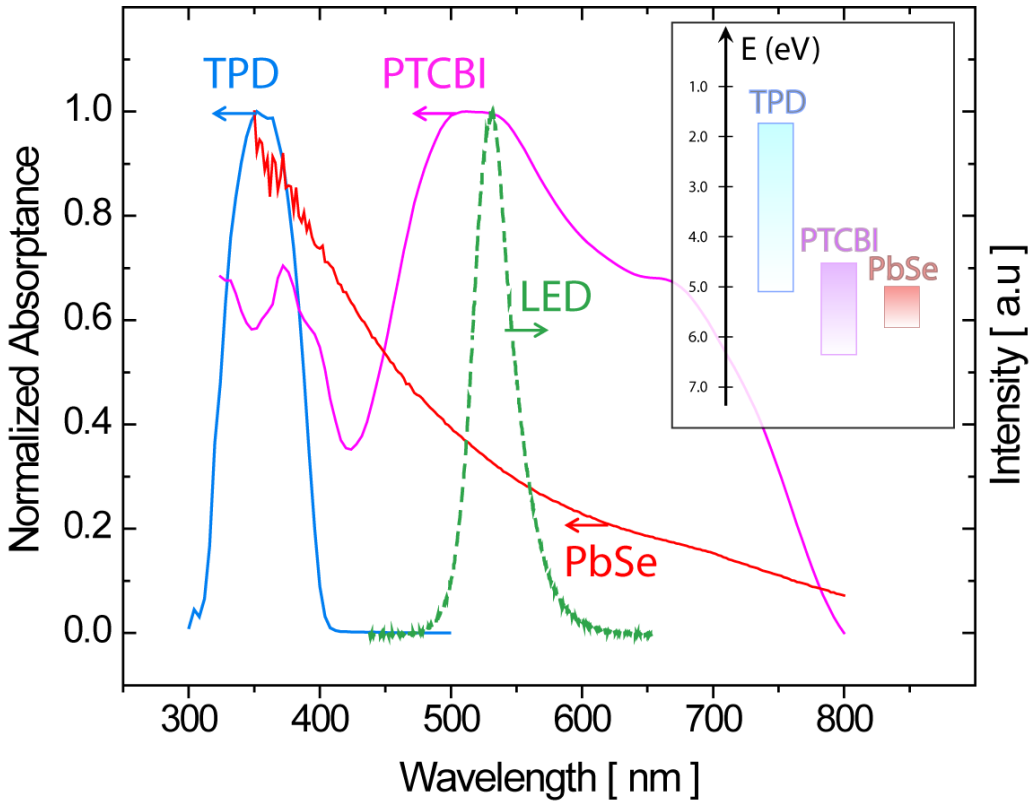

Figure 5-17: Absorption spectra of TPD, PTCBI (each 50 nm thick) and PbSe (10 nm). The green LED emission spectrum ($\lambda_{peak} = 532$ nm), operated at an intensity of 40 mW/cm^2, is included for reference (dashed line). Inset: Suggested energy bands of TPD [14], PTCBI [16], and oleic acid-capped PbSe QDs [39] based on photoemission spectroscopy data, charge transport data, and optical bandgaps.

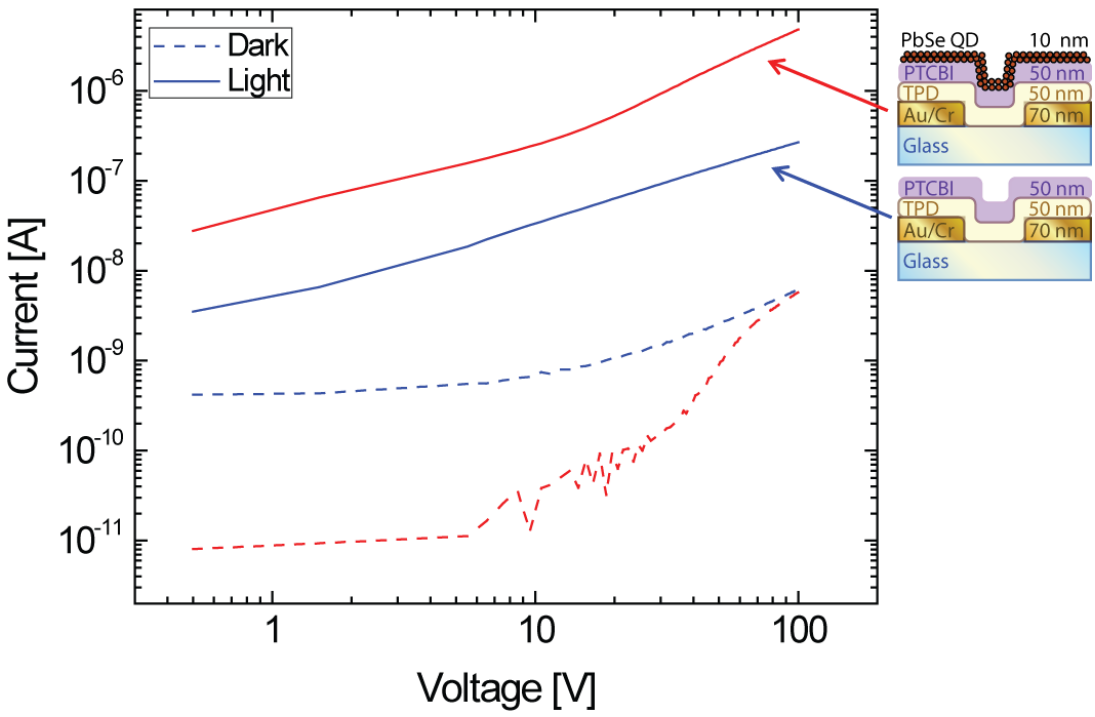

Figure 5-18: Log-log current-voltage characteristics of a TPD/PTCBI bilayer device (blue) and a TPD/PTCBI/PbSe QD trilayer device (red). Inset device cross sections indicate relevant film thicknesses.

PbSe QDs are poor hole transporters [39]. Systematic surface analysis studies of the stamped QD layer in conjunction with electrical characterization and varying thicknesses of the PTCBI film would be required to explore the cause of reduced dark current.

In addition to the reduced dark current there is an order of magnitude increase in the light current that cannot be explained by the increased absorption from the stamped PbSe QD film alone, which only increases the absorption by a factor of 2 at $\lambda = 532$ nm [Fig. 5-19]. Also, the Type-I heterojunction between PTCBI/PbSe QDs would prevent excitons generated in PbSe from dissociating into free carriers. Thus, we must rely on spectrally resolved data to help explain this enhancement.

Observing the EQE data [Fig. 5-20] we see that the spectral response of the PbSe QD trilayer device does not match its absorption profile. In fact, the response appears to share the same spectral profile as that of the bilayer, largely enhancing

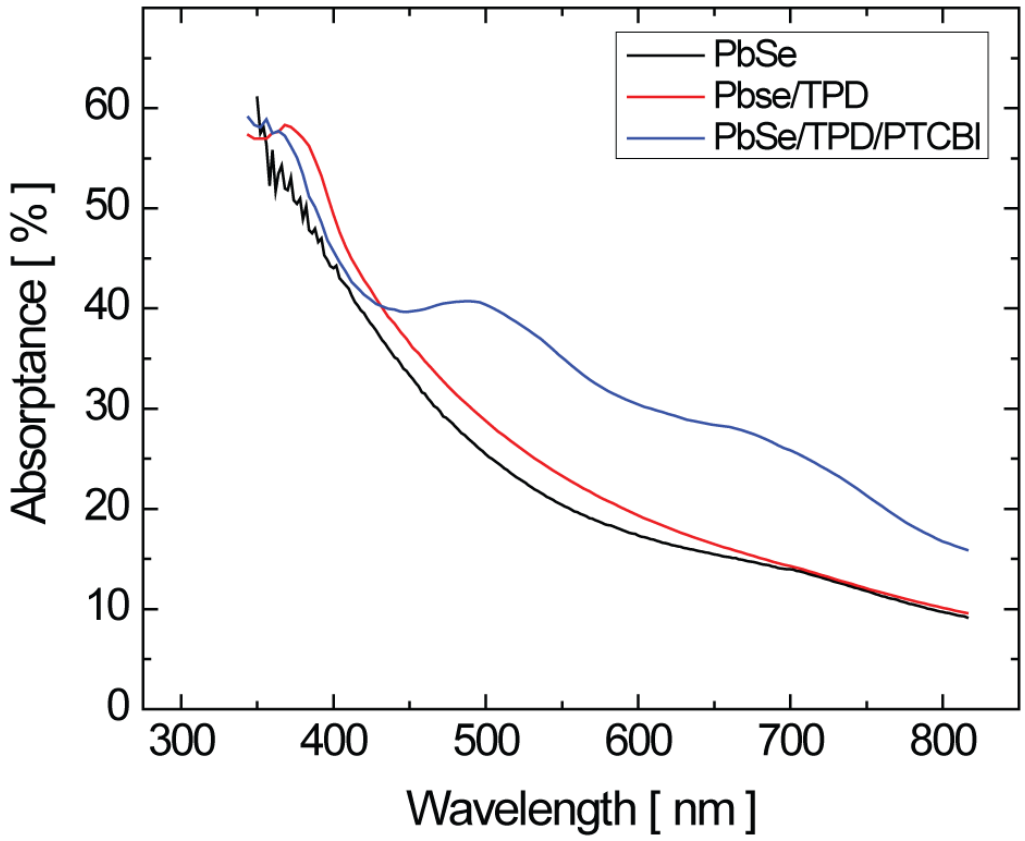

Figure 5-19: Absorption spectra of stamped film of PbSe QD on glass (black), on TPD (red), on TPD/PTCBI (blue).

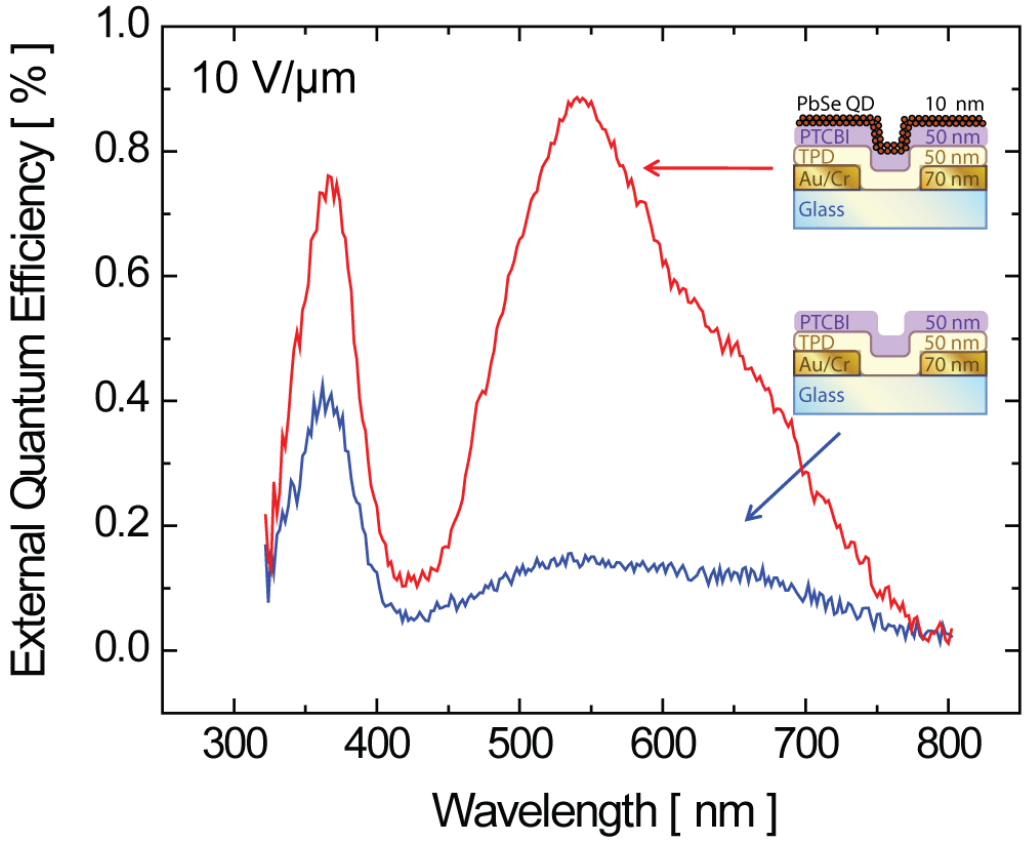

Figure 5-20: Spectral photoresponse of a TPD/PTCBI bilayer device (blue) and a TPD/PTCBI/PbSe QD trilayer device (red) with an applied electric field of 10 V/μm. Inset device cross sections indicate relevant film thicknesses.

the peaks of TPD and PTCBI absorption. This suggests that although PbSe may be generating excitons by absorbing illumination, free carriers are not generated at the PTCBI/PbSe QD interface, consistent with the proposed band alignments. The increase in photocurrent from carriers generated in TPD and PTCBI is likely due to longer lived free electrons generated at the TPD/PTCBI interface that diffuse into the PbSe QDs. Thus, PTCBI effectively acts as a CSL in this case to prevent bimolecular recombination between holes in TPD and electrons in the PbSe QDs.

5.5 Summary

The CSL concept has been demonstrated to enhance photocurrent levels in trilayer devices. One possible explanation for this enhancement is the separation of free carriers, which increases carrier lifetime. Careful time response measurements must be carried out in order to support this hypothesis, and are left as areas for further scientific exploration.

Device modeling is a useful tool to aid the device design process. However, experiments using various materials have indicated the need to factor in other properties in addition to the energy bands, such as polarizability and morphology. While it is important to compare the results of the different trilayer device experiments, we currently do not have enough data to support that discussion and must treat each set of experiments on a case by case basis. Until better control over the energy bands and morphology of deposited films is attained, engineering trilayer devices will remain a difficult trial-and-error process. Because as evidenced by the previous set of experiments, differences in energy band alignment have a significant effect on the recombination processes at the interfaces and consequently the electrical characteristics. Systematic UPS studies and surface analysis techniques should be used in conjunction with electrical characterization in order to elucidate the role of energy bands and deposition conditions on overall photoconductivity in trilayer devices.

Chapter 5 References

[1] E. E. Mendez, G. Bastard, L. L. Chang, L. Esaki, H. Morkoc, and R. Fischer. Effect of an electric field on the luminescence of GaAs quantum wells. *Physical Review B*, 26(12):7101, December 1982.

[2] G. Bastard, E. E. Mendez, L. L. Chang, and L. Esaki. Variational calculations on a quantum well in an electric field. *Physical Review B*, 28(6):3241, 1983.

[3] F. D. Sala, A. D. Carlo, P. Lugli, F. Bernardini, V. Fiorentini, R. Scholz, and J. Jancu. Free-carrier screening of polarization fields in wurtzite GaN/InGaN laser structures. *Applied Physics Letters*, 74(14):2002–2004, April 1999.

[4] E. F. Schubert. Delta doping of III–V compound semiconductors: Fundamentals and device applications. *Journal of Vacuum Science & Technology A: Vacuum, Surfaces, and Films*, 8(3):2980–2996, May 1990.

[5] E. F. Schubert. Optical properties of [delta]-doped doping superlattices. *Surface Science*, 228(1-3):240–246, April 1990.

[6] G. Dohler. Doping superlattices ("n-i-p-i crystals"). *Quantum Electronics, IEEE Journal of*, 22(9):1682–1695, 1986.

[7] S. M. Sze and K. K. Ng. *Physics of Semiconductor Devices*. John Wiley & Sons, Hoboken, third edition, 2007.

[8] S. Sista, Y. Yao, Y. Yang, M. L. Tang, and Z. Bao. Enhancement in open circuit voltage through a cascade-type energy band structure. *Applied Physics Letters*, 91(22):223508–3, November 2007.

[9] B. P. Rand, D. P. Burk, and S. R. Forrest. Offset energies at organic semiconductor heterojunctions and their influence on the open-circuit voltage of thin-film solar cells. *Physical Review B (Condensed Matter and Materials Physics)*, 75(11):115327–11, March 2007.

[10] J. Nelson, J. Kirkpatrick, and P. Ravirajan. Factors limiting the efficiency of molecular photovoltaic devices. *Physical Review B*, 69(3):035337, 2004.

[11] A. C. Arango. *A quantum dot heterojunction photodetector*. M.S. thesis, MIT, 2005.

[12] H. Ishii, K. Sugiyama, D. Yoshimura, E. Ito, Y. Ouchi, and K. Seki. Energy-level alignment at model interfaces of organic electroluminescent devices studied by UV photoemission: Trend in the deviation from the traditional way of estimating the interfacial electronic structures. *IEEE Journal of Selected Topics in Quantum Electronics*, 4(1):24–33, February 1998.

[13] C. W Tang and S. A Vanslyke. Organic Electroluminescent Diodes. *Applied Physics Letters*, 51(12):913–915, 1987.

[14] H. Ishii, N. Hayashi, E. Ito, Y. Washizu, K. Sugi, Y. Kimura, M. Niwano, Y. Ouchi, and K. Seki. Kelvin probe study of band bending at organic semiconductor/metal interfaces: examination of fermi level alignment. *physica status solidi (a)*, 201(6):1075–1094, 2004.

[15] I. G. Hill and A. Kahn. Energy level alignment at interfaces of organic semiconductor heterostructures. *Journal of Applied Physics*, 84(10):5583–5586, November 1998.

[16] W. R Salaneck, K. Seki, A. Kahn, and J. Pireaux. *Conjugated Polymer and Molecular Interfaces*. Marcel Dekker, Inc., New York, 2002.

[17] A. Curioni, M. Boero, and W. Andreoni. Alq_3: ab initio calculations of its structural and electronic properties in neutral and charged states. *Chemical Physics Letters*, 294(4-5):263–271, September 1998.

[18] K. C. Chiu, Z. A. Jian, Y. Z. Luo, J. M. Chung, S. J. Tang, M. C. Kuo, J. L. Shen, W. C. Chou, C. S. Yang, Zhenan Bao, and David J. Gundlach. Effects of substrate temperature on properties of alq3 amorphous layers prepared by vacuum deposition. In *Organic Field-Effect Transistors V*, volume 6336, pages 63361A–9, San Diego, CA, USA, 2006. SPIE.

[19] Z. Jian, Y. Luo, J. Chung, S. Tang, M. Kuo, J. Shen, K. Chiu, C. Yang, W. Chou, C. Dai, and J. Yeh. Effects of isomeric transformation on characteristics of alq_3 amorphous layers prepared by vacuum deposition at various substrate temperatures. *Journal of Applied Physics*, 101(12):123708–6, June 2007.

[20] M. Chun, T. Teraji, and T. Ito. Interfacial charge transfer and hole injection in α-NPD organic overlayer-CVD diamond substrate system. *Applied Surface Science*, 237(1-4):470–477, October 2004.

[21] M. Chun, T. Teraji, and T. Ito. Characterization of α-NPD thermally deposited on Hydrogen-Terminated Single-Crystal Chemical-Vapor-Deposited diamond films. *Japanese Journal of Applied Physics*, 42:5233–5238, 2003.

[22] T. Chasse, C. I. Wu, I. G. Hill, and A. Kahn. Band alignment at organic-inorganic semiconductor interfaces: alpha-NPD and CuPc on InP(110). *Journal of Applied Physics*, 85(9):6589–6592, May 1999.

[23] T. P. I. Saragi and J. Salbeck. Organic heterostructure field-effect transistors using c[sub 60] and amorphous spirolinked compound. *Applied Physics Letters*, 89(25):253516–3, December 2006.

[24] C. Yang, C. Lin, C. Wu, Y. Yeh, C. Cheng, Y. Kuo, and T. Chen. High-contrast top-emitting organic light-emitting devices for active-matrix displays. *Applied Physics Letters*, 87(14):143507–3, October 2005.

[25] J. S. Park, J. W. Lee, Y. M. Kim, S. J. Bae, J. Jang, J. K. Kim, and B. K. Ju. Enhancement of efficiency for White-Organic Light-Emitting diode with a thin

Electron-Blocking layer. *Journal of The Electrochemical Society*, 152(11):H196–H199, November 2005.

[26] E. Bauer. Phaenomenologische theorie der kristallabscheidung an oberflaechen i. *Z. Kristallogr.*, 110:372–394, 1958.

[27] A. Gavezzotti. Molecular free surface: a novel method of calculation and its uses in conformational studies and in organic crystal chemistry. *Journal of the American Chemical Society*, 107(4):962–967, February 1985.

[28] P. Niyamakom. *Influence of deposition parameters on morphology, growth and structure of crystalline and amorphous organic thin films (the case of perylene and NPD)*. PhD thesis, RWTH Aachen University, 2008.

[29] A. Farahzadi. *Systematic Studies on Structural and Optical Properties of Organic Thin Films on Inorganic Substrates*. PhD thesis, RWTH Aachen University, 2007.

[30] X. Ren, J. Li, R. J. Holmes, P. I. Djurovich, S. R. Forrest, and M. E. Thompson. Ultrahigh energy gap hosts in deep blue organic electrophosphorescent devices. *Chemistry of Materials*, 16(23):4743–4747, November 2004.

[31] R. J. Holmes, B. W. D'Andrade, S. R. Forrest, X. Ren, J. Li, and M. E. Thompson. Efficient, deep-blue organic electrophosphorescence by guest charge trapping. *Applied Physics Letters*, 83(18):3818–3820, November 2003.

[32] B. Mazhari. Impact of interfacial barriers on recombination profile in bilayer organic light-emitting diode. *Organic Electronics*, 6(5-6):229–236, December 2005.

[33] J. S. Steckel, S. Coe-Sullivan, V. Bulović, and M. G. Bawendi. 1.3 um to 1.55 um tunable electroluminescence from PbSe quantum dots embedded within an organic device. *Advanced Materials*, 15(21):1862–1866, 2003.

[34] V. Sholin, A.J. Breeze, I.E. Anderson, Y. Sahoo, D. Reddy, and S.A. Carter. All-inorganic CdSe/PbSe nanoparticle solar cells. *Solar Energy Materials and Solar Cells*, 92(12):1706–1711, December 2008.

[35] R. J. Ellingson, M. C. Beard, J. C. Johnson, P. Y., O. I. Micic, A. J. Nozik, A. Shabaev, and A. L. Efros. Highly efficient multiple exciton generation in colloidal PbSe and PbS quantum dots. *Nano Letters*, 5(5):865–871, May 2005.

[36] S. Coe-Sullivan. *Hybrid Organic/Quantum Dot Thin Film Structures and Devices.* Ph.d. thesis, MIT, 2005.

[37] D. C. Oertel. *Photodetectors based on colloidal quantum dots.* Ph.D. thesis, MIT, 2007.

[38] L. Kim. *Deposition of Colloidal Quantum Dots by Microcontact Printing for LED Display Technology.* M. eng. thesis, MIT, 2006.

[39] T. S. Mentzel, V. J. Porter, S. Geyer, K. MacLean, M. G. Bawendi, and M. A. Kastner. Charge transport in PbSe nanocrystal arrays. *Physical Review B (Condensed Matter and Materials Physics)*, 77(7):075316–8, February 2008.

Chapter 6

Bilayer Heterojunction Sensors for Vapor-phase Explosives Detection

There are very few personal problems that cannot be solved through a suitable application of high explosives.

SCOTT ADAMS

Cartoonist

Having explored the multilayer heterojunction device structure and proven its ability to be utilized as a photodetector, we now turn our attention towards adapting the heterojunction photoconductor for chemical sensing applications. An increasingly important, life-saving sensing application is explosives detection. On the battlefields, improvised explosive devices (IEDs) have resulted in 54% of all coalition deaths in Iraq and 59% in Afghanistan [1]. The U.S. military has responded with an intensive program of technology development, spending $12.4 billion over the past three years on counter-IED equipment, technology R&D, training, and other measures through the Joint Improvised Explosive Device Defeat Organization (JIEDDO). "Sniffing" technology, based on fluorescent polymers, has emerged as one of the most sensitive tools in the military's explosives detecting arsenal. Fluorescent polymer sensors (such as the Fido XT™) have demonstrated effective ultra-trace, vapor-phase detec-

tion of TNT at security checkpoints and during vehicular sweeps. Standoff detection capability can be achieved by attaching the Fido portable explosives detector onto autonomous robots that can find hidden explosives at safe distances from the operators.

While the Fido system works well, it does so for only a limited number of explosives. Synthesizing new polymers that are sensitive and specific to different analytes can be challenging, but engineering those polymers to work within the Fido's tight operating tolerances can be even more difficult. Therefore, sensing platforms that utilize fluorescent polymers would benefit from a more direct transduction mechanism and simpler sensor architecture.

6.1 Device Model and Theory of Operation

We employ the bilayer heterojunction to develop an improved explosives detection device with streamlined transduction and simplified architecture. The chemosensor operates in a similar fashion to the bilayer heterojunction photoconductor, with the added functionality of analyte detection in the EGL. This design can improve transduction efficiency as compared to the current generation Fido XT™. Because the heterointerface between the CTL/EGL converts the absorbed photons directly into free carriers, a photodetector is no longer required. Therefore, we eliminate the optical coupling losses associated with collecting the transduction photons emitted by the fluorescent polymer. By designing the energy band alignment between the CTL and EGL to yield a Type-II heterointerface, any chemosensitive fluorescent polymer can be used in this platform. Elimination of the photodetector results in a miniaturizable device that enables wide spread distribution of these sensors for more comprehensive protection.

Conceptually, the device consists of a Type-II bilayer heterojunction deposited on planar electrodes that enables the application of an electric field in-plane with the interface [Fig. 6-1]. The structure of the lateral heterojunction photoconductor exposes the top surface of the EGL to the external environment. If the EGL is a

chemosensing film, the bi-layer photoconductor structure can be used as a chemiresistor. In a traditional chemiresistor, the introduction of a chemical analyte can either cause changes in the chemosensitive film density [2] or can chemically adsorb to the surface of the film while transferring charge [3]. Both processes result in changes in device conductivity. State-of-the-art chemiresistors, attempt to enhance sensor specificity by functionalizing the active material, which directly affects film conductivity. In contrast, the bilayer devices separate the chemosensing and conduction functions across the EGL and CTL, respectively, enabling independent optimization of the two device functions. This separation relaxes the constraint of using a single film to serve both functions. Typically, functionalization of a polymer film (to make it specific to a particular analyte) will negatively impact the film's conductivity. In the bilayer sensor, the resulting device inherits its electrical properties from the CTL and its optical and chemosensing properties from the EGL. Therefore, chemosensitive fluorescent polymers can be tailored to a particular analyte with a focus on specificity and sensitivity without regard for conductivity, just as the CTL can be optimized for carrier transport and collection without regard for specificity.

By incorporating a chemosensitive fluorescent conjugated polymer [4–6] as the EGL, we envision a vapor-phase, solid-state chemical sensor architecture that utilizes the sensing properties of the fluorescent polymer while maintaining the chemiresistor's simple transduction of a chemical to electrical signal. Substitution of the EGL with a chemosensitive fluorescent polymer allows the exciton generation rate of the film to not only depend on the intensity of incident light excitation, but also the presence of analytes in the local environment. The photoluminescence efficiency, η, of chemosensitive fluorescent polymers can be strongly modulated by a chemical signal, which is a signature of a change in the population of excitons that can radiatively decay. Therefore, in the bilayer heterojunction chemosensor the change in exciton population will correspond to a change in charge carrier density at the EGL/CTL heterojunction interface, which will be measured as a change in photoconductivity.

Because the fluorescent polymer produces excited charge carriers from its photogenerated excitons, there remains the possibility that the carrier lifetimes can exceed

the transit times, leading to amplification of the transduced chemical signal. The photoconductive gain is related to the incident light intensity. This characteristic implies that the sensor's sensitivity can be tuned by changing the incident light signal, giving the sensor a potentially large dynamic range. In addition, the chemosensitive lateral heterojunction photoconductor can be driven with a modulated light signal, allowing for locked-in measurements of the photogenerated, transduced chemical signal. These AC measurements remove the contributions from the background DC current flowing through the CTL, relaxing the requirement of high signal-to-noise ratios for extracting useful measurements from chemiresistors.

6.2 Material Sets and Fabrication

In practice, the bilayer heterojunction is realized by spin-casting a chemosensitive, fluorescent polymer on top of a metal oxide. The polymer (insulator) acts primarily as an exciton generation layer (EGL) and the metal oxide (semiconductor) serves as a charge transport layer (CTL). Before investigating the electrical characteristics of the bilayer sensors, it is useful to consider the materials and processes involved in making the devices.

6.2.1 Fluorescent Conjugated Polymers

The advantage of using chemosensitive conjugated polymers (CPs), instead of functionalized small molecule or oligomeric materials, is the ability to collectively respond to small perturbations through the polymer backbone [7]. In contrast to CPs, the luminescent properties of an individual chemoresponsive molecule are only influenced by the local environment. However, electrical transport properties of CPs are delocalized over each conjugated polymer strand, which can yield an amplified response to analytes in a luminescence quenching system.

In order for signal amplification to occur, the properties of a large number of lumophore units must simultaneously change with the presence of a single analyte molecule. The π-electrons that are delocalized along the polymer chain create ex-

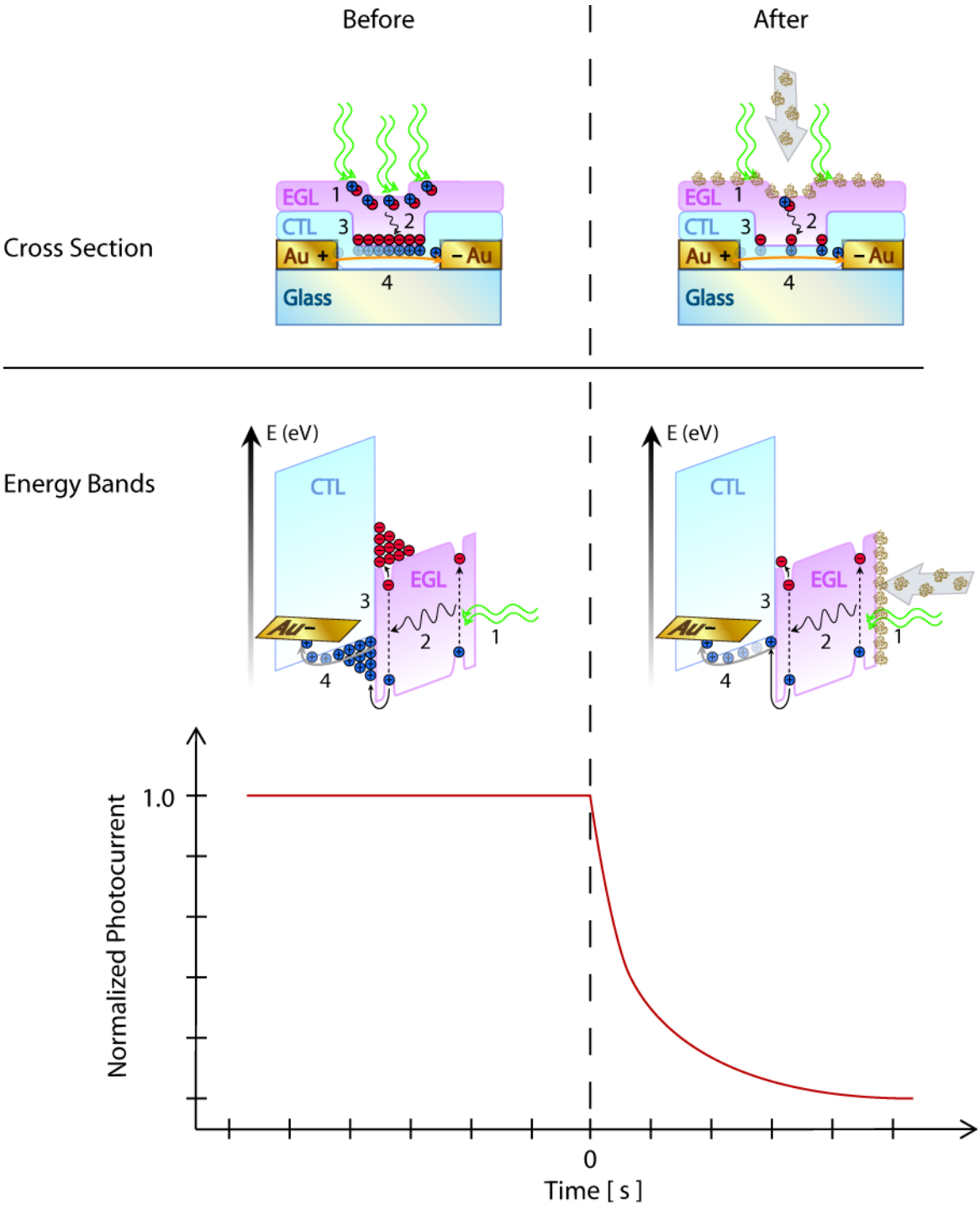

Figure 6-1: Illustration depicting cross-sectional views and energy band diagrams of a chemosensitive bilayer heterojunction photoconductor. These illustrations highlight the impact of the analyte on carrier concentrations at the EGL/CTL interface. The sample graph of photocurrent vs. time demonstrates the effect of the analyte on device photoconductivity.

tended states that form energy bands (conduction and valence) along the polymer backbone. Excitons can travel through these energy bands and the polymer film by either Forster (long-range) or Dexter (short-range) energy transfer. These efficient transport mechanisms allow the excited states to migrate among many more attached lumophore units. In the case of fluorescence quenching, any analyte molecule that is bound to a receptor site within the exciton diffusion length will create an energy trap to quench the excited state, preventing it from emitting light. In other words, the delocalization of excitons along the CP backbone effectively amplifies the luminescence quenching.

Initial luminescence quenching demonstrations in CPs used dilute solutions with integrated receptor units [8], restricting energy transport along a one-dimensional polymer chain. Thin films of conjugated polymers increase sensitivity by allowing excitons to sample receptor sites in three dimensions (inter-chain transport) rather than redundantly sampling sites along the same backbone (intra-chain). In the solid state, however, conjugated polymers often form excimers or exhibit π-stacking, both of which can decrease photoluminescent (PL) efficiencies [9]. In one effective solution to this problem, rigid three-dimensional pentiptycene molecules are incorporated into the polymer backbone. This rigid scaffolding serves three important roles: 1) to prevent aggregation of the polymer, increasing PL efficiency, 2) to increase porosity of thin films for faster analyte diffusion, and 3) to create cavities that can selectively bind analytes based on size. This approach has been used with great success for the selective detection of electron-deficient nitroaromatic compounds such as trinitrotoluene (TNT) [10]. By tuning the electrostatic interaction and film porosity/thickness, it is possible to detect TNT at sub-equilibrium vapor pressures (10-100 femtograms), which is comparable to canine olfactory performance [11].

To further enhance the three dimensional diffusion of excitons, energy migration in three dimensions has been explored through the use of multi-layer films deposited by the Langmuir-Blodgett technique. The construction of these multi-layer films creates aligned polymer backbones that channel exciton migration towards lower bandgap materials deposited on top [12]. This effectively creates a staircase of energy levels,

making it energetically favorable for the excitons to transfer their energy from layer to layer towards smaller bandgap materials. Thus, if the energy migration efficiency is high, then the probability that excitons will revisit molecules on the same chain will be reduced. In addition, some research has centered on trying to extend excited state lifetimes to increase the probability of encountering a bound receptor site. This vein of research continues to yield promising materials for sensing applications [13]. Mathematical modeling of CP sensors has shown that the sensitivity of the CP to changes in analyte concentration has a non-monotonic dependence on the number of receptors on each polymer backbone, increasing with the number of receptors up to a critical value at which point it decreases. In addition, the dynamic range of CP sensors is strongly dependent on the number of polymer backbones and the number of receptors on each backbone [14].

Lasing Action in Fluorescent Conjugated Polymers

As previously discussed, one approach to increasing the signal amplification in CP chemosensors is to change the energy transport properties by increasing excited state lifetimes or improving order in the polymer backbone to improve mobilities. Another approach that can complement other sensitivity enhancement schemes is to use the lasing action of CPs to generate greater differential emission signals.

The sensitivity enhancement due to lasing action is a general principle that is independent of the optical cavity architecture, and it has demonstrated more than a 30-fold increase in detection sensitivity [4]. One of the challenges with this technique is to use a polymer that exhibits high durability, enabling operation at high incident pumping powers in ambient atmosphere. The polymer used in the study cited above incorporated pendant aromatic rings that result in hydrocarbon side chains running parallel to the polymer backbone. These side chains effectively encapsulate the backbone, preventing the aggregation that leads to self-quenching, and may be the source of the polymer's stability in thin films. Another feature of the polymer design is the extensive π-orbital interactions that promote longer exciton diffusion lengths ($\sim$ 7-15 nm).

Another challenge with the lasing approach is the push to use thinner CP films for optimal sensitivity. Unfortunately, thinner films cannot sustain the waveguided modes needed for amplified stimulated emission (ASE) and lasing action. Thinner films are desirable because TNT and DNT (electron-deficient molecules) bind strongly to electron-rich CPs so that short exposures prevent analytes from diffusing into the bulk of the film [9]. Therefore, thin CP films ensure that the effect of exciton quenching at the surface is not overshadowed by emission from the unquenched bulk.

Many CPs, with high solid state PL efficiencies, exhibit low lasing thresholds [15, 16]. This is due mainly to the large Stokes shift that minimizes light reabsorption losses within the film. In addition, the molecular disorder inherent in organic materials creates a dispersion of energies through which excitons can diffuse downhill in energy. Exciton diffusion complements the energy relaxation due to molecular reconfiguration and increases the observed Stokes shift [17]. In general, the Franck-Condon principle is the approximation that electronic transitions occur much faster than nuclei can react. Following absorption and the nearly instantaneous promotion of an electron to an excited state, the surrounding nuclei must rearrange their energetic configurations to reach an equilibrated excited state. After emission, the nuclei are again in a nonequilibrium state and must change configuration to accommodate the relaxed electron. In all organic materials, the nuclear relaxation process causes the observed red shift in the emission profile relative to the absorption profile. These processes can be modeled using a four level system [Fig. 6-2], where the different energy levels represent the following molecular configuration energies: 1) the electronic and nuclear ground state of the molecule, 2) the electronic ground state and the nuclear excited state, 3) the electronic excited state and the nuclear ground state and 4) the electronic and nuclear excited state.

The model idealizes a CP thin film by disregarding energetic disorder (energy levels instead of bands) and places the film within an optical cavity that is excited by an ideal laser source (single wavelength, constant power). Following the treatment in [4], the following approximations can be made. First, the rates of transition from level 4 to level 3 and from level 2 to level 1 are much faster than the transition from level 3

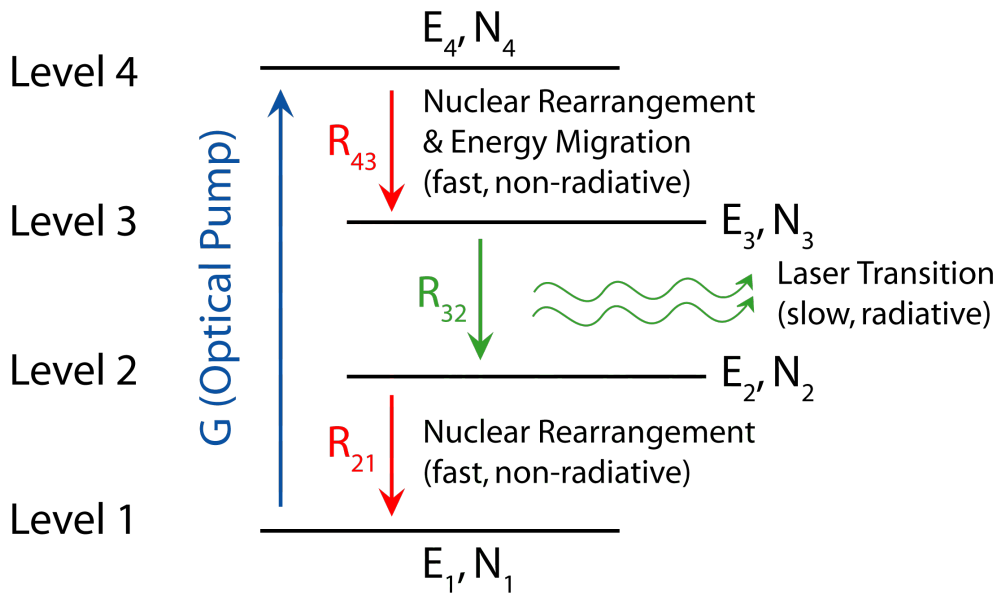

Figure 6-2: Schematic of a 4-level system representative of amplified stimulated emission in a conjugated polymer. E_x are the energies, N_x are the electron populations, and R_{xy} are the rates of transition between the different levels of the 4-level system. After [4].

to level 2. This relative rate has two effects: 1) electrons are approximated as being excited directly into level 3 and 2) the electron population in level 2 is assumed to be negligible. The transition from level 1 to level 4 occurs when an exciton is generated by the optical pumping rate G. The transition from level 3 to 2 occurs through one of four processes: spontaneous emission (with rate R_{sp}), stimulated emission (with rate R_{st}), spontaneous non-radiative decay (with rate R_{nr}), and quenching (with rate R_q). Thus, the following rate equation governs the population in level 3 (N_3),

$$\frac{dN_3}{dt} = G - R_{32}, \tag{6.2.1}$$

where

$$R_{32} = \begin{cases} R_{st} + R_{sp} + R_{nr} + R_q \text{ , above lasing threshold} \\ R_{sp} + R_{nr} + R_q \text{ , below lasing threshold} \end{cases}$$

In the absence of lasing under steady-state conditions (all time derivatives equal zero), the exciton generation rate is equal to the transition rate from level 3 to level 2, which

is the sum of all the relaxation rates:

$$G = R_{32} = R_{sp} + R_{nr} + R_q. \tag{6.2.2}$$

Given that the population in level 2 is negligible ($N_2 \sim 0$), the constant population difference between level 3 and level 2 can be represented by

$$N = G\tau_{32}, \quad \frac{1}{\tau_{32}} = \frac{R_{32}}{N} = \frac{1}{\tau_{sp}} + \frac{1}{\tau_{nr}} + \frac{1}{\tau_q},$$

where the τ's are the lifetimes associated with each relaxation pathway.

To achieve lasing, N must surpass the required threshold population difference (N_{th}) by having the gain due to stimulated emission exceed the optical cavity losses. The optical cavity losses can be categorized by losses due to the gain medium and losses due to the cavity. We can evaluate the losses in the gain medium by first noting that absorption of the lasing wavelength is negligible due to the large Stokes shift in CPs as discussed earlier. Thus, only the mirror losses contribute. Assuming that both mirrors are identical (symmetric cavity), the distributed cavity loss coefficient (γ) can be written as,

$$\gamma = \frac{1}{d} \ln\left(\frac{1}{\Gamma}\right), \tag{6.2.3}$$

where d is the cavity length and Γ is the reflectivity of the mirrors [18]. Below threshold, the effect of stimulated emission on the population is small because the photon flux (Φ) present in the cavity at the lasing mode is relatively low. So, the "small-signal" gain, $g(\lambda)$, is given by,

$$g(\lambda) = N\sigma_{32}(\lambda) = G\tau_{32}\sigma_{32}(\lambda), \tag{6.2.4}$$

where $\sigma_{32}(\lambda)$ is the cross section for stimulated emission at wavelength λ. It is important to note that the product of the photon flux with the cross section for stimulated emission between levels 3 and 2, yields the stimulated emission rate, R_{st}:

$$R_{st} = \Phi\sigma_{32}(\lambda). \tag{6.2.5}$$

This equation shows that the stimulated emission rate is not a function of the quenching rate and will remain the same in the presence of an analyte. Thus, the lasing threshold should occur when,

$$\begin{aligned} &\gamma = g(\lambda) \\ &\Rightarrow \frac{1}{d}\ln\left(\frac{1}{\Gamma}\right) = G\tau_{32}\sigma_{32}(\lambda) \\ &\Rightarrow G_{th} = \frac{1}{d\tau_{32}\sigma_{32}(\lambda)}\ln\left(\frac{1}{\Gamma}\right). \end{aligned} \tag{6.2.6}$$

From this expression, it is clear that the threshold pumping rate will be modified by the quenching rate through τ_{32} alone.

When lasing, nearly every exciton generated above threshold contributes to optical power in the lasing mode, as can be seen by the following relation,

$$P_{laser} \propto P_{pump} - P_{th}. \tag{6.2.7}$$

P_{th} is the pumping optical power necessary to reach threshold and is linearly proportional to the threshold generation rate of excitons, G_{th}. Thus, if the introduction of an analyte causes the overall carrier lifetime (τ_{32}) to change, then the quenched laser power becomes,

$$P'_{laser} \propto P_{pump} - P'_{th}, \quad P'_{th} = \frac{\tau_{32}}{\tau'_{32}P_{th}}$$

where τ'_{32} is the carrier lifetime associated with the transition from level 3 to 2 after quenching. Since quenching will reduce this lifetime by introducing another relaxation pathway, the pumping threshold will shift to higher energies. Now, it is possible to specify the fractional change in intensity of the lasing CP film in the presence of analyte using a fixed pump power,

$$\frac{\Delta I}{I_o} = \frac{P'^{-P_{laser}}_{laser}}{P_{laser}} = \frac{P_{th}\left(1 - \frac{\tau_{32}}{\tau'_{32}}\right)}{P_{pump} - P_{th}} = \frac{P_{th}(1-\beta)}{P_{pump} - P_{th}}, \tag{6.2.8}$$

where,

$$\beta = \frac{\tau_{32}}{\tau'_{32}}.$$

This expression can be compared to the fractional change in PL intensity of the CP film to specify the sensitivity enhancement due to lasing action. The PL efficiency (η) of the CP film can be written as,

$$\eta = \frac{\text{Rate of photon emission}}{\text{Rate of exciton generation}} = \frac{R_e}{G} = \frac{\tau_{32}}{\tau_e}. \tag{6.2.9}$$

Considering that the PL intensity is directly proportional to the PL efficiency, the fractional change in PL intensity becomes,

$$\frac{\Delta I}{I_o}_{PL} = \frac{\eta' - \eta}{\eta} = \frac{\frac{\tau'_{32}}{\tau_e} - \frac{\tau_{32}}{\tau_e}}{\frac{\tau_{32}}{\tau_e}} = \frac{1-\beta}{\beta}. \tag{6.2.10}$$

From these expressions it becomes clear that operating the chemosensing CP film near its lasing threshold post-exposure will yield enhancements in fluorescence quenching, thereby enhancing sensitivity. Simple inspection of Figure 6-3 shows that the optimal sensitivity is obtained when the pump power of the CP is at the onset of amplified stimulated emission (ASE). The devices used for the initial lasing enhanced sensitivity studies were easily fabricated and convenient for evaluating and comparing the lasing characteristics of different CPs. However, these low quality laser cavities give high loss coefficients and higher lasing thresholds. Higher Q-factor laser cavities would lower device operating powers, lengthen CP film lifetimes, and reduce the lasing threshold, allowing for thinner CP active layers. These thinner active layers are expected to provide increased sensitivity and faster analyte response times.

6.2.2 Metal Oxides

In order to utilize chemosensitive fluorescent polymers in a bilayer structure, the polymer must be deposited out of solution to form the topmost layer and EGL. This format ensures that the fluorescent polymer's exciton generating capabilities are exposed to the changing environment. Therefore, the underlying CTL must consist of a material

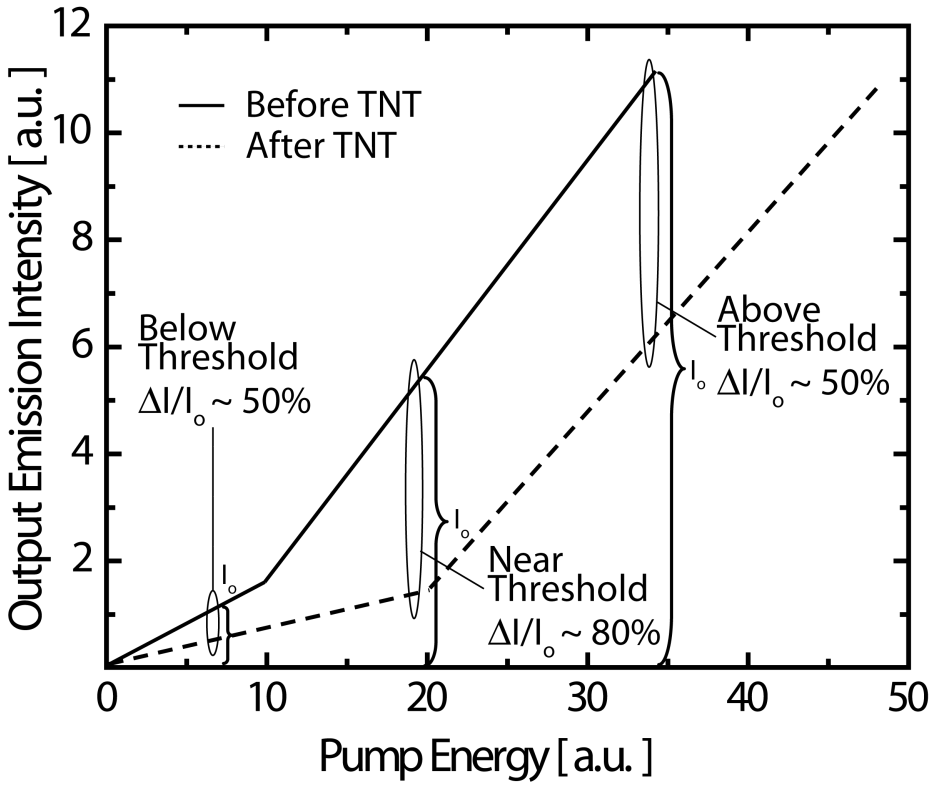

Figure 6-3: An example sketch of the lasing threshold increase after exposure of the CP film to a quenching analyte, such as TNT. The change in the output emission intensity is largest at pump energies near the lasing threshold of analyte-exposed films. After [19].

that is compatible with solvent processing and can withstand the spin-coating process. Metal oxides make a good choice for the CTL for several reasons, including high carrier mobilities, chemical/mechanical robustness and tunable conductivity. Metal oxides typically have the chemical formulas M_xO_y or $M_xN_yO_z$, where M and N are metallic elements and O is oxygen [20]. Metal oxides are used in a wide range of applications including jewelry, transparent conductors, gas sensors, and catalysts. All of the optical, electrical, and mechanical properties of metal oxides can be traced back to the chemical bonds formed between the atoms of metal and oxygen. There are two types of bonding in these materials: ionic and covalent. Ionic bonds form as the result of the Coulombic attraction between oppositely charged ions, occurring only if the energy of the molecular unit is lower than the energy of the separated ions. These bonds typically result in insulating materials with a strong, non-directional bonding pattern. Covalent bonds form as the result of electron sharing between neighboring atoms. This configuration results in directional bonds that depend on which electronic orbitals are sharing the electrons. Therefore, covalent bonds can range in strength and lead to materials that are metallic to semiconducting in nature.

Some of the methods used to deposit amorphous metal oxide thin films include molecular beam epitaxy (MBE) [21], chemical vapor deposition (CVD) [22], atomic layer deposition (ALD) [23], and sol-gel [24]. In this work we use radio-frequency (RF) magnetron sputtering to deposit metal oxides due to the relatively fast deposition rates and high quality films that are achievable.

6.3 Proof of Concept: ZZ-TOP and SnO_2

In fabricating the first proof-of-principle device, we used a robust CP termed ZZ-TOP as the chemosensitive EGL [Fig. 6-4]. This CP has demonstrated stable lasing ability in air and good sensitivity to TNT vapor [4, 19], making it a robust, practical material to use. Pairing this polymer with an appropriate CTL to make a Type-II heterojunction requires first the determination of its HOMO and LUMO levels.

The HOMO level can be obtained experimentally through a technique known

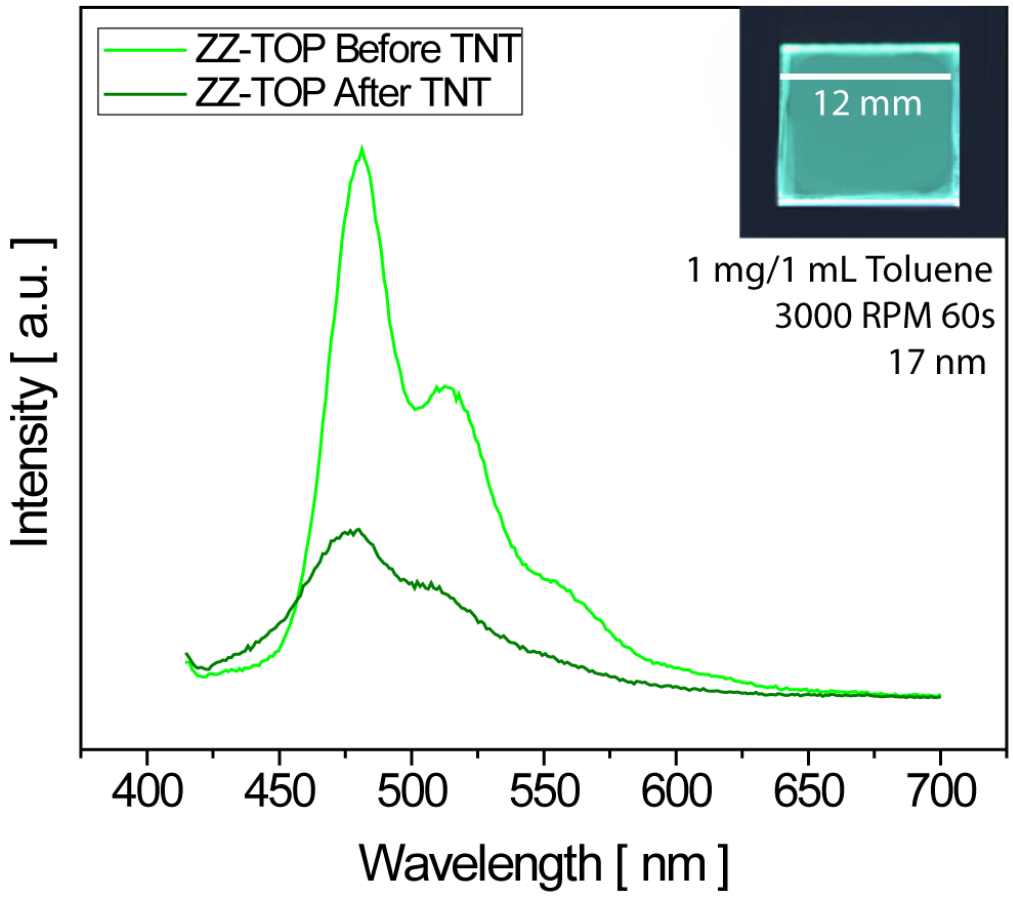

Figure 6-4: Emission spectra of a 17 ± 1 nm thin film ZZ-TOP before (light green) and after (dark green) exposure to saturated TNT vapor. Inset: Digital image of ZZ-TOP thin film spin-coated on a glass substrate and excited by UV illumination.

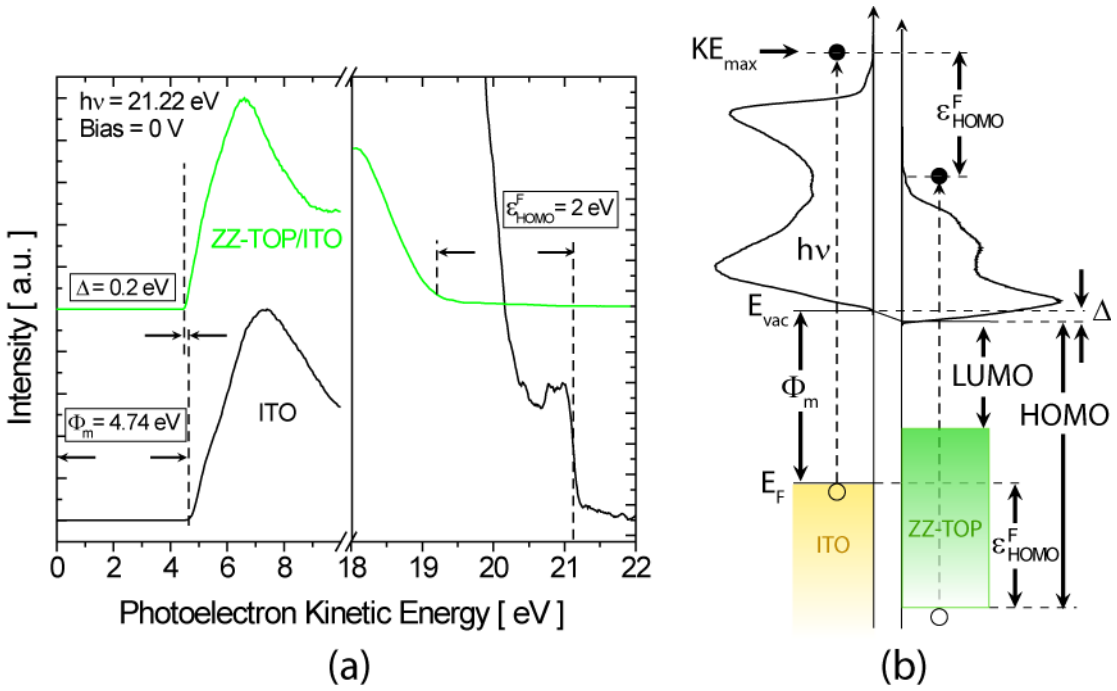

Figure 6-5: (a)Helium I UPS data from ITO sample (100 Ω/□) and ITO coated with 10.0 ± 0.5 nm film of ZZ-TOP polymer with no bias relative to reference electrode. (b)Energy level schematic of UPS spectra superimposed over the energy bands of the sample materials. The work function of ITO (Φ_m) can be extracted from the onset of photoemitted electron collection. Note the small vacuum level shift (Δ) and the large energy difference between the ZZ-TOP HOMO and the ITO Fermi level (ε^F_{HOMO}).

as ultraviolet photoemission spectroscopy (UPS). Data was gathered using a multi-technique surface analysis system for UPS and ultra high vacuum scanning probe microscopy (Omicron Nano Technology GmbH). A 0.1 mg/mL concentration solution of ZZ-TOP is spin-coated onto an indium tin oxide (ITO) chip at 6000 RPM for 60 seconds, resulting in a 10 ± 0.5 nm thick polymer film as measured by AFM. To reduce the effects of adsorbed surface contaminants on the polymer film such as oxygen, water, or excess solvent, samples were left under high vacuum conditions ($< 10^{-10}$ Torr) in the UPS chamber over a 24 hour period. Ultraviolet light, from a Helium lamp emitting at 21.2 eV (He I radiation), illuminated the sample. The low photon energies in UPS means that deep core electron levels cannot be excited. Therefore, only electrons in the valence band or shallow core levels are accessible with this technique.

Figure 6-5(a) highlights the important areas of the UPS spectra at both energy

extremes, more specifically where the photoemitted electrons have the least kinetic energy and the most kinetic energy. The low kinetic energy side is used to determine the work function of a reference material and the vacuum level shift of another material relative to the underlying reference material. The small vacuum level shift of 0.2 eV combined with the energy difference of 2 eV between ZZ-TOP's HOMO and ITO's Fermi level yields a HOMO level of 6.5 ± 0.5 eV for ZZ-TOP [Fig. 6-5(b)]. The large uncertainty in the data stems from variation in the UPS measurement itself and from variations in the surface condition of the polymer film.

The LUMO level of ZZ-TOP can be determined empirically by adding the optical band gap energy to the HOMO level. The optical bandgap energy can be inferred from the onset of ZZ-TOP's absorption spectrum, which starts at $\lambda = 480$ nm corresponding to an energy of 2.5 eV [Fig. 6-6]. Therefore, the HOMO/LUMO levels of ZZ-TOP are 6.5 eV and 4.0 eV, respectively.

Thin film absorption spectra of ZZ-TOP and SnO_2 are captured using a UV-VIS-NIR spectrophotometer (NKD-8000, Aquila Instruments). Pairing ZZ-TOP with SnO_2 as CTL yields a Type-II heterojunction with some overlap in the absorption spectra [Fig. 6-6]. Because the ZZ-TOP absorption peaks at blue (shorter) wavelengths, it is difficult to find materials with wide enough bandgaps to prevent overlap of absorption spectra. The UGH materials would certainly be better from an absorption standpoint, but the additional requirements of a LUMO greater than 4.0 eV and solution processing of ZZ-TOP make those wide bandgap materials incompatible with this particular polymeric system.

Once the optimal components were determined, the designed sensing devices were fabricated. To deposit the SnO_2, an Ar/O_2 gas mixture was used for the sputtering process at a flow ratio of 7 sccm to 3 sccm. The residual gas pressure in the sputtering chamber was roughly 4 mTorr. At a constant RF power of 160 Watts, the deposition rate reached a maximum of 1.0 $\mathring{A}$/s. To remove any target contamination and to prepare the target, a 100 nm thick layer was presputtered at the desired process gas flow and power. The film morphology of SnO_2 films deposited by RF magnetron sputtering depends strongly on the growth pressure. At higher process pressures,

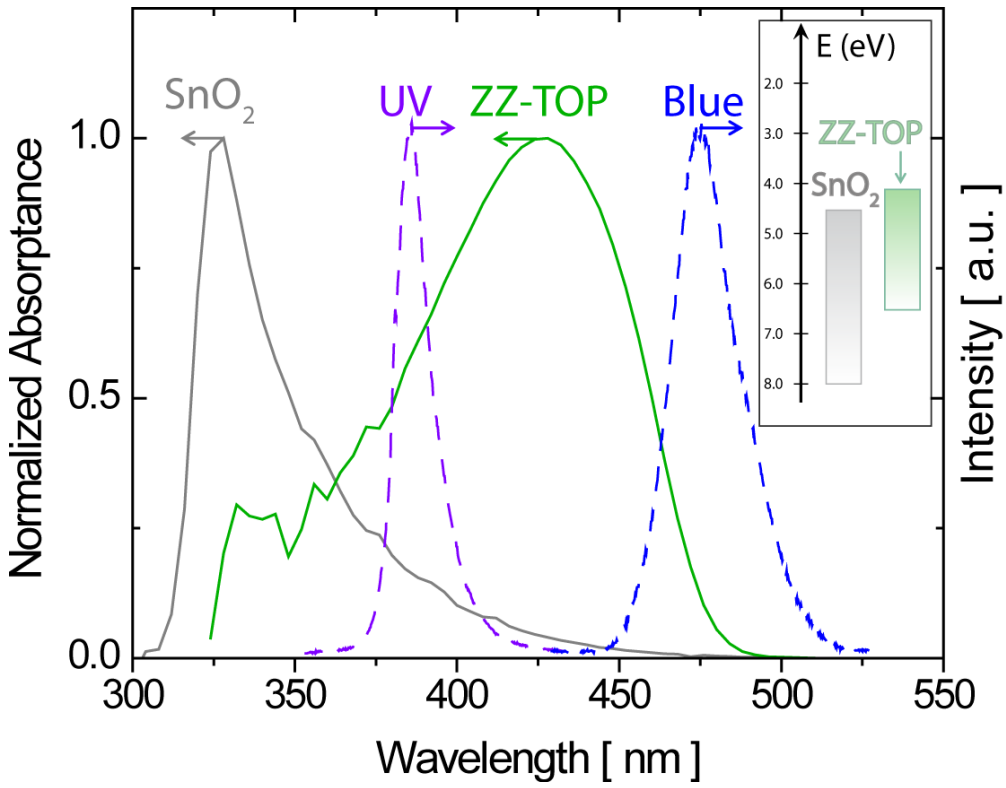

Figure 6-6: Normalized absorption spectra of a 17.0 ± 0.5 nm thick film of ZZ-TOP (green), a 100.0 ± 0.5 nm thick film of SnO_2 (grey), and the emission spectra of a blue (λ_{peak} = 460 nm) and UV LED (λ_{peak} = 385 nm). Inset: Suggested energy bands of ZZ-TOP and SnO_2 [25] based on photoemission spectroscopy data and optical band gaps.

columnar structures are formed, whereas at lower pressures the film consists of closely packed fibrous grains [26]. Figure 6-7 shows an AFM image of the deposited SnO_2 films which suggests a polycrystalline film with an average crystallite size of 50 nm in diameter.

In semiconducting metal oxides, oxygen vacancies that act as electron donors (n-type semiconductors) or excess oxygen atoms that act as electron acceptors (p-type) are responsible for the electronic conductance. Doping the SnO_2 films with 30% oxygen by volume fills oxygen vacancies and reduces conductivity. The practical benefit is that the lower conductivity films are now within measurement range of available testing equipment (Keithley 6487), whereas the undoped films were so conductive as to overload the current measurement.

Figure 6-8 plots the steady state I-V characteristics, both with and without blue LED illumination (Lamina, BL-3000), from a series of devices containing either single films or a bilayer heterojunction of SnO_2 and ZZ-TOP. The blue LED light engine, powered by a sourcemeter (Keithley 2400), provides narrow band excitation (FWHM 50 nm) with intensities up to 30 mW/cm^2 as measured with a calibrated photodetector (Newport, 818-UV). The emission spectrum of the blue LED [Fig. 6-6] was measured using a spectrometer (Ocean Optics, USB4000). Device current-voltage (I-V) characteristics were measured in a dark box using a picoammeter (Keithley 6487). All measurements were conducted in a nitrogen ambient environment provided by a glovebox (MBraun).

Notice that all of the curves are essentially ohmic in nature across the voltage range. Electrons are the majority carrier in SnO_2 making it n-type. That fact coupled with the LUMO level of SnO_2 suggests close Fermi level alignment with that of the gold electrodes, which is consistent with the ohmic conduction observed. The device containing a single (17.0 ± 0.5) nm thick film of ZZ-TOP generates little measurable photoresponse, which reflects 1) the low absorption in the ZZ-TOP film and 2) the inability of ZZ-TOP to dissociate excitons efficiently. The thin film of SnO_2 does generate a moderate photocurrent in response to the blue illumination, which can be discerned by comparing the solid black line to the dashed black line. A thick 100

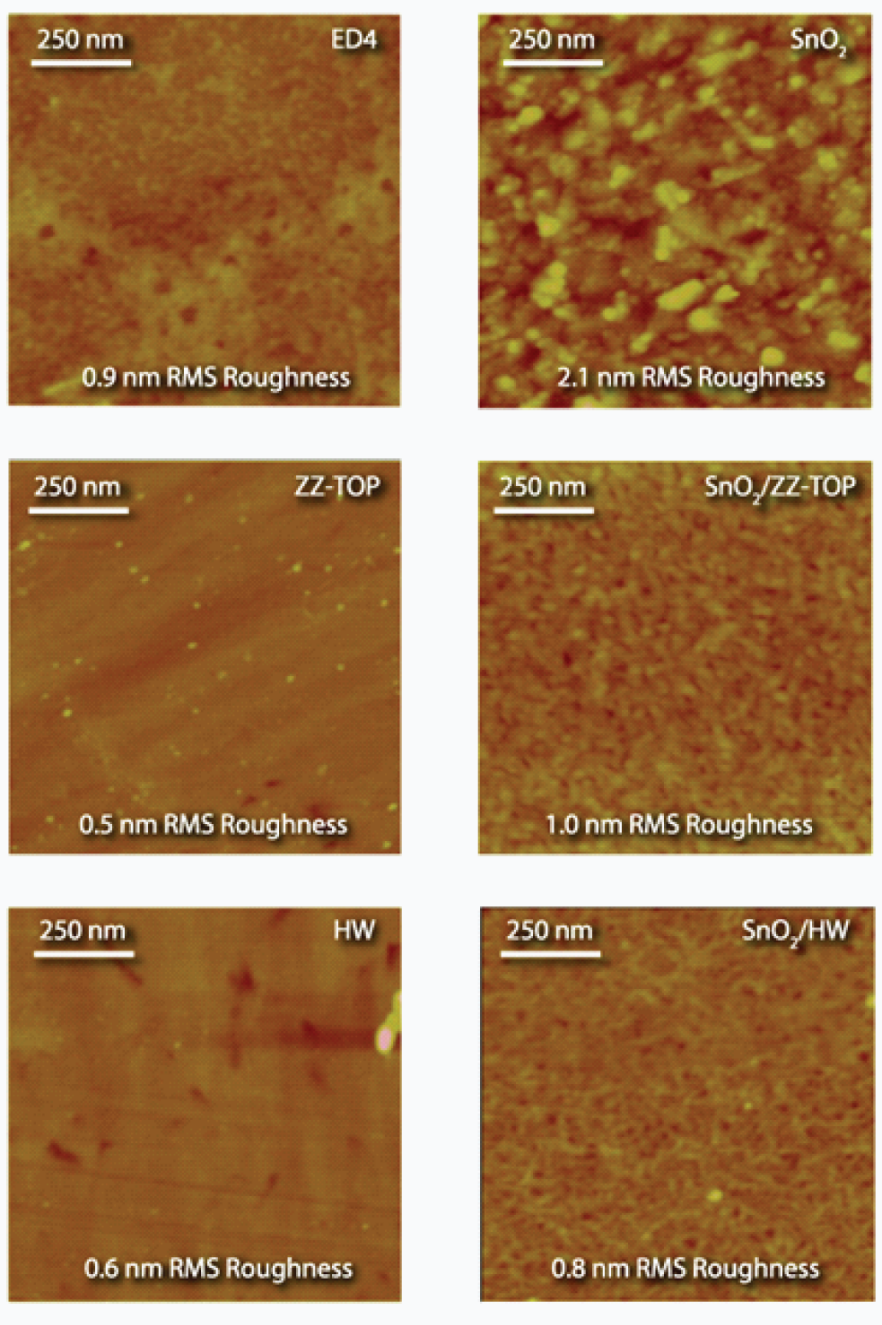

Figure 6-7: AFM images of various fluorescent polymers spin-coated onto glass substrates and SnO_2 films coated with those same polymers. All images have the same height range of 20 nm.

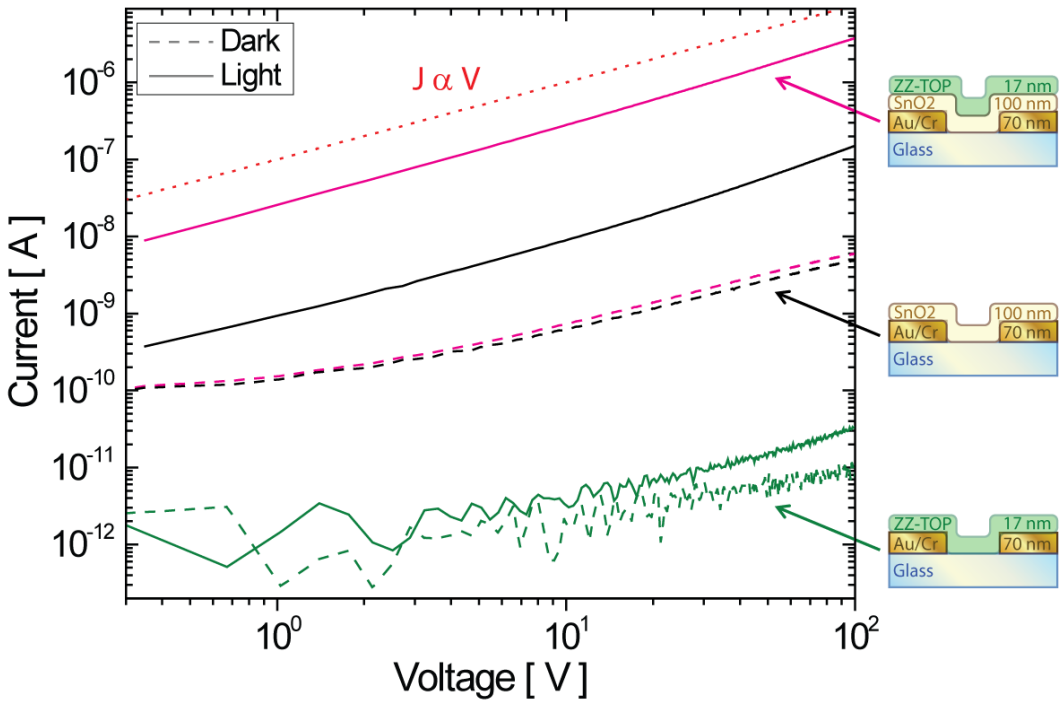

Figure 6-8: Log-log plot of the current-voltage characteristics from a series of lateral photoconductor devices using SnO_2 and ZZ-TOP. Current-voltage sweeps are taken in the dark (dashed) and under illumination (solid) through the glass substrate from a 30 mW/cm^2 Blue LED ($\lambda_{peak} = 532$ nm). The dashed red line is a guide for the eye and follows Ohm's law. The inset cross-sectional diagrams describe the thicknesses and device structures.

nm film significantly contributes to the absorption tail that extends into the LED's emission spectrum. The photogenerated excitons will diffuse to crystallite boundaries [Fig. 6-7] where they can dissociate to contribute to the film's photoconductivity. Therefore, despite the absence of a heterojunction, the SnO_2 film is able to generate a photoresponse.

Comparing the dark currents, it is evident that ZZ-TOP has the lowest overall conductivity. This presents one of the challenges of incorporating ZZ-TOP (and other fluorescent polymers) into a traditional chemiresistor structure, because low conductivity makes the electrical signal more susceptible to environmental noise. On the other hand, the SnO_2 has a high carrier mobility ($\sim 1\ cm^2V^{-1}s^{-1}$) consistent with the polycrystalline nature of metal oxides, resulting in a higher dark current curve. The combined SnO_2/ZZ-TOP bilayer structure has nearly the same dark current as the single film of metal oxide. This indicates that the level of charge transfer at the interface is less than the intrinsic carrier concentration of the SnO_2 film. Given the small vacuum level shift between ITO and ZZ-TOP [Fig. 6-5], a negligible concentration of transferred charge relative to the intrinsic metal oxide carrier concentration is to be expected.

The increased photocurrent of the SnO_2/ZZ-TOP device relative to the SnO_2 device can be explained by the presence of the Type-II heterojunction between ZZ-TOP and SnO_2. Both ZZ-TOP and SnO_2 absorb the blue light and generate excitons, which produces enough carriers to make the interface the most conductive pathway in the device. This dataset suggests that the SnO_2/ZZ-TOP heterojunction interface is efficiently dissociating excitons and generating charge under illumination, which is transported as electrons through SnO_2.

When introducing saturated TNT vapor onto the devices, there was no significant change in any of the current-voltage characteristics. This observation leads to the assertion that the differential signal is too small to be measured with steady-state I-V sweeps. The main factor accounting for this result is the absorptive ability of the thick SnO_2 relative to the thin ZZ-TOP, which affects the ability to preferentially excite ZZ-TOP by using a broad emission spectrum light source (i.e. LED). This absorption

makes it difficult to pick out the differential signal due to ZZ-TOP quenching given the competition from the baseline photoresponse of the SnO_2. Therefore, a locked-in photocurrent measurement with monochromatic excitation is needed to pick out the differential current signal caused by quenching.

The testing setup consists of a 1000 W Xenon arc lamp (Oriel) incident on a monochromator (Acton SpecraPro 300i) with a diffraction grating (600 L/mm) blazed at $\lambda = 500$ nm providing monochromatic illumination across the visible spectrum. A computer-controlled rotary filter wheel prevents secondary harmonics from exciting the samples. In addition, the monochromatic light is fed into a glass fiber which is coupled into a nitrogen-filled glovebox. The light is optically chopped at 40 Hz and locked-in with a digital lock-in amplifier (Stanford Research Systems, SR830), which selects only the photocurrent component of the input signal. Saturated TNT vapor is produced by solid TNT particles placed into a bubbler (Chemglass). Air flow through the headspace of the solid TNT is provided by a diaphragm pump and is controlled by a flow meter, allowing for TNT vapor delivery rates ranging from 0 to 500 cc/min [Fig. 6-9].

Wavelength resolved data enables a more detailed analysis of device operation. Figure 6-10 shows the spectral response of a series of devices containing SnO_2 and ZZ-TOP. The SnO_2 film shows a significant photoresponse out to 500 nm consistent with its absorption profile, while the ZZ-TOP's photoresponse could not be measured. Both results are consistent with the previously obtained current-voltage data. Attempts to boost the relative absorption of the ZZ-TOP over SnO_2 by depositing a thinner SnO_2 film yielded a more photoresponsive device (grey curve). This suggests that thinner SnO_2 films form smaller crystallites, which generates a larger concentration of defect sites for enhanced exciton dissociation in the SnO_2 bulk [27]. The bilayer device exhibits an improved photoresponse relative to SnO_2 by more than an order of magnitude, again consistent with the I-V data. From the spectrally resolved data it is clear that the improvement in photoresponse occurs across both the SnO_2 and ZZ-TOP absorption spectra. However, the large photoresponse of the SnO_2 clearly dominates, with only a slight shoulder at $\lambda = 456$ nm to indicate the presence of the

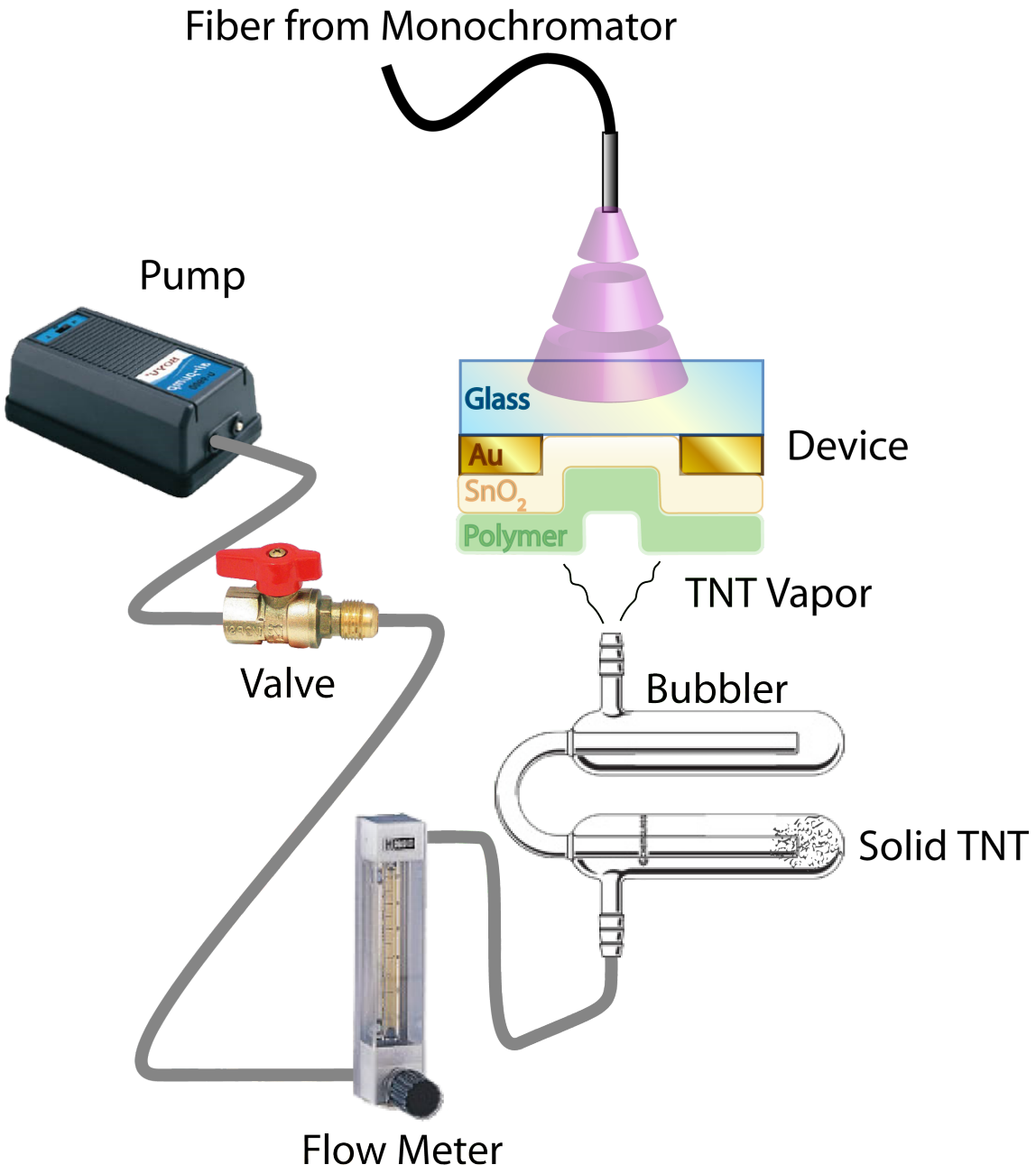

Figure 6-9: Illustration of photocurrent measurement setup incorporating a TNT vapor delivery mechanism.

ZZ-TOP.

After exposure to saturated TNT vapor, the bilayer sensor shows a clear reduction in the shoulder centered at $\lambda = 456$ nm. This shoulder peaks at the point where the ZZ-TOP absorption relative to SnO_2 absorption is at a maximum. Practically, this means that the shoulder peak is red-shifted from the polymer's actual absorption peak. The decrease in the quantum efficiency indicates quenching of the polymer's ability to generate excitons and consequently free carriers. Fixing the wavelength at $\lambda = 456$ nm and measuring the photocurrent versus time provides further evidence for a reduced photocurrent signal due to the introduction of TNT vapor. Aside from the reduced photoresponse of ZZ-TOP, the rest of the bilayer profile remains the same, indicating that TNT cannot diffuse to the SnO_2 film or that SnO_2 does not respond to TNT. Further testing with a single film of SnO_2 reveals that it has no response to saturated TNT vapor. Thus, we have successfully demonstrated the transduction of a chemical signal into a differential photocurrent, and provided more evidence to support the bilayer sensor device model developed earlier.

Reusability of the fluorescent polymer for multiple detection events is directly related to the strength of the interaction between the analyte and the polymer. Weaker interactions such as physisorption impart a greater ability to refresh the polymer (i.e. with a clean gas stream), but it also results in a weaker quenching response. Strong interactions such as chemisorption or charge transfer result in strong quenching but make the removal of adsorbed analyte more difficult. In the SnO_2/ZZ-TOP sensors, the TNT-polymer interaction is most likely a charge transfer event, based on the energy levels of the materials involved, and leads to significant difficulty in refreshing the polymer. Some methods of removing the TNT from the polymer include heating to desorb the analyte and rinsing with methanol to dissolve the TNT. Another effective recovery method involves pulling vacuum (30 inHg) on the sample for 30 minutes. While all of these methods represent effective ways of recovering the polymer film, heating has been shown to be the most practical for real-world applications where portability and speed of response are critical.

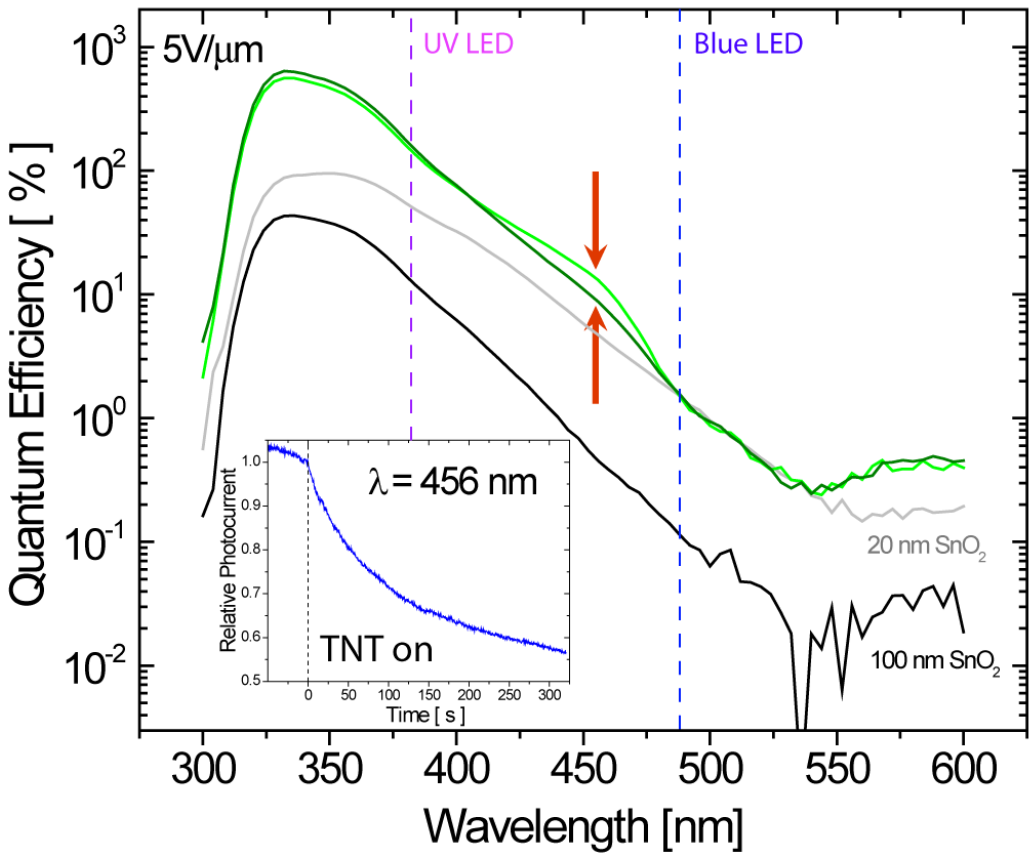

Figure 6-10: Semi-log spectral response characteristics for devices containing SnO_2 and ZZ-TOP. All devices have same applied electric field (5 V/μm). 100.0 ± 0.5 nm SnO_2 film (black) is less quantum efficient than 20.0 ± 0.5 nm SnO_2 film (grey). 100.0 ± 0.5 nm SnO_2/17.0 ± 0.5 nm ZZ-TOP before TNT exposure (green) is plotted against same device after TNT exposure (dark green). Inset: Real-time plot of photocurrent decay at a fixed wavelength of λ = 456 nm upon TNT vapor exposure. TNT vapor is introduced at time t = 0 s.

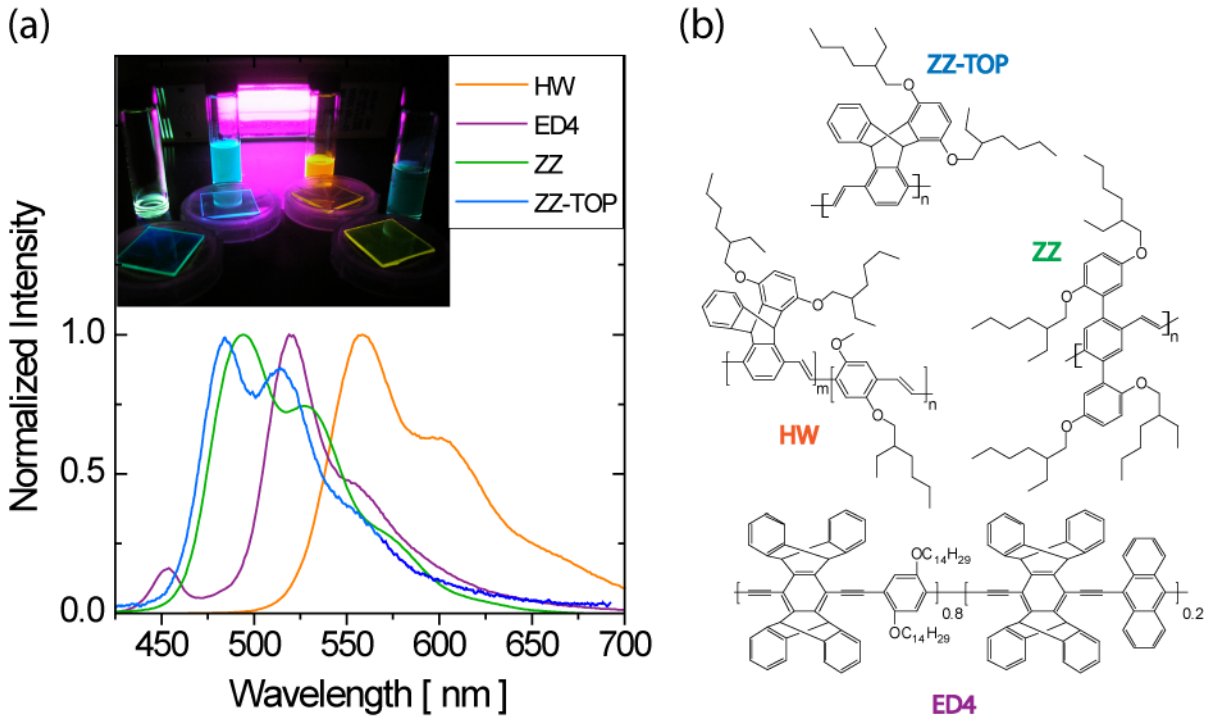

Figure 6-11: (a) Normalized emission spectra of various chemosensitive fluorescent polymers. Inset: photograph of UV-excited polymers in solution and thin film. (b) Chemical structures of various chemosensitive fluorescent polymers.

6.3.1 Developing a Sensor Platform Technology

One of the aforementioned benefits of the bilayer heterojunction photoconductor is that it can act as a sensor platform to incorporate various chemosensitive fluorescent polymers. Proving that this effect is not unique to the combination of ZZ-TOP and SnO_2, we have experimented with a number of different TNT-sensitive fluorescent polymers [Fig. 6-11].

Figure 6-12 compiles the results of photocurrent measurements performed on ZZ, ED4, and HW polymers before and after exposure to saturated TNT vapor. All of the polymers used were solvated in toluene at a concentration of 1 mg/mL and spun at 3000 rpm for 60 seconds. The polymer/SnO_2 sensors exhibited a differential signal due to quenching of the polymer and an improved bilayer photocurrent relative to the single SnO_2 control device, suggesting the formation of a Type-II heterojunction in all cases. However, both the ZZ and HW polymer were spun onto a thinner 20.0 ± 0.5 nm SnO_2 film. In both of these cases, the quenched signal is no longer limited

to the absorption profile of the polymer, affecting the entire absorption spectrum including both the polymer and the metal oxide [Fig. 6-12(a)]. ZZ-TOP and ED4 were spin-coated onto thicker 100.0 ± 0.5 nm SnO_2 films, which do not exhibit a reduced photocurrent over SnO_2's absorption profile.

Without AFM data of the thinner SnO_2 film it is difficult to conclusively explain this phenomenon. However, many metal oxides will exhibit island growth when deposited at similar thicknesses on glass due to poor wetting. Thus, if the 20 nm SnO_2 film is incomplete then the TNT quenching may be negatively affecting the charge carrier collection efficiency of the device. Because as the dissociated carriers must hop through some combination of metal oxide crystallites and polymer regions while traversing the channel, the quenched polymer regions may exhibit lower conductivities which would affect the carriers that were photogenerated by SnO_2.

While each bilayer sensor reacts to the TNT vapor, the response time and magnitude of response was different for each case. Plotting the aggregated real-time data of all four polymer/metal oxide devices, it is evident that the HW/SnO_2 device displays the best performance [Fig. 6-13]. The 70% quench response over 125 seconds is comparable to the amount of fluorescence quenching that occurs in similar polymer films [7, 11, 28, 29].

By varying the flow rate, it is possible to change the amount of TNT delivered to the sensor. Using the HW polymer/metal oxide device as an example, we obtain a plot of response time versus flow rate [Fig. 6-13]. There is a clear saturation point where the time constant approaches 100 ms. By varying the time steps we were able to determine that this saturation point was not an artifact of the measurement but rather intrinsic to the device itself. Thus, it is possible to estimate the amount of TNT necessary to elicit a response.

Without proper gas chromatography and mass spectrometry equipment, it is impossible to know the real dose of TNT being delivered to the samples. However, a reasonable upper bound on sensitivity can be calculated by assuming we have saturated TNT vapor and that there are no effects from convective flow. The following

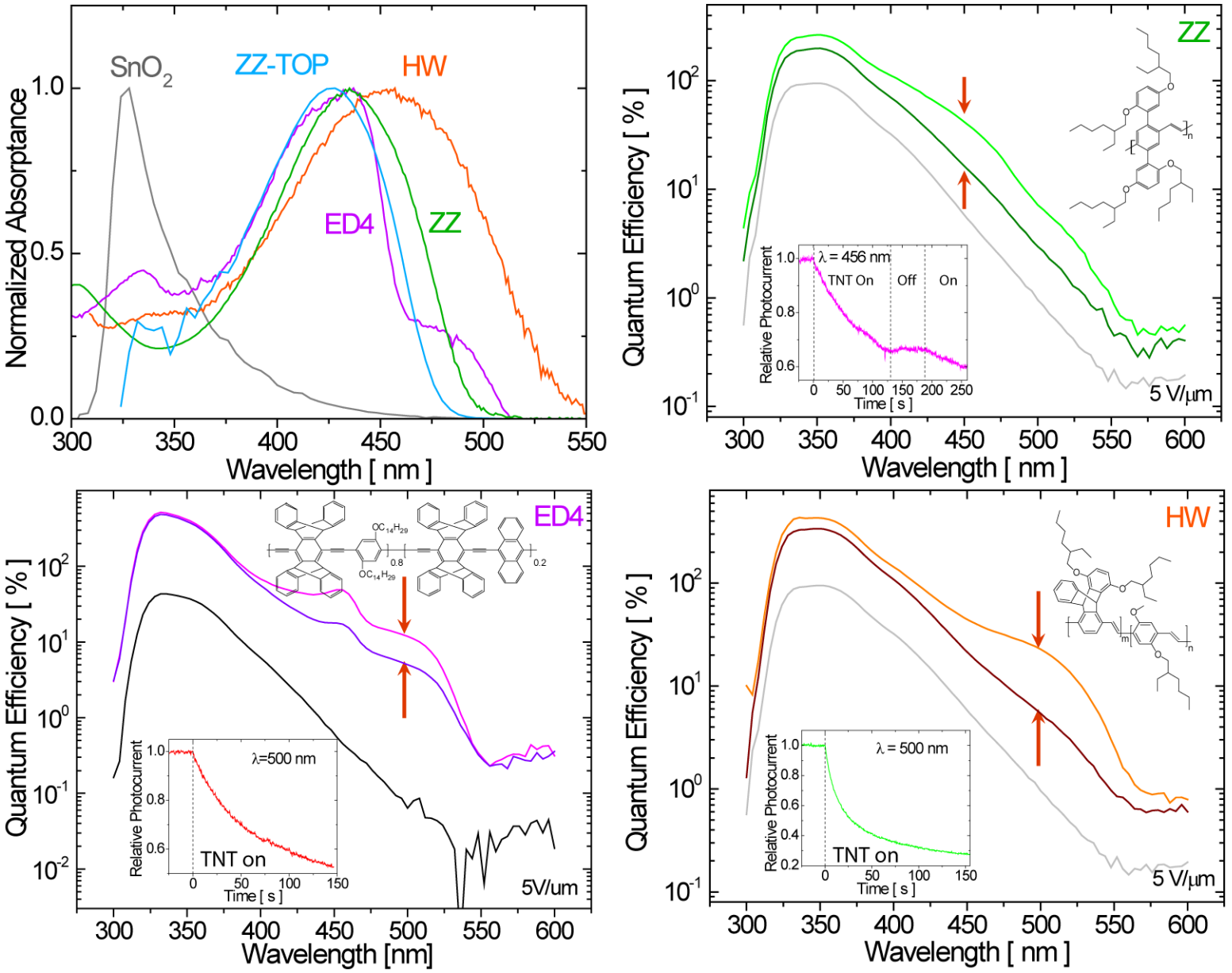

Figure 6-12: (a) Normalized absorption spectra of a 100.0 ± 0.5 nm SnO_2 film (grey), 5.0 ± 0.5 nm HW film (orange), 17.0 ± 0.5 nm ED4 film (magenta), 18.0 ± 0.5 nm ZZ film (blue), and 17.0 ± 0.5 nm ZZ-TOP film (green). Spectral response at 5 V/μm of (b) 20.0 ± 0.5 nm SnO_2/18.0 ± 0.5 nm ZZ (c) 100.0 ± 0.5 nm SnO_2/17.0 ± 0.5 nm ED4 (d) 20.0 ± 0.5 nm SnO_2/5.0 ± 0.5 nm HW before and after exposure to 300 cc/min saturated TNT vapor. Insets: Photocurrent vs. time plot at (b) $\lambda = 456$ nm and (c)/(d) at $\lambda = 500$ nm and TNT vapor on at t = 0 seconds.

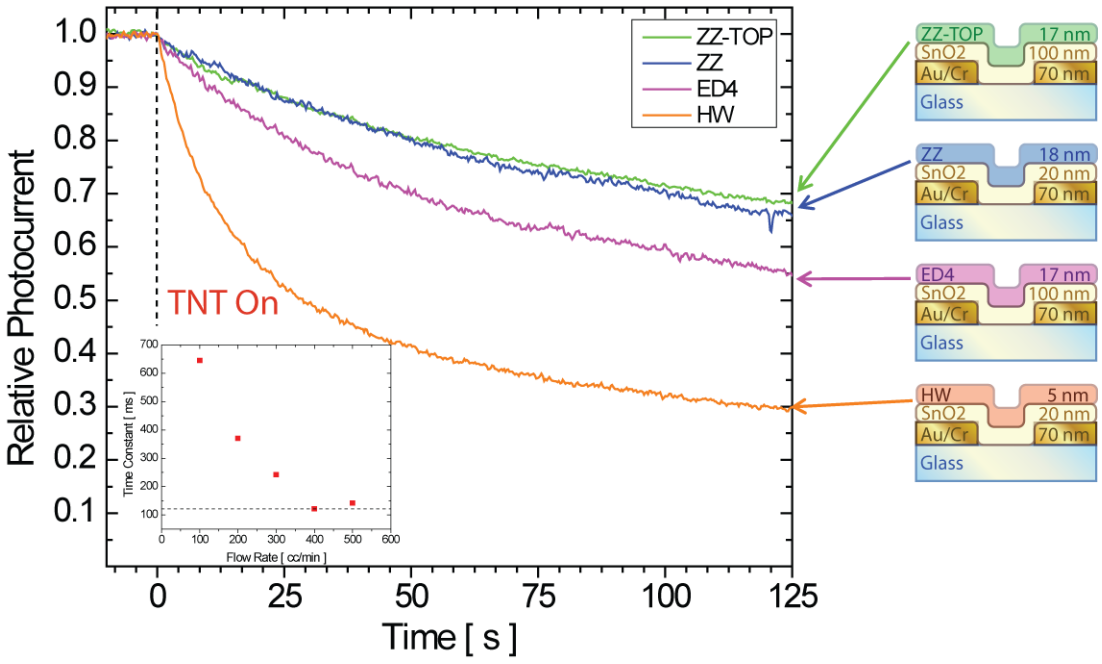

Figure 6-13: Normalized photocurrent vs. time plot of various chemosensitive fluorescent polymer/metal oxide devices. Inset: Time constants from exponential fits vs. flow rate of 20.0 ± 0.5 nm SnO_2/5.0 ± 0.5 nm HW device.

formula, derived from the ideal gas law, can be used for this purpose:

$$MW_{TNT} \times A \times \frac{PV}{RT}, \tag{6.3.1}$$

where MW_{TNT} is the molecular weight of TNT (227 g/mol), A is the ratio of the active device area to the size of the substrate (assuming even distribution of vapor), P is the pressure (in atm), R is the universal gas constant, T is the temperature (in K), and V is the volume (in mL) of TNT delivered to the sensor. The volume of TNT delivered is a function of the flow rate and can be calculated with

$$V = \varphi \times \tau \times \xi\,(T)\,, \tag{6.3.2}$$

where φ is the flow rate (in cc/s), τ is the response time (in s), and $\xi\,(T)$ is the vapor pressure of TNT at a given temperature (10 ppb at room temperature) [30]. By using a signal to noise ratio of 3 to 1, where the noise is the variance of the signal

before TNT vapor is introduced, it is possible to extract a response time from the real-time data. The response time is the difference between the time TNT vapor is introduced and the time when the signal drops an amount equal to 3 times the value of the noise (~ 3 seconds). Thus, the calculation yields a TNT detection limit of roughly 1 picogram. While this level of detection is still 3 orders of magnitude inferior to the commercial Fido sensor, it is on par with other commercially available explosives detection systems. A direct comparison of the proof-of-concept bilayer sensor with the highly engineered Fido system is not entirely fair, given that the bilayer sensor can be further optimized for improved performance. In addition, the ability to transduce the chemical signal directly from any chemosensitive fluorescent polymer into an electrical signal makes this an attractive sensor technology.

6.4 Summary

In this chapter we have successfully demonstrated a bilayer heterojunction explosives sensor and a general sensor platform for chemosensitive fluorescent polymers. Further characterizion of the bilayer heterojunction sensor will greatly improve performance. Careful studies of response times versus polymer and metal oxide thickness are necessary to optimize device sensitivity. Once the device structure is optimized, dosing experiments can be applied to quantify the limits of detection. In addition, specificity testing should be carried out to determine whether that particular polymer attribute is inherited in the bilayer devices. Finally, measuring the change in sensitivity with varying illumination intensity and bias are two more parameter spaces that could potentially lead to the ability to tune the sensitivity, effectively enhancing the sensor's dynamic range.

In order to optimize the bilayer sensor, the devices should incorporate thinner polymer films so that the TNT can quench as much of the film as possible without having to diffuse into the bulk. This modification must be done in conjunction with reducing the photoresponse of the underlying CTL so that the differential signal can be extracted from the background response. One way to accomplish this would be to

synthesize polymers with absorption profiles that are red-shifted away from the metal oxide absorption profile. This shift would prevent the metal oxide photoresponse from swamping out the smaller signal from the thin polymer films.

Chapter 6 References

[1] G. Zorpette. Countering IEDs. *IEEE Spectrum*, September 2008.

[2] T. Gao, M.D. Woodka, B.S. Brunschwig, and N.S. Lewis. Chemiresistors for Array-Based vapor sensing using composites of carbon black with low volatility organic molecules. *Chemistry of Materials*, 18(22):5193–5202, October 2006.

[3] T. C Pearce, S. S Schiffman, H. T Nagle, and J. W Gardner, editors. *Handbook of Machine Olfaction*. Wiley-VCH, Weinheim, 2003.

[4] A. Rose, Z. G Zhu, C. F Madigan, T. M Swager, and V. Bulovic. Sensitivity gains in chemosensing by lasing action in organic polymers. *Nature*, 434(7035):876–879, 2005.

[5] B. Lourdes, D. N Reinhoudt, and M. Crego-Calama. Design of fluorescent materials for chemical sensing. *Chemical Society Reviews*, 36:993–1017, 2007.

[6] S. W Thomas, G. D Joly, and T. M Swager. Chemical sensors based on amplifying fluorescent conjugated polymers. *Chemical Reviews*, 107:1339–1386, 2007.

[7] T. M Swager. The molecular wire approach to sensory signal amplification. *Accounts of Chemical Research*, 31(5):201–207, 1998.

[8] Q. Zhou and T. M Swager. Fluorescent chemosensors based on energy migration in conjugated polymers: The molecular wire approach to increased sensitivity. *Journal of the American Chemical Society*, 117(50):12593–12602, 1995.

[9] J. S Yang and T. M Swager. Porous shape persistent fluorescent polymer films: An approach to TNT sensory materials. *Journal of the American Chemical Society*, 120(21):5321–5322, 1998.

[10] J. Yang and T. M. Swager. Fluorescent porous polymer films as TNT chemosensors: Electronic and structural effects. *Journal of the American Chemical Society*, 120(46):11864–11873, November 1998.

[11] C. J Cumming, C. Aker, M. Fisher, M. Fox, M. J la Grone, D. Reust, M. G Rockley, T. M Swager, E. Towers, and V. Williams. Using novel fluorescent polymers as sensory materials for above-ground sensing of chemical signature compounds emanating from buried landmines. *IEEE Transactions on Geoscience and Remote Sensing*, 39(6):1119–1128, 2001.

[12] J. S Kim, D. T McQuade, A. Rose, Z. G Zhu, and T. M Swager. Directing energy transfer within conjugated polymer thin films. *Journal of the American Chemical Society*, 123(46):11488–11489, 2001.

[13] K. Kuroda and T. M Swager. Self-amplifying sensory materials: Energy migration in polymer semiconductors. *Macromolecular Symposia*, 201:127–134, 2003.

[14] J. Sung and R. J Silbey. Quantitative relationship between analyte concentration and amplified signal intensity of a molecular wire sensor. *Analytical Chemistry*, 77(19):6169–6173, 2005.

[15] N. D Kumar, J. D Bhawalkar, P. N Prasad, F. E Karasz, and B. Hu. Solid-state tunable cavity lasing in a poly(para-phenylene vinylene) derivative alternating block co-polymer. *Applied Physics Letters*, 71(8):999–1001, 1997.

[16] F. Hide, B. J Schwartz, M. A Diaz-Garcia, and A. J Heeger. Conjugated polymers as solid-state laser materials. *Synthetic Metals*, 91(1-3):35–40, 1997.

[17] C. Madigan and V. Bulovic. Modeling of exciton diffusion in amorphous organic thin films. *Physical Review Letters*, 96:046404, 2006.

[18] M. Csele. *Fundamentals of light sources and lasers*. Wiley-IEEE, Hoboken, NJ, 2004.

[19] A. Rose, Z. Zhu, C. F Madigan, T. M Swager, and V. Bulovic. Chemosensory lasing action for detection of TNT and other analytes. *Proceedings of SPIE*, 6333:6330Y1–6330Y7, 2006.

[20] J. L. G. Fierro and J. L. G. Fierro. *Metal oxides*. CRC Press, Boca Raton, 2006.

[21] W. Alan Doolittle, Alexander G. Carver, and Walter Henderson. Molecular beam epitaxy of complex metal-oxides: Where have we come, where are we going, and how are we going to get there? In *J. Vac. Sci. Technol. B*, volume 23, pages 1272–1276. AVS, May 2005.

[22] P. J. Wright, C. J. Anthony, M. J. Crosbie, P. P. Donohue, P. A. Lane, and M. A. Todd. CVD of oxide materials for thermal imaging - the role of precursor chemistry. *Journal of Materials Chemistry*, 14(21):3251–3258, 2004.

[23] M. Ritala, K. Kukli, A. Rahtu, P.. I. Risnen, M. Leskel, T. Sajavaara, and J. Keinonen. Atomic layer deposition of oxide thin films with metal alkoxides as oxygen sources. *Science*, 288(5464):319–321, April 2000.

[24] B. B. Lakshmi, P. K. Dorhout, and C. R. Martin. SolGel template synthesis of semiconductor nanostructures. *Chemistry of Materials*, 9(3):857–862, March 1997.

[25] Y. Xu and M. A. A. Schoonen. The absolute energy positions of conduction and valence bands of selected semiconducting minerals. *American Mineralogist*, 85(3-4):543–556, March 2000.

[26] M. Ruske, G. Bruer, J. Pistner, U. Pfffflin, and J. Szczyrbowski. Properties of SnO2 films prepared by DC and MF reactive sputtering. *Thin Solid Films*, 351(1-2):146–150, August 1999.

[27] J. L. Brousseau, H. Bourque, A. Tessier, and R. M. Leblanc. Electrical properties and topography of SnO2 thin films prepared by reactive sputtering. *Applied Surface Science*, 108(3):351–358, March 1997.

[28] D. Zhao and T. M Swager. Sensory responses in solution vs solid state: A fluorescence quenching study of poly(iptycenebutadiynylene)s. *Macromolecules*, 38(22):9377–9384, 2005.

[29] J. S Yang and T. M Swager. Fluorescent porous polymer films as TNT chemosensors: Electronic and structural effects. *Journal of the American Chemical Society*, 120:11864–11873, 1998.

[30] J. C. Oxley, J. L. Smith, K. Shinde, and J. Moran. Determination of the vapor density of triacetone triperoxide (TATP) using a gas chromatography headspace technique. *Propellants, Explosives, Pyrotechnics*, 30(2):127–130, 2005.

Chapter 7

Concluding Remarks and Future Areas of Research

Great is the art of beginning, but greater is the art of ending.

ROBERT A. HEINLEIN
Author

The interdisciplinary research undertaken in this thesis resulted in the development of a novel solid-state vapor-phase explosives sensor. As an electrical engineer, there was a motivation to develop a device platform that could be customized and optimized while ultimately providing an output that is electrical in nature for downstream readout circuitry. This led to a using a lateral photoconductor architecture that improved upon the simple transduction mechanism of the chemiresistor. Inspiration for separating the chemical sensing function from electrical characteristics came from understanding the benefits of dual-layer photoreceptor drums invented during the heyday of xerographic development and the present challenges of developing fluorescent polymer sensors. Through the design, fabrication, and characterization of lateral heterojunction photoconductors, we have not only developed a viable sensor platform technology, but also a platform for investigating device physics at a heterointerface.

7.1 Research Highlights

Some of the useful findings in this thesis include:

- Extending the dual-layer photoreceptor concept (from xerography) of a CTL and EGL by incorporating the dual-layer structure into a lateral device
- Demonstrating photoconductive gain in a bilayer device
- Demonstrating that recombination rate is dominated by bimolecular recombination in bilayer devices
- Integration of various material sets including QDs, J-aggregates, polymers, and metal oxides into viable photoconductors
- Design of trilayer devices that modulate interfacial carrier dynamics
- Demonstrating solid-state vapor-phase detection of as little as 1 pg of TNT
- Confirming the ability of the bilayer sensor to be a polymer-independent platform

7.2 Research Opportunities

The work performed in this thesis has proved the utility of the bilayer heterojunction photoconductor as a device physics toolkit as well as a platform for chemical sensing. A number of interesting experimental results warrant further scientific attention and investigation, representing opportunities to not only delve deeper into the physics of organic materials at an interface but also the opportunity to extend and improve the solid-state chemical sensing platform.

One pressing need in the field of chemical and biological sensors is the ability to tune the sensitivity of a given sensor. For example, there may be situations that require high sensitivity at the cost of a large number of false positives, while at other times, lower sensitivity with fewer false positives will suffice. If this tuning ability

could be achieved with a simple adjustment, the sensor could be more useful in a wider range of environments and applications. The bilayer sensor has the potential for a wide dynamic range by adjusting either operating temperature or intensity of illumination. In the FIDO™detector, the polymer is heated to promote faster TNT-polymer absorption/desorption kinetics at the surface. Therefore, by heating the bilayer sensor, the TNT will bind less strongly to the polymer and result in lower sensitivities. Heating will also result in larger background dark currents as the metal oxide's free carriers become more mobile. This requires paying close attention to the resulting signal to noise ratio (SNR). Changing the illumination intensity will modify the SNR by providing a "knob" to tune exciton population and consequently the free carrier concentration at the interface. Thus, altering the excitation intensity will ultimately make the sensor more or less sensitive. These two methods of changing sensitivity are simple enough to be incorporated as an electrically tunable parameter made available to the end user.

A simple extension of the bilayer sensor work would be to extend the platform to include solution-phase detection. The sensors in this work incorporate polymeric and metal oxide materials, which will not solvate in aqueous solutions. This would potentially enable the sensors to operate in aqueous environments, which are common to many biomedical applications such as blood diagnostics.

We have demonstrated that extending the lateral heterojunction platform to include multilayers has potential benefits to overall device efficiency. Further exploration of different groups of materials will be necessary to elucidate the physical mechanisms involved. Key to this effort will be utilizing film deposition methods such as atomic layer deposition (ALD) that can exert fine control over film thickness and morphology, both of which are critical in the interpretation of experimental data. Once multilayer devices are well understood, translating those insights into designing multilayer chemical sensors will enable the engineering devices for better sensitivity.

In order to expand the utility of the bilayer chemical sensor platform, adding detection of different high-value analytes will be an important piece of ongoing research. One way to quickly build this capability is to develop a modular library of chemi-

cal building blocks that can be used to synthesize new fluorescent polymers that are specific to any analyte of interest. Another interesting vein of research would be to leverage the growing availability of functionalized nanoparticles such as quantum dots or carbon nanotubes within the bilayer heterojunction device framework.

Finally, the ultimate goal of this work is to enable a new class of solid-state chemical sensors that are amenable to miniaturization and engineering. Towards this goal, this thesis strove to define the available parameter space for optimizing the bilayer heterojunction photoconductor. The results of this work will certainly facilitate the incorporation of many more chemosensitive fluorescent polymers into viable sensors. The potential to fabricate arrays of highly specific and highly sensitive sensors with wide dynamic range holds promise for the bilayer sensor platform to find use in many future applications within the defense, medical, environmental, and industrial processing industries. While this work opens many new avenues for future endeavor, the focus must always remain on the end application, as the sensor will only be as useful as the analyte it is searching for.